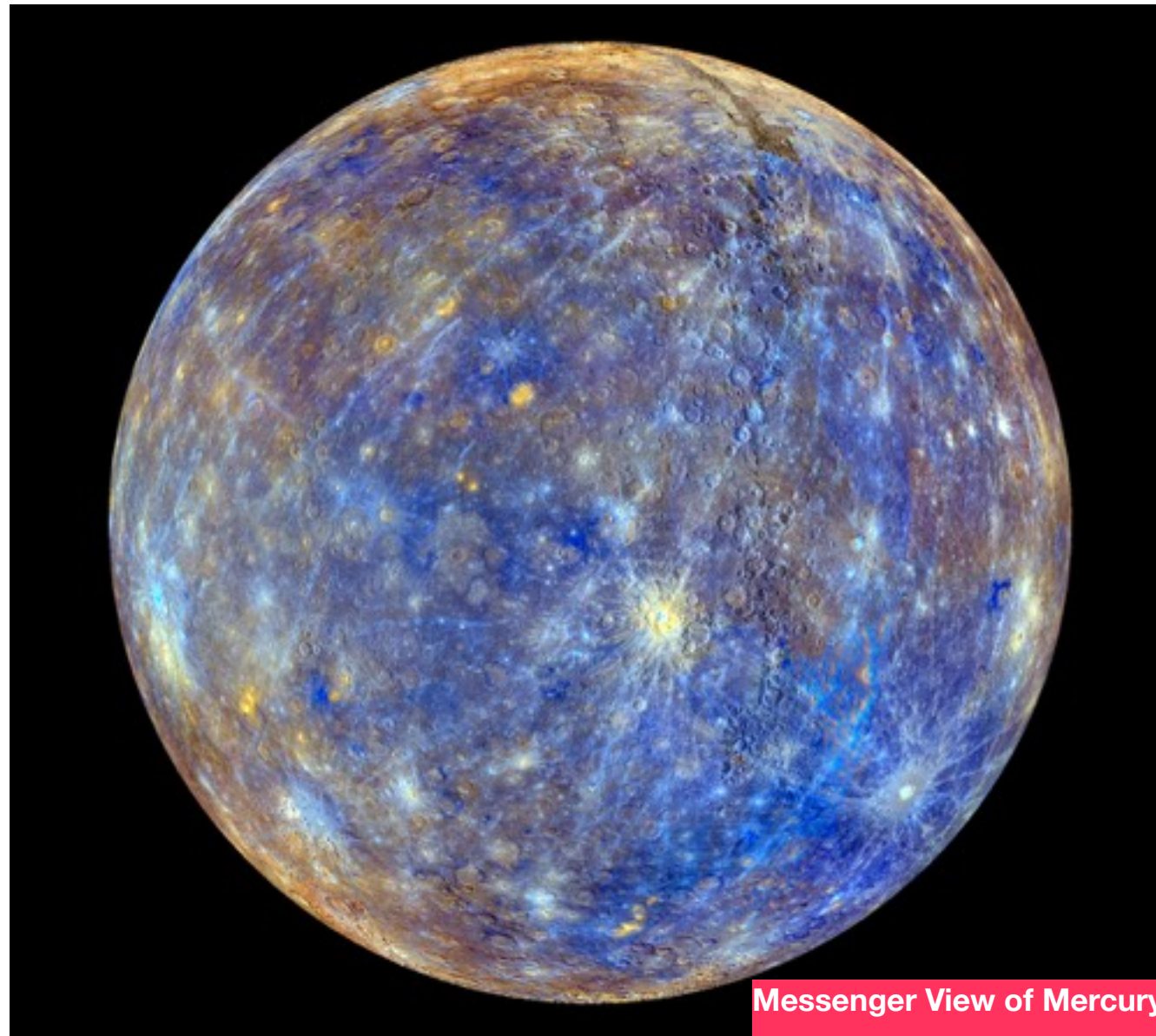
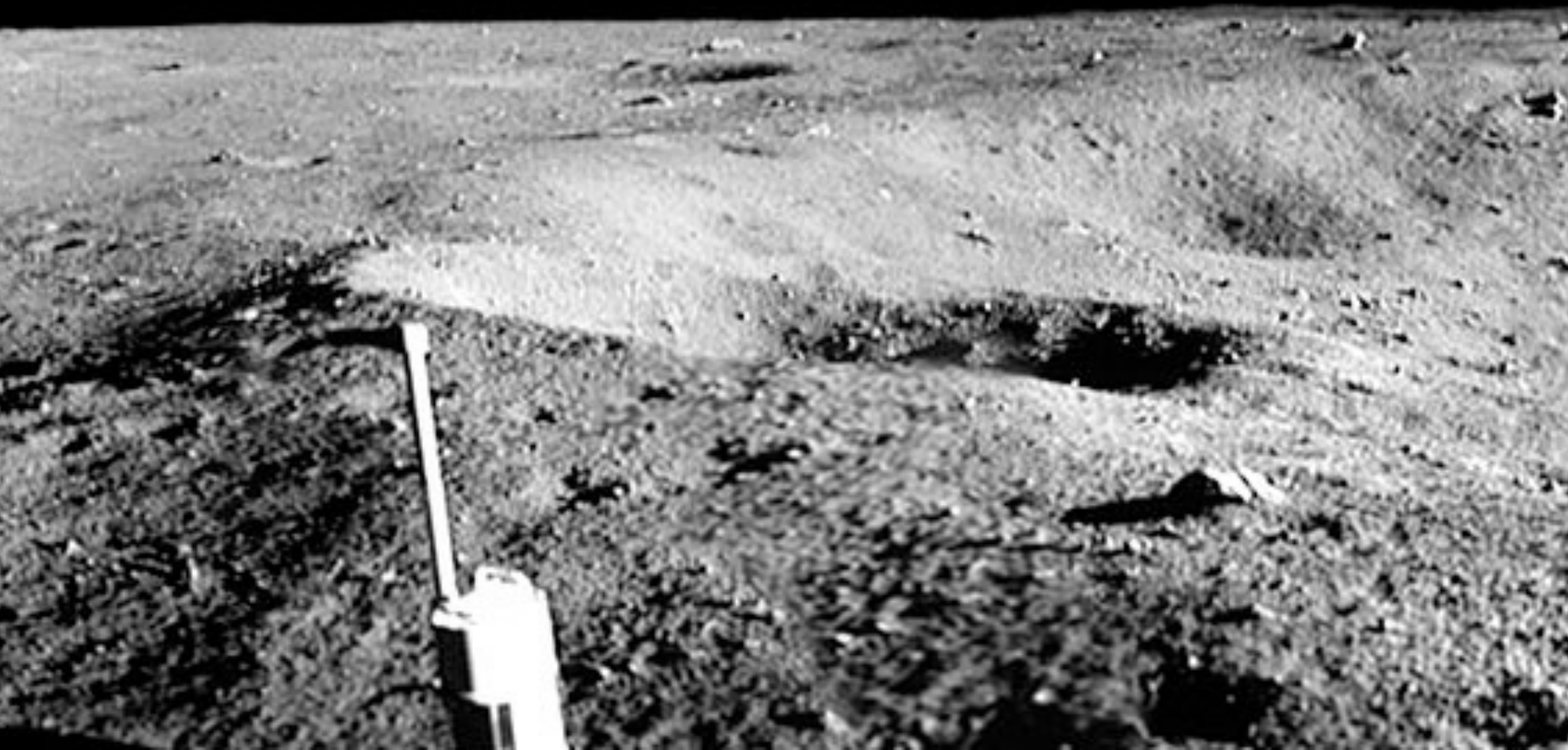


Impact Geology: The Basics



Preface

Rocky Bottom Crater:
Apollo 11



You may ask what motivated a retired metallurgist like me to write a book on Impact Geology. Well it started with a rereading of technical report I co-authored in 1982 which included some experimental data on the behavior of titanium and beryllium resulting from hypervelocity impact of small laboratory-scale projectiles. Shortly thereafter I read H. J. Melosh's book entitled "Impact Cratering: A Geologic Process" which presents an oft quoted impact cratering model, and from the very beginning, Melosh's impact cratering model struck me as inconsistent with my observations of the impact cratering process in either titanium or beryllium. Needless to say, my curiosity was peaked, and as they say, the rest is history.

The primary intent of this volume is to define and present an impact cratering model that is consistent with observational data for most materials at all scales and is consistent with well established scientific principles. This book contains seminal discussions intended to provide a scientific basis for the field of Impact Geology. This is not an encyclopedic coverage of accepted or proposed geologic impact craters, but rather, the focus is on the illustration of the salient features of geologic impact craters and to show how the physics of the problem is demonstrated in accepted and proposed geologic impact structures on Earth.

In order to provide the reader with a sense of the perspective of the field of Impact Geology, the first chapter of this book provides a brief overview and definition of the subject. The following chapters are moderately technical because of the nature and complexity of the impact cratering process and its

general consequences on the surface of and inside a variety of materials, including geologic materials. The second chapter describes in detail the mechanics of impact crater formation based solidly on observation primarily at laboratory-scale, which will be shown to be extrapolatable to full-scale geologic impact structures...the model is significantly different from that proposed by Melosh. The third chapter applies the fundamentals of the impact cratering process to an original analysis of observed structural features of two accepted dry-land geologic impact structures (Upheaval Dome and the Vredefort Dome) and one oceanic impact structure (Chesapeake Bay) found on Earth.

During the research for this book, it became apparent that there was a general lack of understanding of the actual (as opposed to ideal) deformation and fracture behavior of materials, and because understanding the basics of the mechanical behavior of solids is crucial to the field of Impact Geology (and structural geology in general), Chapter 4 is included. Chapter 5 was written to illustrate the application of the science described in Chapter 4 and the previous chapters to several substructures that are commonly associated with probable geologic impact structures on Earth. Chapter 6 provides an example of geologic impact structure identification and verification that further illustrates the application of most of the fundamentals that have been presented in the previous chapters.

Dr. Lynn B. Lundberg, PhD

December 19, 2016

Contact at: lburtlundberg@me.com

Contents

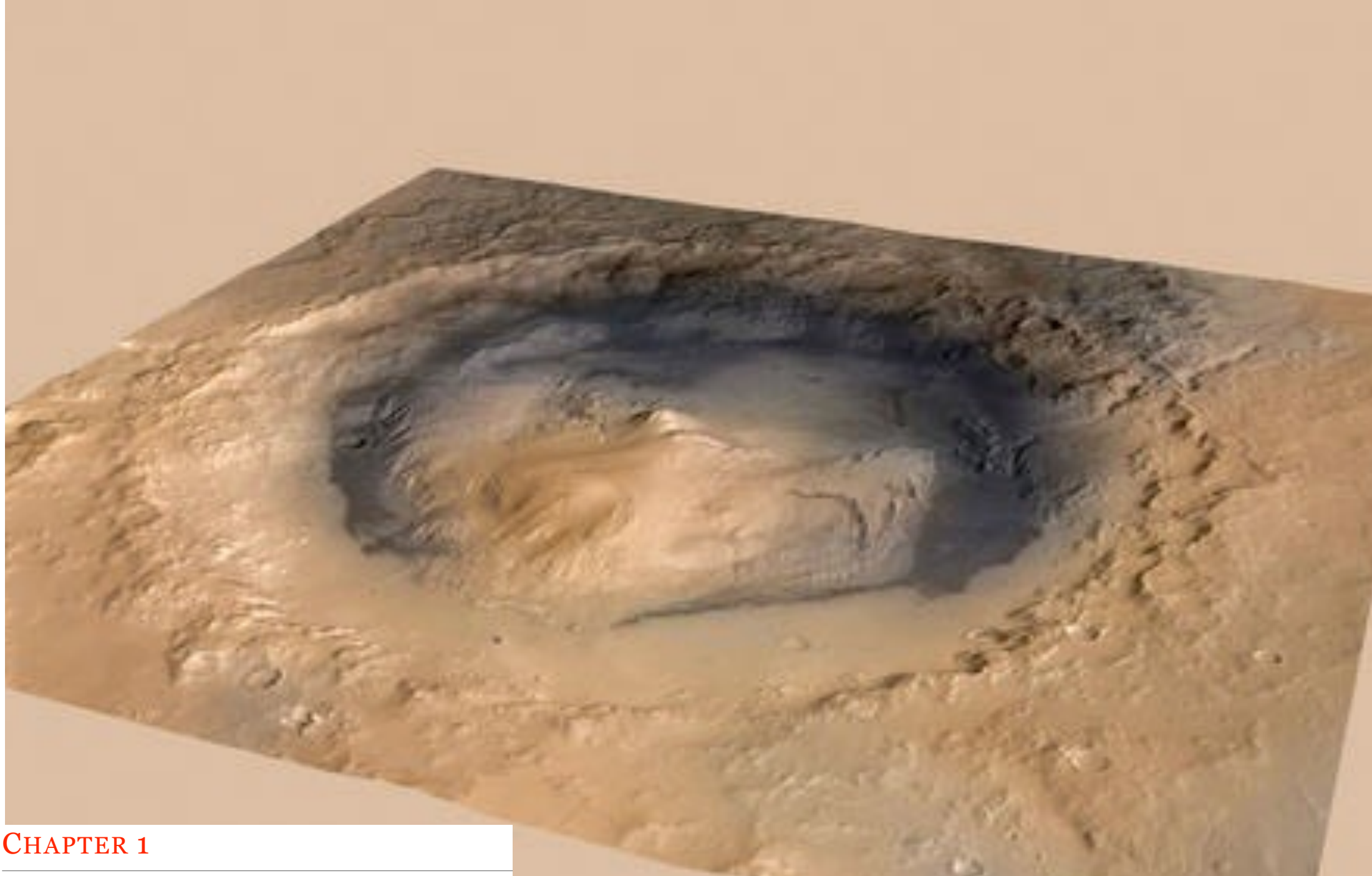
1. Impact Geology?	9
1.1 Impact Structures Everywhere	11
1.1.1 Geologic Impact Structures on Earth's Moon	11
1.1.2 Impact Crater Numbers and Cratering Frequency	14
1.1.3 Dry-Land Geologic Impact Structures on Earth	18
1.1.4 Impact Structures in Earth's Oceans	20
1.1.5 Atmospheric Effects of Incoming Meteors	20
1.2 Extraterrestrial Impactors	24
1.2.1 A Comet up Close	24
1.2.2 Asteroids	26
1.3 Formation of Geologic Impact Structures: A Preview	28
1.3.1 Cratering Dynamics	29
1.3.2 Correlations between Laboratory-Scale and Full-Scale Geologic Impact Structures	32
1.4 Where We go from Here	34
1.5 Chapter 1 Reference	35
2. Mechanics of Impact Structure Formation	37
2.1 Early-Stage Impact Cratering	39
2.1.1 Contact of Impactor and Target	39
2.1.1.1 Ejecta Jetting Effects on Mars and Earth's Moon	40
2.1.1.2 Mechanics of the contact process	41

2.1.2	Impactor Coupling and Primary Crater Formation Dynamics	43
2.1.2.1	Early Normal Incidence Impact Cratering	44
2.1.2.2	Cratering Dynamics Inside the Target	45
2.1.2.3	Impact cratering in water	47
2.1.2.4	Hypervelocity Impact Cratering in and Perforation of Metal Targets	48
2.1.2.5	Crater Scaling in Ductile Metals	50
2.1.3	Early Cratering in Oblique Incidence Impact	53
2.1.3.1	Oblique Impact Cratering Record inside a Dense Solid	53
2.1.3.2	Oblique Impact Crater Planforms in Ductile Metals	55
2.1.3.3	Shock Front Record inside Highly Porous Solids	57
2.2	Late-Stage Impact Cratering	59
2.2.1	Laboratory-Scale Normal Impact Cratering in Beryllium	61
2.2.2	Laboratory-Scale Normal Impact Cratering, Craters and Ejecta for Sandstone	62
2.2.3	Laboratory-Scale Normal Impact Crater Ejecta Mass for Granite	67
2.3	Chapter 2 References	68
3.	Structural Features of Geologic Impact Craters	71
3.1	Structural Features of the Upheaval Dome	73
3.1.1	Upheaval Dome Crater Complex	74
3.1.1.1	Upheaval Dome Central Uplift	74
3.1.1.2	Structural Details of the Primary Crater	76
3.1.1.3	Structural Features of the Secondary Crater	77
3.1.2	Beyond the Upheaval Dome Crater Complex	79

3.1.2.1 Upheaval Dome Ejecta Blanket	79
3.1.2.2 Multi-Ring Structures around the Upheaval Dome	80
3.2 Anatomy of the Vredefort Dome Impact Structure	82
3.2.1 Vredefort Dome Crater Complex	83
3.2.1.1 Some Structural Details of the Central Uplift of the Vredefort Dome	85
3.2.1.2 Some Structural Details of the Primary Crater	87
3.2.1.3 Secondary Crater and the Collar Wall	89
3.2.2 Outside the Vredefort Dome Crater Complex	91
3.3 Anatomy of the Chesapeake Bay Impact Structure	93
3.4 Chapter 3 References	96
4. Flow and Fracture of Real Materials: The Fundamentals	98
4.1 Shear Localization	100
4.1.1 Shear localization in Liquids	101
4.1.2 Shear localization in Metals	102
4.1.3 Localized Shear Branching	106
4.1.4 Localized Shear Band Thickening	107
4.1.5 Shear Localization in Granular Materials	107
4.1.6 Computer Simulation of Localized Shear Deformation	109
4.2 Adiabatic Localized Shear	111
4.2.1 Adiabatic Shear Deformation in Metals	111
4.2.2 Rock Deformation at High Temperatures	112
4.2.3 Localized Shear and Chemical Redistribution	113
4.2.4 Localized Shearing in Silicate Crystals	115
4.2.4.1 Localized Shearing in Zircon Crystals	116
4.2.4.2 Localized Shearing in Quartz Crystals	117
4.3 Chapter 4 References	119

5. Localized Shear in Geologic Structures	122
5.1 Dikes, Pseudotachylites and Shatter Cones	124
5.1.1 Popular Dike Formation Model	124
5.1.2 Observational Based Dike and Pseudotachylite Formation Model	125
5.1.2.1 Impact Dikes and Pseudotachylites in Silicate Rock	126
5.1.2.2 Impact Dikes and Pseudotachylites in Carbonate Rocks	129
5.1.2.3 Shatter Cones	130
5.1.3 Dikes/Faults formed at Low Strain Rates	132
5.1.3.1 Dikes in Ice	133
5.1.3.2 Seismic Dikes/Faults	134
5.2 Dikes as Indicators of Impact Structures	136
5.2.1 Spanish Peaks Dikes	136
5.2.2 Black Dikes of the Teton Range	139
5.3 Chapter 5 References	142

6. Geologic Impact Structure Identification and Verification	144
6.1 Beaverhead/Anaconda Impact Structure	147
6.1.1 B/A-IS Rim Structure	149
6.1.1.1 Beaverhead Range and the B/A-IS	149
6.1.1.2 B/A-IS Overprint Impact Structures at the South End of the Northern Beaverhead Range	152
6.1.1.3 Anaconda Range and the B/A-IS	153
6.1.2 Central Uplift of the B/A-IS	159
6.2 Bitterroot Impact Structure	160
6.2.1 Bitterroot Mylonites	161
6.2.2 Bitterroot Rim Dikes	163
6.2.3 Bitterroot Central Uplift	165
6.3 Chapter 6 References	169
7. Epilogue	171



CHAPTER 1

Impact Geology?

The Gale impact crater on Mars seen above is a classic geologic impact crater that measures 154 km across and has a central uplift that rises 5.5 km above the lowest area inside the crater. This terrestrial impact structure located on a planet with an atmosphere illustrates many structural features that are seen on Earth.

What is Impact Geology, and why should we study the subject? This volume is aimed at answering this question. Here Impact Geology is defined as the branch of geology that deals with the effects of impacts of smaller terrestrial bodies onto the surfaces of larger terrestrial objects such as planets, satellites, asteroids, comets, and other significant cold, solid bodies in our solar system...yes including Earth. The importance of this branch of geology cannot be overemphasized because impacts have played a major role in the formation of most geologic features on the surfaces of every terrestrial object in our solar system.

In this chapter, a few examples of geologic impact structures and related structural features that are currently being cataloged on the surfaces of many terrestrial bodies in our solar system, including Earth, will be introduced. This will include a discussion of the numbers of impact craters that are observed on Earth's moon in order to predict the numbers that we should find on Earth. Next the extraterrestrial impactors that produce these geologic impact structures will be discussed. Finally in this chapter, we will be introduced to the fundamentals of the formation mechanics of geologic impact structures. A detailed discussion of the impact cratering process follows in Chapter 2.

Impact Structures Everywhere

SECTION TOPICS

1.1.1 Geologic Impact Structures on Earth's Moon

1.1.2 Impact Crater Numbers and Cratering Frequency

1.1.3 Dry-Land Geologic Impact Structures on Earth

1.1.4 Impact Structures in Earth's Oceans

1.1.5 Atmospheric Effects of Incoming Meteors

At this point in time, there are fewer than 200 geologic structures on Earth's surface that have been *accepted* (RE: <http://www.unb.ca/passc/ImpactDatabase/>) as being formed by impact even though the surface of the Earth should have encountered a higher impactor flux than its moon. In short, the surface of the Earth should be virtually littered with impact structures much like the surface of Earth's moon, so the challenge remains to identify them and study their features on the basis of their formation mechanics.

Geologic impact structures can be seen in high resolution photographic imagery of the surface of the Earth, Earth's Moon, other planets and moons, and asteroids and comets in our solar system. However, most of the impact structures on Earth lie underwater and are hidden from view. Even though Earth's Moon has no significant atmosphere and consequently has no water or air generated erosional processes, the surface structure of the Moon is analogous to the dry-land surfaces of the Earth. In both cases, older impact structures are modified by subsequent impact overprinting and back-filling by ejecta from subsequent nearby impact events.

1.1.1 GEOLOGIC IMPACT STRUCTURES ON EARTH'S MOON

It has long been recognized that the large number of circular structures seen on the surface of Earth's Moon in [Figure 1.1](#) represent impact structures that have been formed during the lifetime of this dry, airless terrestrial body. As seen, the surface of our Moon is littered with impact structures of varying

sizes, and there is a greater number on the ‘far side’ of the Moon than on the ‘near side.’

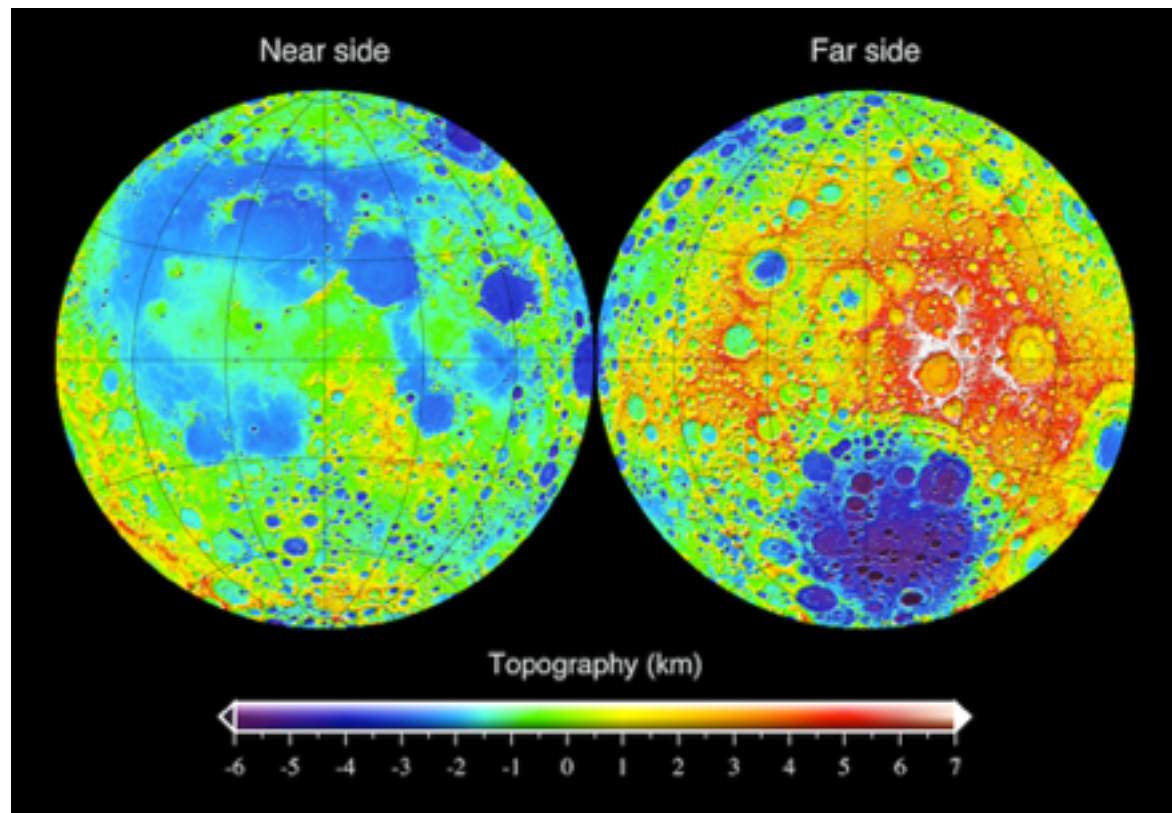


Figure 1.1 Topographic image of the Moon. Data was obtained from NASA’s Lunar Orbiter Laser Altimeter (LOLA) that was flown on the Lunar Reconnaissance Orbiter (LRO).

As the geologic impact structures observed on Earth’s Moon are prototypic of those on Earth, we will briefly examine the Einstein impact structure on the Moon, [Figure 1.2](#), in order to start defining basic features of typical geologic impact structures. Einstein is a relatively large (~300 km across) impact structure that has been overprinted and slightly altered by adjacent and included impacts many times since its formation. The bottom of the primary (inner) crater of the Einstein impact structure lies at least 6 km below the rim of the secon-

dary crater. Interactions from later cratering events are well illustrated in [Figure 1.2](#).

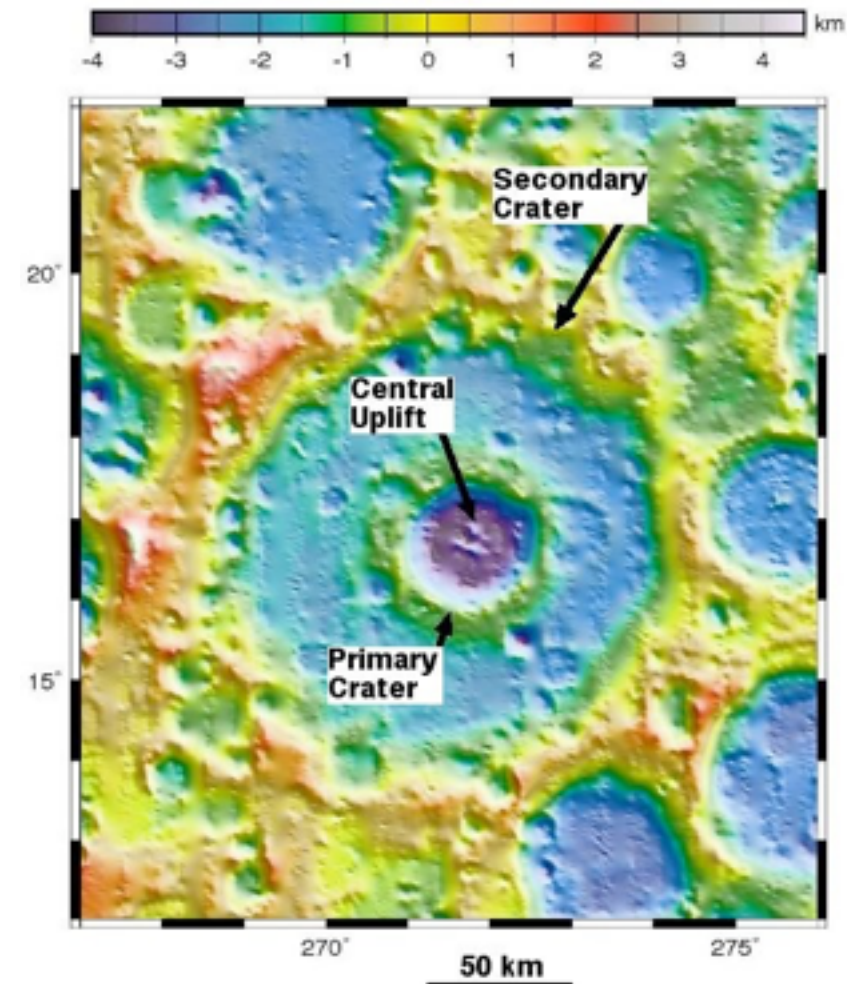


Figure 1.2 Topographic image of the Einstein crater on Earth’s Moon. Data was obtained from NASA’s Lunar Orbiter Laser Altimeter (LOLA) that was flown on the Lunar Reconnaissance Orbiter (LRO).

In this volume, the central crater will be generally referred to as the *primary crater*...frequently referred to in the literature as the transient crater. The primary crater is the first to form during early crater excavation. The outer crater, which forms late in the cratering process, will be referred to in this volume

as the *secondary crater*. The feature seen in the center of a primary crater is frequently referred to as the *central uplift* or *central peak*. The central uplift, which is a common feature in geologic impact structures, forms after the primary crater has been excavated. Central peaks and secondary craters are commonly formed toward the end of the cratering process by rebound flow of material originally located at and below the bottom of the primary crater. (The formation mechanics of central peaks and other structural features will be outlined in Chapter 2.)

An overhead view of the Aristarchus impact crater on the Moon, seen in [Figure 1.3](#), reveals additional structural details of a typical, relatively large impact crater. A small central uplift feature is indicated by the red arrow in the center of the crater. The zone between the rims of the primary and secondary craters is made up of a series of concentric terraces. The color variation in the image in [Figure 1.3](#) reflects differences in reflectivity of material that has been exposed by the crater excavation process.

Both the Moon's Tycho and Copernicus craters exhibit radial ray patterns centered around the crater, see [Figure 1.4](#). These rays, along with the crater, are visible from the

Earth. As will be discussed in Chapter 2, rays around craters indicate blast damage to surrounding surfaces that develops during impactor contact with the target surface.

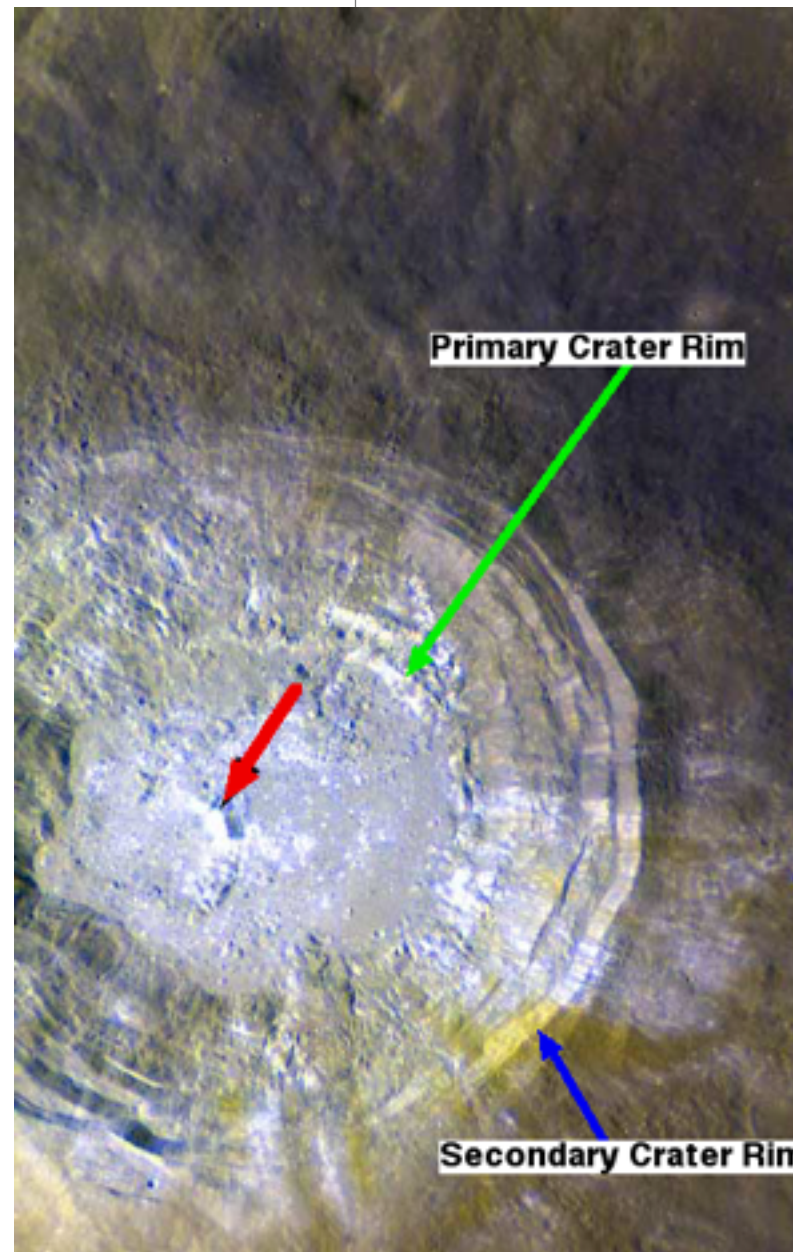


Figure 1.3 Image of the 40-km-diameter Aristarchus crater. Red arrow points to a central uplift. Original image from the NASA's Lunar Reconnaissance Orbiter archives.

Direct surface observations during the Apollo missions have revealed that, except for the very young craters, the impact structures on the Moon are overlain with varying amounts of *regolith*. Regolith is a conglomerate of both indigenous ejecta from impact structures on the Moon and materials accreted from space. Many of the older impact structures are partially or completely buried by ejecta from later impacts.

The Apollo 17 photograph seen in [Figure 1.5](#) reveals many features of the Moon regolith that provide insight into the origin of much of the 'sediment' found on Earth. The flat 'lay-of-the-land' seen in the foreground of the photograph in [Figure 1.5](#) indicates a gravity leveling...sedimentation-like deposition process. There are no erosional mechanisms on the Moon derived from air or water, so regolith lies where it fell as impact ejecta or space dust. Gravity has encouraged downslope material flow. The general makeup of this

regolith is indicated in the tracks left by the Moon rover. The surface is sufficiently competent to have held the weight of the rover wheels even though it includes a significant amount of fine dust within the aggregate.

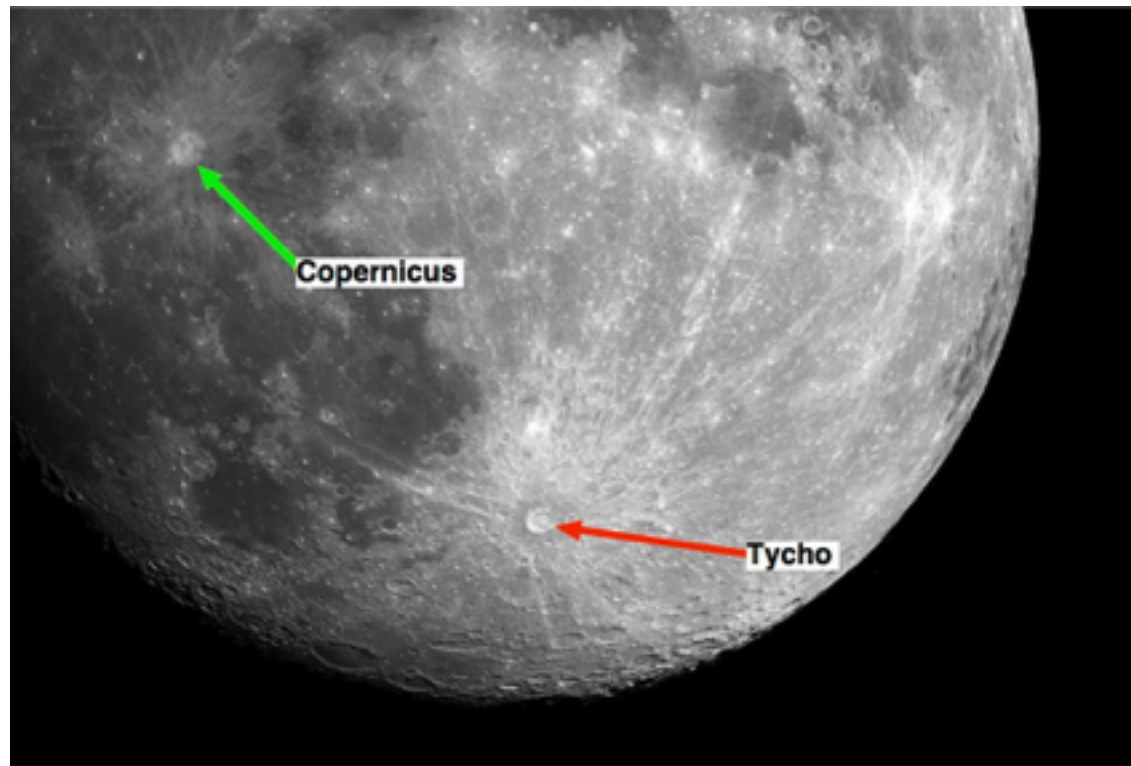


Figure 1.4 Typical rayed craters, Tycho and Copernicus, visible on the near side of the Moon.

The hills surrounding the basin seen in [Figure 1.5](#) is eerily reminiscent of a typical landscape on Earth. Realize that in general the hills seen in the background of [Figure 1.5](#) resulted from the dominant geologic process on the surface of the Moon...impact.



Figure 1.5 Moonscape captured during the Apollo 17 exploration. Photo was found in the Apollo Image Gallery.

1.1.2 IMPACT CRATER NUMBERS AND CRATER-ING FREQUENCY

The surface of Earth's Moon represents a close analog for the morphology as well as the vast number of impact structures that should be found on Earth. It can be stated unequivocally

that there have been significantly more impact structures formed on Earth's surface than on its Moon. Because the Earth and its Moon are located in the same orbit around our sun, these two large terrestrial objects have been subjected to nearly the same overall flux of debris moving through space. However because the overall flux of space debris is enhanced and focused by the gravitational force of the target object, Earth should be subjected to an effective impactor flux that is significantly higher than that of its moon. In fact, Le Feuvre and Wieczorek, 2011 have calculated that the Earth should receive 1.58 times more impacts than its Moon. Fortunately for life on Earth, the overall space debris flux has decreased significantly from the early days of our solar system, and Earth's atmosphere and gravity cause many of the smaller impactors to disintegrate to small, nearly harmless fragments before striking the ground.

The number of impact structures that have accumulated on the surface of the Moon from its beginning is not well known. However, mathematical modeling based on the size, number and distribution of observed impact structures on the Moon provide us with reasonable estimates of the number of impact structures expected to be found on the surface of the Earth. The calculated number of Lunar impact structures having diameters ≥ 1 km is plotted as a function of time in [Figure 1.6](#). The upper graph represents the calculated areal density of craters as a function of time over most of the life of the Moon, while the lower graph focuses on impact events that occurred over the last 900 million years. It should be mentioned that

this model predicts a uniform areal density of impact craters...observed crater clustering is neglected even though crater clusters probably indicate a single impact event. As seen in [Figure 1.6](#), the Lunar impact record indicates that the overall frequency of crater formation has dropped dramatically from the initial formation of this terrestrial body. This graph also indicates that early impact damage was quite pervasive on the Moon and, as can be seen in [Figure 1.1](#), includes several very large impact structures that have been heavily overprinted. In reality, cratering frequency is not uniform (see for example de la Fuente Marcos and de la Fuente Marcos, 2015) mostly due to the fact that extraterrestrial impactors tend to travel in groups or they fragment when they encounter strong gravitational forces or significant atmospheres.

The fragmentation of extraterrestrial impactors plays a major role in a determination of impact frequency. We are learning that comets are especially prone to fragmentation. In fact, the mechanical integrity of comets tends to be so poor that gravitational forces from close approach to planets and our sun can produce breakup. Fragments remaining after breakup can contain sufficient momentum and kinetic energy and structural integrity to cause considerable damage on impact. As an illustrative example, Comet Shoemaker-Levy 9 had been orbiting Jupiter intact, but it eventually demonstrated classic breakup into its more mechanically sound components due to the strong gravitational forces around Jupiter. A photographic image of the many comet fragments resulting from the breakup of Shoemaker-Levy 9 is seen in [Figure 1.7](#). Diame-

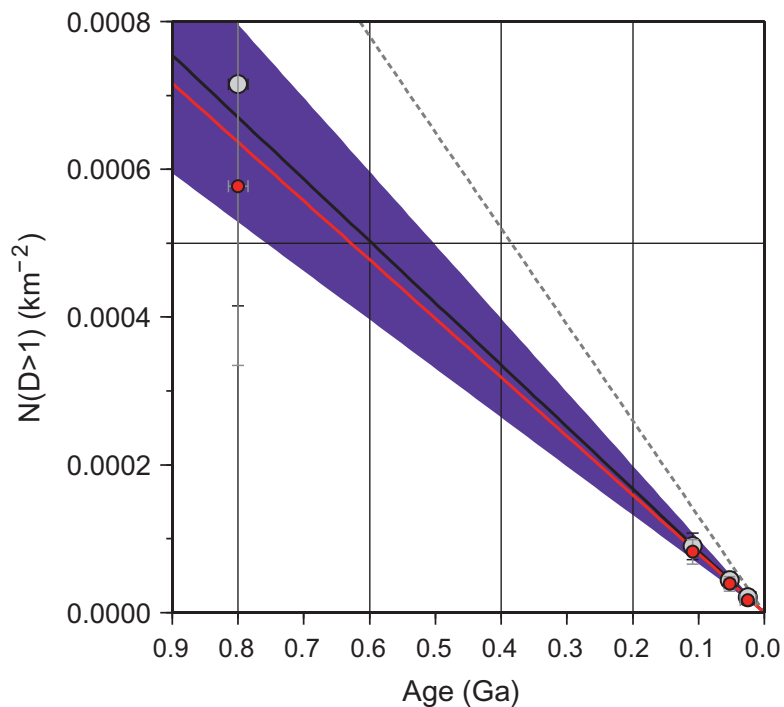
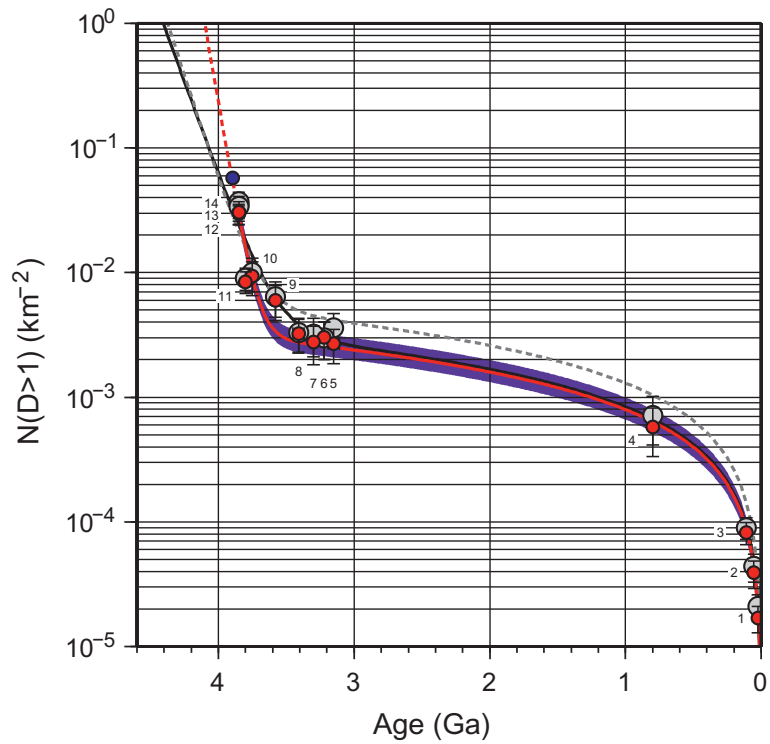


Figure 1.6 Lunar impact crater numbers as a function of time for crater diameters, D , greater than 1 km. From Le Feuvre and Wieczorek, 2011.

ters of the 21 identifiable fragments ranged up to 2 km, and the orbital velocity of the visible objects was measured to be about 60 km/s.

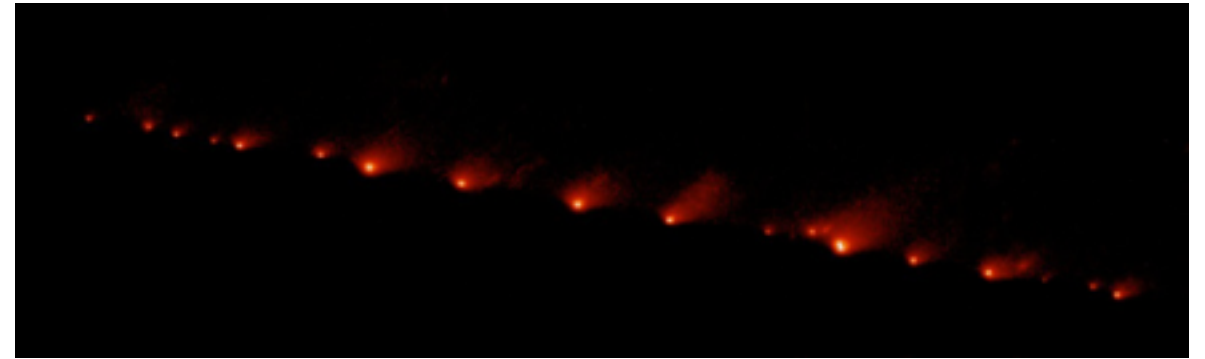


Figure 1.7 String of fragments from comet Shoemaker-Levy 9 prior to impact on Jupiter. Image from Hubble, NASA, ESA, and H. Weaver and E. Smith (STScI).

A train of comet fragments traveled from west to east (left to right in [Figure 1.7](#)) around Jupiter in a degrading orbit and struck the surface of the southern hemisphere at a zenith angle of about 45° . As can be seen in [Figure 1.8](#), the larger fragments created a string of very large impact structures (dark spots) circling the surface of Jupiter around its south pole. The impact events occurred over a period of several Earth days. The largest impact structure (dark spot seen in the upper right corner of [Figure 1.8](#)) observed by the Hubble telescope was measured at 12,000 km across.

Additional breakup can occur when an impactor encounters a sensible gaseous atmosphere. Typical breakup of an extraterrestrial impactor traveling through Earth's atmosphere is illustrated in [Figure 1.9](#). The process of breakup and fragmentation is violent (explosive) and chaotic...it is caused mostly by



Figure 1.8 Hubble view of Jupiter showing the impact structures and their distribution on Jupiter along the impact trajectory of the Shoemaker-Levy 9 fragments. (Photo from Hubble Space Telescope Comet Team and NASA.)

aerodynamic drag forces which also produce extreme frictional heating on the surface of the impactor and its fragments. The smaller fragments have less aerodynamic drag due to reduced frontal area, so they become separated from the larger pieces that lag behind. Ablation of its surfaces will reduce the volume of any Earthbound impactor producing a trail of hot debris behind the impactor like that seen in [Figure 1.9](#). The amount of atmospheric trail-debris depends upon pa-

rameters such as impactor speed, chemical makeup, and structural integrity.



Figure 1.9 Typical extraterrestrial impactor entering Earth's atmosphere. Image from Igor Zh/Shutterstock.

Because typical extraterrestrial impactors can be represented as a collection of objects before they impact the surface of a terrestrial object, the collection of impact craters seen on Mars in [Figure 1.10](#) is typical of a crater pattern that might be found on the surface of any space body...including Earth. The two overlapping, larger craters are marked as “New Craters” while a collection of minor craters are seen inside the green ellipses. Incidentally, Bierhaus, et al, 2005, have pointed out that these simultaneous impacts have not been accurately accounted in developing estimates of impact frequency to determine the age of geologic impact features on terrestrial bodies.

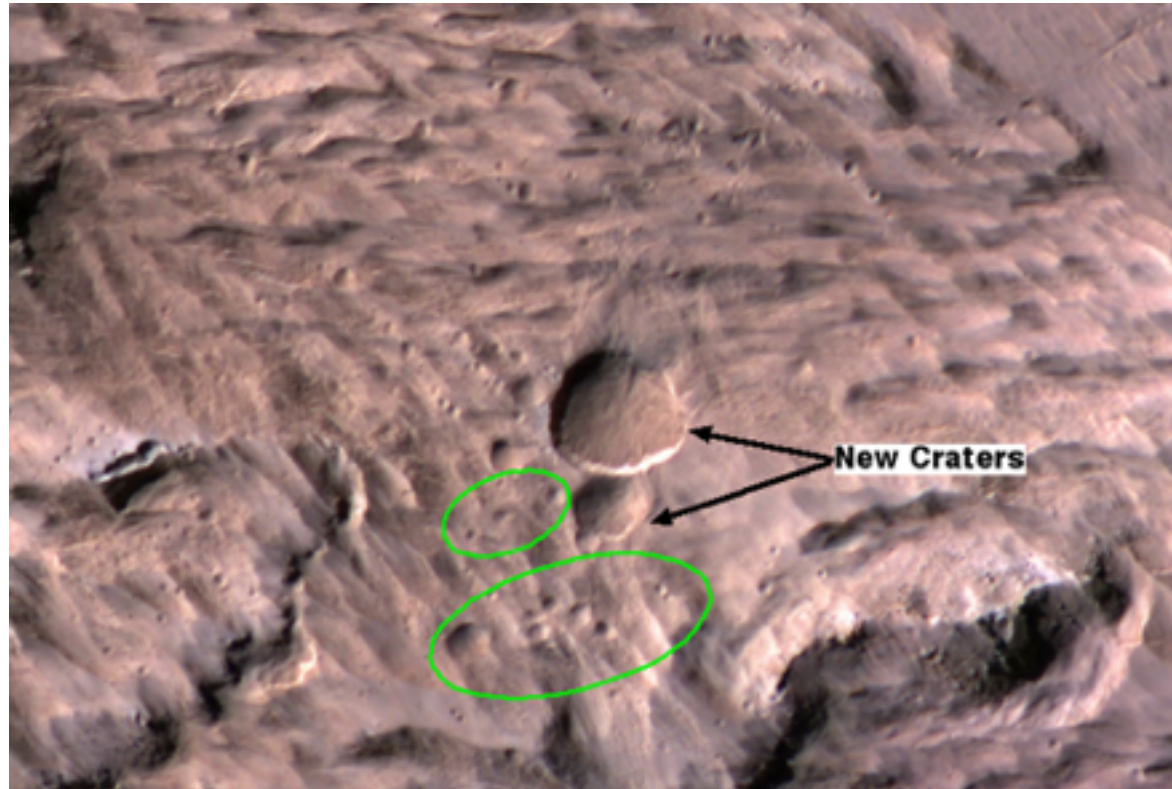


Figure 1.10 Single-event, multiple impact structures on the surface of Mars. Minor, concurrent impact structures are seen inside the green ellipses. This image is centered at 3.34° north latitude, 219.38° east. The original image comes from a 5/22/2014 NASA-Jet Propulsion Laboratory news release.

1.1.3 DRY-LAND GEOLOGIC IMPACT STRUCTURES ON EARTH

Identification, positioning or verification of kilometer-size impact structures on Earth's dry surfaces can usually be best performed by examining satellite imagery. When viewed from high altitude, many circular or arcuate structures are visible on Earth's dry surfaces. In spite of significant impact structure degradation on Earth over time due to overprinting, impact ejecta backfilling and erosion, surface patterns similar to those seen on the Moon should still be visible from space on

Earth's surface. In order to start to gain some perspective, a satellite image of a region of the Earth with a similar projected area as that of the surface of one hemisphere of the Moon (3474.8 km across) is presented in [Figure 1.11](#). The locations of the famous Yellowstone Lake and the west end of Lake Superior are indicated to help orient the reader on the map. Close examination of this Google Earth image reveals many probable impact structures, even though they are not as obvious as we see on the Moon. As a rule, older impact structures on Earth are heavily eroded or mostly buried with large quantities of ejecta from subsequent impacts, volcanic material infilling, and sediment from erosion plus deposition of carbonate rocks formed in warm and hot water basins, especially inside of impact craters, etc.

Many of the older impact structures visible on the region of Earth presented in [Figure 1.11](#) are revealed as arcs, but closer examination reveals many are nearly complete circular structures. Complete circular structures are exceptional partly because impactors rarely strike the surface along trajectories high enough above the horizon that produce circular structures... $\geq 45^\circ$ (to be discussed in subsequent chapters, especially Chapter 2).

Traditionally, most of the surface features seen in [Figure 1.11](#) have been attributed to tectonic movement or volcanism. However, based on the data based mathematical model developed by Le Feuvre and Wieczorek, 2011, we can estimate that at least 12,000 impact structures with a diameter greater than 1 km were formed during the past 900 million years within

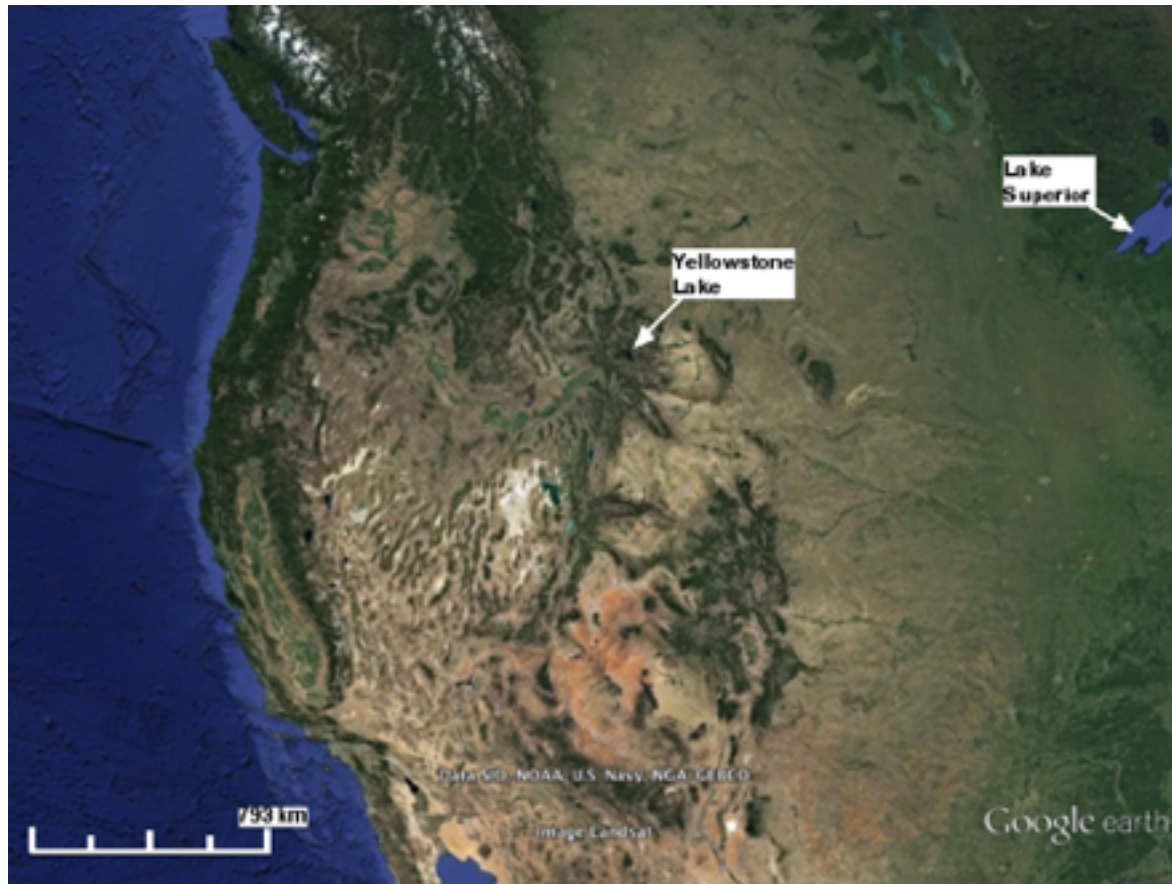


Figure 1.11 Satellite image of western US, southwest Canada, and northwest Mexico. Original image from Google Earth.

the land area shown in [Figure 1.11](#). Even with erosional degradation and covering by volcanic and erosional debris and impact ejecta, a large fraction of these impact structures should still be visible from space.

Several intriguing arcuate patterns that could indicate large impact structures can be seen in [Figure 1.11](#). For example, the long arcuate structure seen on the west coast of the US could indicate the remains of a very old impact structure which could have been as large as 2000 km across. In this view

there are several additional large arcuate structures that could represent overprint impact structures that have developed over time. The outer boundary of one of these candidate overprint structures is marked by the course of the Snake River west of Yellowstone Lake through Idaho and beyond. The popular hypothesis proposes that the Snake River Plain (SRP) was formed by tectonic movement of the North American Plate moving along the trace of the SRP over a stationary deep hot spot, in spite of the fact that this hypothesis contains many inconsistencies that run counter to the basic laws of physics.

The famous Meteor (Barringer) Crater located in northern Arizona...too small to be resolved in [Figure 1.11](#)...is representative of one of these 12,000 unique geologic impact structures expected to be found in that part of Earth's surface. Meteor Crater was formed only about 50,000 years ago, and the high altitude view seen in [Figure 1.12](#) reveals a squarish crater that is slightly over 1 km across and ~180 m deep. As will be discussed in Chapter 2, the planform of the Meteor Crater indicates that the impactor approached the impact point from slightly west of north at approximately 45° above the horizon. Melosh, 1989 and others classify the Meteor Crater as a simple crater. Both of the craters displayed in [Figures 1.2](#) and [1.3](#) would be classified as complex craters. As we shall see throughout this volume, both of these classifications have significance only as an indicator of the mechanical behavior of the target material.



Figure 1.12 Satellite image of the Meteor Crater impact structure located in northern Arizona. Original image from Google Earth.

1.1.4 IMPACT STRUCTURES IN EARTH'S OCEANS

Because 70% of the Earth's surface is currently covered by water, at least 70% of all extraterrestrial impactors have fallen into oceans or lakes for as long as these bodies of water have been around. Consequently, most of the impact structures on Earth are found in or under bodies of water. Actually, it is logical to conclude that many large bodies of water, including oceans, were originally formed as impact structures. The vast majority of impact structures located under oceans has not

been identified nor studied. The structural features of the 35 million-year-old, mostly submerged, Chesapeake Bay impact structure will be examined briefly in Chapter 3.

In addition to the vast amounts of water thrown into the air by an impact into a body of water, much of which will eventually fall back as rain, large waves that will travel away from the impact point and can form giant tsunamis which can cause significant ancillary devastation along shorelines and at great distances inland. Computer modeling indicates that these waves can generate tsunamis as high as 200 m, Hills and Goda, 1993. The studies of Gusiakov, et al., 2009 indicate that a tsunami of this height struck the southern coast of Madagascar where there is evidence that the run-up traveled inland as far as 45 km. Because some shoreline features can further amplify the height of tsunamis, the computed and indicated height probably represent in reality a lower limit.

1.1.5 ATMOSPHERIC EFFECTS OF INCOMING METEORS

There are major effects produced from the interaction of an extraterrestrial object with a gaseous atmosphere, such as that of Earth, regardless of the type of space object...comet or asteroid. In the first place even if a singular space object enters an atmosphere, it is important to recognize that in general these objects will break into many pieces due to the imposed aerodynamic stresses and surface ablation. Because, as will be discussed in Section 2 of this chapter, most extraterrestrial objects possess an irregular geometry, the first effect of atmos-

pheric interaction causes the object to tumble which creates significant body forces that can initiate large scale break-up...exemplified by the behavior of Shoemaker-Levy 7. When extraterrestrial objects of any size or shape first enter Earth's atmosphere (or any planet with a significant gaseous atmosphere), air molecules start to apply a drag force to the leading surfaces of the objects.

The velocity of incoming meteors greatly exceeds the speed of sound in air (0.3 km/s in 1 Earth atmosphere), and the air flow around the main body or its fragments as they enter Earth's atmosphere is graphically illustrated in [Figure 1.13](#). The Mach Cone and the attached, trailing sonic shock front represent the main features of air flow behind any blunt object moving at supersonic velocity, and as will be discussed in detail later, this flow model applies equally to solids and liquids. The length of the Mach cone is proportional to the velocity of the projectile relative to the speed of sound in the flowing target medium. The air inside the body of both shock fronts is highly compressed under nearly adiabatic conditions causing extreme heating of the gas. Even if the the main object or its fragments disperse and disintegrate before striking the ground, the air shocks generated while they were still intact at high altitude, can strike the ground causing considerable damage to life and property.

A graphic illustration of the atmospheric shock effects of a sizable meteor entering Earth's atmosphere and fragmenting but not creating an impact crater was recently presented over Chelyabinsk Oblast, Russia on February 15, 2013. A collection

of informal videos that graphically recorded the event can be viewed at <https://youtu.be/dpmXyJrs7iU>. One large air shock followed by a series of minor shocks was recorded as one large sonic boom followed by a barrage of minor booms on the ground close below the meteor's trajectory. The strongest air shock was felt below the entry trajectory causing considerable property damage on the ground and injury to over 1000 people (no fatalities). No craters were found on the ground, with the possible exception of a 7 x 8 m elliptical hole in 0.7 m-thick ice on Chebarkul Lake. The ground effects of

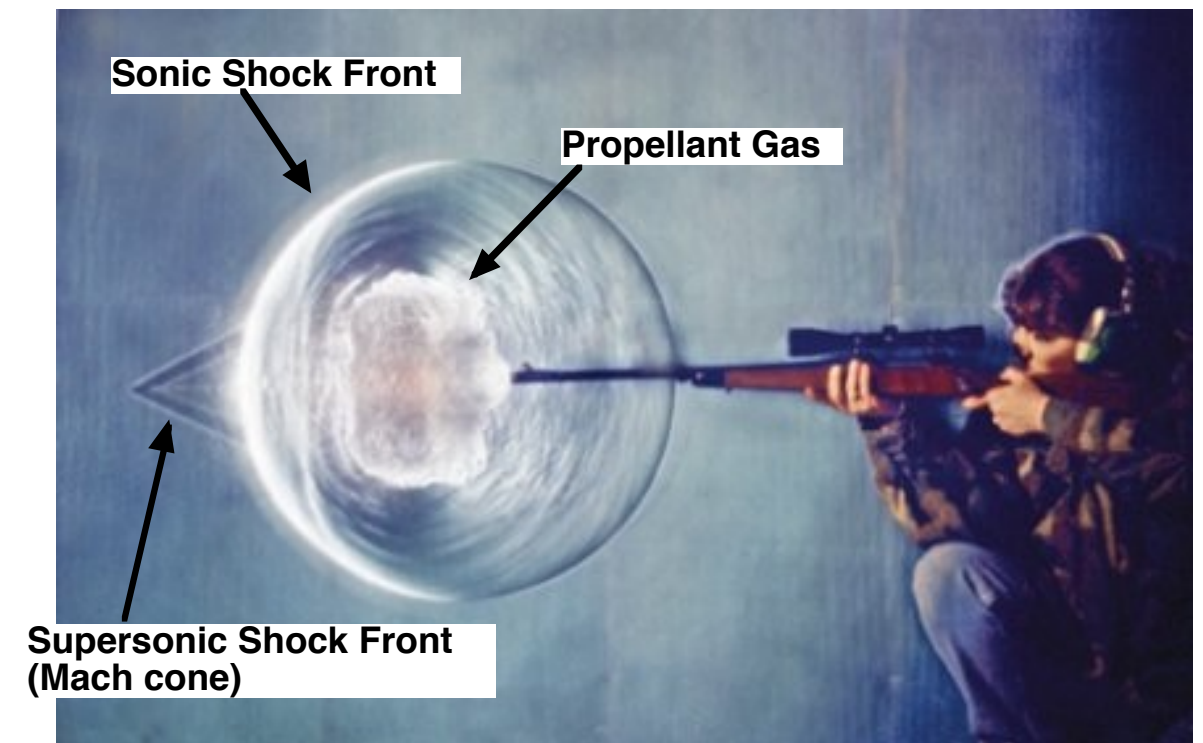


Figure 1.13 Photographic (Schlieren) record of shock fronts generated by a bullet traveling through air at supersonic velocity. The original photograph was downloaded from the Internet at: http://www.phschool.com/science/science_news/articles/images/revealing_covert_actions_02.jpg

the Chelyabinsk event were the largest since the 1908 Tunguska event...see for example Rubtsov, 2009.

The air shock waves generated by the Chelyabinsk meteor at the high altitudes were still strong enough on the ground under the path of the meteor to knock people off of their feet and blow out windows along with their frames. Window breakage generated by the air shock was reported for a distance of ~120 km normal to the trajectory and ~80 km near the end of its track...derived from data in Fig. 3 in Popova, et al., 2013. The pattern of window breakage is consistent with one expected from the intersection of the sonic shock wave illustrated in [Figure 1.13](#) when it contacts the ground at a low angle...the damage pattern on the ground indicated an $r^{2.6}$ dependence on the distance, r , from the 'airburst', Popova, et al., SOM, 2013. Incidentally, many of the witnesses on the ground near the Chelyabinsk meteor's trajectory noted a sulfurous smell in the air that persisted for most of the day, Popova, et al., 2013.

A large amount of real time data relative to the Chelyabinsk event was collected and analyzed, Popova, et al., 2013. This extraterrestrial object entered the atmosphere at ~18° above the horizon at ~19 km/s after it had orbited the Earth at least once. Based on its kinetic energy derived from infrasound measurements, the meteor entered the atmosphere with an initial mass of approximately 1.3×10^7 kg which produces a calculated spherical diameter of ~20 m and an approximate density of 3300 kg/m³. Consistent with the predictions of Hills and Goda, 1993, this meteor disintegrated into dust and small frag-

ments that struck the snow covered ground at terminal velocities without producing impact craters.

Smoke-like trails and hot debris fragments, like that seen in [Figure 1.9](#), were generated by material breaking and ablating from the meteor at high altitude. The surfaces of the fragments were heated to temperatures higher than the surface of our sun by atmospheric friction and oxidation of the meteoric materials. Observations indicated that the leading surface of the impactor was heated sufficiently by aerodynamic friction to be first visible at an altitude of about 97 km, while significant ablation and fragmentation of the meteor became noticeable at an altitude of about 83 km. Between 29 and 26 km, parts of the smoke trail were observed to be radiating at around 700 K, Popova, et al., SOM, 2013. The majority of the meteoroid breakup occurred at an altitude of about 30 km where a distinct division of the debris trail into at least two parts was observed...similar to that seen in [Figure 1.9](#). Most of the kinetic energy of the main body and fragments was deposited in the atmosphere, major fractions in bursts between 34 to 27 km and 24 to 19 km above the Earth. The major visual bursts coincided with observed major meteor break-up events. Fragments were collected on the ground close under the meteor's trajectory for a distance of at least 80 km...derived from data in Fig. 3 in Popova, et al., 2013. Several sizable meteorites were retrieved and studied in the laboratory.

Major break-up altitudes of the Chelyabinsk meteor are comparable to those reported for the space object observed over western Canada in early 2000. Many meteorite fragments

were collected from the ice covered surface of Tagish Lake, British Columbia, Brown, et al., 2000. In the case of the Tagish Lake event, the fragmentation of the incoming object was observed to start at an altitude of about 50 km and end at about 32 km, and based on the optical record of the Tagish Lake event, the break-up was punctuated by two major bursts, Brown, et al., 2002. The Tagish Lake meteor was last observed visually at an altitude of 29 km where its velocity was measured at 9 km/s. On the other hand, the trail of the Chelyabinsk meteor was visible in the sky as low as ~18 km where its velocity was clocked at 13.5 km/s, and three major fragmentation bursts were recorded during its descent, Popova, et al., SOM, 2013.

Both the Chelyabinsk and Tagish Lake events were miniature versions of the Tunguska event that occurred over and inside Siberia on the morning of June 30, 1908. The air shocks associated with the Tunguska event caused considerably more destruction on the ground...including flattening and burning of trees over an area of 2150 km²...see Longo, et al., 2005 or Rubtsov, 2009. The air shocks caused people to be blown out of their beds, chums (huts) blown away and burned, and sulphurous smells to be noted as far away from the tree-fall center (generally referred to as the “epicenter”) as 35 km, Rubtsov, 2009, p. 232. The Tunguska air shock is universally referred to as an explosion, but it is clear that a sonic shock front like that illustrated in [Figure 1.13](#) represents the main energy source for the strong pressure pulse that struck the ground.

Bursts of fragmentation certainly contribute to the pressure pulse generated by incoming meteor, but the vast majority of the total kinetic energy absorbed by the atmosphere occurs over a time frame of seconds rather than milliseconds which characterizes the time frame of explosions. A record of optical light radiated power as a function of time for the Tagish Lake event revealed two major power peaks within a period of two seconds, Fig. 1 in Brown, et al., 2002. These peaks represent short duration flares that infer major break-up events that register as explosions.

Intense thermal radiation caused by atmospheric frictional heating of the incoming impactor can produce major fires to be ignited on the ground. Major seismic activity will also derive from these larger impacts. Electromagnetic effects are also also associated with the passage of large meteors through the atmosphere much like that associated with nuclear explosions at high altitude...see for example the discussion in Rubtsov, 2009.

Extraterrestrial Impactors

SECTION TOPICS

1.2.1 A Comet up Close

1.2.2 Asteroids

There are innumerable, potential Earth-impactors moving throughout our solar system on a variety of orbits especially around our Sun and the planet Jupiter. The vast majority of these objects are leftovers from the supernova that produced most of the bodies in our Solar System...see for example Gribbin, 2000. Even though the probability of impact is quite low, these objects can collide with Earth's atmosphere at intercept velocities as high as 70 km/s. Iron-nickel meteors with major dimension >80 m, and meteors with bulk densities as low as 500 kg/m³ (typical comets) and major dimension >1600 m can be expected to strike Earth's surface with sufficient intact mass and kinetic energy to cause impact cratering and other serious damage, Hills and Goda, 1993.

In this section we will briefly examine examples of observational data on two classes of extraterrestrial objects that can offer serious impact threats to Earth...comets and asteroids.

1.2.1 A COMET UP CLOSE

Comets are usually defined as celestial bodies that travel around the sun in highly eccentric orbits and emit trails of debris that reflect sunlight sometimes making them visible in the sky during daylight hours. Surface erosion and evaporation create the characteristic comet tails (comas) that are directed away from the sun by the force of its electromagnetic radiations and solar wind.

The structural features of comets that lead to their unique behavior as impactors are currently being elucidated by direct, closeup observations from spacecraft. For example, Comet

67P/Churyumov-Gerasimenko (67P/C-G) is being examined in great detail by instruments onboard the Rosetta spacecraft that started orbiting the comet on August 6, 2014...the spacecraft was put together and launched by the European Space Agency (ESA) in collaboration with NASA. This comet reached perihelion in August 2015 in its 6.4-year circuit that crosses Jupiter's orbit slightly before and after aphelion. Perihelion occurs at about 186 million kilometers from the Sun... between the orbits of Earth and Mars, so it is not an impact threat to Earth in its current orbit.

As seen in [Figure 1.14](#), 67P/C-G is shaped like a dumbbell whose bulbous ends are connected by a short neck. The long dimension of the comet measures about 7 km, Sierks, et al., 2015, so it is expected to be mechanically unstable and likely to easily break at least into two major fragments during an encounter with a strong gravitational field or a significant planetary atmosphere...like the breakup of Shoemaker-Levy 9 by the gravitational field of Jupiter

The makeup of the coma of 67P/C-G is being studied in detail, and the preliminary data indicates that it consists mostly of objects gravity bound to the comet nucleus ranging from 4 cm to ~2 m across, Rotundi, et al., 2015. The median of the size distribution of these companion objects is much larger than expected. Many of these detached objects are lagging behind the comet producing a long trail of debris that is commonly associated with streams of meteorites like those that periodically generate meteor showers in the sky over Earth. A typical source of material in the coma is illustrated by the stream of

material seen to be emanating from the neck between the two lobes of 67P/C-G in [Figure 1.14](#).

As is commonly seen for both comets and asteroids, the surface of both lobes of the nucleus of 67P/C-G is seen to be heavily damaged by impact (three craters are indicated in [Figure](#)

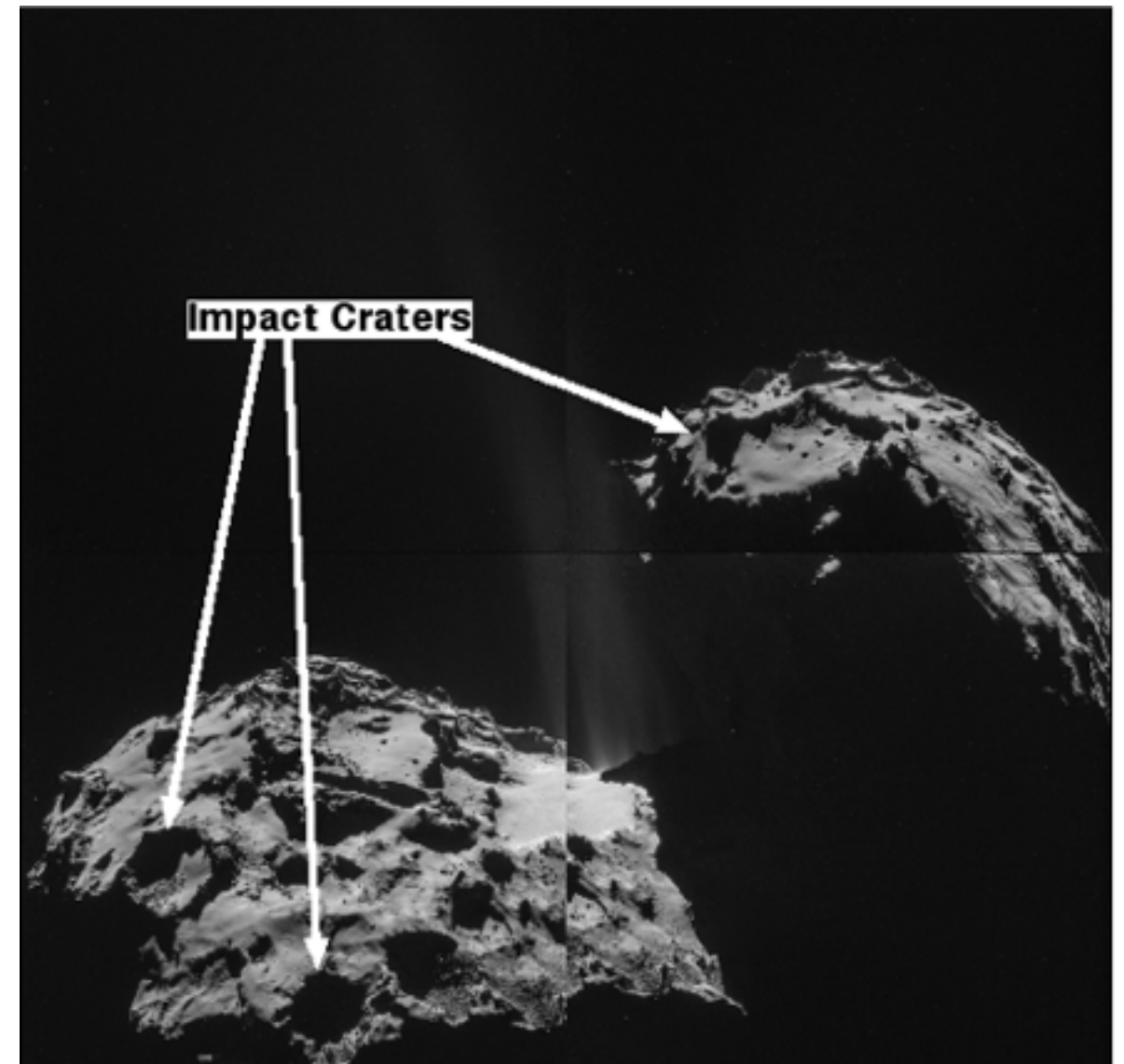


Figure 1.14 Planar area in Imhotep region of comet 67P/C-G with steps (Shear Lines) formed by avalanches of crater-fill (regolith). Original photo released by ESA on January 22, 2015.

1.14), and the rims of the impact craters appear to be quite dense and possess considerable structural integrity. These craters are filled to varying depths with material that flows and settles by force of gravity forming flat to gently sloping plains. For example, the indicated impact crater at the bottom-left of the photograph in [Figure 1.14](#) appears to be one of a set of four in a row with similar crater-fill levels that are notably less than several other nearby craters. These four craters were probably formed at the same instant by a collection of impactors.

The crater-fill appears to be a weakly bonded aggregate that can be compared to regolith found on Earth's Moon...recall [Figure 1.5](#). The bulk density of comet 67P/C-G is estimated at 470 kg/m^3 , Sierks, et al., 2015, so if we assume that the density and size distribution of the crater-fill material is comparable to the gravity-bound objects in the coma... $(1.9 \pm 1.1) \times 10^3 \text{ kg/m}^3$, Rotundi, et al., 2015, we can conclude that 67P/C-G contains many interior cavities that comprise perhaps 3/4 of the total volume of the comet nucleus.

In general, large areas of crater-fill appear to be lying at their natural angle of repose, but broken lines seen in the photo data on the crater-fill in [Figure 1.15](#) indicate that a series of avalanches or landslides has occurred over time causing slabs of material to move upward in this photograph. This avalanche phenomenology is comparable to that commonly observed on Earth in snow lying on slopes close to its local angle of repose. Avalanches in snow or other poorly bonded particulate materials can be triggered by localized shear resulting

from a variety of changes in the global stress state...for a review of localized shear deformation see Walley, 2012. Stress state effects on sudden, localized fracture of materials will be discussed in detail in Chapter 4.

1.2.2 ASTEROIDS

Asteroids are frequently termed as minor planets that are found numbering in the millions in orbits around the sun in the inner Solar System. Even though the probability of impact of large asteroids on Earth is extremely low, the damage produced by impact of even one small asteroid is expected to be extreme. Asteroids are representative of a class of impactors

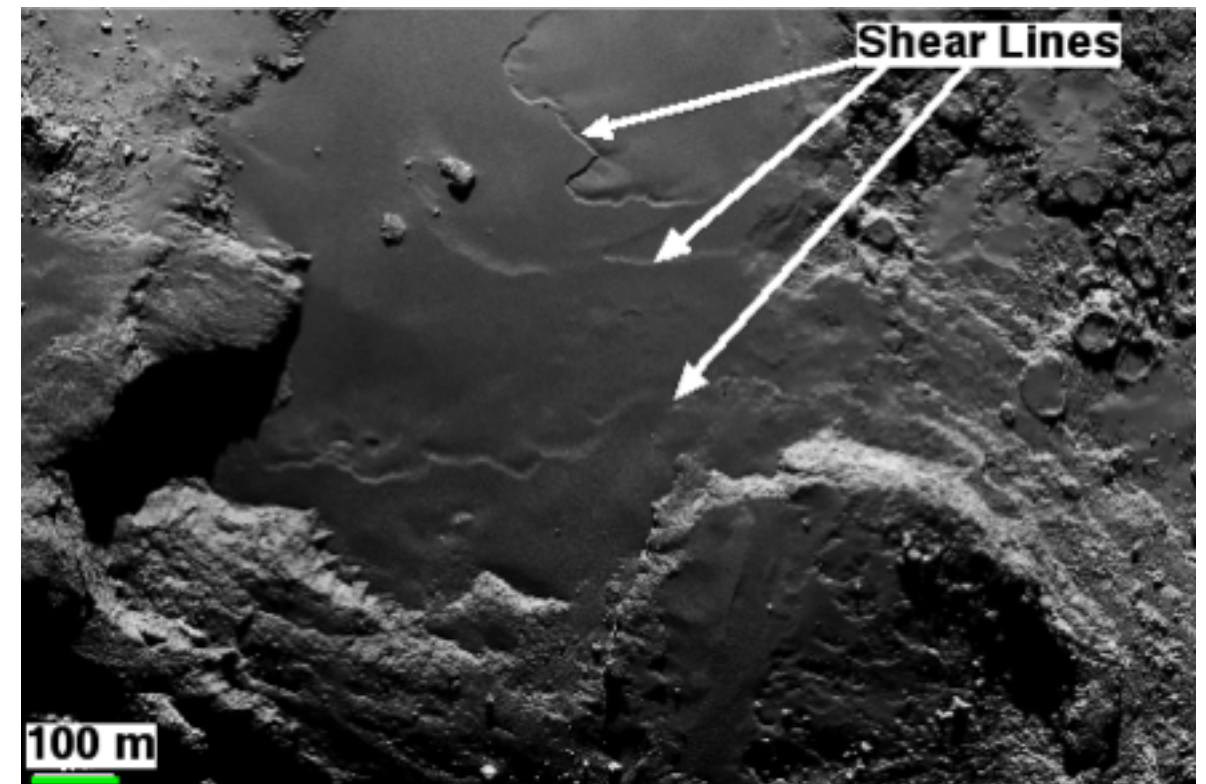


Figure 1.15 Planar area in Imhotep region of comet 67P/C-G with steps (Shear Lines) formed by avalanches of crater-fill (regolith). Original photo released by ESA on January 22, 2015.

that have relatively high density and a high degree of structural integrity. Fragments of this type of space object >220 m across have a finite probability of striking the surface of the Earth at hypervelocity, Hills and Goda, 1993.

Large asteroids such as 4 Vesta (573 x 557 km across) tend toward spherical shapes, but the potato shaped 433 Eros, with approximate dimensions, 34 x 11 km, is typical of smaller asteroids...see [Figure 1.16](#). The asteroid 433 Eros has an orbital velocity of 24.36 km/s and a mean density of 2670 kg/m³...see for example http://en.wikipedia.org/wiki/433_Eros. At present, 433 Eros orbits outside of Earth's orbit and does not cross it, so at this point in time, 433 Eros offers no impact threat to the Earth.

Even though rare, asteroids have been observed to emit debris like comets, and at least one is observed to have an orbiting moon...243 Ida which is also potato shaped and has dimensions of 54 x 15 km. As with comets, impact damage to the surface of asteroids tends to be extensive. Observations of the surfaces of asteroids from spacecraft has revealed the presence of many impact craters of varying sizes...see [Figure 1.16](#). These past impacts could have ejected many smaller objects into space resulting in serious degradation to the integrity of the asteroid. Incidentally, it has been observed that the 50 km diameter 253 Mathilde has an impact crater that is half its diameter which infers that a major fraction of its original mass has been scattered into space.



Figure 1.16 Six orientations of asteroid 433 Eros as viewed by NASA's NEAR-Shoemaker spacecraft in February 2000.

Formation of Geologic Impact Structures: A Preview

SECTION TOPICS

1.3.1 Cratering Dynamics

1.3.2 Correlations between Laboratory-Scale and Full-Scale Geologic Impact Structures

So far, we have been introduced to the macro effects of impact on the surfaces of terrestrial bodies and the bodies found in outer space that produce these effects. In this section and in the following chapters we will be examining the formation mechanics of impact structures. As previously mentioned, geologic impact structures are formed as a result of impact by these extraterrestrial bodies that are traveling through space at intercept velocities as high as 70 km/s. It is important to recognize that these impact velocities exceed the sound speed in all geologic materials. Consequently, the impact process can produce supersonic flow in geologic materials, and the formation of impact structures is based initially on the science and technology of the mechanical behavior of fluids.

As previously indicated, the cratering process can be conveniently separated into early- and late-stages due to the significantly different phenomenologies that produce characteristic structural features in the final crater. A primary crater is formed in the early stages of the cratering process after the momentum and energy contained in the impactor is coupled into the target. Secondary cratering and other effects of target material deformation and fracture are produced during the late stages. In geologic materials, structural features produced by these secondary effects represent many of the prominently displayed identifying features in the final impact structure.

1.3.1 CRATERING DYNAMICS

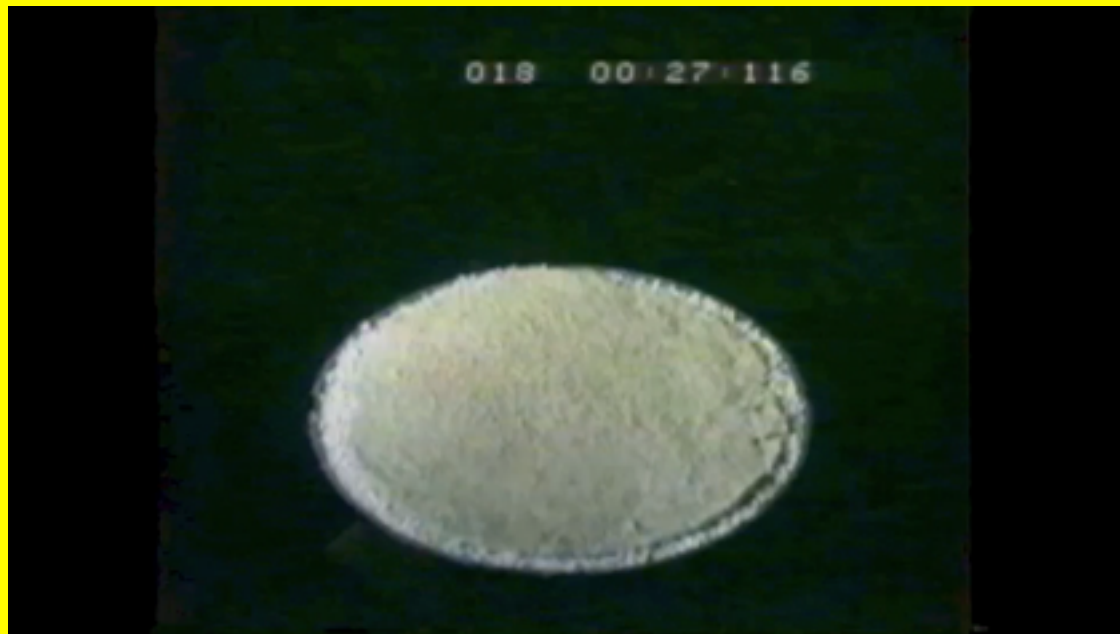
The impact response of a brittle surface layer over a low strength substrate seen in the above-surface view in the video in [Figure 1.17](#) graphically illustrates many of the dynamical characteristics of the entire impact cratering process. This high-speed video recorded effects of the impact of a projectile into a material with a frozen surface layer (dust, ice, window cleaner and Worcestershire sauce) placed over a loosely packed, granular target material (garden perlite). The dynam-

ics of the process seen in [Figure 1.17](#) can be correlated directly to the formation of geologic impact structures.

As can be observed in the video, the cratering process starts with ejecta streaming from close around the impact point. Soon after impact, the brittle layer starts to break up into large, pie-shaped pieces. At this juncture, material from a forming crater is ejected up-range along with pie shaped surface fragments. Formation of these pie shaped fragments is relevant to geologic impact structures because it illustrates a process that can cause long distant transport of large blocks of target material. The crater formed in the granular substrate is eventually revealed at the end of the video.

A set of sequential photographs of the above surface view of a similar chronology of impact cratering in pumice is presented in [Figure 1.18](#). The structural patterns of the ejecta created as a result of oblique (60° above the horizon) impact of a copper sphere into pumice are illustrated through the cratering process. The initial contact between the impactor and the target surface caused a bright, visible flash that indicates that the ejecta contains ionized atoms or molecules...see the frame marked "Contact" in [Figure 1.18](#). The early frames illustrate the fact that off-normal impacts cause the early-stage ejecta trajectories to be directed predominately downrange from the very beginning of the cratering process. As can be seen in the frames preceding the 'Shock Front Breakthrough' in [Figure 1.18](#), ejecta flows out of a small hole in the target surface formed by the growing primary crater...much like that seen in the video in [Figure 1.17](#). As illustrated in both [Figures 1.17](#) and

Figure 1.17 Video of the above-surface effects of an impactor propelled by an air-gun into perlite covered by a frozen surface. This video was recorded at the Vertical Gun Range, NASA Ames Research Center for Peter Schultz, Brown University...found on the Internet.



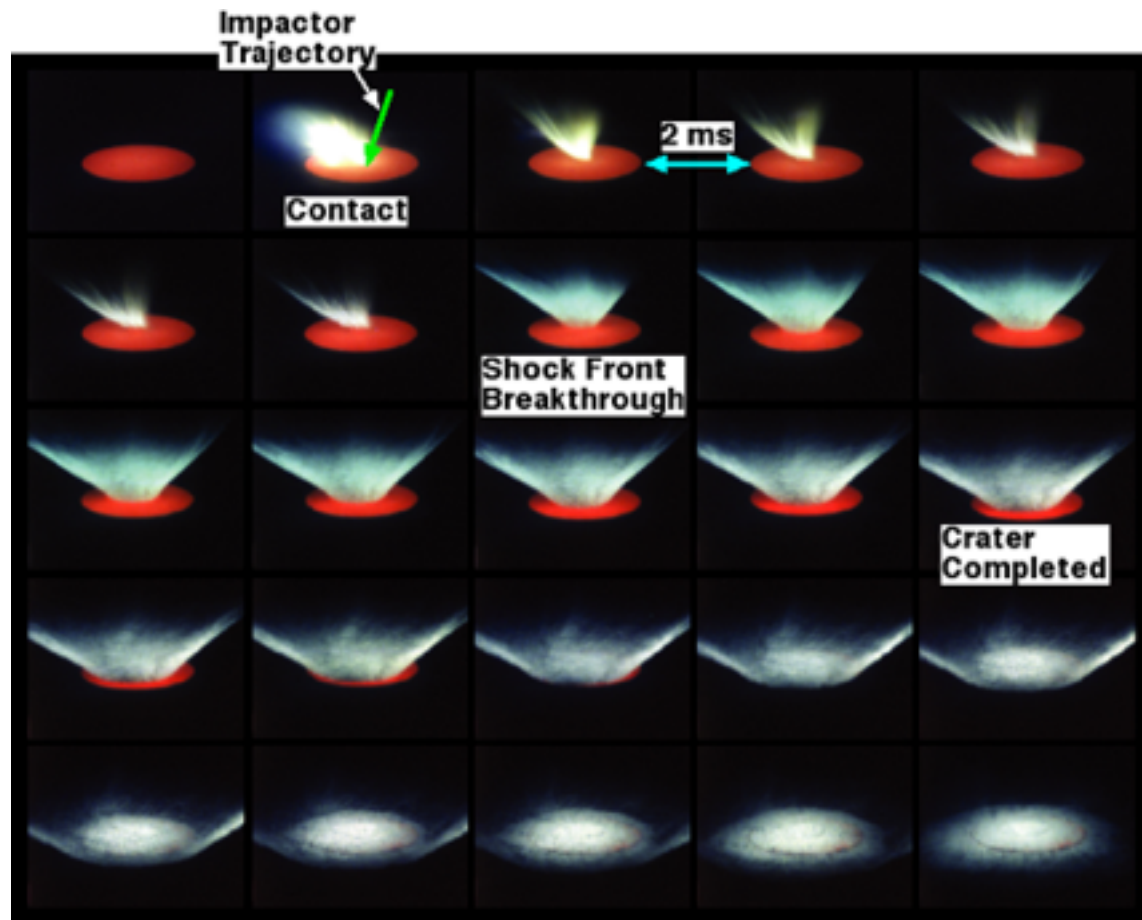


Figure 1.18 High-speed (500 frames/s) photographic record of an impact of a porous particulate target (pumice) by a copper sphere traveling at 4.5 km/s on a trajectory 60° above the horizon. Impact occurred under a vacuum. (Original images from Vertical Gun Range, NASA Ames Research Center; Peter Schultz, Brown University.)

1.18, when the surface of the shock front that developed inside the target breaks through the surface there is a major jump in the base diameter of the ejecta cone. Based on the level of self-illumination of the ejecta, the material in this new ejecta cone is noticeably cooler than indicated for the earlier cratering phase.

Real materials respond to an impact of a finite projectile by producing a characteristic set of waves that surround the impact point in the target material. The response of a liquid to an impact provides a credible analog of the impact dynamics in geologic materials. The photo sequence of a liquid drop impacting the surface of a like fluid at subsonic velocity seen in [Figure 1.19](#) presents a graphical illustration of the formation mechanics of a geologic impact structure. A close examination of the image in [Figure 1.19\(b\)](#) reveals that the impactor starts the cratering process by burying itself into and mixing with target material. In this early-stage of the cratering process, the kinetic energy and momentum of the impactor are transferred to the target material, and this initial phase is concluded when the trailing surface of the impactor reaches the level of the original surface of the target, i.e. when the total energy and momentum of the impactor has been transferred to the target.

The primary crater is formed in the early-stage of the cratering process by fluid flow due to the compressive forces which are derived from the impact during the interval seen in [Figure 1.19\(b\)](#) thru [Figure 1.19\(d\)](#). As the crater expands, a mixture of impactor and target material (ejecta) flows up-range confined to a shock front that defines the surface of the forming primary crater. The value of the maximum stress vector derived from the impact passes through zero in the target material when the primary crater is completed...[Figure 1.19\(d\)](#). Beyond this point, the maximum stress vectors oscillate between compression and tension in the material immediately sur-

rounding the primary crater, and they are derived from target material elastic rebound, gravity induced flow and atmospheric effects.

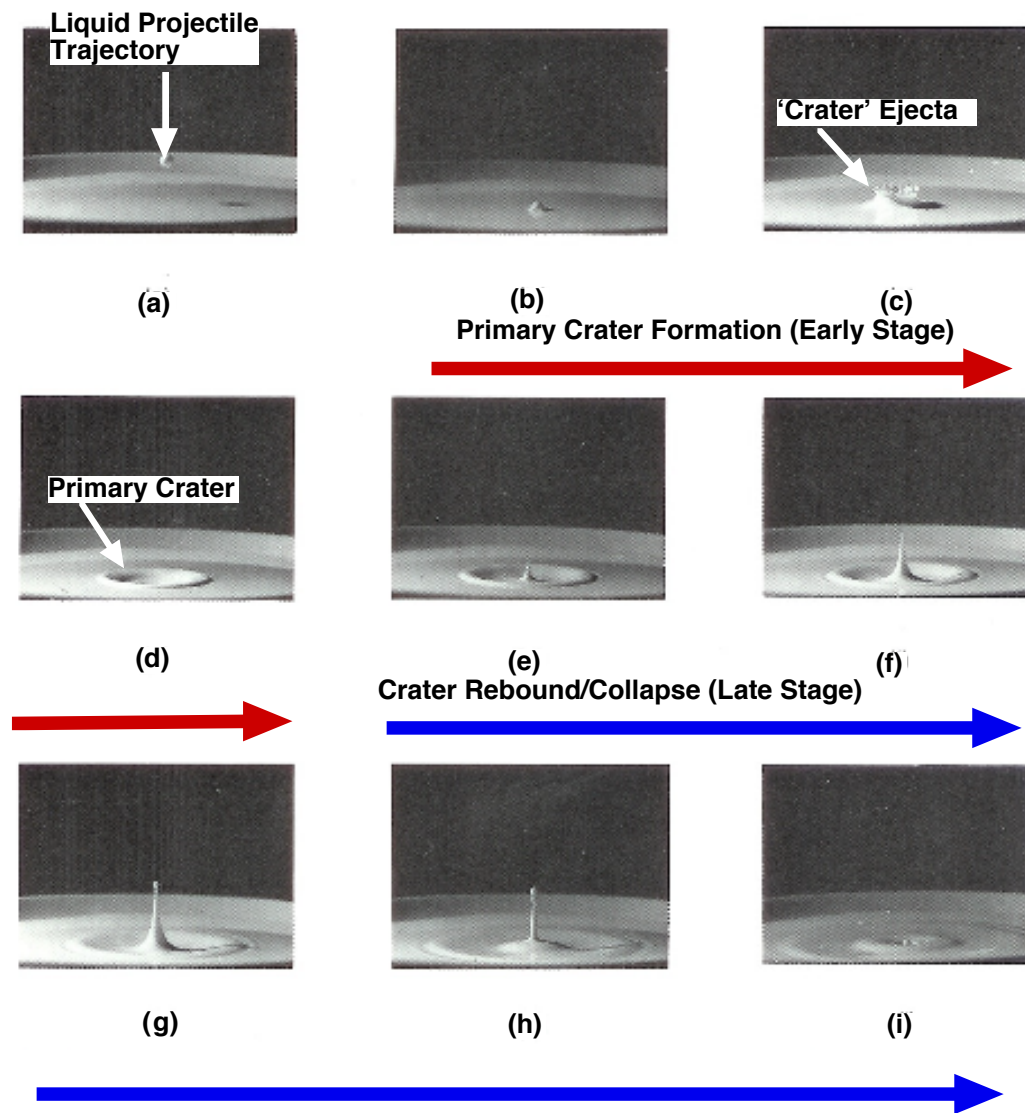


Figure 1.19 Time-lapse photographs of surface phenomenology resulting from normal incidence, subsonic velocity impact of a spherical fluid drop into a fluid target in a gravity field and under Earth atmospheric pressure (original photo sequence from Melosh, 1989, p. 148).

During the late-stage portion of the cratering process, the crater tends to collapse due to rebound of the target material,

and the geometry of the primary crater is modified...illustrated in [Figures 1.19\(e thru i\)](#). In this volume, the concluding phase of impact structure formation will be termed *crater rebound/collapse* (Melosh, 1989, refers to the late-stage part of the cratering process as “modification and collapse”).

The photograph in [Figure 1.19\(e\)](#) recorded early formation of a central uplift or peak that results from fluid flow reversal. This central peak continues growing through [Figure 1.19\(g\)](#), while beyond that time material fall-back is observed from the central uplift along with the formation of secondary (seismic or Rayleigh) waves that will eventually dissipate or interact with a rebound wave moving in the opposite direction...[Figure 1.19\(i\)](#). This late surface wave expansion can also produce multi-ring craters like those commonly seen on the surface of Mercury and Earth’s moon, and when impactors fall in oceans on Earth, these late generated waves can become the precursors to mega-tsunamis that can cause significant damage at large distances from the impact point.

In geologic contexts, very large earthquakes will also be generated as secondary effects of the impact cratering process. For example, Hills and Goda, 1993, calculated that a 520 m diameter stony meteorite entering Earth’s atmosphere on a normal trajectory traveling and at 20 km/s before impacting the ground will produce an earthquake with a Richter magnitude of 8.8 as a result of impact. They also calculated that the Chicxulub impact (Cretaceous/Tertiary boundary event) generated an 11.5 magnitude earthquake.

1.3.2 CORRELATIONS BETWEEN LABORATORY-SCALE AND FULL-SCALE GEOLOGIC IMPACT STRUCTURES

Many of the structural features observed in geologic impact structures are commonly produced by impact experiments in the laboratory. For example, the terraced walls of the Aristarchus crater (recall [Figure 1.3](#)) are regularly observed in impact structures generated at laboratory scale. For example, the morphological features of hypervelocity impact craters in high strength ferritic steel (α -Fe), Shockey, et al., 1975, and titanium, Lundberg, et al., 1982, created in the laboratory by hypervelocity impact are similar to those observed inside the Aristarchus impact crater. An illustration, based on experimental data, Shockey, et al., 1975, of a typical hypervelocity impact crater cross-section in a high strength low alloy (HSLA) steel produced by a low density projectile is presented in [Figure 1.20](#).

The terraces along the crater wall seen in [Figure 1.20](#) are correlated with shear bands that are seen extending downward from the inside of the crater. These terraces were formed by localized shear failure around the inside surface of crater near the end of the cratering process...the same process as that which formed the Aristarchus impact crater, recall [Figure 1.2](#). For the case of the HSLA steel, the observed cracks, that developed along shear planes, generally stop short of the 'Plastic Deformation Boundary' which marks the surface where the stresses produced around the inside of the forming crater by the impactor generated shock front drop below the elastic

limit of the target material and plastic deformation ceases...deformed grains are not observed downrange from this boundary.

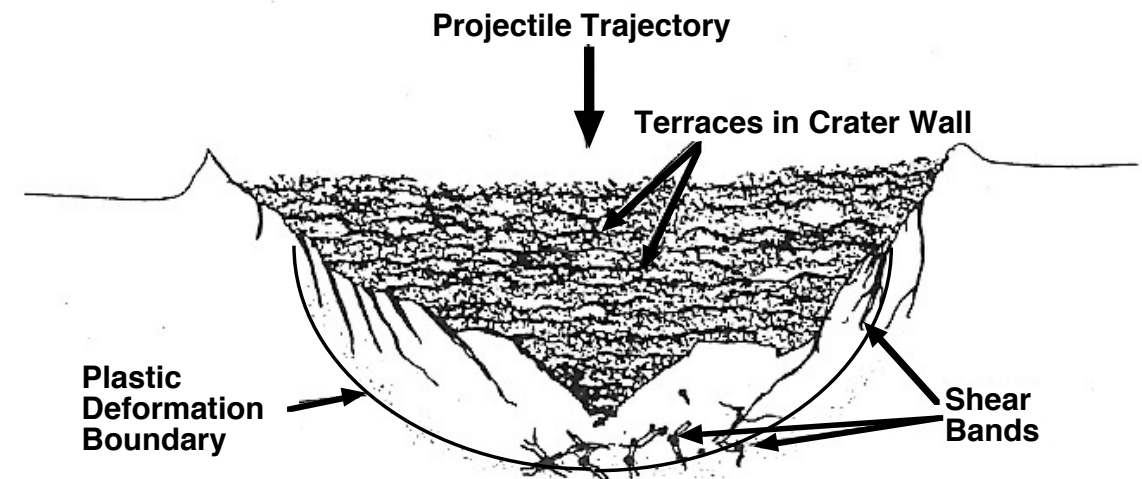


Figure 1.20 Diagram of the salient features of a polished and etched cross-section of a crater in a HSLA steel plate impacted at 6.03 km/s with a water-filled polycarbonate sphere traveling on a trajectory normal to the target surface (original illustration from Shockey, et al., 1975).

The shear bands indicated in [Figure 1.20](#) below the crater bottom represent adiabatic shear bands (ASB's), i.e. planes of shear deformation that generate intense local heating on the resolved shear planes which can produce metal softening or melting on localized, periodic shear planes...see for example Walley, 2012. A similar shaped zone was seen below the bottom of a laboratory-scale hypervelocity impact crater in nephrite, a brittle geologic material, Moore, et al., 1962. This zone was referred to as containing "crushed rock." The structure and mechanics of the formation of ASB's will be discussed in

in later chapters along with the many other correlations between laboratory and full scale geologic cratering.

Where We go from Here

A clear understanding of the impact cratering process is basic to the development of the foundation principles of Impact Geology, so the next chapter is devoted to an examination of the physics of the processes that produce geologic impact structures. The data on which the physics of the process is derived comes mostly from laboratory-scale observations of the results of hypervelocity impacts into a wide variety of materials...including geologic materials. Consequently, data from laboratory-scale impact experiments will be critically examined, discussed and used throughout the following chapters to define and extrapolate the concepts presented on the formation of full scale geologic impact structures.

A few examples of the application of the theoretical basis for full-scale geologic impact cratering developed in Chapter 2 will be presented, after a thorough discussion of the formation mechanisms, in Chapter 3. Examples will be presented that illustrate the formation of many geologic structures, e.g.

mountain ranges, based on fundamental impact mechanics which run counter to the currently popular hypotheses of continental drift and plate tectonics.

Because of a serious deficit in the understanding of the real mechanical behavior of materials throughout much of the scientific and engineering communities...even in much of the mechanics of materials community, a discussion of the mechanics of the deformation and fracture of real materials is included in Chapter 4 to define the basics. The material presented in Chapter 4 has implications for understanding the formation of most geologic structures...even those that occur at slow rates.

In Chapter 5 we will examine examples of substructures formed by localized shear in previously undefined geologic impact structures. In Chapter 6, an exercise in impact structure identification and verification will be illustrated through an examination of structural features of two probable, large geologic impact structures.

Chapter 1 References

Bierhaus, E. B., Chapman, C. R., and Merline W. J., 2005, Secondary craters on Europa and implications for cratered surfaces, *Nature*, 437, pp. 1125-1127.

Brown, P. G., Hildebrand, A. R., Zolensky, M. E., and 19 other authors, 2000, The Fall, Recovery, Orbit, and Composition of the Tagish Lake Meteorite: A New Type of Carbonaceous Chondrite, *Science*, Vol. 290 pp. 320-325.

Brown, P., ReVelle, D. O., Tagliaferri, E. and Hildebrand, A. R., 2002, An entry model for the Tagish Lake fireball using seismic, satellite and infrasound records, *Meteoritics & Planetary Science* 37, pp .661–675.

de la Fuente Marcos, C. and de la Fuente Marcos, R., 2015, Recent multi-kiloton impact events: are they truly random?, *MNRAS Letters* 446 (1): L31-L35. doi: 10.1093/mnrasl/slu144.

Gribbin, J. with Gribbin, M., 2000, *Stardust*, Allen Lane-The Penguin Press, ISBN 0-713-99336-7.

Gusiakov, V., Abbott, D. H., Bryant, E. A., Masse, W. B., and Breger, D., 2009, Mega Tsunami of the World Oceans: Chevron Dune Formation, Micro-Ejecta, and Rapid Climate Change as the Evidence of Recent Oceanic Bolide Impacts, pp. 197-227 in *Geophysical Hazards*, International Year of Planet Earth, T. Beer (ed.), Springer Science+Business Media B. V., doi: 10.1007/978-90-481-3236-2_13.

Hills, J. G. and Goda, M. P., 1993, The Fragmentation of Small Asteroids in the Atmosphere, *The Astronomical Journal*, Vol. 105, No. 3, pp. 1114-1144.

Le Feuvre, M. and Wieczorek, M. A., 2011, Nonuniform cratering of the Moon and a revised crater chronology of the inner Solar System, *Icarus*, 214, pp. 1-20.

Longo, G., Di Martino, M., Andreev, G., Anfinogenov, J., Budaeva, L., and Kovrigin, E., 2005, A new unified catalogue and a new map of the 1908 tree fall in the site of the Tunguska Cosmic Body explosion. In: *Asteroid-comet Hazard-2005*, Institute of Applied Astronomy of the Russian Academy of Sciences, St. Petersburg, Russia, pp. 222–225.

Lundberg, L. B., Bless, S. J., Girrens, S. P. and Green, J. E., 1982, *Hypervelocity Impact Studies on Titanium, Titanium Alloys, and Beryllium*: Los Alamos National Laboratory Report LA-9417-MS, August 1982.

Melosh, H. J., 1989, *Impact Cratering: A Geologic Process*, Oxford University Press, NY.

Moore, H. J., Gault, D. E., and Lugn, R. V., 1962, *Experimental Hypervelocity Impact Craters in Rock*: United States Department of the Interior Geologic Survey Report No. N 62 13994, March 1962.

Popova, O. P., and 58 co-authors, 2013, Chelyabinsk Airburst, Damage Assessment, Meteorite Recovery and Characterization, *Science* 29 November 2013: Vol. 342 no. 6162, pp. 1069-1073, DOI: 10.1126/science.1242642.

Popova, O. P., and 58 co-authors, 2013, SOM (Supporting Materials), Chelyabinsk Airburst, Damage Assessment, Meteorite Recovery and Characterization, *Science* 29 November 2013: Vol. 342 no. 6162, pp. 1069-1073, DOI: 10.1126/science.1242642.

Rotundi, A., et al. (80 co-authors), 2015, Dust measurements in the coma of comet 67P/Churyumov-Gerasimenko inbound to the Sun, *Science*, 23 January 2015, Vol. 347 Issue 6220, aaa3905-1.

Rubtsov, V., 2009, *The Tunguska Mystery*, Astronomer's Universe, Springer Science+Business Media, LLC, DOI 10.1007/978-0-387-76574-7_1.

Shockey, D. A., Curran, D. R. and DeCarli, P. S., 1975, *Damage in Steel Plates from Hypervelocity Impact. I. Physical Changes*

and Effects of Projectile Material: *Journal of Applied Physics*, Vol. 46, No. 9, p. 3766-3775.

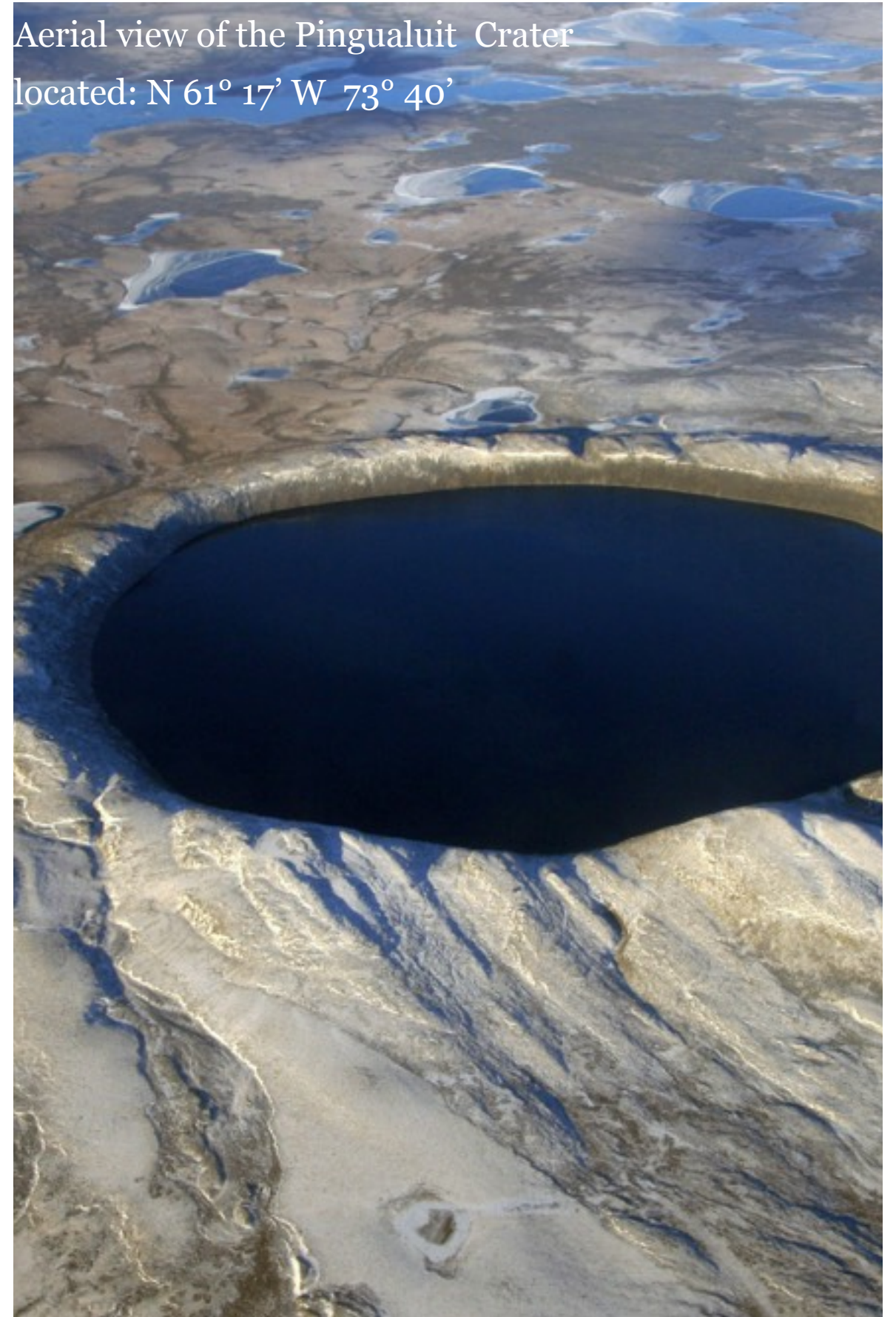
Sierks, H., et al. (65 co-authors), 2015, On the nucleus structure and activity of comet 67P/Churyumov-Gerasimenko, *Science*, 23 January 2015, Vol. 347, Issue 6220 aaa1044-1.

Walley, S. M., 2012, *Strain Localization in Energetic and Inert Granular Materials*, Chapter 7 in *Adiabatic Shear Localization: Frontiers and Advances*, Eds. Dodd, B. and Bai, Y., 2nd Edition, Elsevier:, 32 Jamestown Road, London NW1 7BY, pp. 267-310.

Mechanics of Impact Structure Formation

The mechanics of impact crater formation can be universally applied regardless of scale. Laboratory-scale hypervelocity impact experiments using two-stage light- gas guns to propel small projectiles has provided us with large amounts of data that if appropriately extrapolated can be directly applied to the formation of full-scale geologic impact structures.

Aerial view of the Pingualuit Crater
located: N 61° 17' W 73° 40'



Interpretation of structural features observed in and around geologic impact structures depends upon an accurate understanding of the mechanics of impact crater formation. The aim of this chapter is to provide the reader with a picture of the foundational processes that produce geologic impact structures that is based on data and sound scientific principles. Most of what has been learned about the mechanics of impact structure formation is derived from laboratory-scale hypervelocity impacts of small projectiles onto solid surfaces of a wide variety of materials. Data acquired from laboratory-scale impact simulations can be extrapolated directly to field observations of geologic impact structures, so the logical and consistent connections between these sets of data can be used to verify any hypothesized cratering process.

Most laboratory-scale hypervelocity impact studies have been performed in two-stage light-gas gun facilities, which are generally capable of propelling and impacting only millimeter sized projectiles at velocities up to 10 km/s. However, this maximum impactor velocity exceeds the sound speed of most geologic materials, so the material flow model illustrated in Figure 1.13 for supersonic gas flow around a blunt object can be applied inside impacted solid geologic target materials. The volumetric kinetic energy of laboratory scale hypervelocity impactors can range up to about 10 MJ/m³, and the frontal area kinetic energy densities can range up to about 100 kJ/m². Due to the fact that kinetic energy varies with the square of velocity, these laboratory-scale impactor energy density val-

ues are comparable only to the lower end of the values for the velocity of potential extraterrestrial impactors.

As noted in the previous chapter, geologic impact structures can exhibit concentric primary and secondary craters. Many of the final structural features of impact craters, including the formation of primary and secondary craters, can be attributed separately to early- or late-stage phenomenology, so this natural separation in the impact cratering process has been used to organize the following discussion. As illustrated by the shapes of the ejecta cones in Figures 1.17 and 1.18, the demarcation between early- and late-stage cratering phenomena is generally not well defined primarily because impact structure development is a continuous process. As will be discussed below, early-stage cratering is basically controlled by shock physics, fluid dynamics and the physical properties of both the impactor and target materials, while late-stage cratering is controlled mostly by the mechanical behavior of the target material.

Early-Stage Impact Cratering

SECTION TOPICS

2.1.1 Contact of Impactor and Target

2.1.2 Impactor Coupling and Primary Crater Formation Dynamics

2.1.3 Early Cratering in Oblique Incidence Impact

The first step in the formation of a hypervelocity impact crater involves the contact process that starts when the front surface of the impactor touches the target surface and effectively ends when the rear surface of the impactor is even with the surface of the target. Initially in the contact process, material is jetted laterally from the contact interface. Eventually, the momentum and energy of the impactor are coupled into the target material, and shock fronts similar to those seen in [Figure 1.13](#) develop inside the target and expand away from the impact point below the surface of the target. This early-stage, decaying shock front is responsible for the formation of the primary crater as material moves along the shock front and generates material flow toward the contact (free) surface. Late-stage phenomenology, which will be discussed later in this chapter, is derived from the deformation and fracture of the target material due to stresses that have developed around the primary crater after the initial, supersonic shock front has dissipated substantially.

2.1.1 CONTACT OF IMPACTOR AND TARGET

The first step in the formation of a hypervelocity impact crater involves the contact process that starts when the front surface of the impactor first touches the target surface and effectively ends when the rear surface of the impactor is even with the original surface of the target.....as illustrated in [Figure 1.19](#). At this point it is important to highlight the fact that the trailing surface of the impactor is undisturbed, as illustrated in [Figure 1.19\(b\)](#), until it reaches the bottom of the forming crater

when the momentum and energy of the impactor have been transferred into the target.

Initially in the contact process, material is propelled laterally from the contact interface, but as the impactor continues to penetrate the target surface, the trajectory of the impact ejecta swings up-range as observed in [Figures 1.17](#) and [1.18](#). As will be discussed in **Section 2.2**, the momentum and energy of the impactor will eventually couple into the target to excavate material to form the crater. The contact process is extremely short-lived compared to the rest of the cratering process, but many secondary effects observed around geologic impact structures can be attributed to the early stages of the contact process.

2.1.1.1 EJECTA JETTING EFFECTS ON MARS AND EARTH'S MOON

The contact process is responsible for the formation of crater rays prominently displayed on the surfaces of Mars, Mercury, and Earth's Moon. Ray traces emanating from a recently formed small crater on Mars, seen in [Figure 2.1](#), are marked by jetted material deposited on surfaces close around the impact point during initial contact of the impactor.

The overall planform of the ray pattern seen in [Figure 2.1](#) indicates that the impactor struck the ground at a shallow angle on a trajectory from the upper right corner of the photograph causing most of the jetted ejecta to be deposited on the surface downrange and to the sides of the crater. It should also

be noted that the planform of the newly formed main crater tends toward square, which, as will be discussed later in this chapter, is another indicator of an oblique incidence impact. Incidentally, the small crater that is visible immediately downrange from the main crater probably resulted from near simultaneous impact of a smaller companion impactor fragment.

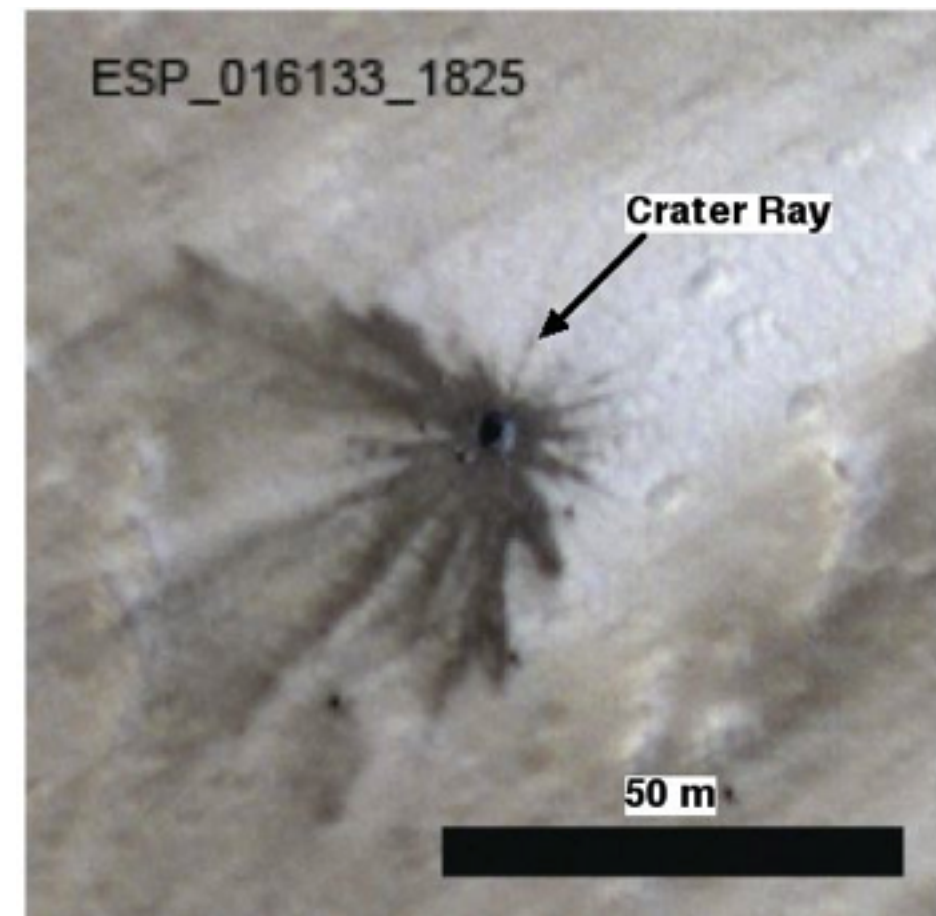


Figure 2.1 Photograph of a small, oblique rayed crater on Mars formed between February and July 2005. Original photograph from Daubar, et al, 2013.

As illustrated in [Figure 2.2](#), large fragments of the jetted ejecta has created prominent, separate, oblique impact structures in conjunction with the ray traces that emanate from the main crater. The planform of these radially distributed craters indicate that many large, solid secondary impactors were accelerated laterally to very high velocity from the impact point striking the surface at very shallow angles forming typical oblique impact structures...impact crater planforms will be examined as a function of impact angle later in this chapter...**Section 2.1.3**. The origin of these secondary impact structures that are produced by contact jetting was suggested early on by Shoemaker, 1962.

In addition, the Apollo 16 astronauts identified and explored ray traces on the ground on the Moon associated with newer, small impact craters, Freeman, 1981. They found that ray traces could be recognized on the ground by an abundance of rock fragments laying on the surface and an increased number of radially distributed small craters...similar to those seen in [Figure 2.2](#).

2.1.1.2 MECHANICS OF THE CONTACT PROCESS

Laboratory scale experiments have been used to define the effects of the contact process and elucidate the phenomenology. Observing the impact contact process in the laboratory represents a significant challenge due to the very short duration of the event. Never-the-less, Kurosawa, et al., 2014 have succeeded in recording the above-surface contact effects produced by hypervelocity impact of a spherical projectile onto a solid target surface. The above-surface phenomenology of the impactor/target contact process for a 45° impact without atmospheric effects is well illustrated in the ultra-high speed photographic

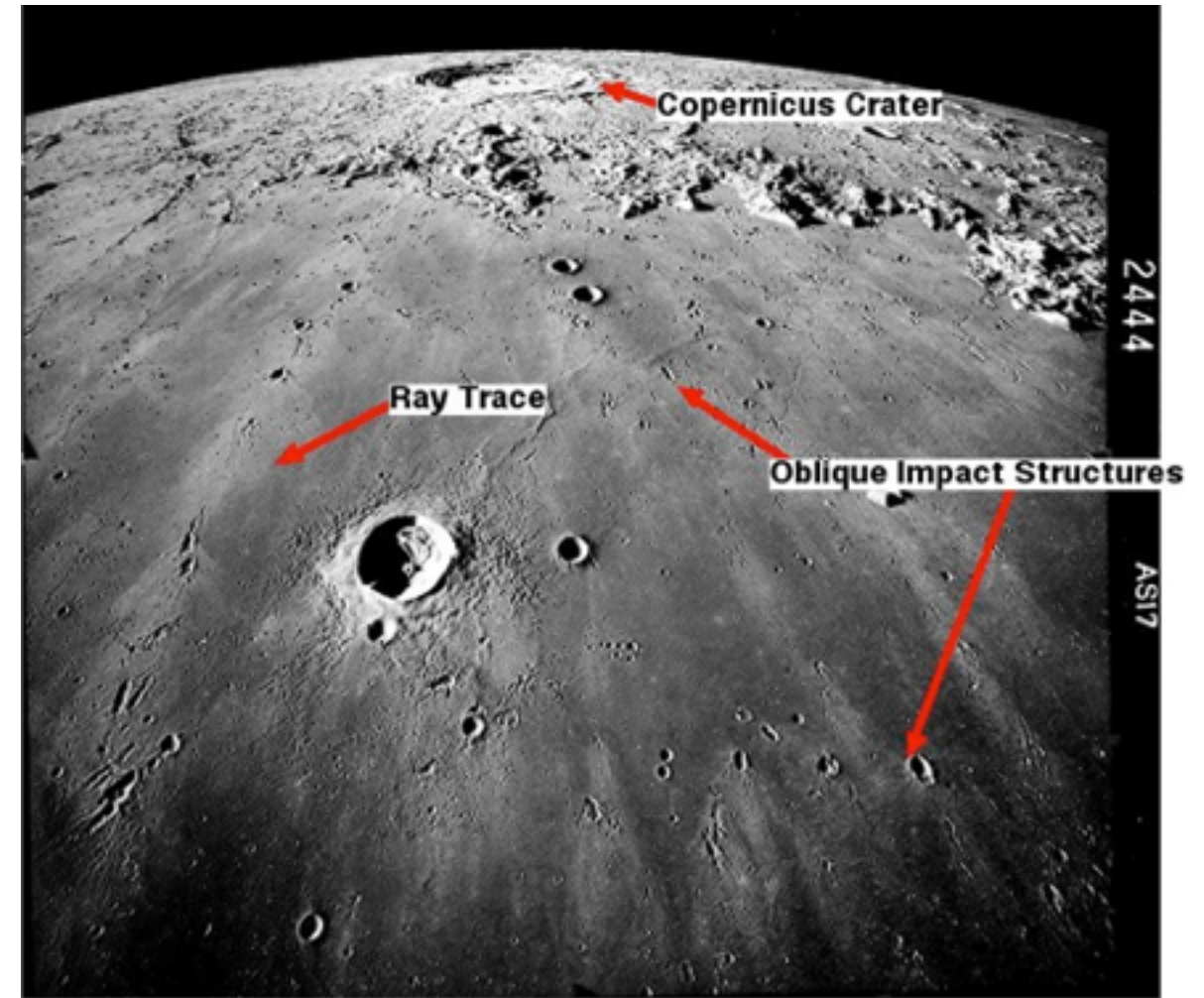


Figure 2.2 Apollo 17 aerial photograph of the 93-km-diameter Copernicus crater and its surroundings. Original photo from Apollo archives.

sequence presented in [Figure 2.3](#). This photographic record of a polycarbonate sphere impacting the surface of an aluminum target illustrates both impactor disintegration and the ejecta jetting phenomenologies.

When the leading surface of the impactor contacts the target surface, extreme, transient pressure gradients develop at the interface between the impactor and target. Lateral jetting of both impactor and target material radially away from the line of contact

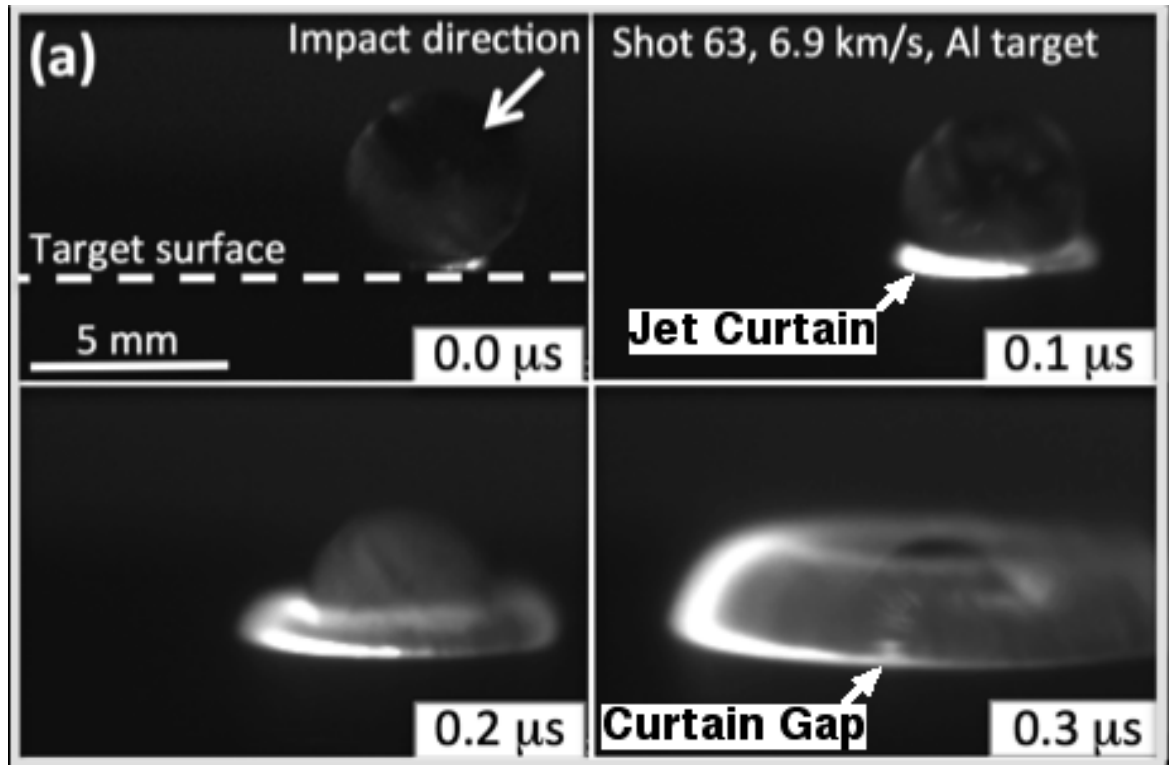


Figure 2.3 Ultra-high-speed photographs of a polycarbonate sphere impacting an aluminum surface at 45° at hypervelocity. Original image from Kurosawa, et al., 2014.

is initiated at contact by the radial pressure gradients. The line of contact lies at the apex of the two planar surfaces found at the interface between the impactor and the target. The leading edge of the jet curtain seen in [Figure 2.3](#) has accelerated to about 15 km/s between 0.1 to 0.2 μs and to about 45 km/s between 0.2 to 0.3 μs . In this case, the velocity of the impactor was 6.9 km/s for an impact angle of 45° above the target surface.

The earliest shape changes in the ejecta sheet are well documented in the sequential frames in [Figure 2.3](#) that span the first 0.3 μs of the cratering process. As indicated by the progression to the curved, doughnut shape of the ejecta curtain, the ejecta trajectory from the point of contact starts almost

parallel to the target surface, and as the impactor nears the end of its coupling with and penetration into the target surface, the angle of the ejecta curtain out of the forming crater above the target surface is approaching higher, steady excavation angles... previously illustrated in [Figure 1.18](#).

As documented in the photo sequence in [Figure 2.3](#), the trailing geometry of the impactor is unaltered throughout the contact/coupling process...precisely as also recorded in [Figure 1.19\(b\)](#). The trailing surface of the impactor seen at the 0.3 μs exposure time in [Figure 2.3](#) is pristine...no indication of impactor disintegration due to a reflected shock front, as is generally proposed. These observations of undisturbed trailing surfaces of impactors presented here are contrary to the popular model that claims a shock front reflected off of the trailing surface of the impactor causes its subsequent disintegration...see for example Melosh, 1989. As will be discussed later in this chapter, disintegration of the impactor is generally observed to occur inside the forming primary crater due to mechanical interaction, and the degree of impactor disintegration depends on the physical and mechanical properties of both the impactor and the target materials.

The obvious z-shaped gap in the ejecta curtain seen in the 0.3 μs frame of [Figure 2.3](#) is comparable to the segmentation of radially expanding fluid sheets generated by localized shear in the ejecta sheet produced when a liquid droplet impacts a liquid surface as seen in [Figure 1.19](#). The segmentation of the ray traces seen on Mercury, Mars and Earth's Moon are formed by the same mechanism. These gapped structures are derived from the stress pattern that develops during the circumferential and radial

expansion of this early ejecta curtain...to be discussed in more detail in **Section 4.1.1**.

A composite of the transforming geometry of the jetting ejecta curtain is also illustrated in [Figure 2.4](#). Comparing the photograph in [Figure 2.4](#) with the ejecta curtain images in [Figures 1.18](#) and [2.3](#) we can observe that the image in [Figure 2.4](#) represents a composite of the 'Contact' through the 'Shock Front Breakthrough' images in [Figure 1.18](#). The well defined curved ejecta structures that are spreading laterally away from the center of the impact at the base of the primary crater ejecta cone were well removed from view when the camera started recording the event. A stable ejecta cone angle, that represents primary crater excavation, develops later in the cratering process.

Very high temperatures are observed for material in ejecta curtains derived from hypervelocity impact. For example, ejecta temperatures as high as 5000 K have been measured at the beginning of the cratering process in tungsten, impacted by an iron sphere traveling at 7.4 km/s, Collette, et al, 2013. In these experiments, the ejecta temperatures were measured to drop to about 3500 K within about 2.5 μ s after impact due to radiative heat transfer, and within 20 μ s after impact, the ejecta temperature fell to about 3000 K. The elevated temperature of the ejecta is indicated by its self illumination...white areas in the photographs in [Figures 2.3](#) and [1.18](#). These early-stage high temperatures are also well illustrated in [Figure 2.4](#) where the earliest, highest temperatures are indicated as white in the image near the target surface and the later, cooler temperatures (orange) in the ejecta curtain well above the target surface.

Jetting Ejecta



Primary Crater Ejecta Cone

Figure 2.4 Photograph of ejecta produced in a vacuum from limestone by impact of a 1.9-mm-diameter aluminum sphere traveling normal to the target from right to left at 5 km/s. Original image from Giacomuzzo, et al, 2006.

2.1.2 IMPACTOR COUPLING AND PRIMARY CRATER FORMATION DYNAMICS

As an impactor traveling at supersonic velocity relative to the target material becomes buried in the target, its momentum and energy are coupled into the target material, and shock waves similar to those seen in air in [Figure 1.13](#) are generated below the surface of the target, i.e. a Mach Cone will trail immediately behind the impactor followed by an attached sonic shock front. For impactors possessing velocities in excess of the speed of sound

inside the target, the coupled sonic shock front cannot completely develop in the target until the trailing surface of the impactor reaches the original surface of the target. As will be demonstrated in this section, the morphology of the shock fronts coupled inside a solid target is governed by the same physical processes illustrated in [Figure 1.13](#).

2.1.2.1 EARLY NORMAL INCIDENCE IMPACT CRATERING

The process of impactor energy and momentum coupling and early primary crater excavation is illustrated in the diagram presented in [Figure 2.5](#). As a supersonic shock wave couples into the target material, the ejecta curtain transitions from impact surface hugging jet curtain seen in [Figure 2.4](#) to a steady conical structure like that marked as the “Primary Crater Ejecta Cone” in [Figure 2.5](#). A mixture of impactor and target materials flows along the surface of this ejecta cone for as long as it takes to excavate a primary crater.

Early in the primary crater excavation process in a solid target, the typical ejecta stream contains a mixture of vapor, liquid and solid derived from both the impactor and target materials. Vapor and liquid are produced by extreme heating of the impactor and target materials due to extreme compression inside both the supersonic and sonic shock fronts and heat generated by material failure... heat effects from material failure will be discussed in Chapter 4. If the impact velocity of the projectile exceeds the sound speed in the target material, ejecta will initially flow along the surface of a Mach Cone similar to that indicated in [Figure 1.13](#).

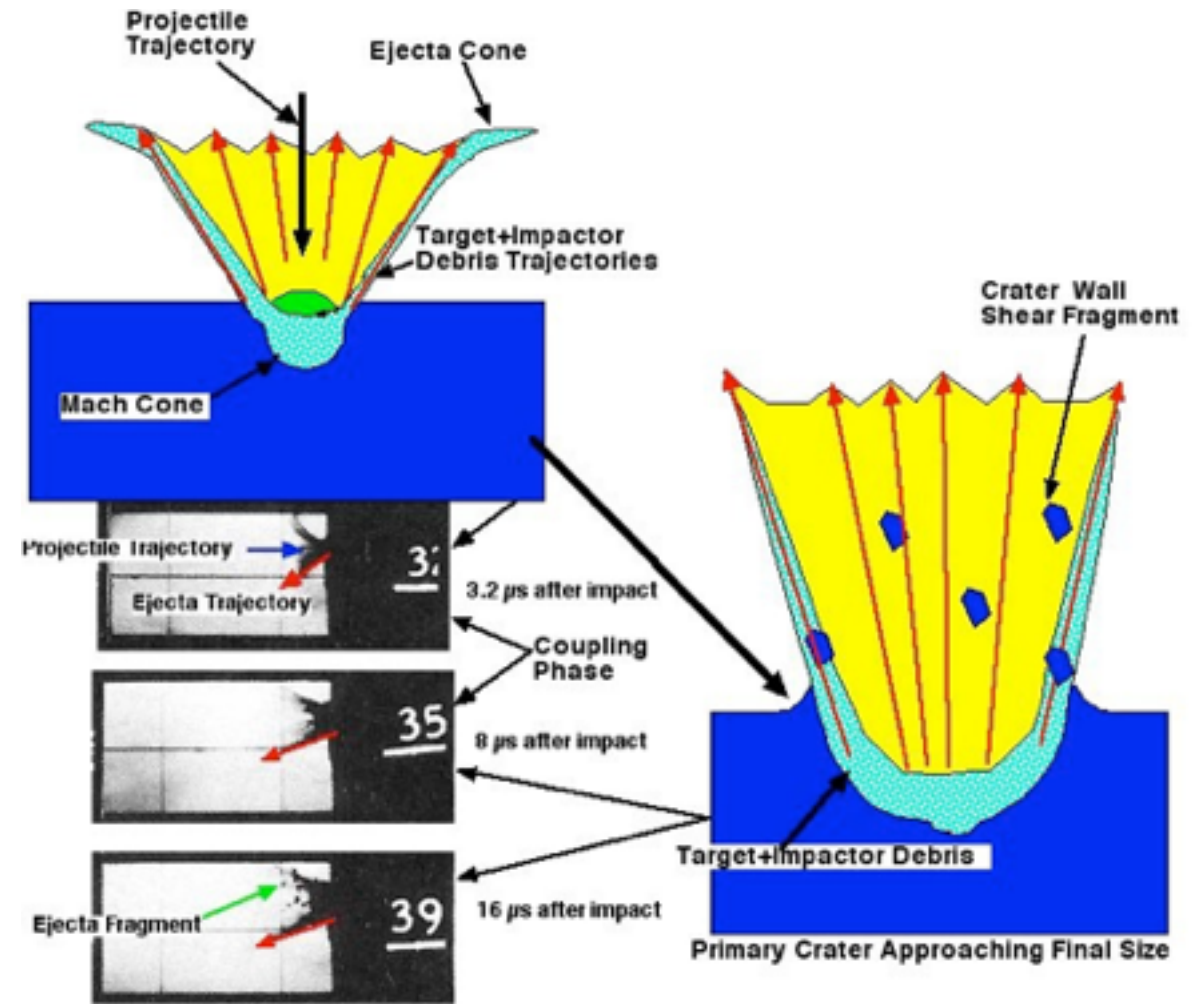


Figure 2.5 Diagram of Coupling and Steady, Primary Crater Excavation for normal impacts into ductile materials. Shadowgraphs illustrate hypervelocity impact ejecta from titanium resulting from impact by a 1.4-mm-diameter glass sphere traveling normal to the target surface at 7.3 km/s, from Lundberg, et al, 1982.

As observed in [Figure 2.5](#) in the sequential shadowgraphs of impact ejecta from titanium, significant numbers of solid fragments are sheared from the inside surface of the forming crater and become entrained in the ejecta flow inside this target within 16 μs after impact. Ejecta flows away from the centroid of the growing crater initially along the surface of the Mach Cone and subsequently along the sonic shock front, i.e. along the flow paths

illustrated in [Figure 2.5](#). The ejecta flow eventually becomes confined to a thin curtain guided by the inside surface of the developing crater...mostly along the sonic shock front from the primary crater because ejecta along the surface of the Mach Cone disappears when the velocity of the impactor remnants and its associated shock front degrade to below the sonic velocity of the target material. A steady ejecta cone angle is seen for the 8 to 16 μs interval for the titanium impact target depicted in [Figure 2.5](#) which infers the duration of primary crater excavation flow.

2.1.2.2 CRATERING DYNAMICS INSIDE THE TARGET

The cratering behavior and the progression of shock fronts inside a solid is clearly demonstrated in the set of flash x-radiographs recorded by Yasui, et al, 2012 during hypervelocity, normal impact of stainless steel spheres into gypsum targets that contained about 50% porosity. As seen in the earlier frames in [Figure 2.6](#), a sonic shock front defined by the boundary of a truncated ellipse is seen to develop and expand at a declining rate below the surface of the target. The early crater excavation process involves both material flow along the shock front, and significant compaction of material around the expanding cavity...both processes are involved in the development of primary craters in porous materials. The hole through which material is ejected expands at a slower rate than the minor diameter of the sonic shock front inside the target. The expanding shock front eventually breaks through the free surface explosively up-range as also observed in [Figures 1.17](#) and [1.18](#). The thickness of the sonic shock front inside the target increases and becomes more diffuse with time, Yasui, et

al, 2012, indicating a steady peak pressure reduction inside the front.

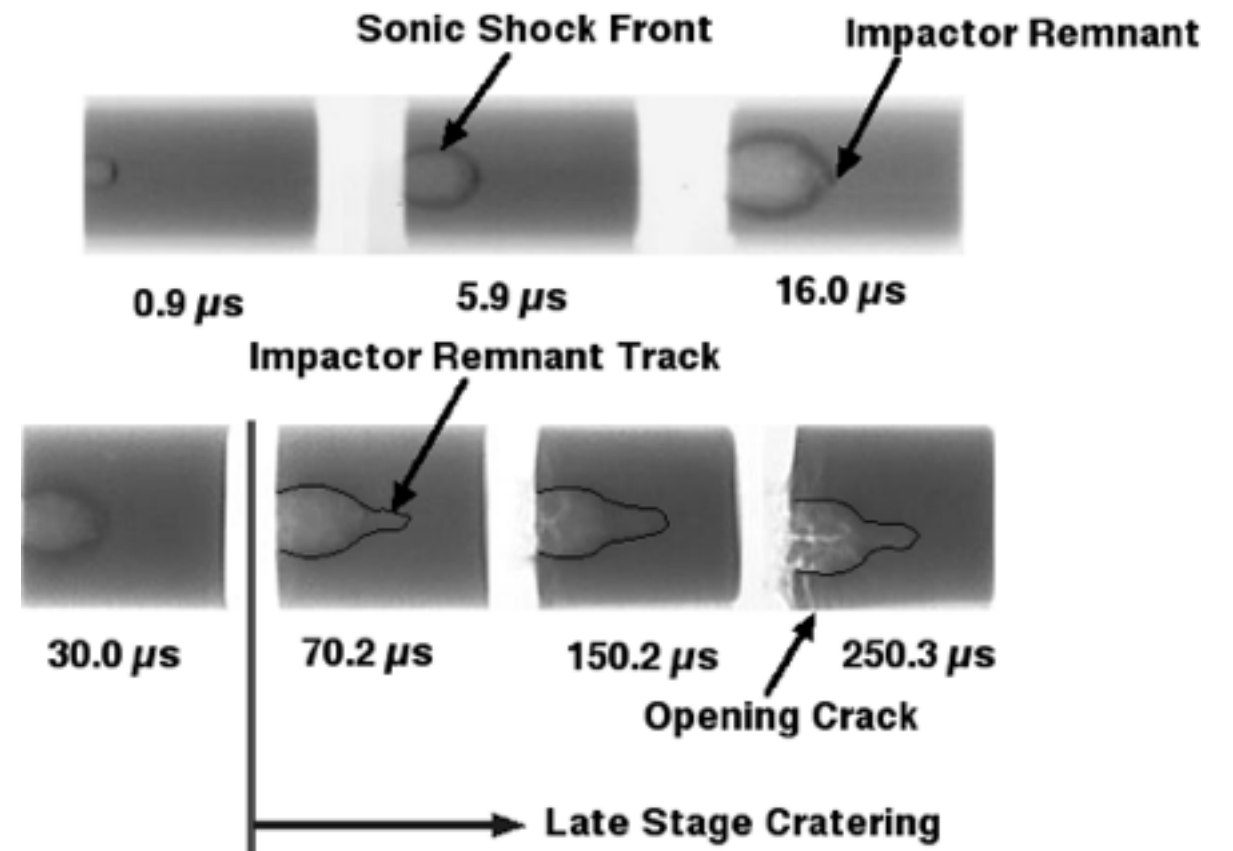


Figure 2.6 Set of x-radiographs from different shots that illustrate the cratering process in porous gypsum resulting from impact of 3.2-mm-diameter stainless steel spheres traveling at 5.6-6.4 km/s under low atmospheric pressure. Original radiographs from Yasui, et al, 2012.

As the primary crater nears completion, the expanding sonic shock front breaks through the target surface...between the 70.2 and 150.2 μs frames, and secondary cratering commences (compare with sequences in [Figures 1.17](#) and [1.18](#)). As Early-Stage Cratering ends and Late-Stage Cratering begins, target material is sheared from the perimeter of the ejecta hole creating a straight-walled crater rapidly increasing total

crater volume. The cracks that are seen to be opening in the 250.3 μs frame will eventually lead to the spallation of target material from around the perimeter of the primary crater forming a secondary crater. This late-stage phenomenology will be examined in more detail later in this chapter.

A large pressure gradient persists through the thickness of the sonic shock front that is produced inside the target material. Also, there is a large pressure drop from the bottom of the forming primary crater to the target surface along the shock front. When the sonic shock front breaks through the target surface up-range, producing effects like that observed in [Figures 1.18](#) and [2.6](#), both target and impactor debris flow out of the forming primary crater up-range along the shock front down the pressure gradient.

As the shock front excavation and expansion of the primary crater comes to a close, an elastic wave begins to expand away from the inside of this crater into undamaged target material. However, residual pressures immediately outside of the excavated crater remain at levels high enough to cause plastic deformation and fracture of the target material which can contribute significantly to the final excavated volume and modify the final shape of the impact structure.

A lens shaped remnant of the impactor is clearly visible in the 0.9 μs frame in [Figure 2.6](#) at the leading edge of the ballooning shock front. As time progresses, the image of the remnant impactor becomes less distinct indicating further impactor deformation and disintegration. Late in the process, intact frag-

ments of the disintegrating impactor continue downrange after the sonic shock front is arrested. The track of the impactor fragments is prominent in the 70.2 μs frame and beyond. However, the impactor remnant has been arrested at the 70.2 μs mark after which the momentum and energy of the impactor fragment is arrested and Early-Stage penetration stops. The depth of penetration of the impactor fragment actually decreases between the 150.2 and 250.3 μs frames in [Figure 2.6](#)... confirmed by data listed in Table 1 in Yasui, et al, 2012. This apparent reduction in penetration is due to the start of spring-back from the compressive stresses produced by the impact...consistent with the late-time stress relaxation. During spring-back, the maximum resolved stresses in material surrounding the cavity eventually become tensile which leads to crack opening around the crater...note especially the 250.3 μs frame in [Figure 2.6](#).

The 'impactor remnant track' indicated in [Figure 2.6](#) is very similar to the penetration track produced by a stainless steel sphere impacting a porous gypsum target at about 2 km/s, Yasui, et al, 2012...seen in [Figure 2.7](#). In this example of a low velocity impact, the projectile was minimally altered during target penetration, and a minimal sonic shock front was coupled into the target. The track of the remnant impactor is tubular indicating that lateral expansion of the shock front is small and forward momentum dominates the shape of the shock wave soon after impact.

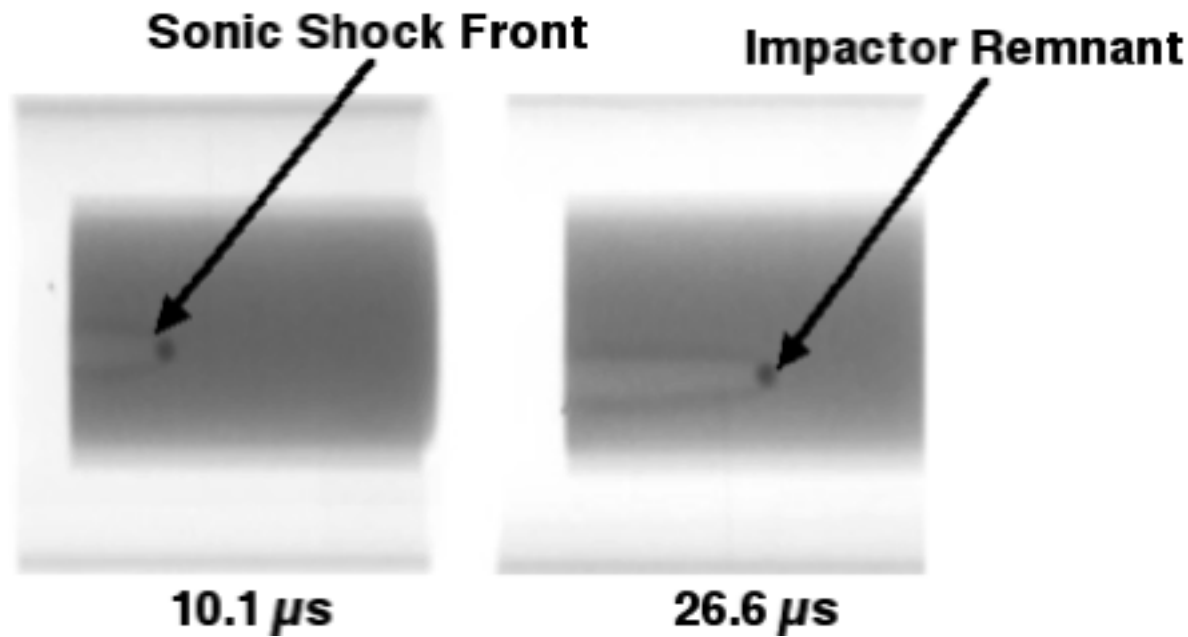


Figure 2.7 X-radiographs of impact structures forming in porous gypsum by 3.2-mm-diameter stainless steel spheres traveling at 2 km/s. Original images from Yasui, et al, 2012.

2.1.2.3 IMPACT CRATERING IN WATER

Laboratory scale supersonic impacts experiments into water targets are prototypic for the early stages of the impact process in geologic materials. The high speed photograph presented in [Figure 2.8](#) captured the early-stage effects of normal hypervelocity impact of a finite, blunt object (aluminum sphere) into water. A sonic shock front has developed inside the target because the velocity of this impactor exceeded the sonic velocity of water. As previously seen for other materials, ejecta from this developing cavity originates from the surface of the sonic shock front.

The shape of the ejecta plume seen in [Figure 2.8](#) has been modified partly by the presence of a significant air pressure

over the target surface. Reducing overpressure results in a more conically shaped ejecta plume...see Mader and Gittings, 2003. The ejecta plume seen here is prototypic of that pro-

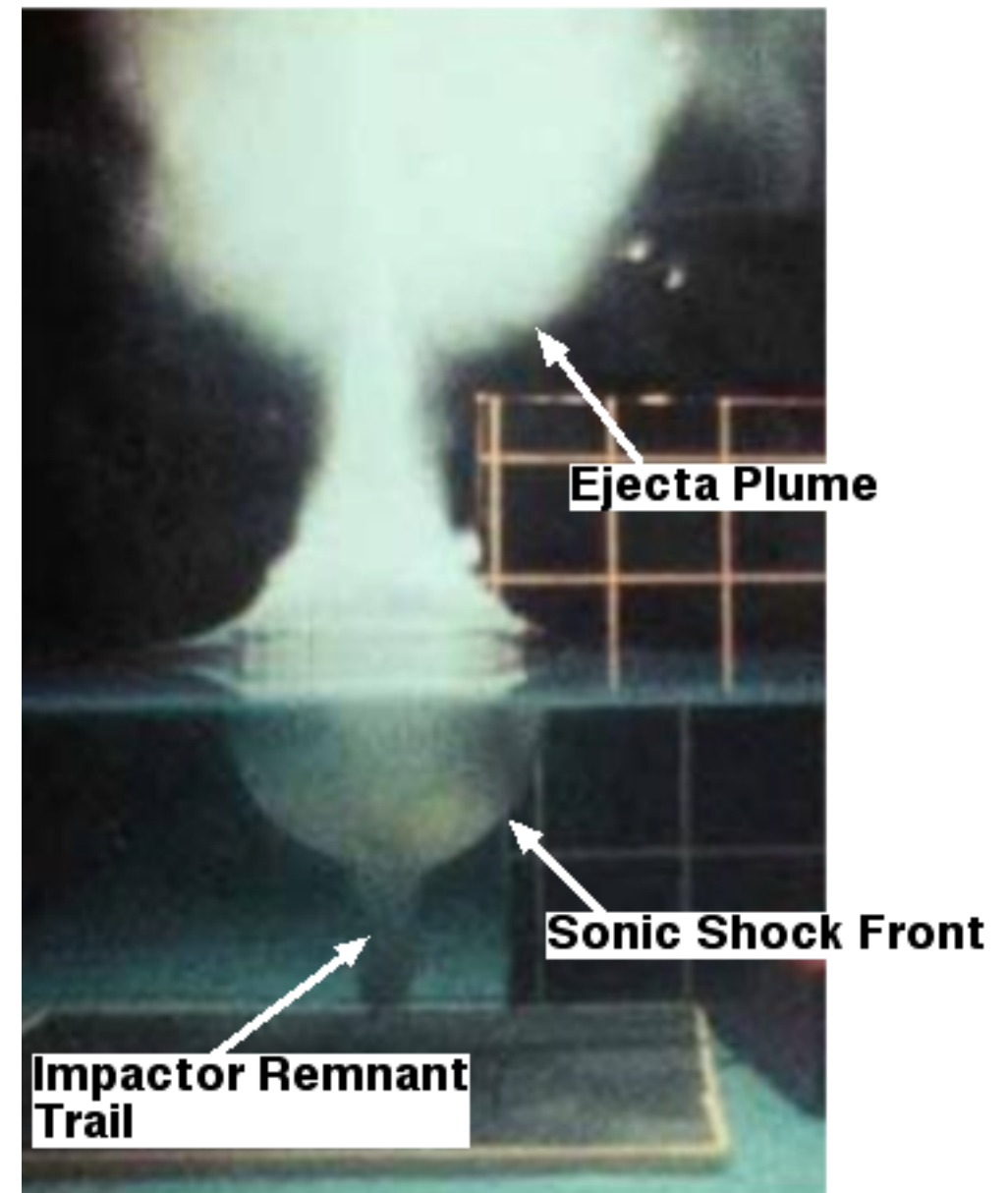


Figure 2.8 Photographic record of shock waves generated shortly after impact in water by a 3.2-mm-diameter aluminum sphere traveling through air at atmospheric pressure and impacting the water surface at 2.5 km/s. Original photograph from Mader and Gittings, 2003.

duced early-on after meteoric impact into deep water on Earth.

2.1.2.4 HYPERVELOCITY IMPACT CRATERING IN AND PERFORATION OF METAL TARGETS

Examination of hypervelocity impact response of metals can be highly instructive relative to impact cratering mechanics in geologic materials. Shadowgraphs of impact perforation of a thin metal sheet seen in [Figure 2.9](#) illustrate several important features of shock front behavior resulting from normal impact. The expansion of the coupled shock front inside a thin titanium target is clearly illustrated in the two high speed shadowgraphs. The rear surface bulge indicated in [Figure 2.9\(a\)](#) reflects the surface contour of the sonic shock front that has developed inside the target during the coupling process. It appears that the primary crater has stopped growing at the instant of image capture in [Figure 2.9\(a\)](#) because there is virtually no increase in the base diameter of the ejecta cone in the interval to the subsequent frame...[Figure 2.9\(b\)](#). In addition, the external record of the expanding impact crater seen in [Figure 2.9\(a\)](#) closely resembles the internal record, presented in [Figure 2.6](#) for times up to 30 μ s. The rear surface bulge in [Figure 2.9\(a\)](#) reflects the shape of the front surface of the shock wave which deviates from true hemispherical much like that seen in [Figure 2.6](#).

The rear surface bulge has expanded sufficiently between the frames in [Figure 2.9\(a\)](#) and [Figure 2.9\(b\)](#) to cause a circular fracture at the top of the bulge which generates a 'spall cap'

that is propelled downrange. The spall cap is produced as a result of stresses derived from the expanding shock front rather than interaction with elastic waves reflected from the rear surface, as frequently hypothesized in the literature.

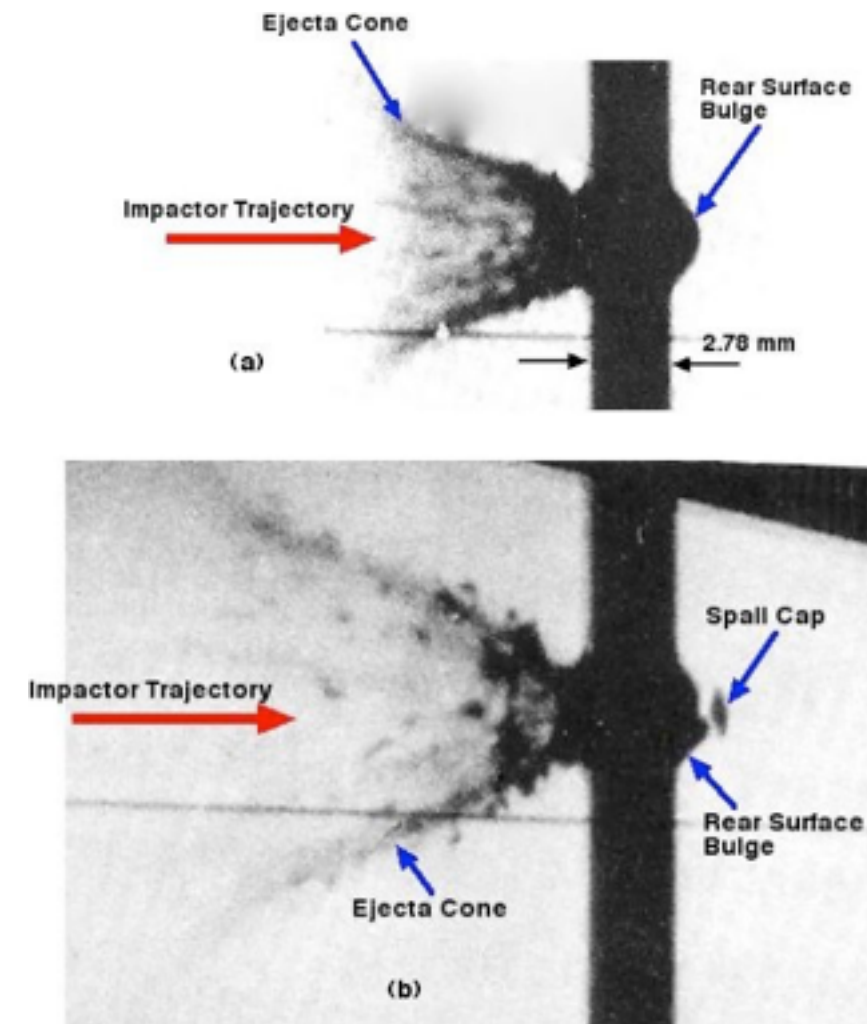


Figure 2.9 Sequential shadowgraphs of a Grade 2 titanium sheet maintained at room temperature under a vacuum and impacted by a 1-mm-diameter glass sphere traveling normal to the target surface at 6.12 km/s: (a) just prior to rear surface failure and (b) just after rear surface perforation. Original images from Lundberg, et al, 1982.

The morphology and makeup of a typical ejecta cone emanating from a forming primary crater is also demonstrated in [Figure 2.9](#). The bottom of the ejecta cone is observed to change shape from [Figure 2.9\(a\)](#) to [Figure 2.9\(b\)](#) including an increase of ejecta cone angle as cratering progresses. The base of the ejecta cone is seen to have become essentially columnar in [Figure 2.9\(b\)](#) which means that ejecta is starting to rebound from the bottom of the primary crater and its trajectory is constrained by the shear strength of the walls of the primary crater. In both frames, the ejecta cone is also seen to contain many large fragments that have been striped from the forming crater walls... even though titanium is a relatively ductile metal.

Fractures that developed along the shear bands indicated in [Figure 2.10](#) indicate the source of these large ejecta fragments. The 'plastic deformation boundary' indicated in [Figure 2.10](#) represents the surface where the late-stage residual stresses produced by the expanding shock wave have become elastic in the titanium target...plastic deformation ceases at this surface and beyond. A detailed discussion of material deformation mechanics in and around an impact structure in a wide range of materials will be presented in Chapter 4.

The up-range bulge seen around the ejecta curtain on the target impact surface in [Figure 2.10\(a\)](#) reflects the shape of the up-range surface of the shock wave that was coupled into the target material...recall especially [Figure 2.7](#). As indicated in [Figure 2.10\(a\)](#) by the convex curvature of the ejecta curtain near its base, crater perimeter up-range surface breakthrough

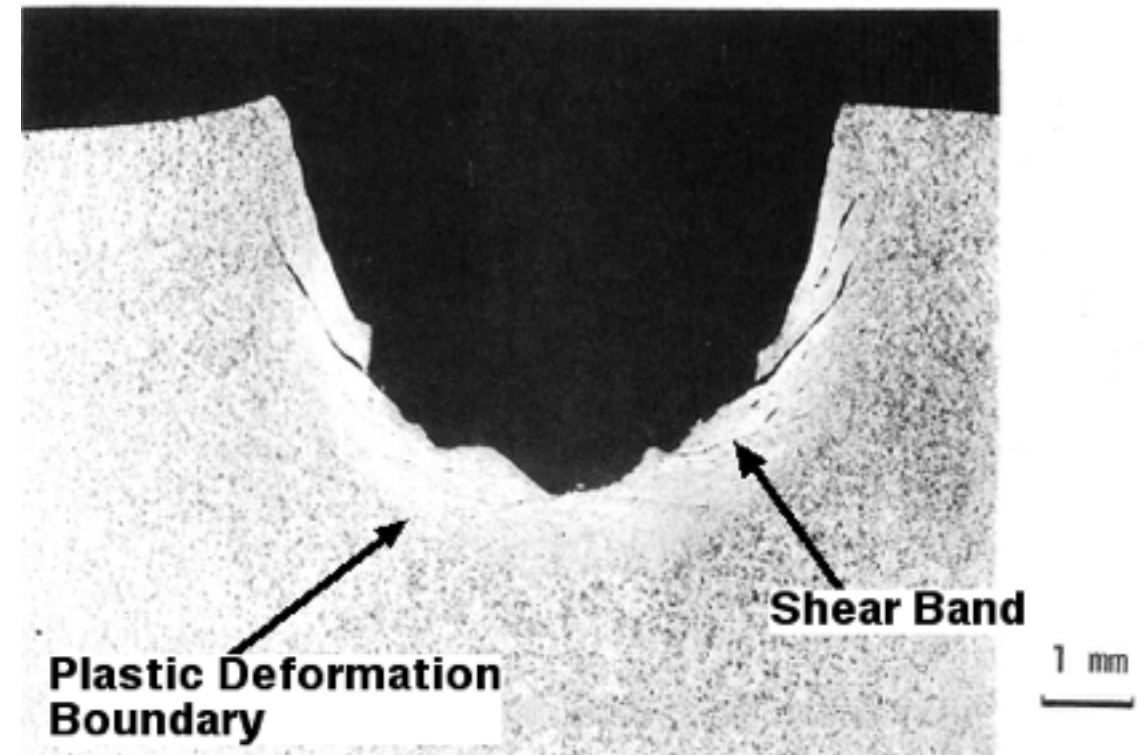


Figure 2.10 Crater midline cross-section in titanium bar maintained at room temperature and impacted on a normal trajectory by a 1.59-mm-diameter copper sphere traveling at 5.80 km/s. Original photomicrograph from Lundberg, et al, 1982.

of the internal shock front has started. When breakthrough occurs, large chunks of target material enter the ejecta curtain...seen in [Figure 2.10\(b\)](#). In a ductile metal, the breakthrough process can commonly form a rollover crater lip at the perimeter of the primary crater like that seen in [Figure 2.11](#).

At this point, it is worth comparing some of the structural features of the crater seen in [Figure 2.11](#) with those seen in cross-section in [Figure 2.10](#). The rings seen in the bottom the crater shown in [Figure 2.11](#) are consistent with the bumps along the

bottom surface of the crater in [Figure 2.10](#). It is important to note that these bumps correlate with the ends of adiabatic shear bands (ASB's) that have intersected the inside surface of the primary crater. These structural features correlate with

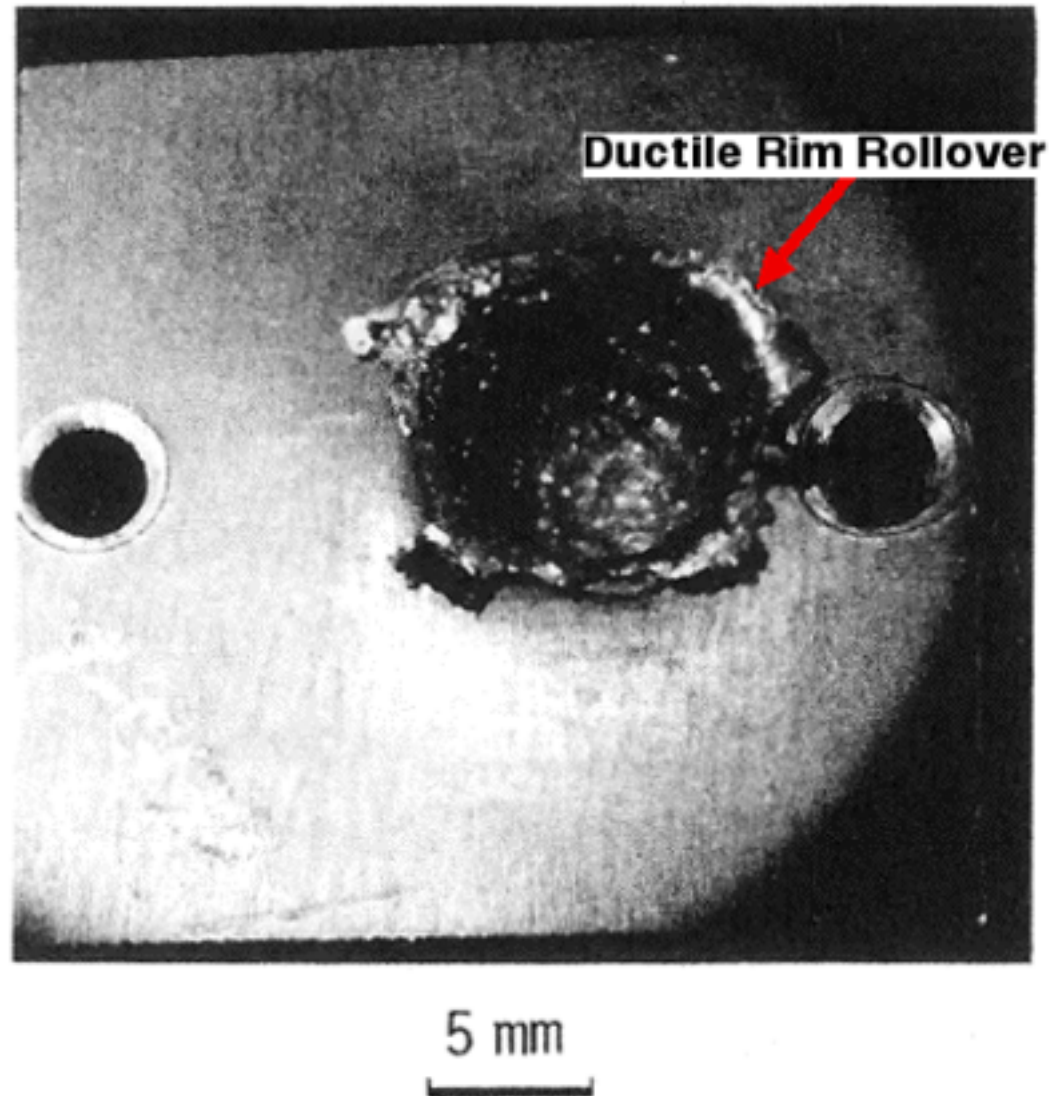


Figure 2.11 Crater in a semi-infinite titanium plate heated to 775 K and impacted on a normal trajectory with a 1.59-mm-diameter copper sphere traveling at 7.29 km/s. Original photograph from Lundberg, et al, 1982.

those previously noted for the Aristarchus impact crater on Earth's Moon...recall [Figure 1.3](#).

2.1.2.5 CRATER SCALING IN DUCTILE METALS

Mathematical scaling models that correlate the size of hypervelocity impact craters with impactor mass and velocity must accurately reflect the cratering process in order to produce credible extrapolations to full size geologic craters, and these models must be consistent with the physics of the process, including the effects of both the energy and momentum of the projectile. Crater dimensions and shape have been shown to also be dependent upon the cratering resistance of the target material, their physical and mechanical properties, and angle of incidence of the impact. Crater volume or mass loss provide the most precise measure of correlated effects of impact of projectiles with their varying mass and velocity.

Impact cratering in ductile metals generally concludes with the formation of the primary crater, so examining data for the final dimensions of impact craters in this class of materials can offer considerable insight into the physics of the early stage cratering process. Scaling of the size and shape of laboratory-scale hypervelocity impact craters to full size geologic impact craters has been and continues to be a primary goal of both experimental and theoretical studies of cratering behavior. The development of crater scaling models involves correlating crater volume and other dimensions observed for laboratory-scale craters in a variety of target materials with the impactor velocity, size and mass.

From a historical perspective, early normal impact crater scaling models were based on a viscous fluid cavity expansion model...see for example Moore, et al., (1), 1962. The hypervelocity projectile impact cratering in solid targets was recognized early-on to be analogous to phenomenology of projectile impact into fluids. This correlation model represents the basis of the famous Charters-Summers multi-factor, single-term, impactor kinetic energy based, multi-parametric crater scaling equation, Charters and Summers, 1959. This model assumes hemispherical expansion of the coupled shock front inside the target. The primary goal of the Charter-Summers equation was to scale the depth of penetration of high velocity impactors possessing different densities into a variety of ballistic armor materials, but neither the fluid dynamics nor projectile momentum effects are explicitly included in this equation. Also, there is no differentiation of the cratering behavior relative to the speed of sound in the target material in the Charter-Summers model.

Hypervelocity impact crater morphology in ductile metals is typical of that seen in [Figures 2.10](#) and [2.11](#). It should be noted that the general crater shape deviates significantly from hemispheric even though the leading surface of the plastic deformation boundary is very nearly hemispheric.

Analyses of a significant amount of normal impact data (for example from Denardo, 1962, Denardo, et al., 1967, and Lundberg, et al, 1982) indicate that the following simple equation, that includes both momentum and energy of the projectile precisely, expresses crater volume, $V(m_p, v_p)$, as a function of pro-

jectile mass, m_p , and velocity, v_p , for a particular combination of projectile and impactor materials:

$$V(m_p, v_p) = m_p(\mathbf{a} + \mathbf{b}v_p + \mathbf{c}v_p^2) \quad \mathbf{2.1}$$

The constant in the first term, \mathbf{a} , in **Equation 2.1**, represents both physical and mechanical properties of both the impactor and the target materials and has units of inverse density. The term that includes the first order dependence on velocity of the impactor, \mathbf{b} , is a vector constant and represents effects of momentum upon crater volume, and the constant for the second order term of velocity, \mathbf{c} , represents the kinetic energy dependence of crater volume. Values of these constants for impact crater volumes determined for pure and alloy aluminum and titanium are presented in **Table 2.1**. Note that all three of these constants incorporate parameters that are unique to particular impactor and target material combinations and includes heats of fusion and vaporization plus strength parameters. The listed R^2 values, the correlation coefficients from the least-squares analysis of the data, indicate the high precision of fit of the data to **Equation 2.1**. This small data scatter is illustrated by the data plot in [Figure 2.12](#) for the measured impact crater volumes in the aluminum alloy Al-2024-T4.

Laboratory-scale impact data are limited, but the veracity of the simple cratering model expressed in **Equation 2.1** is reinforced by the fact that they were produced from hypervelocity, normal impacts of a variety of impactor shapes and sizes. The 20.3-mm-diameter polyethylene bullet shaped projectiles referred to in [Figure 2.12](#) and sketched in [Figure 2.13](#) (data from

Table 2.1 Constants for Equation 2.1

Target Material	a, m ³ /kg	b, m ³ /kg·(m/s)	c, m ³ /kg·(m/s) ²	R ²	Reference
Al-2024-T4	-8.59x10 ⁻⁴	6.59x10 ⁻⁷	1.50x10 ⁻¹⁰	0.95	Denardo, 1962 Denardo, et al., 1967
Al-1100-0	-7.98x10 ⁻³	4.96x10 ⁻⁶	-8.56x10 ⁻¹¹	0.9	Denardo, et al., 1967
Ti @ 295 K	-1.40x10 ⁻²	4.72x10 ⁻⁶	2.84x10 ⁻¹⁰	0.7	Lundberg, et al., 1982

Denardo, 1962) generated crater volumes consistent with those produced by hard aluminum spheres having four different diameters ranging from 1.6 to 13 mm, Denardo, et al., 1967. These projectiles were all accelerated inside separable sabots in two-stage light gas guns over a range of velocities from about 3 to 8.6 km/s and in powder-gas guns for the lower velocities. Impactor velocities and original projectile masses were accurately determined, and the dimensions of and ejecta masses from the resulting impact craters were measured. Crater volumes were determined directly by measuring the volume of wetting-agent-containing-water or the amount of solidified plaster needed to fill the crater to the level of the original surface...indicated by the red line in [Figure 2.13](#). The impact crater geometry produced in Al-2024-T4 differs from those formed in Al-1100-0...highly ductile commercially pure and annealed aluminum in which only primary craters are produced by normal impacts. The hint of a secondary crater indicated by the reduction of the angle of the crater wall just below the red line in [Figure 2.14](#) was generated in the less ductile aluminum alloy.

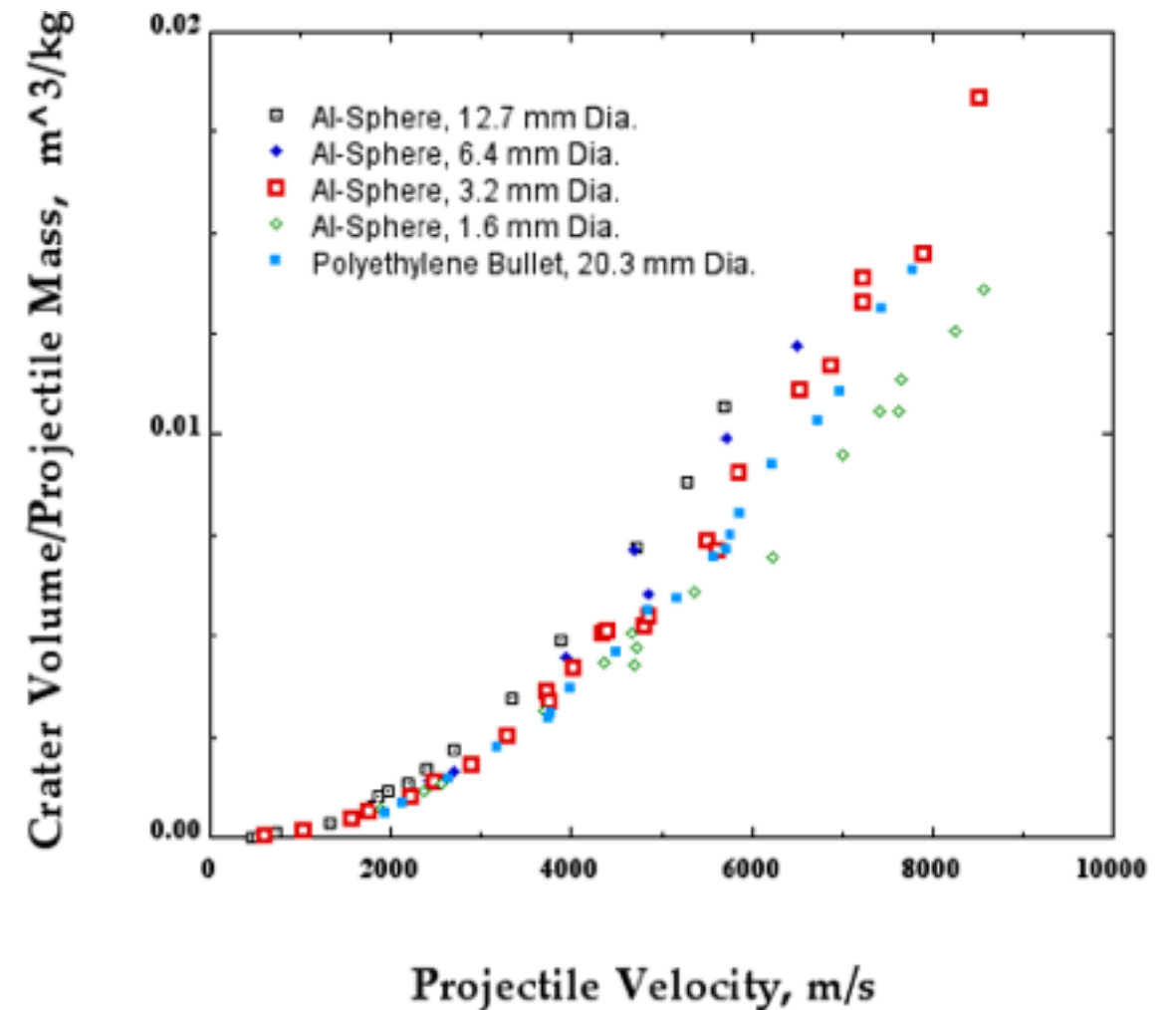


Figure 2.12 Plot of data from impacts into semi-infinite Al-2024-T4 targets maintained at room temperature. Data for Al-Sphere impactors comes from Denardo, et al., 1967, while data for the Polyethylene Bullet impactors comes from Denardo, 1962.

Regardless of target ductility, $P/D > 1$, much like that previously seen for impact craters in titanium...recall [Figure 2.10](#). The momentum of the impactor contributes to a deviation from crater hemisphericity. As illustrated in [Figure 2.13](#), the measured values of P and D are somewhat arbitrary whereas the volume measurement is less subject to interpretation making it the best choice for determining and verifying scaling models.

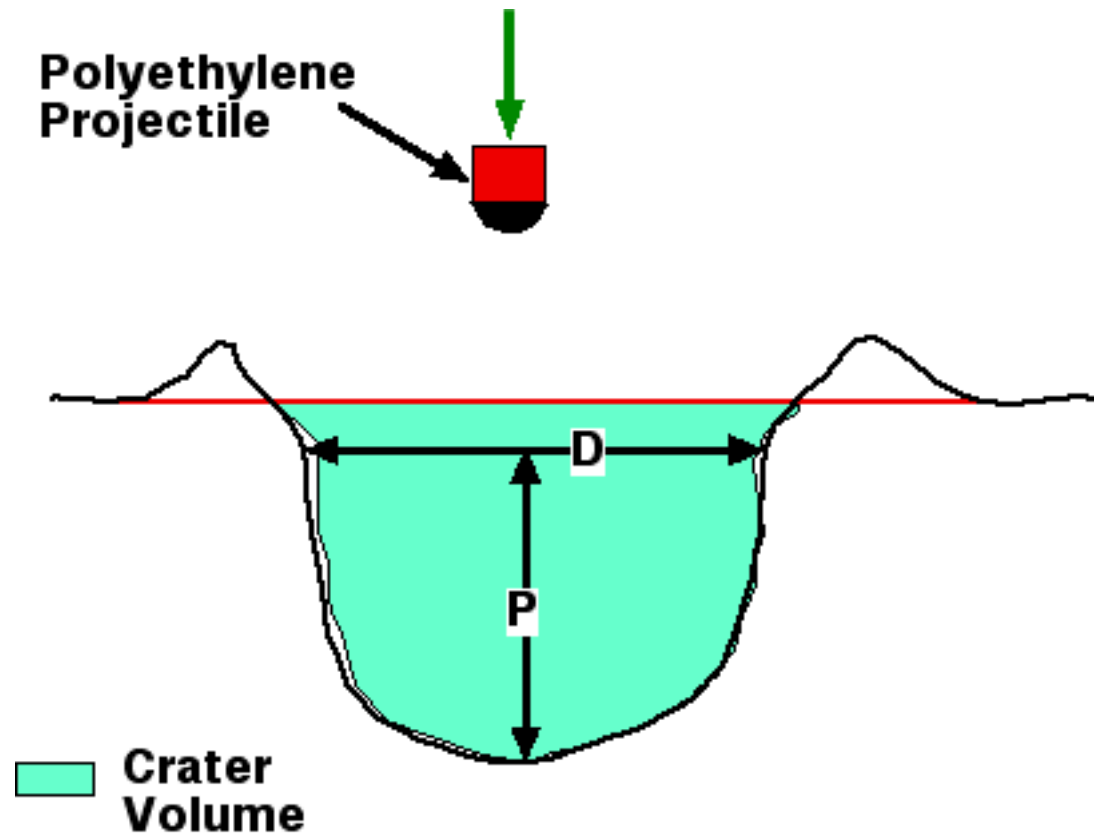


Figure 2.13 Schematic of typical cross-sections of hypervelocity, normal impact craters into Al-2024-T4. This Polyethylene Projectile design was used by Denardo, 1962.

The data presented in [Figure 2.12](#) include the transition in cratering behavior from subsonic to supersonic impacts. The slope of the curve increases significantly with increasing impactor velocity above the sound speed of the target material (5 km/s for aluminum). This indicates that projectile momentum is significant below the sound speed in the target material; whereas, projectile energy becomes dominant above the target sound speed.

It has been observed for the aluminum alloy 2024-T4 that the volume of a hypervelocity impact crater is approximately twice the volume calculated from mass loss, Denardo, 1962.

For ductile metals, this differential is derived from the fraction of the crater volume produced by plastic deformation around the primary crater. This differential is not expected for primary craters in brittle materials which generally exhibit little or no plastic deformation.

2.1.3 EARLY CRATERING IN OBLIQUE INCIDENCE IMPACT

Examination of the physics of early stage impact crater formation due to normal trajectory impact provides a foundation for understanding the cratering process. However, most impactors found in full scale geologic context strike the surface off normal, so it is necessary to expand to a consideration of the instructive laboratory data relevant to oblique impacts.

2.1.3.1 OBLIQUE IMPACT CRATERING RECORD INSIDE A DENSE SOLID

Observations of oblique impacts into transparent, solid materials at laboratory scale can provide considerable insight into the oblique cratering process. The progression of the crater surface profile resulting from a 30° impact into polymethylmethacrylate (PMMA), an optically transparent, brittle solid is seen in [Figure 2.14](#), Stickle and Schultz, 2011. The impactor is illustrated to scale in the 8 μs frame in [Figure 2.14](#), and the photographic image in this frame indicates that the early-

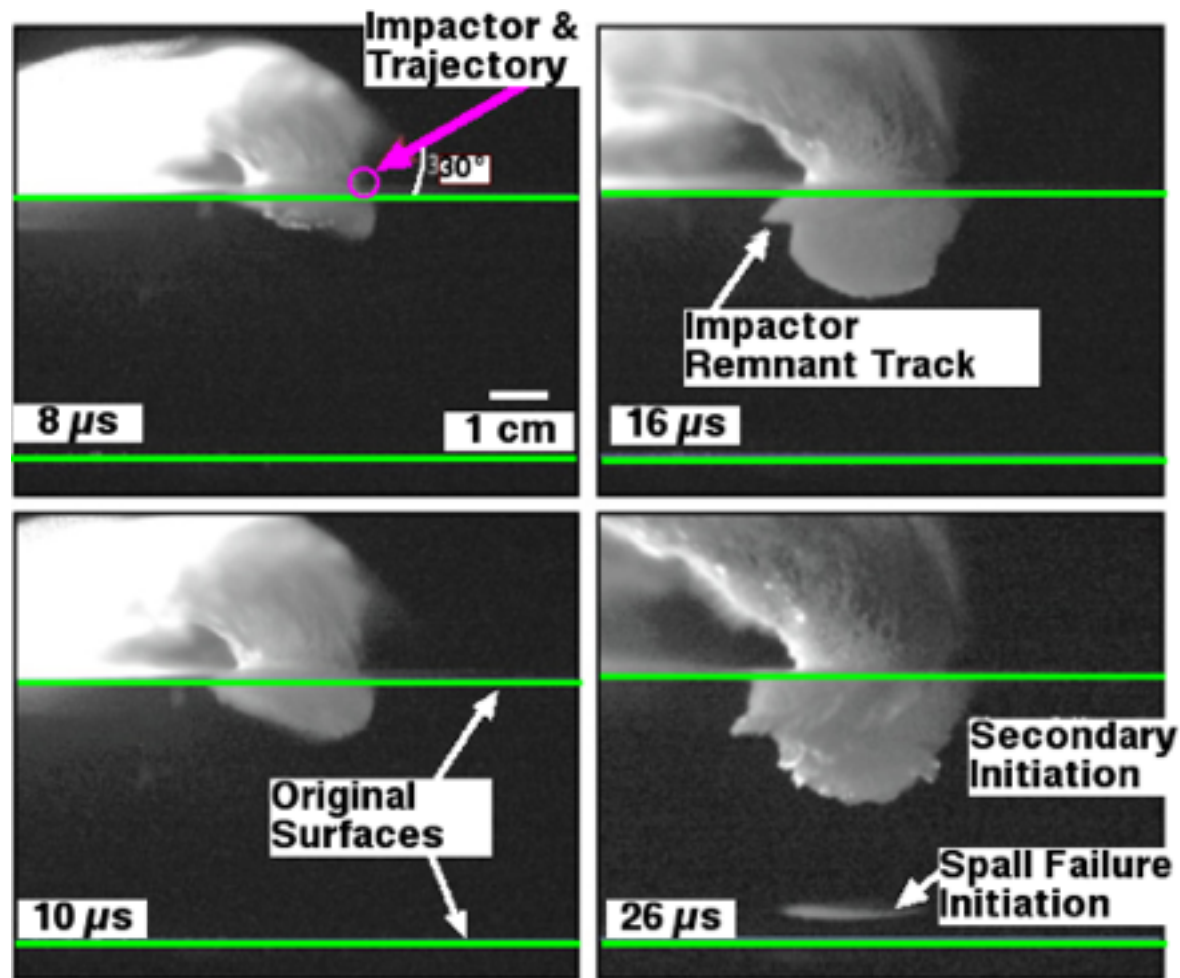


Figure 2.14 High speed sequential photographs of an impact structure forming in PMMA resulting from a 30° impact by a 6.35-mm-diameter Pyrex sphere traveling at ~ 5 km/s. Target was maintained at low atmospheric pressure during impact. Original image from Stickle and Schultz, 2011.

stage shock front shape possesses added complexity. First, the energy and momentum of the impactor have clearly coupled into the target by the $8 \mu\text{s}$ frame producing a distinct hemispherical shock front inside the target plus an associated, smaller bulge on the up-range side of the developing crater. The up-range bulge appears to develop below the target surface shortly after initial contact of the Pyrex glass impactor and appears to be related to a separate shock front produced

during the contact/coupling process and initial deformation and disintegration of the impactor. Traces of this additional structural feature persist throughout the photographic record...becoming more prominent at $10 \mu\text{s}$ but nearly obliterated at $26 \mu\text{s}$. This 2-dimensional view of the major arcuate structure observed below the target surface in the $8 \mu\text{s}$ frame is comparable to the record of the sonic shock front seen in the earliest frames of crater formation in porous gypsum seen in [Figure 2.6](#). The impactor remnant track in PMMA becomes well defined in the $16 \mu\text{s}$ frame and follows the impactor's original trajectory.

The bright, periodically spaced ruffles seen on the bottom of the developing primary crater below the impactor remnant track in the $26 \mu\text{s}$ frame appear to be caused by late-stage expansion of the crater cavity which produces localized shear (to be discussed in detail in Chapter 4). These data indicate that this late-stage target material damage pattern along the expanding crater surface is similar to that seen in [Figure 2.6](#) and was developed after the energy and momentum of the sonic shock front has been mostly arrested and when the quasi-static mechanical behavior of the target material starts to dominate the cratering process. Also, the local bright contrast seen in the $26 \mu\text{s}$ frame in [Figure 2.14](#) of the two protrusions from the lower left quadrant of the cavity is due to self illumination caused by heating produced by local adiabatic shear failure of the target material. The bright spots seen in the ejecta curtain in $26 \mu\text{s}$ also represent hot fragments of target

or impactor materials that have been excavated from the inside surface of the primary crater.

The crater diameter has stopped increasing between the 16 μ s and the 26 μ s frames. This is indicated by comparing the downrange side of the developing crater in these two frames... this side of the crater wall beneath the impact surface has been displaced downrange ahead of the downrange side of the base of the ejecta cone.

The beginning of Late-Stage Cratering is indicated by comparing the 16-26 μ s frames. The damage pattern that leads to Late-Stage Cratering around the forming primary crater is clearly displayed in the 26 μ s frame of [Figure 2.14](#) where the subsurface damage is seen to have expanded well beyond the base-diameter of the curtain of material ejected from the primary crater. The shock front on the leading edge of this damage zone will eventually break through to the surface and initiate secondary cratering in this brittle material...an examination of impact structures formed in brittle materials follows in **Section 2.2**.

An indication of incipient rear-surface spall is seen in [Figure 2.14](#) in the 26 μ s frame. The location of this spallation zone is controlled by the strength of the target material and the strength of the remnant, expanding elastic shock wave. Even though the normal stress vector is elastic at this point, the unrestrained back surface of the target allows the development of resolved shear stresses that exceed the fracture strength of the target material...recall **Section 2.1.2.4** and [Figure 2.9](#).

2.1.3.2 OBLIQUE IMPACT CRATER PLANFORMS IN DUCTILE METALS

The structure and formation of oblique, primary impact craters in ductile metals are prototypic for solids and can be correlated with the early-stage cratering mechanics and the ultimate morphology of geologic impact structures. Variation in hypervelocity impact crater planforms in 1100 aluminum foils as a function of impactor trajectory angles off-normal is displayed in [Figure 2.15](#). The planform for normal incidence (0° in [Figure 2.15](#)) impact trajectories starts to transition from circular to elliptical at about 25° off-normal and progresses toward a teardrop shape between 55° and 65° . In addition to asymmetry in the crater planform, material buildup on the downrange rim increases with obliquity up until about 65° off-normal. Up to this angle, the downrange rim height is greater than that on the up-range side. At trajectories beyond 65° off-normal, the downrange side of the crater tends to be blasted away causing the up-range side to be higher for the higher obliquities. The oblique hypervelocity impact cratering behavior in aluminum is very similar to that observed for stainless steel, Gardner and Burchell, 1997.

The shape of the crater rim also becomes increasingly asymmetric above impact angles of 35° off-normal...especially evident in the right side of [Figure 2.15](#). As the impactor trajectory increases off-normal from 35° to 65° , the plastically deformed crater lip tends toward a butterfly shape...similar to the ejecta pattern in [Figure 2.2](#). At impactor trajectories of

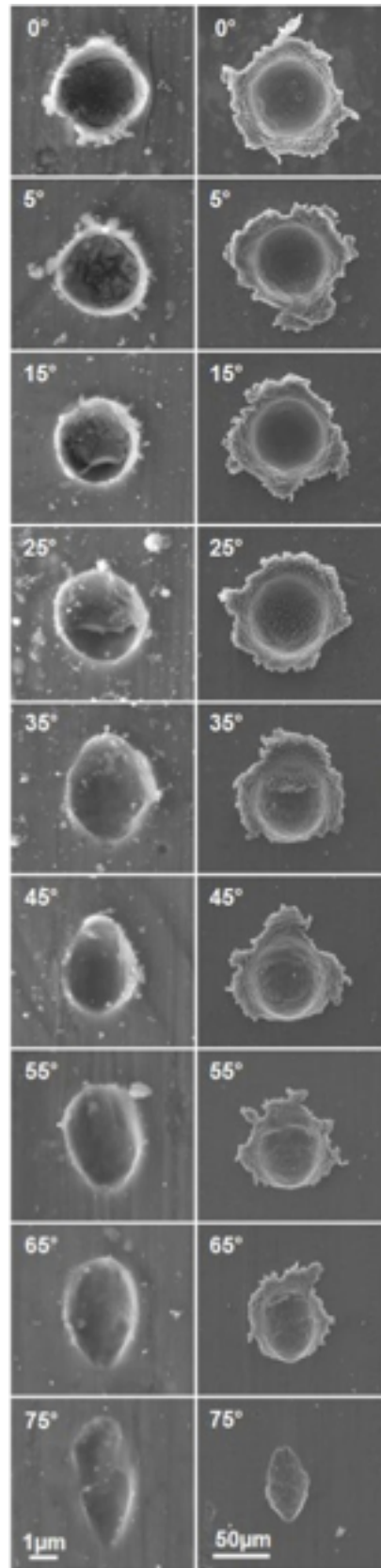


Figure 2.15 Impact craters formed in 1100 aluminum foil by 2- μm -diameter silica (right frames) and 22- μm -diameter glass projectiles traveling at ~ 5 km/s. Impactor trajectories are from bottom-to-top of the photos and angles from normal impact are indicated. Data from Wozniakiewicz, et al, 2013.

75° and above, most of the ejecta has been determined to be directed downrange, Gardner and Burchell, 1997.

Microstructural effects of the stress asymmetry derived from the normal stresses at the shock front that are produced in a titanium (a ductile metal) target by a 45° impact are illustrated in [Figure 2.16](#). Shear displacement derived from this compressive stress asymmetry is indicated around the inside of the crater, especially on the downrange side of the crater...[Figures 2.16\(a\)](#) and (c).

Shear displacement on the downrange side of the crater wall is indicated by the step structures in the crater wall. Localized shear bands, some of which correlate with these wall steps, are also seen to extend into the crater wall...[Figure 2.16\(c\)](#), and there is evidence that melt-

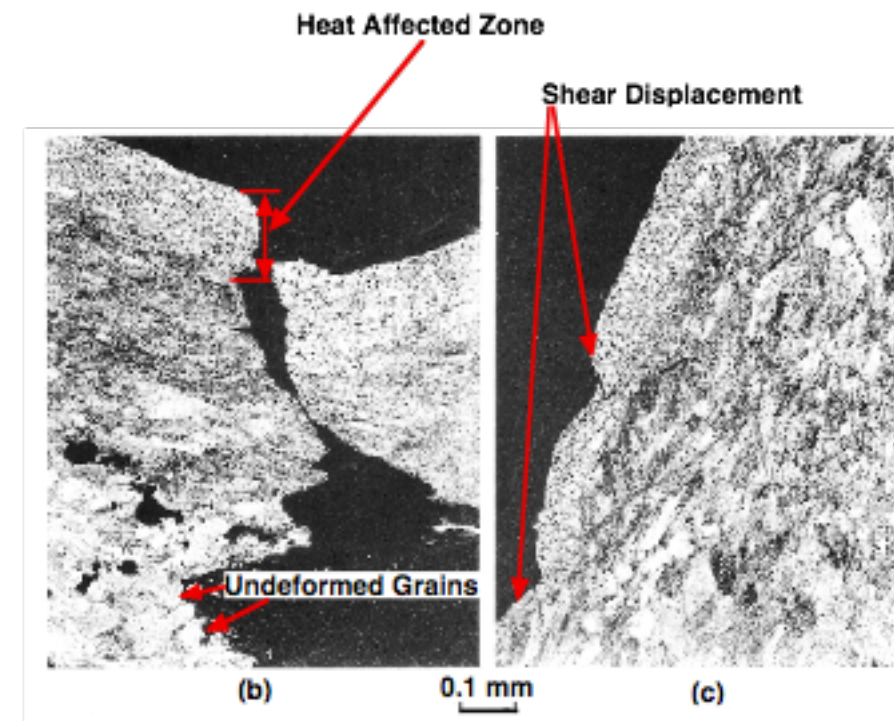
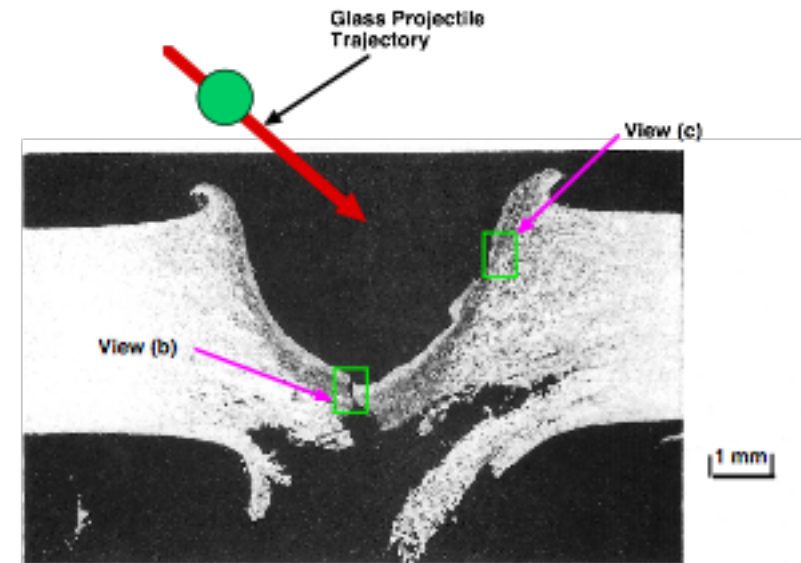


Figure 2.16 Polished and etched cross-section of a 3.94-mm-thick titanium plate heated to 775 K and impacted with a 4.39-mm glass sphere traveling at 6.8 km/s on a trajectory 45° above the target surface. Original photomicrographs from Lundberg, et al, 1982.

ing has occurred on the surfaces of these shear planes. Rear-surface spall produced by the expanding sonic shock front was the major contributor to the plate perforation, but shear failure at the bottom of the crater was the primary cause of the eventual perforation of the target plate...cross-section of the shear failure is seen in [Figure 2.16\(b\)](#).

A heat affected zone is indicated in [Figure 2.16\(b\)](#). This feature, which is visible at all magnifications, is an indicator of the high temperatures that persisted on the inside surface of the crater to the end of the excavation process. The dark region just outside of the heat affected zone, seen in [Figure 2.16](#), is representative of a zone of plastic deformation which, much like that seen in [Figure 2.10](#), reflects the late-stage shape of the shock front generated by the impactor. The geometry of a plastic deformation zone also reflects the asymmetry of the stress pattern imposed on the inside of the crater at the end of its formation.

2.1.3.3 SHOCK FRONT RECORD INSIDE HIGHLY POROUS SOLIDS

Impact structures on comets, discussed in **Section 1.2.1**, are representative of craters in low density solids. The shape of low speed shock fronts in gypsum ([Figure 2.7](#)) is analogous to that generally observed for impacts into solids that are highly porous. Hypervelocity impact of small projectiles onto a very low density open cell, silicate glass foam, called aerogel, leaves a clear record of the sonic shock front as it develops and dissipates inside highly porous materials. Cross-sectional views of

typical oblique hypervelocity impact structures in aerogel are seen in [Figure 2.17](#). The morphology of these impact structures record the development and decay of the sonic shock front in addition to low velocity tracks at the end of the track that further illustrates the damage caused by remnants of the impactor at subsonic velocities...similar to that observed for porous gypsum in [Figures 2.6](#) and [2.7](#).

An indication of damage generated by the Mach Cone is found at the entrance to the impact structures seen in [Figure 2.17](#). The entrance hole generated by the Mach Cone likely produced an ejecta plume similar to that observed in the early frames in [Figures 1.17](#) and [1.18](#), but the energy of the trailing part of the sonic shock front is so strongly but diffusely absorbed by the target material that its up-range surface has only partially broken through the target surface. The truncated hemispherical up-range surface of the impact cavity seen in [Figure 2.17\(a\)](#) is a record of the shape of the sonic shock front (recall the early frames in [Figure 2.7](#)) and its partial surface breakthrough.

A cylindrical track is formed initially inside the aerogel at the diameter of the sonic shock front, but its cross-sectional area eventually decays exponentially with distance downrange reflecting the exponential reduction of the impactor's kinetic energy and momentum. Projectile momentum becomes more important as the velocity of its remnants is reduced, so the solid remnant of the projectile can continue forward some distance before stopping inside the structurally weak aerogel. The projectile will also lose mass before it comes to a stop be-

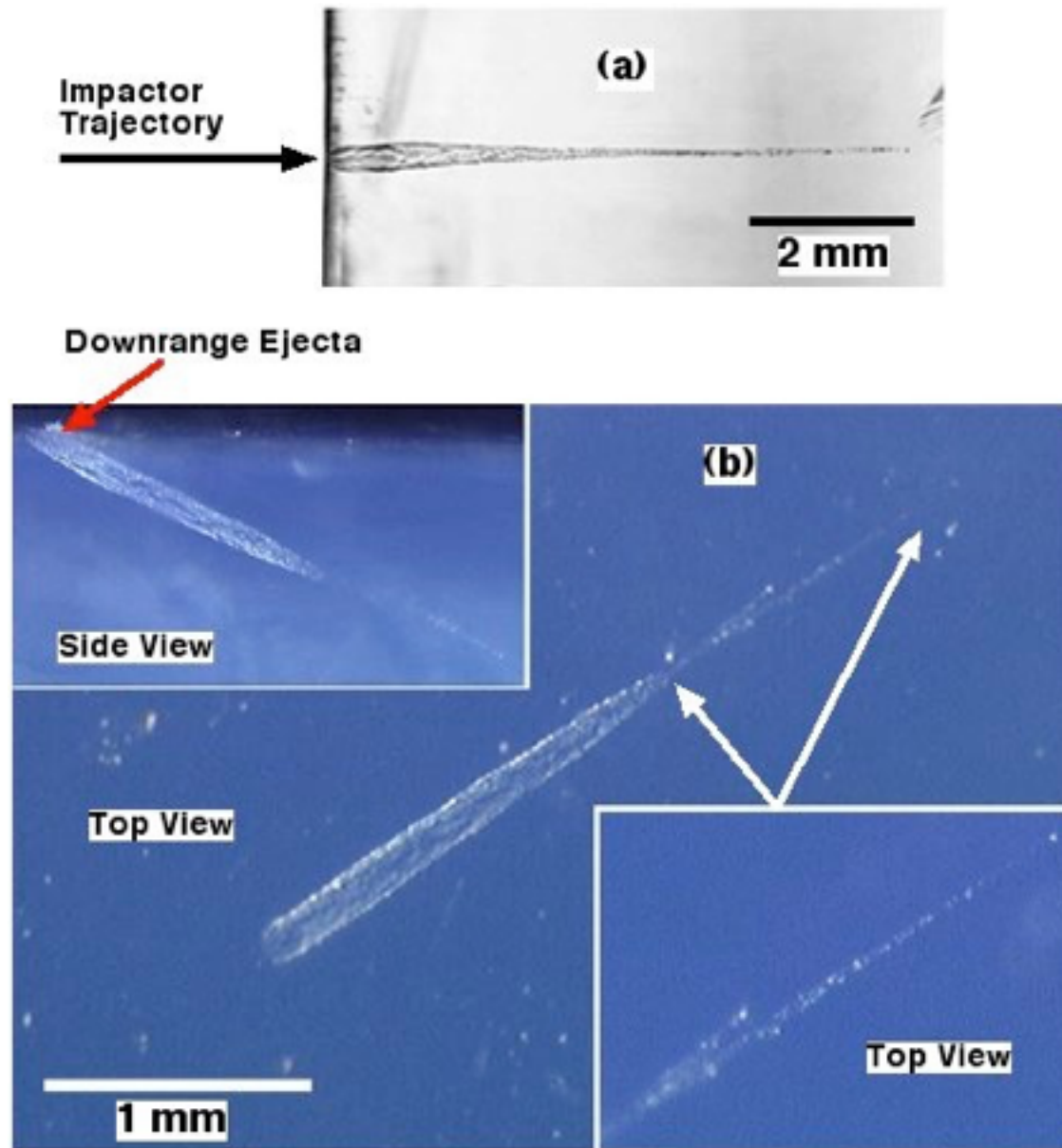


Figure 2.17 Cross-sections of characteristic impact structures in aerogel, (a) laboratory scale normal impact with a 50- μm -diameter glass sphere traveling at 6 km/s and (b) oblique impact in a target exposed to space environment on MIR. Original photographs downloaded from <http://setas-www.larc.nasa.gov/> at the MEEP project website.

cause significant quantities of its frontal surface will be ablated before it enters the velocity regime where impactor momentum becomes dominant. As seen in [Figure 2.17\(b\)](#), the

remnant space dust particle is eventually fragmented in the slower velocity regime, similar to that commonly observed for extraterrestrial impactors passing through a sensible gaseous atmosphere...recall [Figure 1.9](#).

The ejecta pileup indicated in [Figure 2.17\(b\)](#) downrange from the crater opening was deposited as a result of the oblique trajectory of the impactor. This downrange ejecta was not blown away during the early crater excavation as might be expected partly due to poor coupling of the shock front in the aerogel and the mechanical behavior of aerogel.

Late-Stage Impact Cratering

SECTION TOPICS

2.2.1 Laboratory-Scale Normal Impact Cratering in Beryllium

2.2.2 Laboratory-Scale Normal Impact Cratering, Craters and Ejecta for Sandstone

2.2.3 Laboratory-Scale Normal Impact Crater Ejecta Mass for Granite

Late-stage phenomenology, is derived from the deformation and fracture behavior of the target material due to stresses that have developed around the primary crater after the initial, supersonic shock front has substantially dissipated. As the formation of the primary crater draws to a close, stresses in the surrounding material remain high and increasingly asymmetric producing late-stage cratering processes, and the amount of material excavated from this point on is controlled by the quasi-static mechanical behavior of the target material. Consequently, the majority of the unique structural features observed in geologic impact structures are produced in the late stages of the crater formation process.

A diagram illustrating the stress history at the surface of the expanding primary crater and in the surrounding area later in the process is presented in [Figure 2.18](#). Throughout the early-stage of the cratering process, the peak stress at the shock front is compressive and degrades exponentially to zero, but due to elastic rebound within the target material, residual stresses inside the surrounding intact material oscillate between tension and compression. The early local pressures inside the shock front in the primary crater excavation zone are sufficient to cause melting and vaporization of the target material, but as the shock front energy is dissipated, the pressure drops to levels where the quasi-static mechanical behavior of the target material controls the cratering process and only *plastic deformation* or *fracture* of the target material are possible.

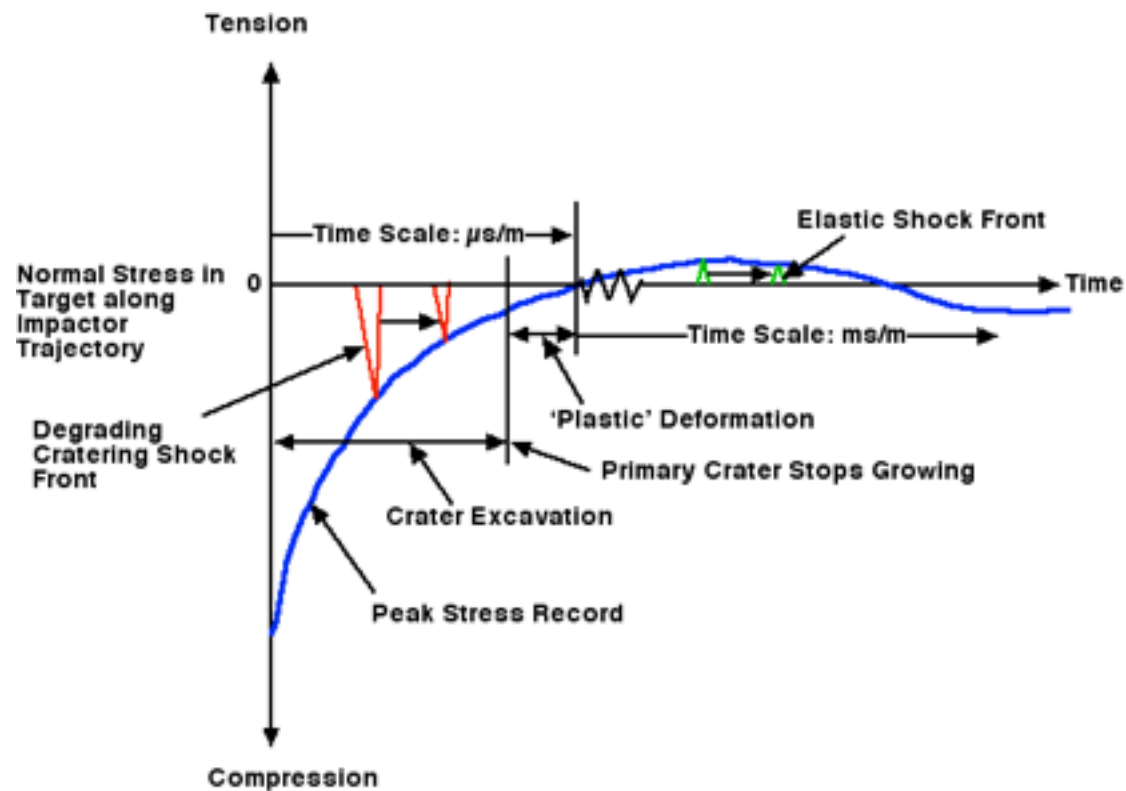


Figure 2.18 Schematic of the integrated normal stress history around the inside of an expanding hypervelocity primary impact crater. The time scales are relevant to millimeter size projectiles.

It is important to recognize that flow and fracture in solid materials is initiated in the shear mode. Under asymmetric, triaxial loading, deformation and fracture starts by shearing on planes lying approximately 45° to the maximum stress vector. It is well known that the maximum resolved shear stress vector, τ_{max} , inside a solid body subjected to triaxial loading is related to the local orthogonal stress vectors according the following relationship...see for example Dieter, 1961, p 27:

$$\tau_{max} = \frac{\sigma_1 - \sigma_3}{2} \quad 2.2$$

where σ_1 =the maximum normal stress vector and σ_3 =the minimum normal stress vector. Thus the shear strength of the body determines the combined stresses required to initiate flow and fracture inside the target material starting in the “Plastic” Deformation zone indicated in [Figure 2.10](#). It is worth noting that when the shock pressures are very high small *relative* differences in the normal stresses around the expanding primary crater can develop a local τ_{max} that exceeds the shear strength of material in the body.

Late in the cratering process as the energy and momentum of the impactor are absorbed by the target, an elastic wave starts to move ahead of the plastic shock front at the sonic velocity of the target material. The surface of demarcation between plastic and elastic deformation along the shock front was previously illustrated for ductile materials in [Figure 2.10](#). As long as the peak shock pressure is high enough to cause plastic deformation in the target material, the elastic wave front does not separate significantly from the plastic shock front, while the overall shock front profile only broadens with time along with a steady reduction of the peak stress...recall [Figure 2.18](#).

The transition from early- to late-stage cratering is related to the point at which quasi-static deformation and fracture behavior of the target material dominate the cratering process. For ductile materials, the structural features formed during the late-stage tend to represent only a small part of the overall, but for brittle materials, late-stage structural features dominate the final form of an impact structure. These additional features include secondary craters and spall zones that

develop around the primary crater, and these later formed structures can destroy many of the initially produced structural features of the primary crater. Most important to this discussion, late-stage geologic crater excavation will produce the majority of the ejecta from an impact event. Many sub-structures associated with geologic impact structures, such as shatter cones, dikes and pseudothacylites, are created by the late-stage impact stresses. Because there is a general misunderstanding of the deformation and fracture mechanics of materials, a discussion of the details of the mechanical behavior of materials will be presented in Chapter 4. In the meantime, we will examine late-stage cratering behavior of brittle materials at laboratory scale that can be extrapolated to full-scale geologic impact structures.

2.2.1 LABORATORY-SCALE NORMAL IMPACT CRATERING IN BERYLLIUM

The impact structure seen in a laboratory-scale beryllium target in [Figure 2.19](#) displays most of the structural features commonly produced by hypervelocity impact into brittle materials. Only a remnant of the primary crater is left at the bottom of the structure, and only a roughly defined perimeter of the secondary crater remains in this sample. In addition to a significant loss of the target structure from the primary and secondary craters, large pie-shaped ejecta fragments are seen to have been spalled out of the target outside of the perimeter of the secondary crater. These pie-shaped fragments are analogous to those seen ejected after impact in the video in [Figure](#)

[1.17](#). As seen in [Figures 2.19](#) and [2.20](#), both the primary and secondary craters are nearly obliterated by the ejection of the pie-shaped pieces. The majority of the material ejected from this structure was derived from the spall zone. It is estimated that at least twice as much target material was excavated from the secondary crater and spall zone than from the primary crater alone. In addition, the radial cracks indicated in [Figure 2.19](#) and the circumferential fracture seen in [Figure 1.17](#) define the outer perimeter of the pie-shaped pattern in the spall

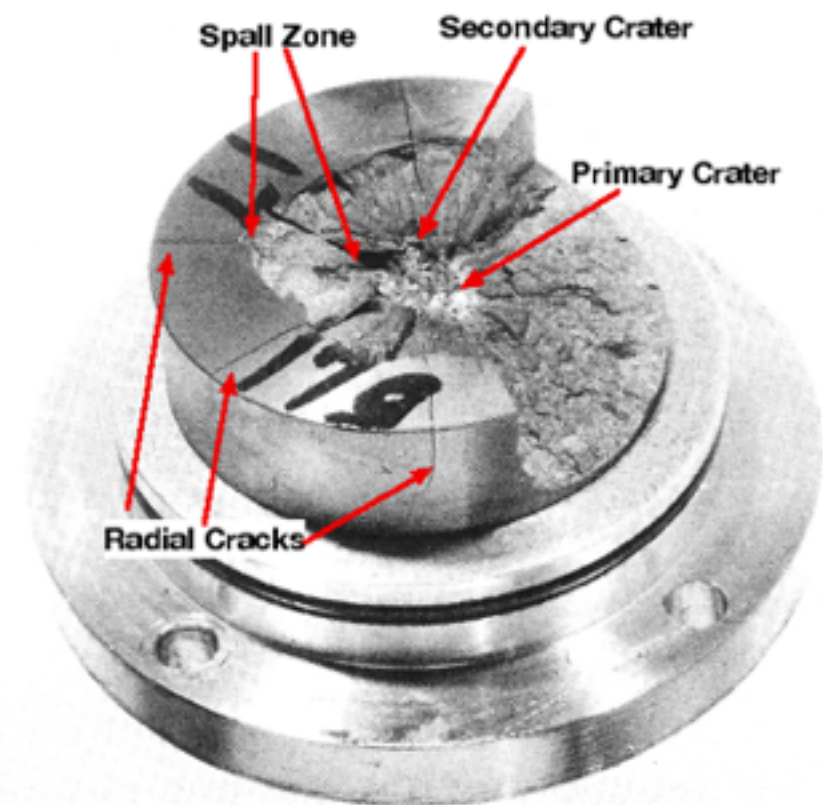


Figure 2.19 Impact structure in a semi-infinite beryllium target maintained at 295 K. Target was impacted with a 1.6-mm-diameter copper sphere traveling at 7.11 km/s normal to the surface. The diameter of the secondary crater is ~16 mm. Original image from Lundberg, et al., 1982.

zone, and as illustrated in [Figure 2.20](#), cracks also radiate from the bottom of the primary crater.

The approximate (virtual) cross-section of the primary crater, before it was mostly destroyed later in the cratering process, is depicted in [Figure 2.20](#). Dufresne, et al, 2013 have also recognized that this cratering model applies equally to hyperveloc-

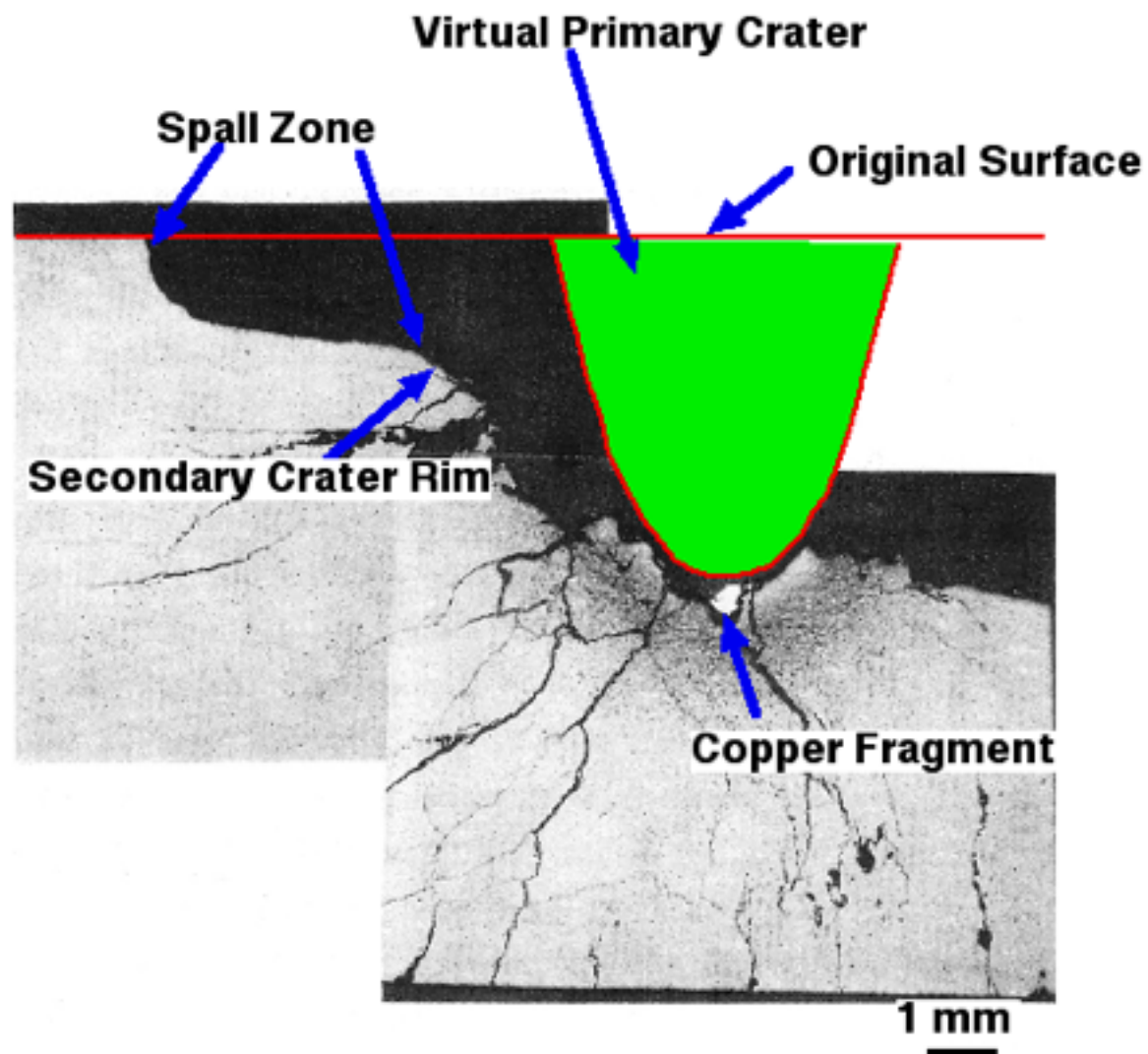


Figure 2.20 Cross-section of a beryllium target maintained at 295 K and impacted with a copper sphere traveling at 7.11 km/s normal to the surface. (Original image from Lundberg, et al, 1982.)

ity normal impact cratering in sandstone. The rim of a secondary crater is also indicated in [Figure 2.20](#) along with a fragment of the copper impactor located at the bottom of the primary crater. This fragment, that shows clear signs of melting, sits in a hemispherical cavity that measures across slightly less than half of the original diameter of the copper impactor. The presence of a remnant of the copper impactor at the bottom of the primary crater is similar to that observed in [Figures 2.6](#) and [2.17](#).

2.2.2 LABORATORY-SCALE NORMAL IMPACT CRATERING, CRATERS AND EJECTA FOR SANDSTONE

Several impact structures found on Earth were generated primarily in sandstone...e.g. the Upheaval Dome located in southern Utah and Meteor Crater in northern Arizona. Sandstone is a typical brittle geologic material whose hypervelocity impact behavior has been studied extensively in the laboratory by the Multidisciplinary Experimental and Modeling Impact Research Network (MEMIN)...a consortium of German university personnel and experimental facilities. This group has published a considerable amount of data on the hypervelocity impact behavior of (high quartz) sandstone. The following discussion represents considerable reinterpretation of their published data based on the fundamental impact cratering principles described above.

Sequential, time resolved images of the ejecta excavated from a developing hypervelocity impact structure in a dry sand-

stone block that was maintained under a partial air atmosphere when impacted are presented in [Figure 2.21](#), Hoerth, et al, 2013. The sonic velocity in the dry, high silica sandstone samples used in the MEMIN studies ranged from 2.2 to 2.6 km/s, and the average porosity was measured at 23%, Moser, et al., 2013. The laboratory-scale impact data indicate that at least four distinct phases of the crater excavation process can be identified. However prior to settling into the first stage of the cratering process, the ejecta curtain from the contact/coupling phase of the cratering process (discussed in **Section 2.1.1**), whose trajectory starts close to the target surface, has already exited the field of view by the time the first frame is exposed...38 μs in [Figure 2.21](#).

Stage 1

The first phase of crater excavation is indicated by the orange (color indicates temperatures $>1000\text{ K}$) conical feature observed in the first frame left of the top of the primary ejecta cone. This feature is indicative of a small amount of very high temperature ejecta that flows up-range along the supersonic shock front (Mach cone) during Early-Stage cratering. The indicated high temperature infers that the material ejected along the Mach cone includes molten or gaseous material that originates from both the impactor and target sandstone. This first stage ejecta cone is similar to that observed in the early frames of the video in [Figure 1.17](#) and the early frames of the sequential photos presented in [Figure 1.18](#). The ejecta from the subsequently excavated material observed in [Figure 2.21](#)

consist mostly of solid fragments of varying sizes whose temperatures are indicated to be only slightly above ambient.

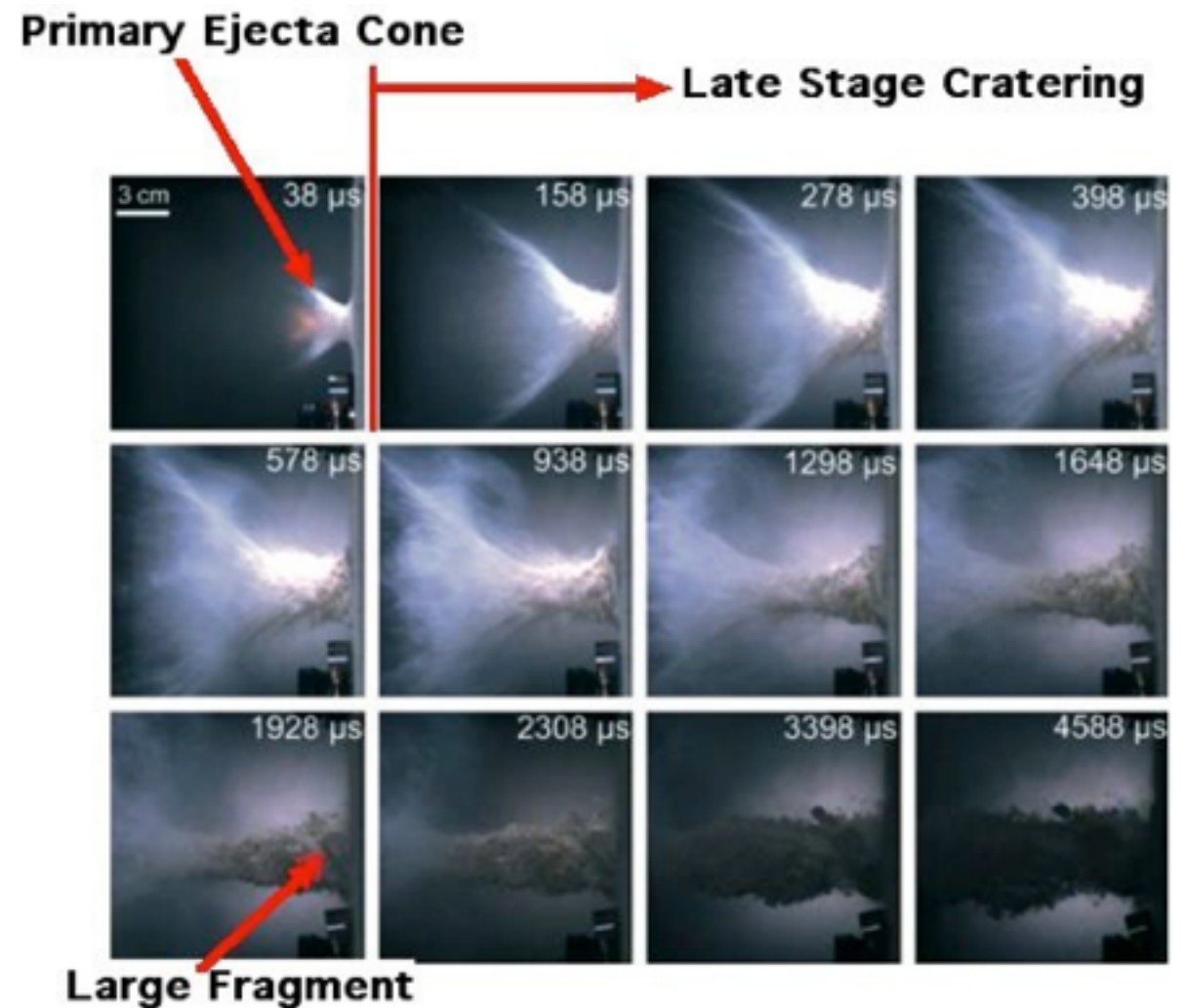


Figure 2.21 Sequential images of ejecta from dry sandstone that was impacted by a 2.5-mm-diameter steel sphere traveling at 4.8 km/s through air maintained at 10 kPa (100 mbar) on a trajectory normal to the target surface. Data from Hoerth, et al, 2013.

Stage 2

The development and growth of the primary crater represents the second phase of crater excavation. In [Figure 2.21](#), the pri-

primary crater is probably still growing at the 38 μ s point after impact because the trailing surface of the impactor should not have reached the target surface until about 52 μ s, when the impactor's energy and momentum is expected to have coupled into the target and formed an elliptical sonic front below the front surface of the target...recall [Figure 2.6](#). The cross-section of this primary crater is expected to be similar to the virtual primary crater in beryllium presented in [Figure 2.20](#).

The trajectory of material in the ejecta cone derived from the primary crater was defined on the surfaces of fragment catchers used for laboratory-scale impacts into sandstone, Sommer, et al., 2013. By comparing with the image in [Figure 2.21](#), we can conclude that ejecta from the primary crater was removed from the central red area in [Figure 2.22\(a\)](#). The red circle on the catcher board seen in [Figure 2.22\(c\)](#) was best defined for impact velocities greater than 4.5 km/s, and the half-angle of this ejecta cone was measured at 41° ($\theta=49^\circ$) for the samples impacted, based on the circle of red particles imbedded in the catcher, Sommer, et al., 2013. The ejecta angle determined from the red ejecta circle for the same sample seen in [Figure 2.22](#) is consistent with the primary crater cone angle observed in the 38 μ s image in [Figure 2.21](#).

Stage 3

The formation of a secondary crater, the third cratering phase, appears to be well underway at the 158 μ s mark in [Figure 2.21](#)...indicated by the fact that ejecta from the secondary crater is traveling primarily inside the surface of a cone with a

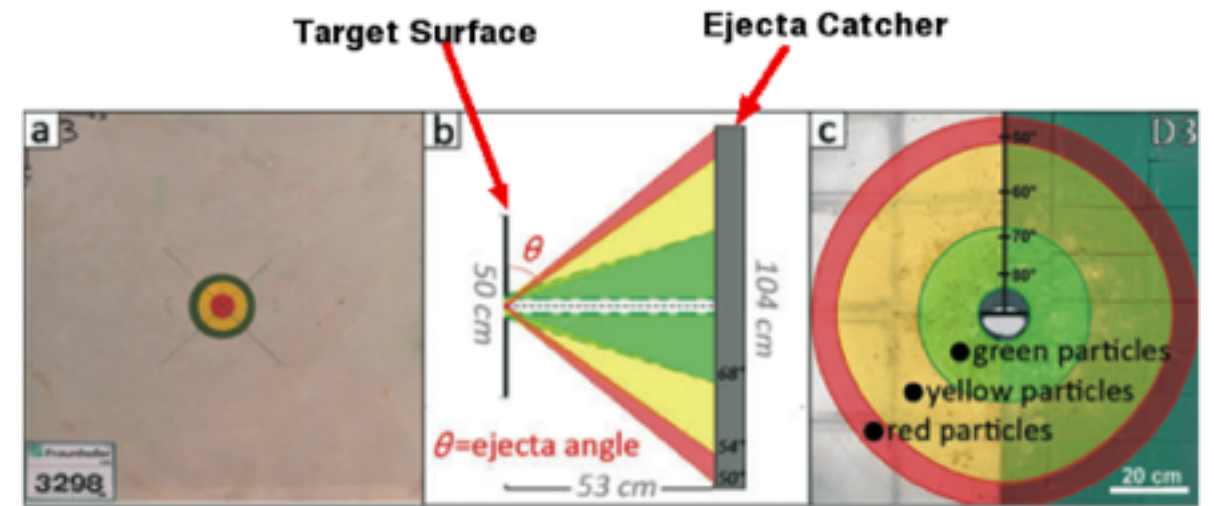


Figure 2.22 Schematics of (a) pre-impact color circles on sandstone targets; (b) cross-sectional view of observed distribution of crater ejecta based on color; and (c) planar view of observed ejecta distribution. Original image from Sommer, et al., 2013.

smaller cone half-angle ($\sim 24^\circ$) than produced from the primary crater ($\sim 44^\circ$). There is a significant increase in the base diameter of the ejecta cone between the 38 μ s and the 158 μ s marks in [Figure 2.22](#), which indicates a jump to a larger crater diameter in this interval. Also at the 158 μ s mark, the primary ejecta cone has become disconnected from the target surface as it moves up-range faster than the following ejecta from the secondary crater, and the primary ejecta cone appears to be blooming outward...partly due to aerodynamic drag produced by the ambient atmosphere. At this point, a steady cone of debris ejected from a secondary crater has evolved. This secondary ejecta cone angle is constant for at least the next 140 μ s, while the secondary ejecta cone base diameter grows only about 20% during this interval. As indicated by the growth of the diameter of the secondary ejecta cone, the formation of

the secondary crater appears to have been completed by the 398 μs mark in [Figure 2.21](#). The distribution of material ejected along the ejecta cone from the secondary crater correlates with the yellow circle in [Figure 2.22](#). The ejecta curtain generated from the secondary crater was observed to be more diffuse than from the primary crater, Sommer, et al., 2013.

Stage 4

The target surface is seen to bulge up-range around the base of the ejecta cone in the earliest frame in [Figure 2.21](#). This infers that the up-range side of the sonic shock front is expanding inside the target and starting to uplift and fracture the surface surrounding the forming crater...similar to that observed in [Figure 2.9](#). Also as observed in [Figure 2.21](#), the surface of the bulge is already showing clear signs of target surface breakup in the 278 μs frame...similar to that observed in the early frames of the video in [Figure 1.17](#), and the surface surrounding the secondary crater appears to be completely broken away by the 578 μs frame. Discrete fragments can be easily resolved in the ejecta plume at 578 μs , the beginning of the fourth cratering phase, and the numbers and sizes of these large fragments increase as the Late-Stage excavation progresses. A more detailed view of the breakup of the bulge and the ejecta cone can be seen in [Figure 2.23\(a\)](#) where the general shape and trajectory of fragments that were spalled and ejected from around the secondary crater are better resolved. The structural details observed on the surface of the ejecta cone in [Figure 2.23\(a\)](#) illustrate the heterogeneity of the fragment sizes inside the ejecta cone that contains mostly material

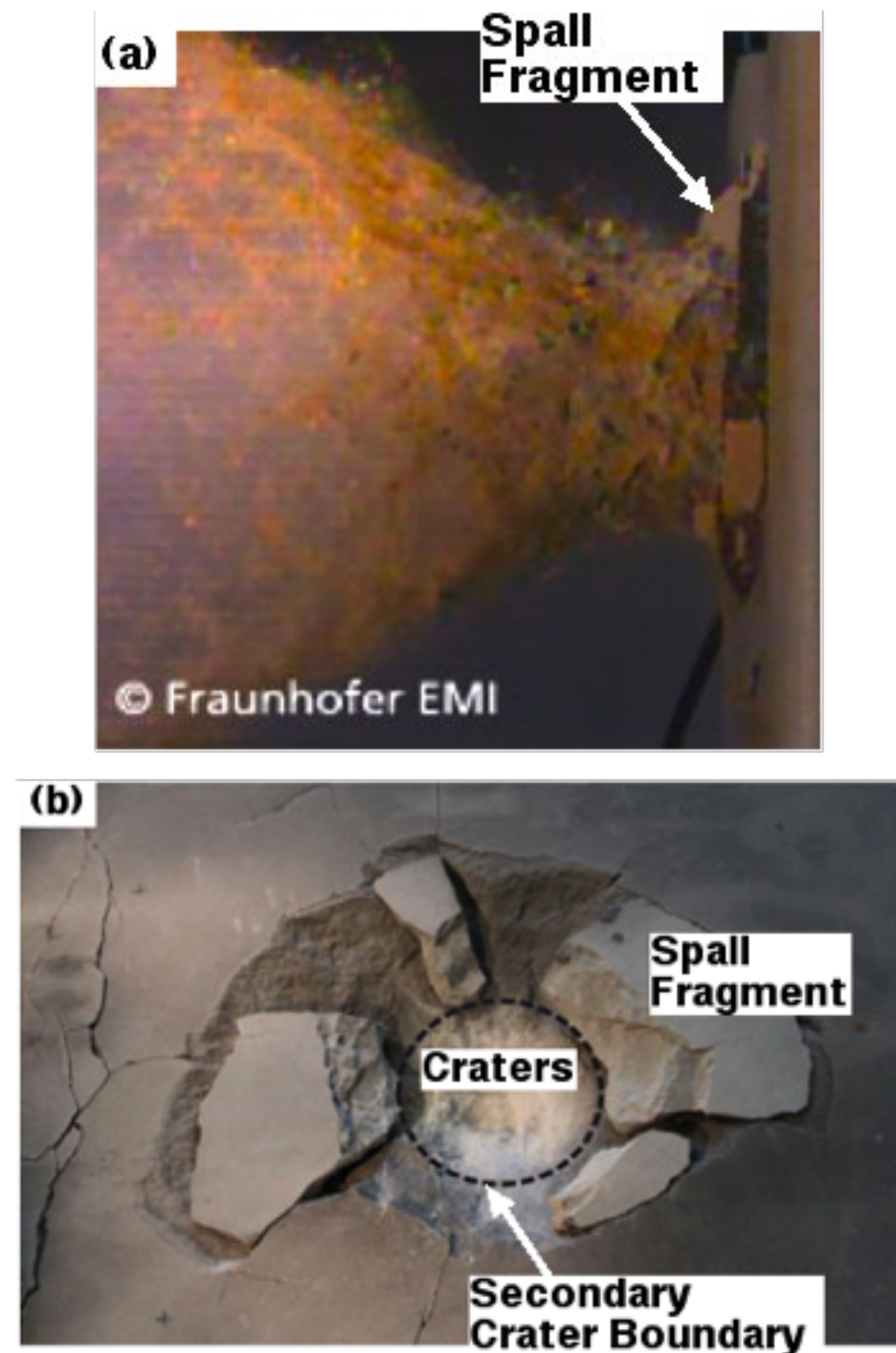


Figure 2.23 Ejecta cone (a) and overhead view of impact craters and refitted spall fragments (b) from dry sandstone that was impacted by a 2.5-mm-diameter steel spheres traveling at ~ 5 km/s through air maintained at 10 kPa (100 mbar). Data from Dufresne, et al, 2013.

excavated from the secondary crater.

The general shape of the ejecta plume above sandstone seen in [Figure 2.21](#) at 938 μs and beyond is similar to the impact ejecta plume over water seen in [Figure 2.8](#). A waist is developing in the ejecta column well above the sandstone target indicating a beginning of the cessation of excavation of the secondary crater that develops when the energy and momentum of the impactor have been completely coupled into the target. Starting at the 1298 μs frame, elastic rebound (recall [Figure 2.6](#)) from the target body is causing loose, fragmented material to be ejected from inside of both the primary and secondary craters. The overall crater diameter expands slightly beyond this point due to stress induced mechanical failure of the brittle target material beyond the perimeter of the secondary crater. Elastic rebound excavation continues to the end of the photo sequence and forms a straight-walled column of ejected material that includes many large fragments that have been sheared from outside of the perimeter of the secondary crater creating a spall zone. The rebound ejecta have produced the green circle in [Figure 2.22](#). This late-stage ejecta have clearly overprinted any ejecta from the Mach Cone and all other ejecta that might have been collected on a stationary catcher surface at an earlier time.

Atmospheric effects on the ejecta plume are noticeable but small in the photographic images in [Figure 2.21](#). Vortices of fine particles caused by interaction with low pressure gas in the test chamber are visible just below the remnant primary ejecta cone in the 578 μs thru 1648 μs frames.

The “Large Fragment” indicated in the 1928 μs frame of [Figure 2.21](#) and the spall fragment indicated in [Figure 2.23\(a\)](#) are similar to the pie shaped pieces ejected from a brittle surface over a granular substrate...recall especially the [Figure 1.17](#) video. The shapes and original locations of these large spall fragments are illustrated in [Figure 2.23\(b\)](#). These large fragments can represent as much as 80% of the material removed from hypervelocity impact craters in sandstone, Dufresne, et al, 2013. It is important to note that some of these large fragments remain mostly in place and are delineated by cracks exposed on the surface of the target sandstone much like those previously seen in beryllium...recall [Figures 2.19](#) and [2.20](#). As we shall see in Chapter 3, this regular crack pattern is found in and immediately outside of the rims of *accepted* impact craters of both the Upheaval Dome and the Vredefort Dome.

Remnants of the rims of both a primary crater and a secondary crater are seen in the overhead photograph in [Figure 2.23\(b\)](#), and 3-D laser scanned profiles of the cross-sections of typical hypervelocity impact craters in both dry and water saturated sandstone formed by AISI 4130 steel spheres are presented in [Figure 2.24](#). The morphology of the cross-section of the impact ‘craters’ in the sandstone produced in the MEMIN studies is similar to those recorded in the previous section for impact cratering in beryllium...compare [Figures 2.19](#), [2.20](#) and [2.23\(b\)](#). Remains of both the primary and secondary craters are better defined in the water saturated sandstone targets compared to the dry sandstone. This is also true for the spall zone, which is better defined for the water

saturated sandstone. The hemispherical bottom of the primary crater in the wet target indicates that the effective brittleness of wet sandstone is reduced significantly compared to that of the dry sandstone. The ejecta trajectories estimated in [Figure 2.24](#) for the two crater bottom profiles reflect a more definite distinction between primary (**Stage 2**) and secondary crater formation (**Stage 3**) for the water saturated sandstone.

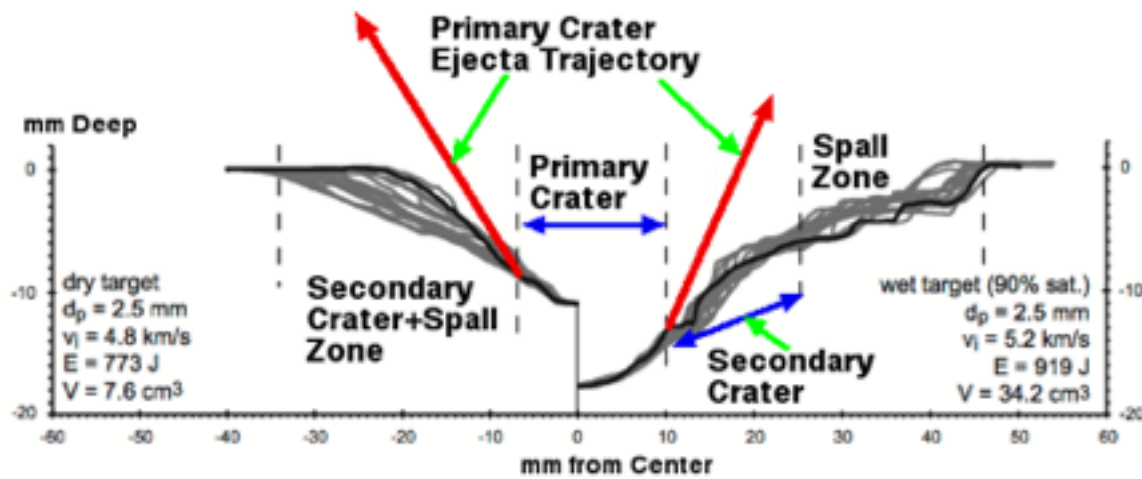


Figure 2.24 Hypervelocity impact crater 3-D laser profiles in sandstone formed by 2.5-mm-diameter steel spheres. Legend: d_p =projectile diameter; v_i =impact velocity; E =impactor kinetic energy; V =crater volume. Original image and data from Dufresne, et al, 2013.

The volumes of material ejected from the cross-sections of the impact structures diagrammed in [Figure 2.24](#) vary with both impactor mass and velocity plus water content of the sandstone target. Data from Dufresne, et al, 2013 have been fitted to **Equation 2.1** to generate **Equation 2.3** below (SI units):

$$V(m_p, v_p) = m_p(6.91 \times 10^{-3} + 1.65 \times 10^{-5}v_p + 2.23 \times 10^{-9}v_p^2) \quad \mathbf{2.3}$$

The fit was not particularly good, $R^2=0.641$, but the data were sparse and mostly concentrated around impactor velocities 4 to 5 km/s. Both aluminum and steel spheres were used as impactors in these impact experiments.

2.2.3 LABORATORY-SCALE NORMAL IMPACT CRATER EJECTA MASS FOR GRANITE

The form of **Equation 2.1** also applies equally to the correlations with crater ejecta mass from granite...as confirmed by analysis of data published by Burchell and Whitehorn, 2003 for ejecta mass from impact craters in granite even though their ejecta mass data include all of the material excavated from the primary crater, secondary crater, and the spall zone. The excavated mass in grams $M(m_p, v_p)$ reported by Burchell and Whitehorn, 2003 can be represented by:

$$M(m_p, v_p) = m_p(-42.396 + 87.74v_p + 0.80849v_p^2) \quad \mathbf{2.4}$$

with v_p in terms of km/s and a correlation coefficient, $R^2=0.943$.

Chapter 2 References

Burchell, M. J. and Whitehorn, L., 2003, Oblique incidence hypervelocity impacts on rock, *Monthly Notices of the Royal Astronomical Society*, 341 (1). pp. 192-198. ISSN 0035-8711.

Charters, A. C. and Summers, J. L., 1959, Some comments on the phenomena of high-speed impact, in *Decennial Symposium*, May 26, 1959, White Oak U. S. Naval Ordnance Laboratory, Silver Spring, MD, pp. 1-21.

Collette, A., Drake, K., Mocker, A., Sternovsky, Z., Munsat, T., and Horanyi, M., 2013, Time-resolved temperature measurements in hypervelocity dust impact, *Planetary and Space Science*, <http://dx.doi.org/10.1016/j.pss.2013.02.007>.

Daubar, I. J., McEwen, A. S., Byrne, S., Kennedy, M. R., Ivanov, B., 2013, The current Martian cratering rate, *Icarus*, 225, 1, pp. 506-516.

Denardo, B. P., 1962, Measurements of Momentum Transfer from Plastic Projectiles to Massive Aluminum Targets at Speeds up to 25,600 Feet per Second, NASA TN D-1210, March 1962.

Denardo, B. P., Summers, J. L. and Nysmith, C. R., 1967, Projectile Size Effects on Hypervelocity Impact Craters in Aluminum, NASA TN D-4067, July 1967.

Dieter, G. E., Jr., 1961, *Mechanical Metallurgy*, McGraw-Hill Book Company, Inc., NY.

Dufresne, A., Poelchau, M. H., Kenkmann, T., Deutsch, A., Hoerth, T., Schäfer, F., Thoma, K., 2013, Crater morphology in sandstone targets: The MEMIN impact parameter study, *Meteoritics & Planetary Science* 48, Nr 1, pp. 50–70, doi: 10.1111/maps.12024.

Freeman, V. L., 1981, Regolith of the Apollo 16 Site, Central Lunar Highlands, Chapter F. in *Geology of the Apollo 16 Area, Central Lunar Highlands*, Eds. Ulrich, G. E., Hodges, C. A., Muelhberger, W. R., Geological Survey Professional Paper 1048, United States Government Printing Office, Washington: 1981, pp. 147-159.

Gardner, D. J. and Burchell, M. J., 1997, Proceedings of the Second European Conference on Space Debris, ESOC, Darmstadt, Germany, 17-19 March 1997, (ESA SP-393, May 1997), pp. 481-486.

Gasperini, L., Bonatti, E., Albertazzi, S., Forlani, L., Accrosi, C. A., Longo, G., Ravaioli, M., Alvisi, F., Polania, A., Sacchetti, F., 2009, Sediments from Lake Cheko (Siberia), a possible impact crater for the 1908 Tunguska Event, *Terra Nova*, 21, No. 6, pp. 489–494.

Giacomuzzo, C., Ferri, F., Toson, E., A. Bettella, A., D., Pavarin, Francesconi, A., Flamini E. and Angrilli, F., 2006, Investigation of Impact Cratering Processes into Porous Targets through Hypervelocity Experiment Simulations: European Space Agency First International Conference on Impact Cratering in the Solar System ESTEC, Noordwijk, The Netherlands, 08 - 12 May, 2006.

Hoerth, T., Schäfer, F., Thoma, K., Kenkmann, T., Poelchau, M. H., Lexow, B., and Duetsch, A., 2013, Hypervelocity impacts on dry and wet sandstone: Observations of ejecta dynamics and crater growth, *Meteoritics & Planetary Science*, 48, No. 1, pp. 23-32, doi: 10.1111/maps.12044.

Kurosawa, K., Nagaoka, Y., Hasegawa, S., Sugita, S., and Matsui, T., 2014, Ultrafast imaging observations of the impact jetting during oblique impacts, 45th Lunar and Planetary Science Conference, paper no. 1856.pdf.

Lundberg, L. B., Bless, S. J., Girrens, S. P. and Green, J. E., 1982, Hypervelocity Impact Studies on Titanium, Titanium Alloys, and Beryllium: Los Alamos National Laboratory Report LA-9417-MS, August 1982.

Mader, C. L. and Gittings, M. L., 2003, Dynamics of Water Cavitation: Science of Tsunami Hazards, Volume 21, Number 2, pp. 91-102.

Moore, H. J., Gault, D. E., and MacCormack, R. W., (1), 1962, Fluid Impact Craters and Hypervelocity- -High Velocity Impact Impact Experiments in Metals and Rocks, United States Department of the Interior Geologic Survey Report No. N 64-22459, November, 1962.

Moore, H. J., Gault, D. E., and Lugn, R. V., (2), 1962, Experimental Hypervelocity Impact Craters in Rock, United States Department of the Interior Geologic Survey Report No. N 62-13994, March 1962.

Moser, D., Poelchau, M. H., Stark, F., and Grosse, C., 2013, Application of nondestructive testing methods to study the damage zone underneath impact craters of MEMIN laboratory experiments, *Meteoritics and Planetary Science* 48, Nr 1, pp. 87-98, doi: 10.1111/maps.12000.

Shoemaker, E.M., 1962, Interpretation of lunar craters, In: Kopal, Z. (Ed.), *Physics and Astronomy of the Moon*. Academic Press, New York, pp. 283–359.

Sommer, F., Reiser, F., Dufrense, A., Poelchau, M. H., Hoerth, T., Duetsch, A., Kenkmann, T., and Thoma, K., 2013, Ejection behavior characteristics in experimental cratering in sandstone targets, *Meteoritics and Planetary Science* 48, Nr 1, pp. 33-49, doi: 10.1111/maps.12017.

Stickle, A. M., and Schultz, P. H., 2011, Exploring the role of shear in oblique impacts: A comparison of experimental and numerical results for planar targets, *International Journal of Impact Engineering*, 38, pp. 527-534, doi: 10.1016/j.ijimpeng.2010.10.025.

Structural Features of Geological Impact Craters



Overhead view of the Upheaval Dome from Google Earth. Located in southern Utah inside Canyonlands National Park.

As mentioned in **Section 1.1.3**, the dry surface of the Earth should appear structurally similar to the surface of Earth's moon. All of the structural features of impact structures observed on Earth's moon can serve as guides for identifying impact structures on the dry surface of Earth. Even though the surface of the Earth is being continually altered by erosional processes, it is still obvious that Earth's surface should be littered with arcuate structures that are representative of impact structures. The following discussion should demonstrate that only minimal pattern recognition skills and a basic understanding of crater formation processes presented in this volume are required to identify and interpret unique geologic impact structures.

The morphological patterns observed in full-scale geologic impact structures are also analogous to those produced by hypervelocity impact in the laboratory. In order to demonstrate the validity of the extrapolation of physical principles observed in the laboratory- to field-scale, we will explore and compare the structural details of the middle-aged Upheaval Dome, the oldest accepted impact structure on the dry surface of Earth...the Vredefort Dome, and a well studied oceanic impact structure...the Chesapeake Bay impact structure. These prototypic geologic impact structures include structural details that can be observed in the laboratory and in field studies of most accepted and candidate impact structures on Earth.

Structural Features of the Upheaval Dome

SECTION TOPICS

3.1.1 Upheaval Dome Crater Complex

3.1.2 Beyond the Upheaval Dome Crater Complex

The relatively small Upheaval Dome impact structure and its surrounding terrain is viewed from high overhead in [Figure 3.1](#). As has been previously discussed, a collection of several impact structures will be most commonly found on the surfaces of terrestrial bodies rather than singular, unique structures, so this lone impact structure is a rare find. The well preserved, unique Upheaval Dome crater complex, located in southern Utah inside the Canyonlands National Park, exhibits most of the main structural features found in and around a small, medium aged, eroded impact structure found on dry, hard rock surfaces of the Earth. The impact event that formed the Upheaval Dome is estimated to have occurred sometime after deposition of the Jurassic Navajo sandstone stratum, which is found at the top of its secondary crater walls. However, the age of the Upheaval Dome has not been precisely determined, Huntoon, 2000.

The structural features of the Upheaval Dome are representative of geologic impact structures in sandstone, so a close examination of its structure can be instructive for comparison of the structural features observed in geologic impact craters with those produced in the laboratory...recall **Section 2.2.2**. In spite of a vast number of publications describing many of the structural features of the crater complex of the Upheaval Dome (including for example Kriens, et al., 1999), many of its structural features remain poorly defined and inaccurately interpreted. The following discussion notes many observations of the structural details that require original interpretations of many aspects of this impact structure based on the fundamen-

tals of impact cratering discussed in Chapter 2 and the mechanical behavior of materials to be discussed in detail in the next chapter.



Figure 3.1 Overview of Upheaval Dome and the surrounding terrain. Original image from Google Earth.

3.1.1 UPHEAVAL DOME CRATER COMPLEX

In addition to the primary crater indicated in [Figure 3.1](#), the presence of a well defined, concentric secondary crater reflects the brittle mechanical behavior of the target material (sandstone layers). In many ways, the crater complex of the Upheaval Dome compares with that previously described for laboratory-scale hypervelocity impact structures in both beryllium and sandstone.

The Upheaval Dome crater complex rises prominently above the surrounding terrain. A closer overhead view presented in [Figure 3.2](#) reveals many of the major structural details of this well preserved, unique crater complex, including a well defined central uplift. Drainage patterns in and around the crater complex that have developed over time also highlight many of the significant impact structural features. For example, drainage from the crater complex has cut a canyon, (Upheaval Canyon) through both primary and secondary crater walls. This canyon drains west-northwest and eventually dumps into the Green River...marked in [Figure 3.1](#). The drainage direction of this canyon infers the original lowest side of the crater complex post-impact. The crater rim height asymmetry indicates an oblique impactor trajectory that roughly parallels the track of Upheaval Canyon. This same impactor trajectory is further indicated by the squaring of the downrange (SE) side of the primary crater, and by comparing this downrange crater rim geometry with that observed for laboratory-scale hypervelocity impact structures in [Figure 2.15](#), one can estimate that the impactor's trajectory probably ranged from 35° to 55° above the horizon. Scherler, et al., 2006 have also concluded an oblique impact from the same direction based on imbrication of strata in the central uplift.

3.1.1.1 UPHEAVAL DOME CENTRAL UPLIFT

A well defined central uplift substructure is found near the center of the Upheaval Dome primary crater, and based on the previous discussion, it was formed as a direct result of rebound from the bottom of the primary crater. The Upheaval

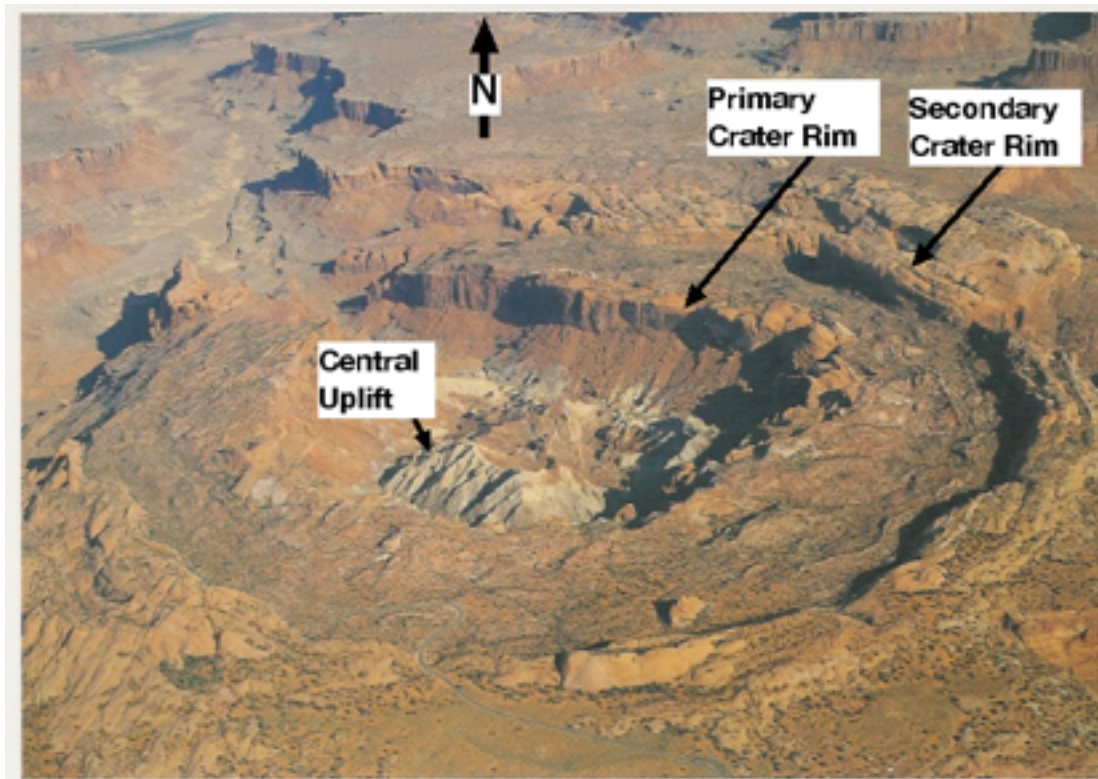


Figure 3.2 Upheaval Dome impact crater complex. The secondary crater rim of the structure is ~2.5 km across. Original photograph from Google Earth.

Dome central uplift is a miniature version of the central uplift inside the 82-km-diameter Tycho crater on Earth's moon seen in [Figure 3.3](#). The similarity of the central peaks seen in [Figures 3.3](#) and [3.4](#) is quite striking. The presence of a central uplift infers that the flow behavior of the material that was originally at the bottom of the primary crater behaved in a fluid-like manner during the later stages of the cratering process... recall late-stage impact fluid flow illustrated in [Figure 1.19](#).

Maps of the internal structure of the central uplift in the Upheaval Dome derived from seismic and borehole data indicate a series of periodic downward descending faults (with displace-

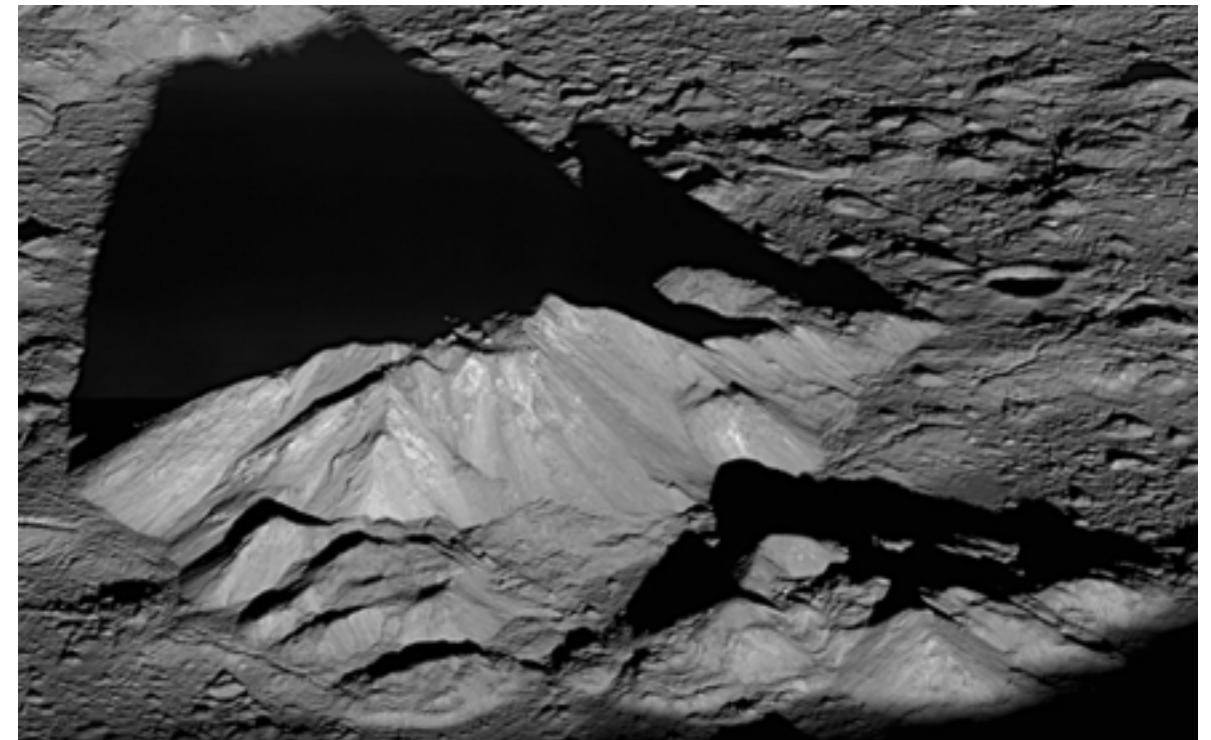


Figure 3.3 Central peak of the Tycho impact structure located on the Moon at 43.37°S, 348.68°E. The Tycho crater is about 82 km in diameter. This uplift complex is ~15 km across. The summit of the central peak is 2 km above the crater floor, and Tycho's floor is about 4.7 km below its rim. Credit: NASA Goddard/Arizona State University.

ments more than 2 m) that rotate in a helical pattern below the center of the uplift structure, Kenkmann, et al., 2005. The dike/fault structure under the Upheaval Dome central peak is analogous to that observed under laboratory-scale primary hypervelocity impact craters...recall the cross-sectional view of impact cratered beryllium in [Figure 2.20](#).

The central uplift of the Upheaval Dome indicated in [Figure 3.2](#) and seen close-up in [Figure 3.4](#) can be generally characterized as a ring structure. The central uplift of the Upheaval Dome contains many dikes and faults that reflect a typical de-

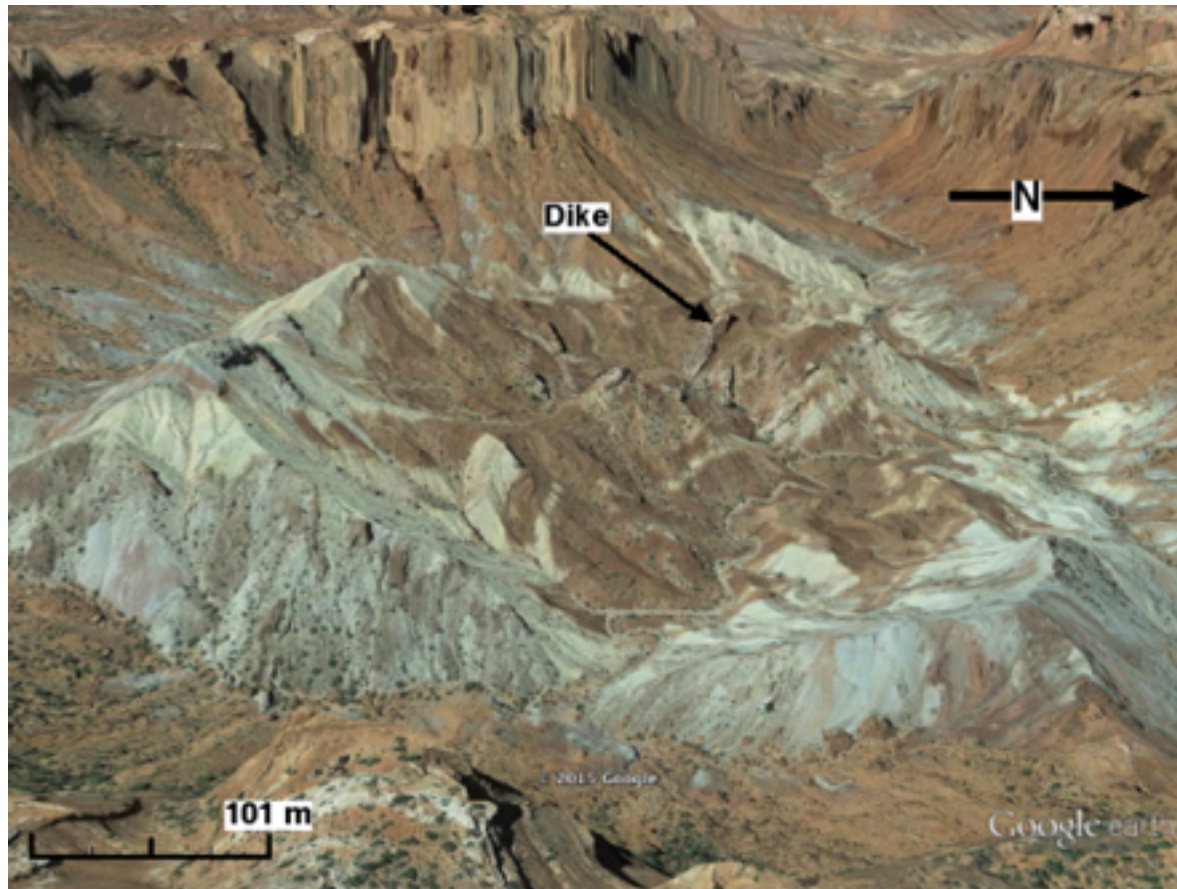


Figure 3.4 View from east of the central uplift in the Upheaval Dome. Original image from Google Earth.

formation and fracture pattern produced in the target materials during rebound of material from below the bottom of a primary crater. A radial dike that is typical of several others exposed on the surface of the central uplift is marked in [Figure 3.4](#). Because as will be discussed in Chapter 4 the interior of these dikes contain melted material and are denser than the surrounding material, their exposure has been enhanced by the fact that they are more resistant to erosion than the surrounding material. As will be discussed in Chapter 4, these dikes were formed by localized shear rather than intrusion into existing cracks from and an external source...as is gener-

ally hypothesized. A close-up view of one of these dikes exposed on the east side of the central uplift is seen in [Figure 3.5](#).



Figure 3.5 Sandstone dike located on the east side of the central uplift in the Upheaval Dome. Original image from Huntoon, 2000.

3.1.1.2 STRUCTURAL DETAILS OF THE PRIMARY CRATER

The overall structural features of the Upheaval Dome primary crater are well displayed in [Figures 3.1](#) and [3.2](#). The walls of this small primary crater, approximately 700 m

across, have preserved many of the structural consequences of late-stage cratering. For example, concentric, periodic, outwardly uplifted strata appear along the primary crater rim and close outside its outer perimeter. These structures formed as a result of the radial-upward resolved maximum stress vectors generated by the expansion of the shock front as it emerged from the original surface...recall [Figure 2.6](#) and related discussion. Additional structural details can be viewed by touring

around and zooming in up to the maximum unpixelated resolution in Google Earth.

The stratigraphic record indicates that the primary crater in the Upheaval Dome penetrated below the original surface to about 450 m, Key and Schultz, 2011. If we assume that prior to the rebound of the central uplift, the primary crater was roughly hemispherical, we estimate from its current diameter that the primary crater was excavated to only about 350 m...a reasonable comparison to the stratigraphic record.

Shatter cones, which are considered to be the most important identifier for geologic impact structures, and shatter 'surfaces' are found inside the primary crater, Kriens, et al., 1999...most commonly observed on the surfaces of the central uplift. This location of shatter cones in the crater complex is consistent with the location of shatter cones inside a laboratory-scale, hypervelocity, primary impact crater formed in dolomite...based on data from Moore, et al., 1962 and noted by Lundberg, 2009. The structure and mechanics of formation of shatter cones and shatter 'surfaces' are representative of late-stage cratering processes and will be discussed in Chapters 4 and 5.

3.1.1.3 STRUCTURAL FEATURES OF THE SECONDARY CRATER

The rim of the secondary crater is clearly seen in [Figure 3.1](#) and marked in [Figures 3.2](#) and [3.6](#). The inner surfaces of the boundary walls of the secondary crater are nearly vertical much like that previously seen around a laboratory-scale sec-

ondary hypervelocity impact crater in beryllium...recall [Figures 2.19](#) and [2.20](#). Brittle mechanical behavior of the target sandstone and the greatly reduced impact stresses resident during the late stages of the cratering process allowed for the formation of the nearly vertical cliffs on the inner wall of the secondary crater (recall laboratory-scale crater profiles in beryllium in [Figure 2.20](#) and sandstone in [Figure 2.24](#)). The strata exposed at the rim of the secondary crater of the Upheaval Dome tends to tilt sharply downward away from the

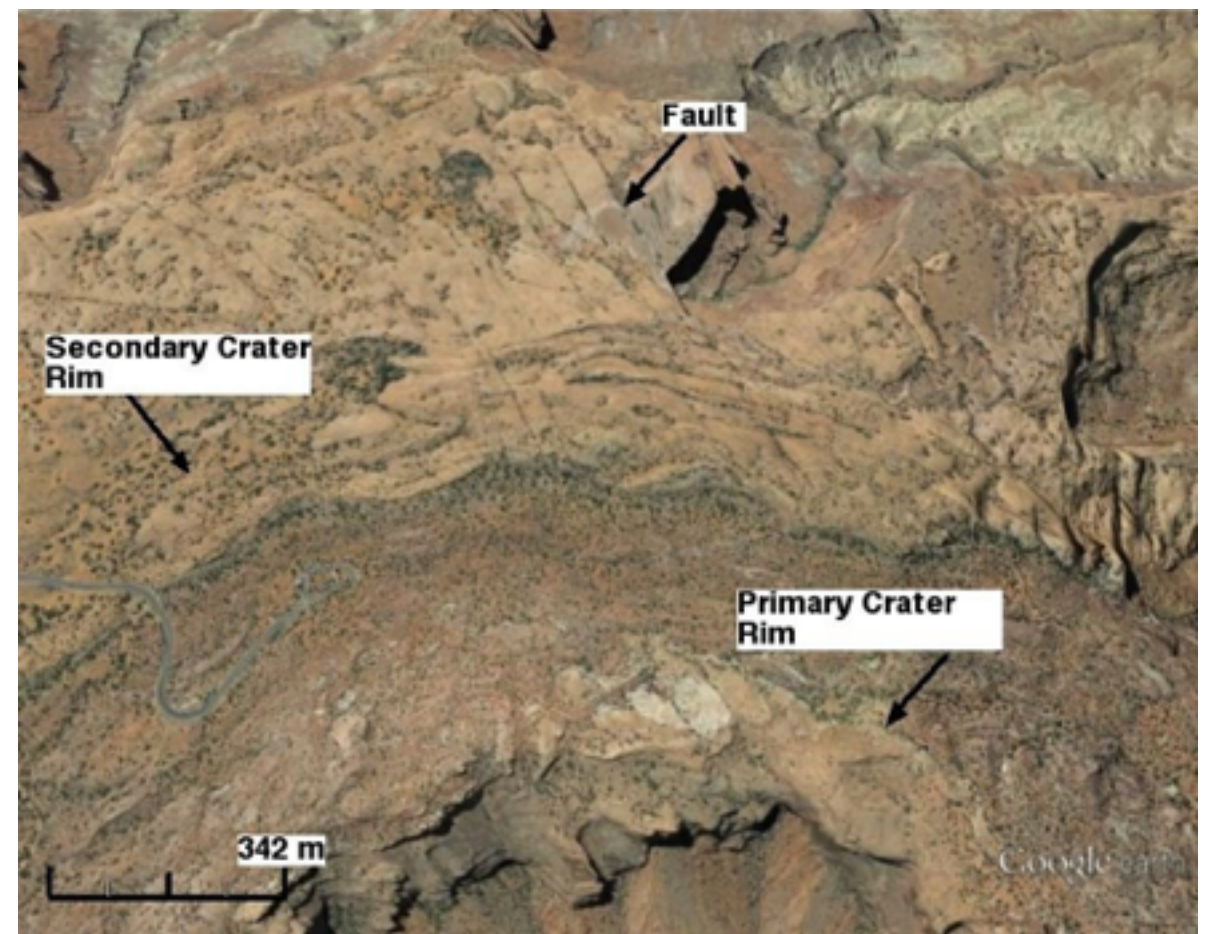


Figure 3.6 Overhead view of the south side of the rims of the primary and secondary craters in the Upheaval Dome. Original image from Google Earth.

crater center due to the late-stage stress pattern which involves an upward maximum stress vector.

Concentric, periodic wave lines seen to circle inside and around the outer perimeter of the primary crater are also found in and around the rim of the secondary crater...seen in [Figures 3.2](#) and [3.6](#). These circular, wavy structures are cut radially at an angle approaching 45° to the tangents of the circles in the rims of both the primary and secondary craters. These straight structures, which are noted as faults in [Figure 3.6](#), represent dikes or faults in a strongly, asymmetrically compressed sandstone, and they were formed during late-stage deformation and fracture of material inside and adjacent to the crater complex. As will be discussed in Chapter 4, dikes and faults are closely related as they are both manifestations of localized shear deformation and fracture that occur in response to the stresses around impact craters. The large number of correlated angled radial dikes/faults can be observed by careful examination of the overhead view in [Figure 3.2](#) and more easily in the close-up in [Figure 3.6](#). These dikes and faults are visible at several locations within and outside of the crater complex starting at the inside perimeter of the secondary crater rim and moving outward.

As clearly illustrated in [Figure 3.6](#), the marked fault and its related faults have had a direct effect on the formation and the current structure of the blind canyon that the marked fault heads. The relative weakness along the straight fault line allowed large blocks of debris to eventually fall into the canyon below over time as it developed via water erosion post-impact.

Preferential erosion progressed along these dike/fault lines. Two similar short, angular walled canyons are seen on the east-southeast side of the crater complex. The orientation of the walls of these canyons also closely correlate with the trajectories of the dike/fault lines.

Five parallel, angled-radial dikes are also prominently exposed in a close-up view of part of the east-southeast face and outside of the secondary crater rim, [Figure 3.7](#). The exposures of these dikes on the wall of the secondary crater rim are meters wide, but the shear offset between the blocks bound by these dikes/faults is small. This pattern of correlated circumferential and radial dikes/faults is analogous to that generally displayed around laboratory-scale hypervelocity impact craters in brittle materials...recall [Figures 2.19](#) and [2.20](#).

As seen in [Figure 3.8](#), both radial and circumferential dikes/faults are also prominently exposed on the outer surface of the north side of the secondary crater rim. The full extent of this patch of dikes/faults can be seen on the left side of the secondary crater rim in [Figure 3.2](#). A prominent, partially exposed circumferential dike that intersects radial dikes/faults in this patch is indicated in [Figure 3.8](#). The orientation and angle of inclination of the marked dike (the localized shear plane is $\sim 45^\circ$ down) is consistent with the maximum compressive stress vector immediately outside the secondary crater wall during its formation.

Vegetation is seen growing along the trace of this dike as well as down the line of the radial faults...similar to that seen in the

angled radial dikes/faults outside of the south side of the secondary crater rim...recall [Figure 3.7](#). This suggests the presence of comminuted material in these dikes/faults.

3.1.2 BEYOND THE UPHEAVAL DOME CRATER COMPLEX

Partly because the Upheaval Dome and many of its surrounding structural features have selectively resisted erosion, many of the characteristic features of this geologic impact structure are well preserved and in some cases enhanced by the effects of erosion. Significant areas of the ejecta blanket and parts of



Figure 3.7 East-southeast side of the secondary crater rim in the Upheaval Dome. Original image from Google Earth.

at least one tertiary ring can be found outside of the crater complex.



Figure 3.8 North rim of the Upheaval Dome secondary crater...viewing south. Original image from Google Earth.

3.1.2.1 UPHEAVAL DOME EJECTA BLANKET

An upper limit for the volume of material excavated from the crater complex can be obtained by assuming a hemispherical primary crater with a diameter of 700 m and a 100-m-deep cylindrical secondary crater diameter with a 2.5 km diameter. This analysis yields an estimated ejecta volume of 1.4 km³. If this ejecta volume were distributed uniformly at a depth of 15 m around the crater complex, the ejecta blanket would cover about 90 km². If as the evidence indicates the Upheaval Dome was formed by an oblique impact, the majority of the

material excavated as a result of the impact would be found downrange, east-southeast...recall **Section 2.1.3.2**.

The ejecta blanket produced during the Upheaval Dome cratering event appears to be greatly altered by post-impact erosion, but never-the-less, the surface of the area seen generally south of the crater complex, above the crater complex in [Figure 3.1](#), appears to be quite different from most of the surrounding terrain, especially the light grey-brown area in the upper left corner of the image. This is a logical location for most of the remnants of the ejecta blanket. The area of the apparent ejecta coverage downrange from the crater complex is roughly 75 km², which is a number close to the estimate derived from the calculated crater volume.

The top of the stratigraphic sequence seen in [Figure 3.9](#) on the southeast side of Aztec Butte is consistent with the expected appearance of an ejecta blanket derived from the Upheaval dome crater complex. (Aztec Butte is located southeast of the crater complex near the head of a canyon that cuts through the local strata and eventually drains into the Green River...see [Figure 3.1](#).) This ‘rubble cap’ stratum, which is less than 20 m thick, appears to be the most recently deposited, and it consists of a conglomerate that ranges from angular boulders to loose sand. This stratum appears to be capped with a dense, fine grain sandstone that has protected this area of the ejecta blanket located on the top of the Aztec Butte from erosion.

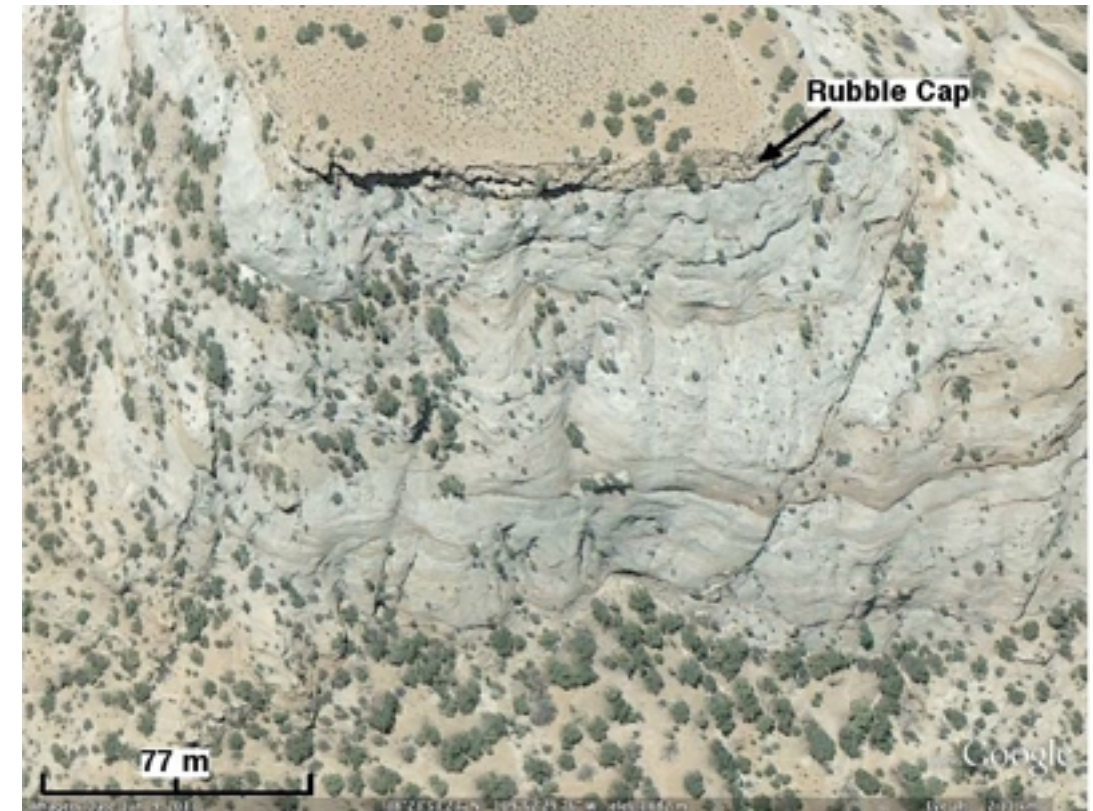


Figure 3.9 Southeast face of Aztec Butte located southeast of the Upheaval Dome crater complex. Original image from Google Earth.

3.1.2.2 MULTI-RING STRUCTURES AROUND THE UPHEAVAL DOME

There is evidence for the existence of a multi-ring structure that surrounds the Upheaval Dome crater complex...a circular wave pattern like that seen in [Figure 1.19](#). Fragmented segments of the first ring of a multi-ring structure can be seen on close examination of [Figure 3.1](#), especially around the west-northwest half of the secondary crater. The segment of the first ring seen immediately north of the secondary crater rim appears to represent part of the first of a multi-ring structural feature. At this point in time, a heavily eroded semicircular

canyon marks the syncline that separates the anticline of the ring outside the secondary crater. Kriens, et al., 1999 called this canyon “Syncline Valley.” This canyon drains into the main crater complex exit canyon (Upheaval Canyon) that eventually drains into the Green River.

Anatomy of the Vredefort Dome Impact Structure

SECTION TOPICS

3.2.1 Vredefort Dome Crater Complex

3.2.2 Outside the Vredefort Dome Crater Complex

Remnants of the *accepted* Vredefort Dome impact structure are prominently exposed ~120 km southwest of Johannesburg, South Africa. As noted in [Figure 3.10](#), Vredefort Dome is located just inside the southwestern perimeter of the Witwatersrand Basin. The source of 40% of the world's gold is found in various locations on the perimeter of the Witwatersrand Basin...the Witwatersrand Goldfield. The towns of Vredefort and Parys are located inside the perimeter of the Vredefort Dome crater complex. This well studied World Heritage Site is claimed to be the oldest known impact structure on Earth...formed 2.02×10^9 years ago, Kamo, et al., 1996. As indicated by the many additional arcuate structures visible in the satellite image in [Figure 3.11](#), the land surface shown in the high altitude view of southern Africa appears to be also littered with many additional impact structures...including for example the small, *accepted*, young Tswaing crater (center located at $25^{\circ} 24' 31.02''$ S, $28^{\circ} 04' 58.65''$ E). In reality within the view presented in [Figure 3.11](#), one should have expected about 200 or more impact structures whose diameter is >1 km to have formed since the Vredefort Dome impact event (estimated from the graph in [Figure 1.6](#)). Many more impact structures should have been formed in this area prior to the formation of the Vredefort Dome, but few remnants of these earlier impact structures are likely to be identifiable today.

The structural features of the Vredefort Dome are prototypic of large, relatively old impact structures. In spite of its age and subsequent erosional and impact overprint modification, most of the main structural features remain intact. In fact as

will be discussed, the Vredefort Dome possesses many structural similarities with the younger Upheaval Dome. Also as with the Upheaval Dome, most of the structural features of the Vredefort Dome can be related to impact features produced at laboratory-scale.

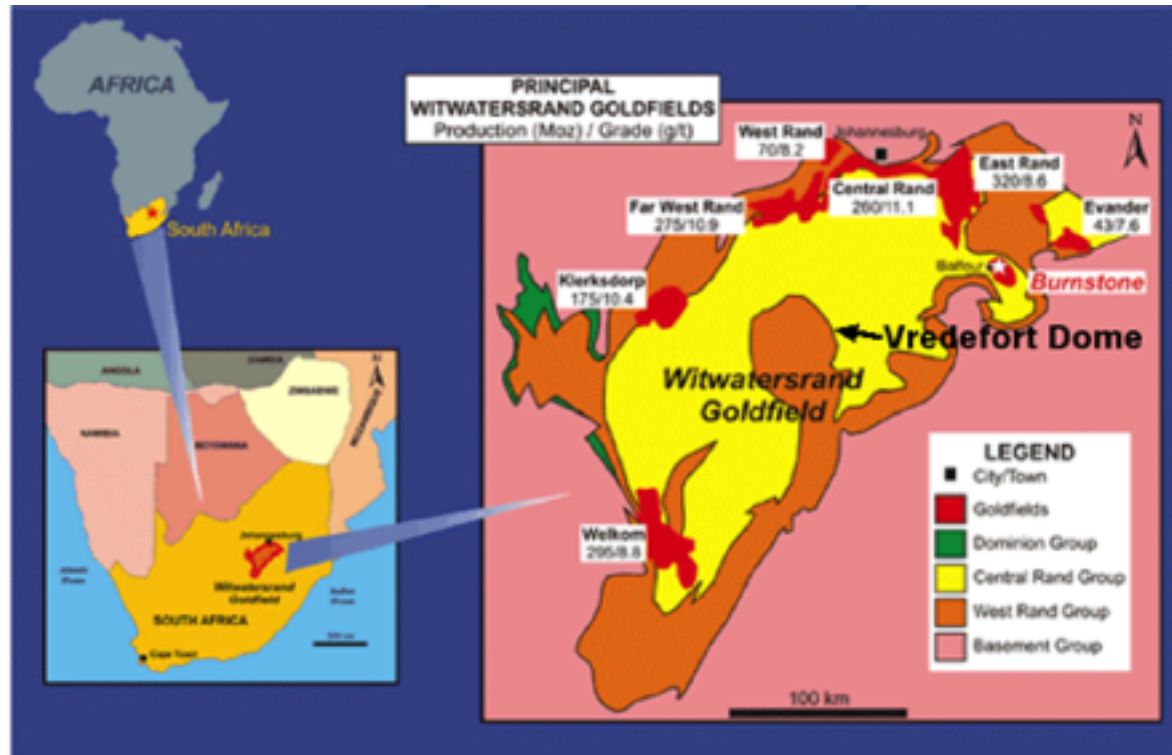


Figure 3.10 Diagram of the location of the Vredefort Dome impact structure and the Witwatersrand Goldfield. Original image from Great Basin Gold website.

3.2.1 VREDEFORT DOME CRATER COMPLEX

The reported diameter of the Vredefort Dome impact structure varies from 160 km, <http://www.unb.ca/passc/ImpactDatabase/>, to 300 km, Wieland, 2006. However, the size and overall structure of the crater complex are clearly visible in both [Figures 3.12](#) and [3.13](#). A well delineated partial crater rim, whose diameter measures



Figure 3.11 High altitude view of the region of southern Africa that includes the Vredefort Dome. Original image from Google Earth.

at ~60 km, is seen in both of these images. This prominent semicircular structural feature is commonly referred to as the “collar wall,” e.g. Wieland, 2006...highlighted in [Figure 3.12](#). A structure referred to as the “Rand Anticline” has also been indicated because it represents a structural feature within the outer rim of one of the larger proposed Vredefort Dome impact structures...see Wieland, 2006. However as will be discussed later in this section if the “Rand Anticline” is associated with the Vredefort Dome, it is outside of the main crater complex and one of several circumferential wave-like structures that represent multiple rings perhaps produced immedi-

ately after the crater complex stops growing...recall [Figure 1.19\(i\)](#).

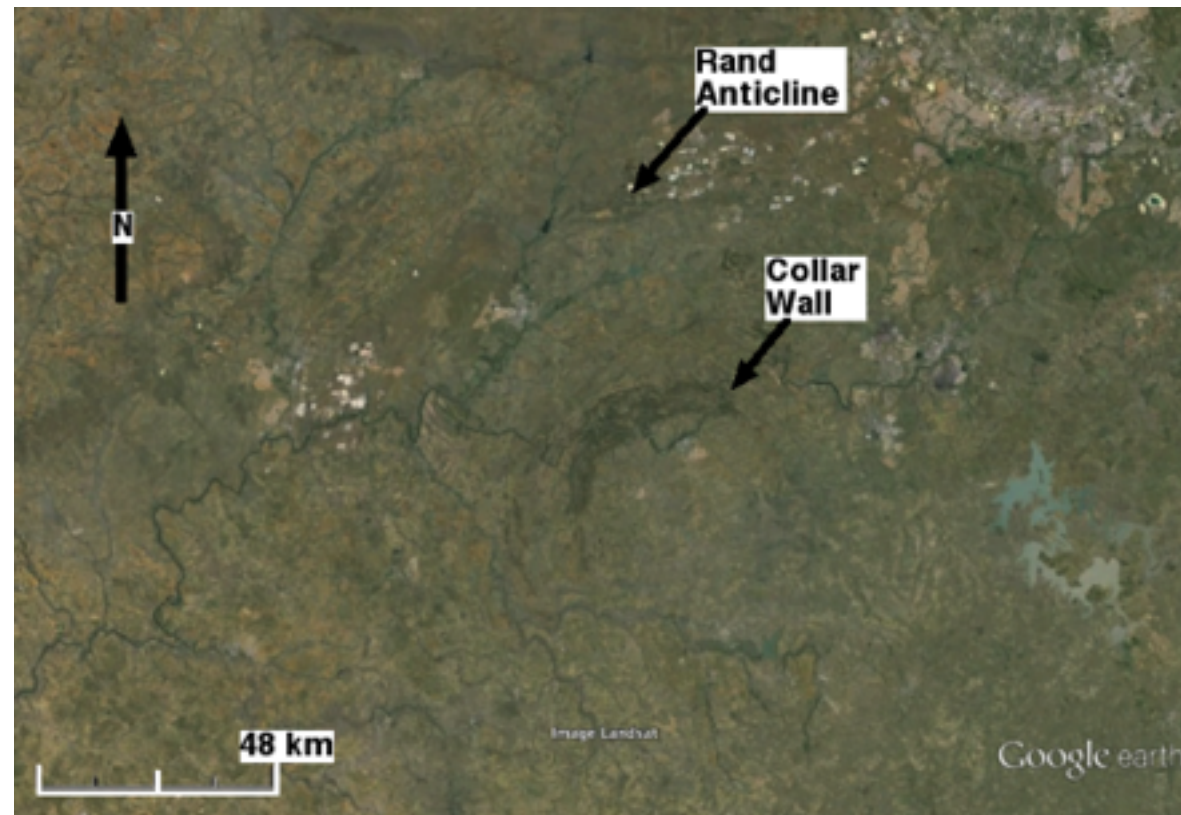


Figure 3.12 High altitude overview of the remnants of the Vredefort Dome crater complex and environs. Original image from Google Earth.

Based primarily on the geometry of the collar wall...marked in [Figures 3.12](#) and [3.13](#), the Vredefort Dome was formed by an oblique impact from the southeast. The pattern of elevation differentiation around the crater rim also indicates an oblique impact from the southeast. Comparing the planform of the Vredefort Dome with laboratory scale craters formed by hypervelocity impact, recall [Figure 2.15](#), the impactor's trajectory is estimated to have been between 55 and 60° above the horizon. It is interesting to note that the planform of the distribution of

Central Rand Group rocks presented in [Figure 3.10](#) is also suggestive of an ejecta distribution pattern for an oblique impact for the Vredefort Dome...recall [Figures 2.1](#) and [2.2](#).

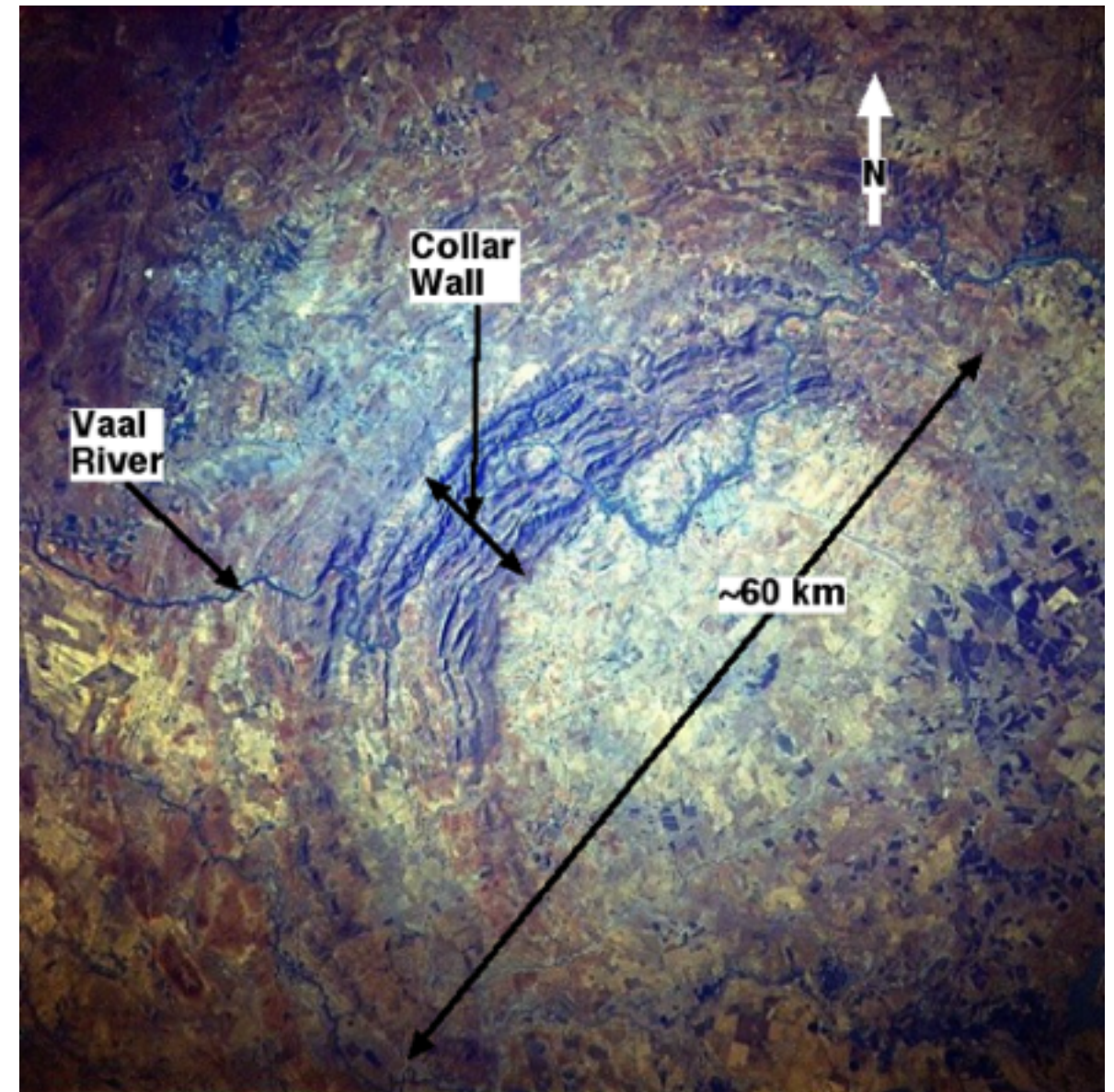


Figure 3.13 Landsat image of the northwestern half of the Vredefort Dome impact structure.

3.2.1.1 SOME STRUCTURAL DETAILS OF THE CENTRAL UPLIFT OF THE VREDEFORT DOME

The central uplift in the Vredefort Dome is not as well defined as that in the Upheaval Dome. A general-consensus-partial-boundary for the Vredefort central uplift is indicated in [Figure 3.14](#) by a green line. The interior region of the Vredefort Dome central uplift is partially marked by a proliferation of exposed archaean rocks ($\sim 3.5 \times 10^9$ years old, Graham, et al., 2005), categorized as Inlandsee Leucogranofels, and several “G” structures which are presumed to have been formed in conjunction with the formation of the Vredefort Dome. Otherwise, the central uplift has been nearly obliterated by erosion and overlying sediment burial. Today the top of the Vredefort Dome central uplift lies ~ 200 m below the rim of the secondary crater.

An example of dikes that remain exposed and marked in [Figure 3.14](#) inside the central uplift can be seen in [Figure 3.15](#). These dikes are generally referred to as “Vredefort Granophyre,” and each represents the terminus of an adiabatic localized shear band that is analogous to the “Shear Band” marked in [Figure 2.10](#) around the inside of a hypervelocity impact crater in titanium. As will be discussed in detail in Chapter 4, it is not coincidental that two parallel dike structures are seen in the photo as they are typically of those formed by localized shear...a periodic process. Similar dikes are found on the perimeter of the primary crater...noted in [Figure 3.14](#). Age of the Vredefort Dome (2.023×10^9 years) is derived from zir-

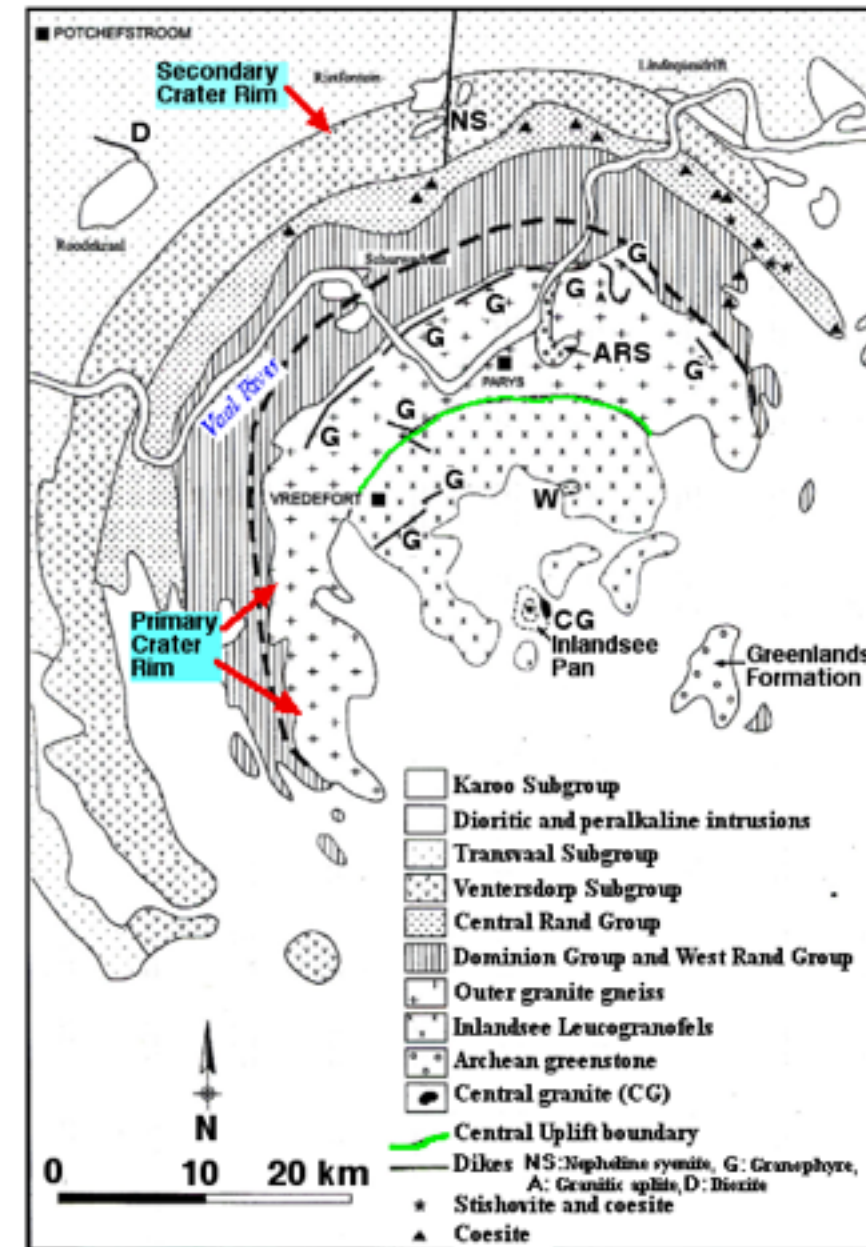


Figure 3.14 Schematic map of lithologies and other features of the Vredefort Dome impact structure. Original image from Lieger, 2011...Fig. 1.7.

cons found in the Vredefort Granophyre in the central uplift, Kamo, et al., 1996, and the ages of the upturned strata within the collar wall vary consistently from inside to out with the youngest rocks on the top of the stack that is exposed at the outer rim of the secondary crater, Graham, et al., 2005.



Figure 3.15 Typical exposure of dikes found within the central uplift and at the perimeter of the primary crater. Original image found at the website of the National Research Foundation of South Africa...<http://www.hartrao.ac.za/other/vredefort/vredefort.html>.

The close-up structure of a typical fragment of a Vredefort Granophyre dike is seen in [Figure 3.16](#). The black matrix of this



Figure 3.16 Rock, ~0.4 m across, from a section of a Vredefort Granophyre dike. Original image from Wieland, 2006.

rock represents material that was melted during the deformation and fracture process inside the localized shear zone. The clasts represent fragments of rock that were not fully incorporated into the melt due to insufficient thermal energy generated by deformation and fracture inside the shear zone. In other words, the kinetics of the melting process prevented these clasts from being totally consumed before the surrounding molten matrix rock cooled and solidified. These clasts represent material that resided along the shear line in the target material prior to impact rather than in an external reservoir...which is commonly postulated. The secondary dike that

is seen cutting halfway through this rock could easily have formed by stresses that developed in the rock producing localized shear even before cooling to a solid state.

3.2.1.2 SOME STRUCTURAL DETAILS OF THE PRIMARY CRATER

The inner perimeter of the ~10 km radially thick collar wall noted in [Figure 3.13](#) is located outside the outer boundary of the primary crater, which is approximately 40 km across. It should be noted that Wieland, 2006 and many other authors have extended the inner boundary of the collar wall to include part of the primary (transient) crater outside of the central uplift. The dimensional approximations presented here are consistent with the lithological record of the crater complex, that is presented in [Figure 3.14](#) where the boundaries marking the outer limits of both the primary and secondary craters are indicated. The inner boundary of the primary crater is marked both by a differentiation in the lithology and a line of near vertical dikes...also indicated in the figure by “G” in [Figure 3.14](#).

The original depth of the primary crater prior to the formation of the central uplift has been estimated at 25 km, Hart, et al., 1981, which is consistent with the estimated depth of a normal impact. It is generally believed that erosion has lowered the crater rim and central uplift by 8-11 km, but based on the expected number of additional impacts in the area, it is rather more likely that the original crater was mostly back-filled with sediment from subsequent impacts in the neighborhood such as seen on Earth's Moon. This back-fill material eventually

filled most of the primary crater allowing the Vaal River (marked in [Figure 3.13](#)) to flow out of the crater complex toward the west, draining all of the water that probably filled the original crater for long periods after the crater formed.

The rim of the primary crater is also occasionally marked by an exposed granite ridge-line that rises about 90 m above the inside of the crater and whose partial trace is indicated in [Figure 3.17](#). The observed segmentation of the ridge is expected to have been due to the circumferential stresses that develop as a result of crater expansion. The shear dike pattern that is seen in [Figure 3.17](#) was probably developed in cold, solid rock as a result of the three dimensional stress pattern during late-stage cratering. This dike pattern is similar to that observed around both the primary and secondary craters of the Upheaval Dome.

The segment of the primary crater rim inside the red square in [Figure 3.17](#) is magnified in [Figure 3.18](#). This segment contains surface exposures of parallel, circumferential dikes, marked ASB's, that are analogous to the shear bands seen along the walls of the primary hypervelocity impact crater in titanium in [Figure 2.10](#). The structures seen here can also be classified as Vredefort Granophyre dikes, which were formed by adiabatic localized shear during the late-stage of primary crater excavation...the formation mechanics will be discussed in Chapter 4. The planes of these ASB's appear to be sloping downward away from the center of the Vredefort Dome. A radial 'shear dike,' indicated by a radial line of vegetation in the upper right

of the photograph, is also seen to have cut through this segment of the primary crater wall.

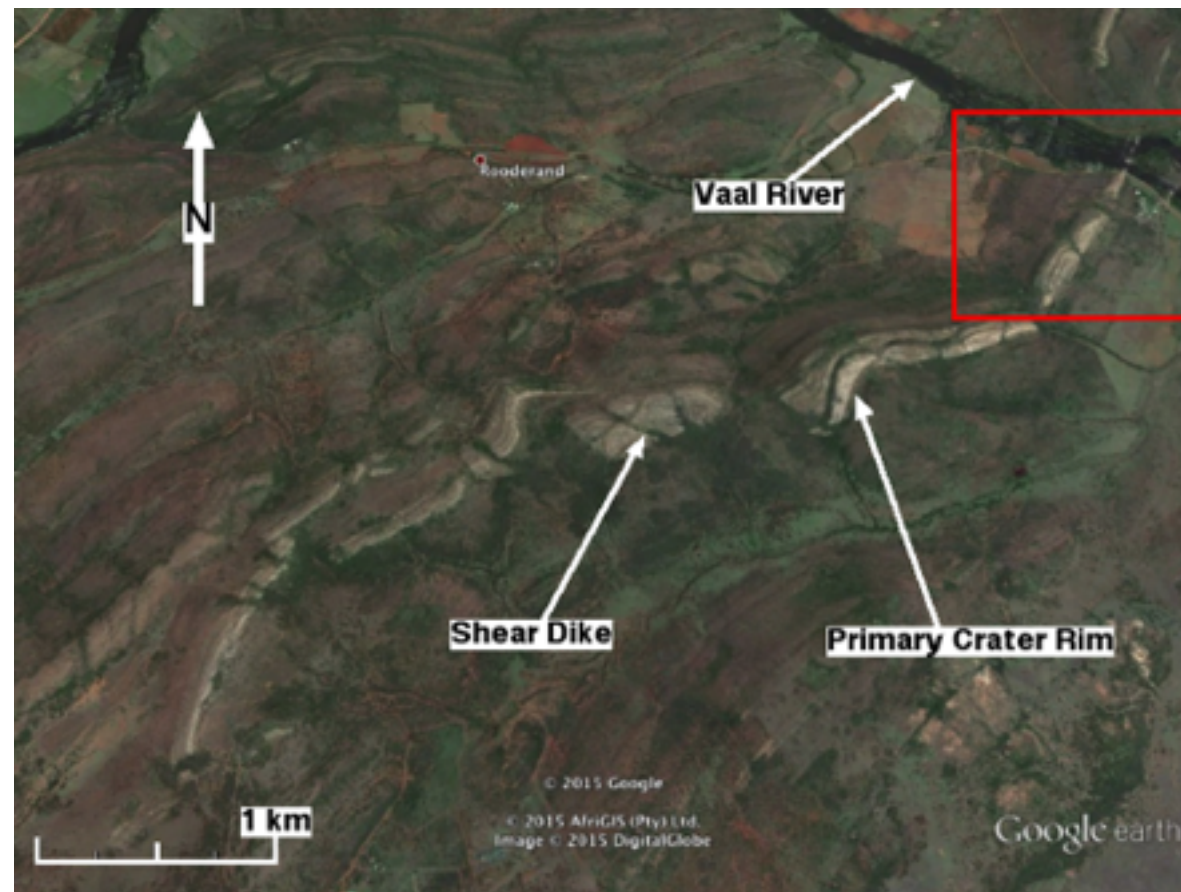


Figure 3.17 High altitude view of the primary crater rim in the northwest quadrant of the Vredefort Dome. Original image from Google Earth.

Another common structural feature observed near the rim of the primary crater has been generally referred to as pseudotachylite. The term *pseudotachylite* was first coined by Shand, 1916 to distinguish melted features that were found associated with the Vredefort Dome impact structure. The structure of a pseudotachylite is similar to a tachylite which is a structure characterized as ‘clasts within a basaltic glass ma-

trix.’ The Vredefort Dome is well known for its many prominent exposures of pseudotachylite.

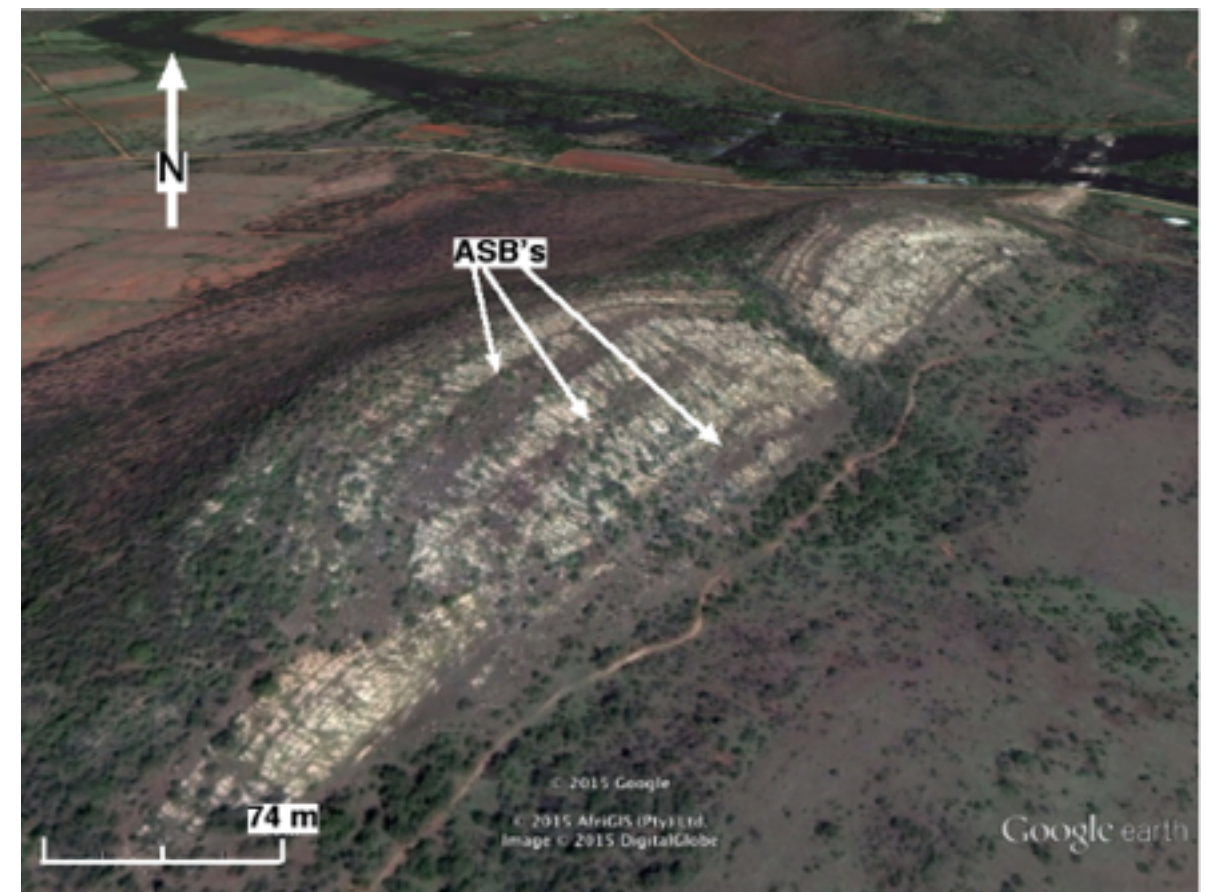


Figure 3.18 High resolution view of the segment of the primary crater rim located inside the red square in [Figure 3.17](#). Original image from Google Earth.

An example of three cross-sections of a large band of pseudotachylite behind the two-headed arrow in [Figure 3.19](#) is clearly exposed on cut faces in the Parys Quarry located inside the primary crater. The structural features of these pseudotachylite exposures are typical...a band of a black matrix that contains light colored, boulder size clasts. As will be discussed in Chapter 4, these bodies are formed by adiabatic localized shearing during late-stage cratering that causes partial melting of the

surrounding material. The three levels of pseudotachylite exposed under the double-headed arrow in [Figure 3.19](#) indicate that the formation slopes downward away from the center of the Vredefort Dome like the dikes seen in the primary crater rim...[Figure 3.18](#). The orientation of the plane of this pseudotachylite infers that it was turned upward by late-stage shear forces along the inner wall of the primary crater.

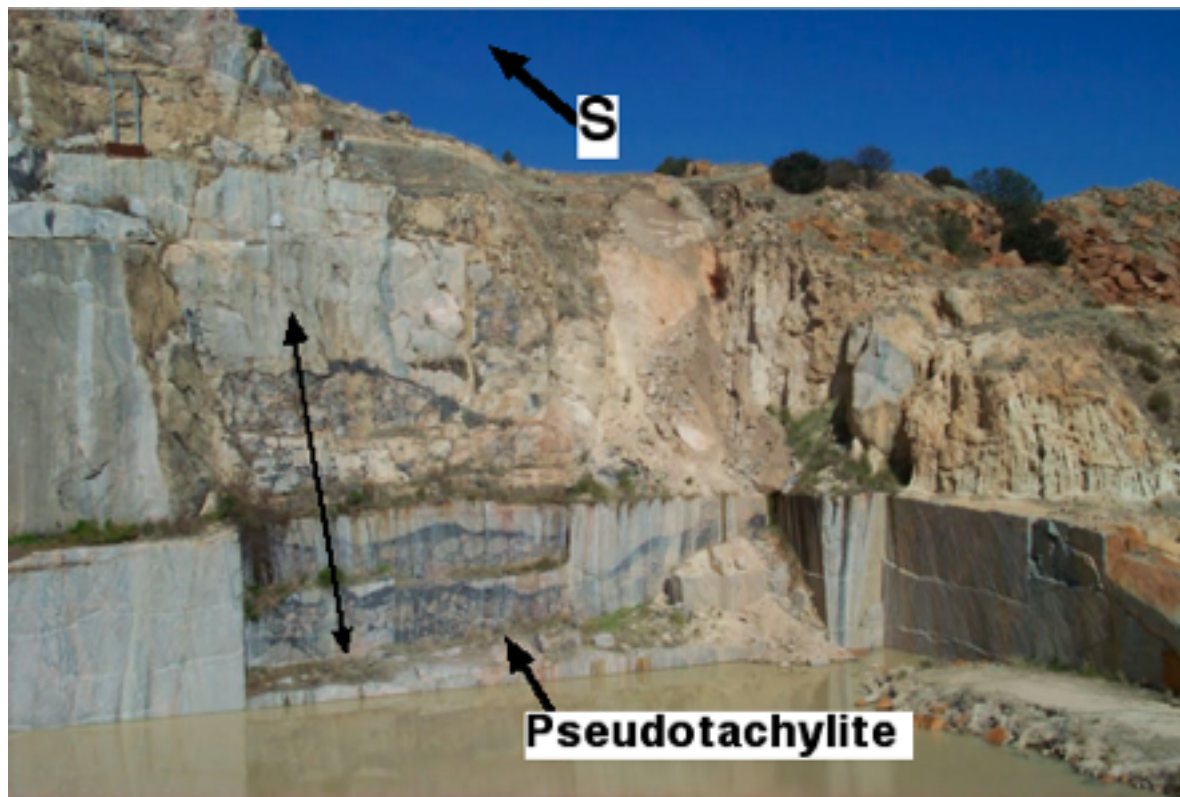


Figure 3.19 Typical pseudotachylite exposed in the Parys Quarry that is located inside the primary crater of the Vredefort Dome. Original image posted on the Internet at Panoramio by Martin Tuchscherer.

The location of the Parys Quarry inside the primary crater rim of the Vredefort Dome is marked in the satellite image in [Figure 3.20](#). The course of the Vaal River is seen to loop around the quarry. Incidentally as observed in [Figure 3.20](#), the Parys

Quarry is located on the south perimeter of a circular structure that could represent the remnants of an overprint impact structure.

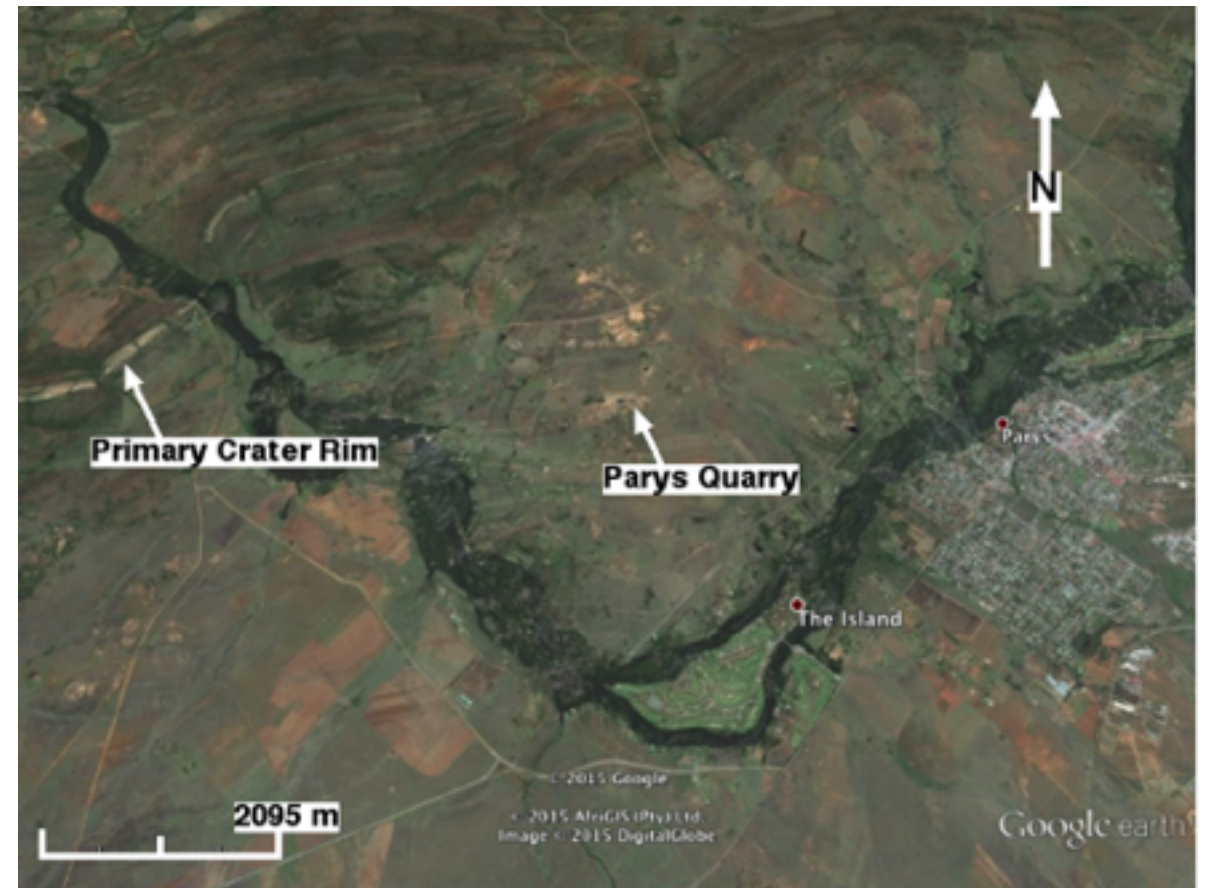


Figure 3.20 View of the location of the Parys Quarry inside the primary crater of the Vredefort Dome. Original image from Google Earth.

3.2.1.3 SECONDARY CRATER AND THE COLLAR WALL

The outer perimeter of the collar wall marked in [Figure 3.14](#) defines the outer limit of a secondary crater that is ~60 km across. As seen in a closeup view of the northwest section of the collar wall in [Figure 3.21](#), the circumferential, periodic, segmented ridge lines in the Vredefort Dome collar wall closely resemble the region of the Aristarchus Moon crater between



Figure 3.21 Northwest segment of the collar wall of the Vredefort Dome where several chevron patterned dikes are well exposed. Original image from Google Earth.

its primary and secondary crater rims ([Figure 1.3](#)) as well as on the rim of the secondary crater in the Upheaval Dome... recall [Figure 3.6](#). As defined in this volume, the exposure of the collar wall of the Vredefort Dome measures about 10 km from inside to outside with the thickest region residing on the down-range side of the secondary crater...northwest region.

As can be seen by examining the image in [Figure 3.13](#), periodic segmentation of the concentric ridge-lines is observed all along the exposed collar wall similar to that observed in the primary crater rim but with a longer period. The planform of

the individual circumferential segments tends toward an arcuate shape again much like that seen in the primary crater rim, both of which have been interpreted as a series of folds...Wieland, et al., 2005; Wieland, 2006. This collection of concentric arcuate ridges can be characterized as uplift structures possessing exposed stratigraphic layers that point to the center of the impact structure...the general tilt of the strata inside the ridges is downward away from the center of the Vredefort Dome.

These arcuate ridge segments are separated radially by shear dikes that formed as a result of the three dimensional stress pattern of the outwardly reducing force vectors that remained toward the end of the cratering process. The resolved shear stresses defined by **Equation 2.2** produced localized shear that generated the angular shear dike patterns seen in [Figures 3.17, 3.18](#) and [3.21](#). The dikes/faults, seen more definitively as we scan our view outward around the secondary crater outer periphery, appear to result from localized shearing in relatively cold bedrock (a brittle material) at an intermediate strain rate...late-stage cratering strain rates. The orientations and patterns of the dikes and faults in the rim of the secondary crater rim are consistent with a maximum compression vector pointing generally radially and upward...recall the fracture pattern around the secondary hypervelocity impact crater in beryllium...[Figures 2.19](#) and [2.20](#) and the rim of the secondary crater of the Upheaval Dome, [Figure 3.6](#).

Radial canyons have been formed along multiple radial dike traces in the collar wall. The display of the angular radial dike

pattern in the outer edge of the collar wall in [Figure 3.21](#) has been enhanced by differential erosion inside the dike and along its trace. The higher erosion rate within and along the dike traces relative to the surrounding material also indicates that the internal structure of these features contained significant amounts of poorly consolidated material that is more easily removed by wind or water erosion than the surrounding material...a characteristic of localized shearing in cold, brittle rock formed at slow strain rate...to be discussed in Chapter 4. This is the same erosion behavior previously discussed for dikes observed on the outer rim of the secondary crater of the Upheaval Dome. In both cases, the comminuted material in these dikes has allowed increased vegetative cover along the dike trace...also noted by Wieland, 2006 for various parts of the collar wall of the Vredefort Dome.

As previously mentioned, there is consensus that shatter cones represent a primary indicator for the verification of geologic impact structures. Many shatter cones have been found mostly in the collar wall of the Vredefort Dome, Wieland, F., et al, 2006. The surface of these shatter cones exhibit the typical 'horse-tail' pattern...surface morphology is among the primary identifiers for shatter cones. An extended discussion of shatter cones and their formation mechanics will be presented in Chapter 5.

3.2.2 OUTSIDE THE VREDEFORT DOME CRATER COMPLEX

The 'Rand Anticline' marked in [Figure 3.12](#) is analogous to the Syncline Valley located around the Upheaval Dome, both of which represent a wave ring like those illustrated in [Figure 1.19\(i\)](#). In other words, the Rand Anticline is a feature likely to have been produced by response of the area surrounding the Vredefort Dome to the induced wave generated by the impact that formed the crater complex...recall especially [Figure 1.9\(i\)](#).

As one should expect, there is evidence of one or more overprint impact structures in and around the Vredefort Dome. For example, evidence of an overprint impact structure in the wall collar is indicated in [Figure 3.22](#). Here a small, ~2 km across, oblique crater-like structure is indicated. This crater is reminiscent of the many overprint impact structures seen in and around the Einstein crater on Earth's moon...recall [Figure 1.2](#).

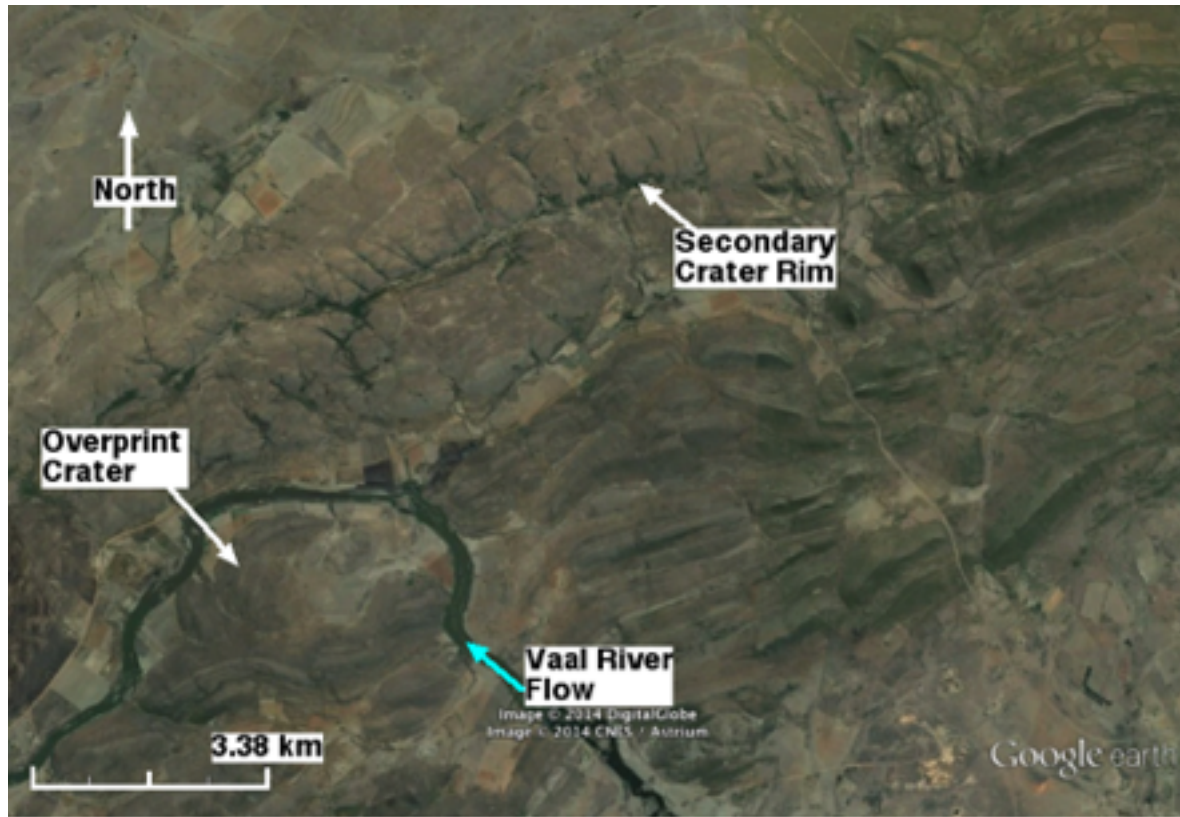


Figure 3.22 High altitude image of a probable overprint impact structure in the collar wall of the Vredefort Dome. Original image from Google Earth.

Anatomy of the Chesapeake Bay Impact Structure

Most of the impact structures on Earth are covered with water, and consequently, very few of these impact structures have been located and verified relative to the numbers found on dry land. However, the structural features of the submerged impact structures are fundamentally the same as those found in and around dry-land impact structures. In order to illustrate this point, we will briefly examine the structural features of the accepted Chesapeake Bay impact structure.

The *accepted* 35-million-year-old (late Eocene) Chesapeake Bay impact structure, which has been studied extensively by core drilling and seismic mapping, is located at the entrance to Chesapeake Bay, which is located on the east coast of the United States, and it is currently mostly submerged under seawater, sediment, impact damaged material, and impact ejecta. A view of the planform of this relatively large impact structure and its location are seen in the diagram in [Figure 3.23](#). As in-

dicated, the impact structure consists of a central uplift, a primary crater, and a secondary crater.

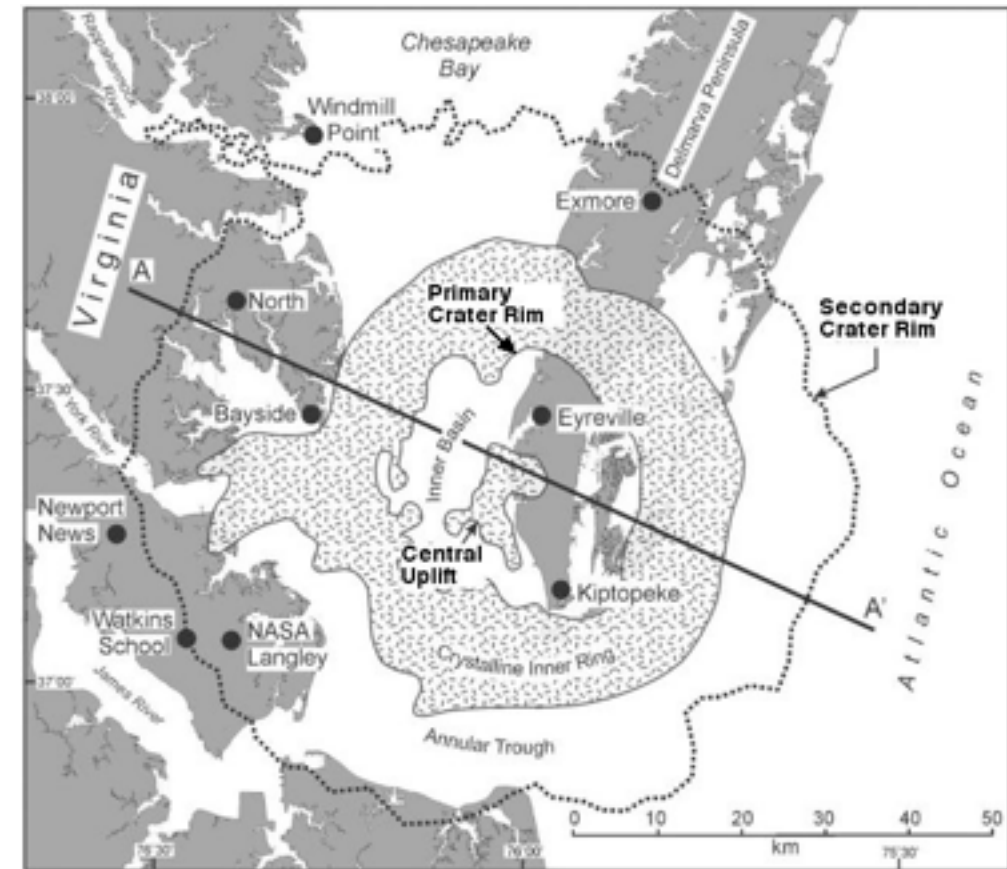


Figure 3.23 Diagram of the overhead view of the Chesapeake Bay impact structure. Black dots indicate core drilling sites. Original image from Poag, 2012.

The central uplift of the Chesapeake Bay impact structure is mostly submerged under the Bay, but as noted in [Figure 3.23](#), a minor part of it is exposed on dry land...near the south end of the Delmarva peninsula. The primary crater is approximately 30 km across, and the secondary is approximately 85 km across. The annular trough (“Inner Basin” in [Figure 3.23](#)) surrounding the central uplift represents the floor of the primary crater. The “Crystalline Inner Ring” and the “Annular

Trough” represent structural details of the inside of the secondary crater.

A cross-sectional schematic diagram of the Chesapeake Bay impact structure is seen in [Figure 3.24](#). This diagram of the main features of the Chesapeake Bay impact structure illustrates that most of the structural features seen in dry-land impact structures are also found preserved on and under the ocean floor. The Chesapeake Bay impact structure is typical of impact structures formed in relatively shallow water...water was estimated to have been 0-170 m deep on the western edge at the time of impact, Horton, et al, 2003. The height differential across the rim of the primary crater rim indicated in [Figure 3.24](#) suggests that the impactor’s trajectory was generally from the east and was between 20° to 45° above the horizon. Results of recent studies that included some examination of the planform of the ejecta blanket, Griscom, 2012, appear to be consistent with this proposed impactor trajectory.

Immediately after impact, the bottom surface of the primary crater is estimated to have penetrated as deep as 15 km so that we can deduce that the bottom of the primary crater rebounded upward over 12 km. The central uplift stalled after being propelled upward about another kilometer above the current bottom of the primary crater.

As indicated in [Figure 3.24](#), both the primary and secondary craters are filled with “Displaced megablocks”...the Exmore formation and post-impact sediment. The “Shock-altered crys-

talline rocks” are found primarily at the bottom of the primary crater.

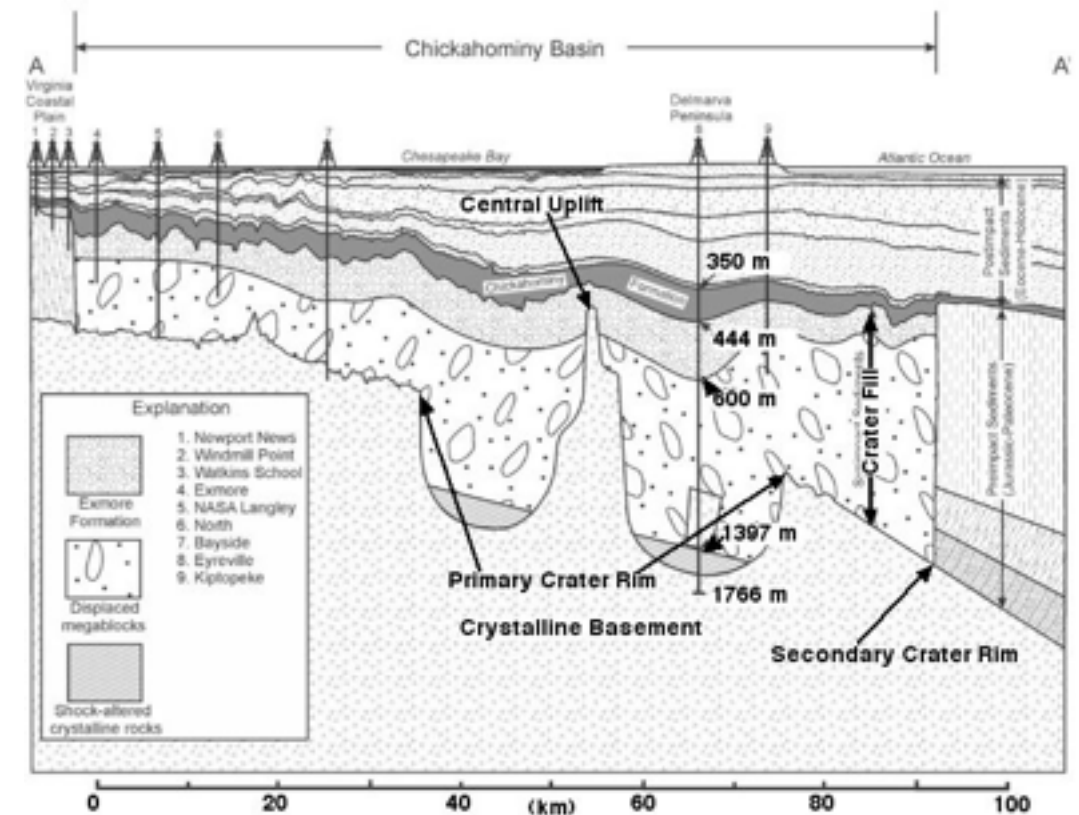


Figure 3.24 Schematic diagram of the A-A' cross-section in Figure 3.23 of the Chesapeake Bay impact structure. Original image from Poag, 2012.

The “Displaced megablocks” area in [Figure 3.24](#) appears to represent a zone of impact damaged material that lies immediately below the surface of both the primary and secondary craters. This damage zone is comparable to that seen around the primary hypervelocity impact crater in titanium seen in [Figure 2.10](#) except for the fact deformation and fracture of brittle materials is more heterogenous and as discussed previously,

especially in Chapter 2, creates a wider range of ejecta fragment sizes than produced in ductile metals.

During late-stage impact cratering, localized shear failure in brittle materials creates ejecta that has a wide range of particle sizes. Localized shear failure around the inside of both the primary and secondary craters also creates large quantities of high-temperature, fine ejecta particles that contribute significantly to formation of the matrix for impact breccia such as that found in the “Displaced megablocks” zone.

Chapter 3 References

Graham, I. T., De Waal, S.A., and Armstrong, R.A., 2005, New U–Pb SHRIMP zircon age for the Schurwedraai alkali granite: Implications for pre-impact development of the Vredefort Dome and extent of Bushveld magmatism, South Africa, *Journal of African Earth Sciences*, 43, pp. 537–548.

Griscom, D. L., 2012, In plain sight: the Chesapeake Bay crater ejecta blanket, *Solid Earth Discussions*, 4, pp. 363–428.

Hart, R. J., Welke, H. J. and Nicolaysen, L.O., 1981, Geochronology of the deep profile through the Archaean Basement of Vredefort, with implication for early crustal evolution. *Journal of Geophysical Research*, 86, pp. 10663–10680.

Horton, J. W., Jr., Powars, D. S., Gohn, G. S., 2003, Studies of the Chesapeake Bay Impact Structure-Introduction and Discussion, Chapter A of Studies of the Chesapeake Bay Impact Structure—The USGS-NASA Langley Corehole, Hampton, Virginia, and Related Coreholes and Geophysical Surveys, Profes-

sional Paper 1688, Edited by J. Wright Horton, Jr., David S. Powars, and Gregory S. Gohn, U.S. Department of the Interior U.S. Geological Survey.

Huntoon, P. W., 2000, Upheaval Dome, Canyonlands, Utah: Strain Indicators that Reveal an Impact Origin, *Geology of Utah's Parks and Monuments*, 2000 Utah Geological Association Publication 28, D.A. Sprinkel, T.C. Chidsey, Jr., and P.B. Anderson, editors.

Kamo, S. L., Reimold, W. U., Krogh, T. E., and Colliston, W. P., 1996, A 2.023 Ga age for the Vredefort impact event and a first report of shock metamorphosed zircons in pseudotachylitic breccias and granophyre. *Earth and Planetary Science Letters*, 144, pp. 369–388.

Kenkmann, T., Jähn, A., Scherler, D., and Ivanov, B. A., 2005, Structure and formation of a central uplift: A case study at the Upheaval Dome impact crater, Utah, Kenkmann, T., Hörz, F., and Deutsch, A., eds., *Large meteorite impacts III: Geological Society of America Special Paper 384*, pp. 85–115.

Key, W. R. O. and Schultz, R. A., 2011, Fault formation in porous sedimentary rocks at high strain rates: First results from the Upheaval Dome impact structure, Utah, USA, *GSA Bulletin*; May/June 2011; v. 123; no. 5/6; p. 1161–1170; doi: 10.1130/B30087.1.

Kriens, B. J., Shoemaker, E. M. and Herkenhoff, K. E., 1999, Geology of the Upheaval Dome impact structure, south east Utah, *Journal of Geophysical Research*, v. 104, pp. 18,867-18,887, doi: 10.1029/1998JE000587.

Lundberg, L. B., 2009, *Impact Geology: Fundamentals of Impact Crater Formation*, *Northwest Geology*, 38, pp. 67-88.

Moore, H. J., Gault, D. E., and Lugin, R. V., 1962, *Experimental Hypervelocity Impact Craters in Rock*, United States Department of the Interior Geologic Survey Report No. N 62-13994, March 1962.

Poag, C. W., 2012, Foraminiferal repopulation of the Late Eocene Chesapeake Bay Impact Crater, *Micropaleontology*, vol. 58, nos. 1-2, pp. 1-206.

Shand, S. J., 1916, The pseudotachylyte of Parijs (Orange Free State) and its relation to “trap-shotten gneiss” and “flinty crush-rock,” *Quarterly Journal of the Geologic Society of London*, 72, pp. 198-221.

Scherler, D., Kenkmann, T., Jahn, A., 2006, Structural record of an oblique impact, *Earth and Planetary Science Letters*, 248, p. 43 - 53.

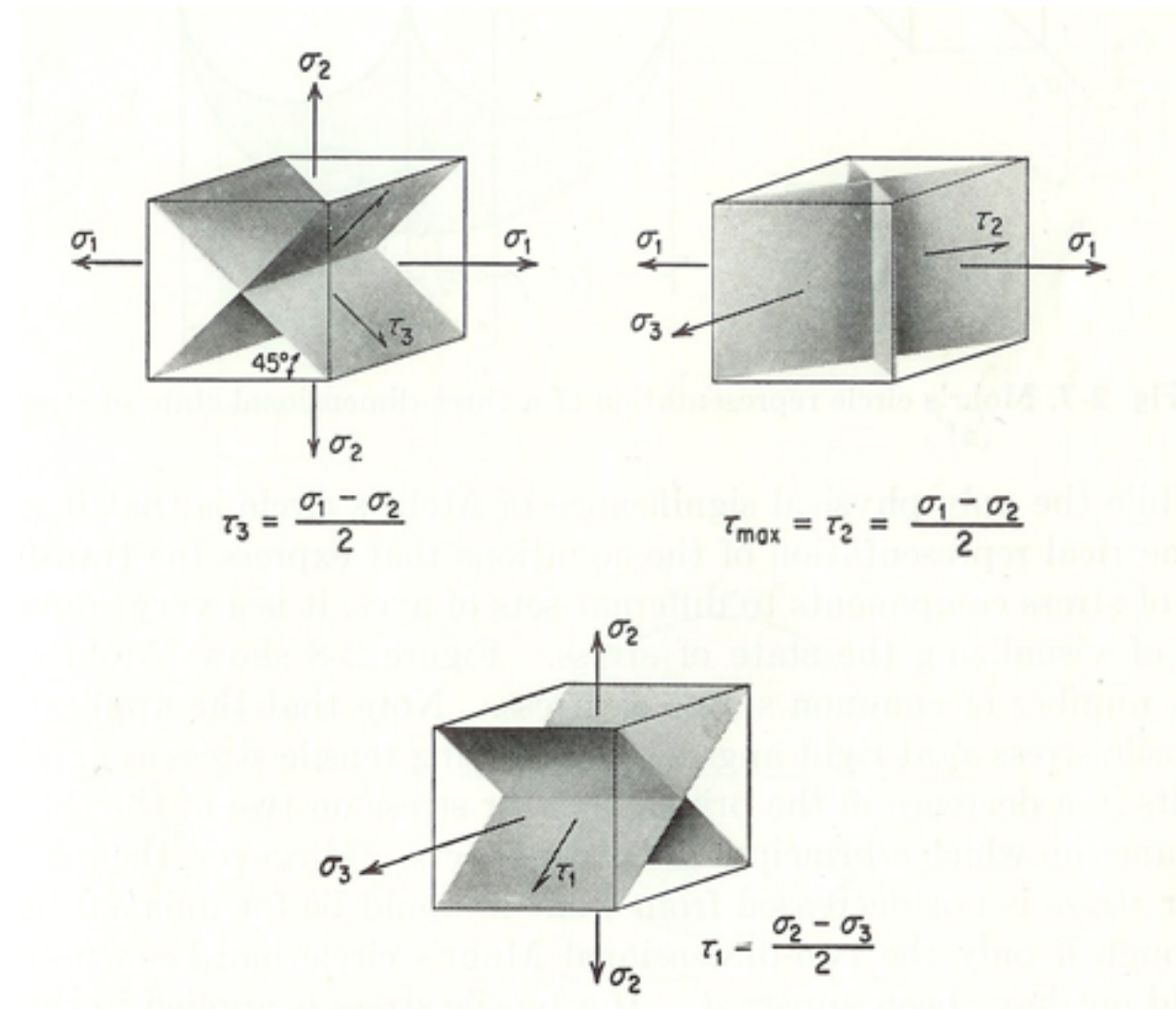
Wieland, F., Gibson, R. L., and Reimold, W. U., 2005, Structural analysis of the collar of the Vredefort Dome, South Africa— Significance for impact-related deformation and central uplift formation, *Meteoritics & Planetary Science* 40, Nr 9/10, pp. 1537–1554.

Wieland, F., Reimold, W. U., and Gibson, R. L., 2006, New observations on shatter cones in the Vredefort impact structure, South Africa, and evaluation of current hypotheses for shatter cone formation, *Meteoritics & Planetary Science* 41, Nr 11, pp. 1737–1759.

Wieland, F., 2006, *Structural analysis of impact-related deformation in the collar rocks of the Vredefort Dome, South Africa*, Thesis submitted to the Faculty of Science, University of the Witwatersrand, Johannesburg, South Africa, in fulfillment of the requirements for the degree of Doctor of Philosophy.

Flow and Fracture of Real Materials: The Fundamentals

The deformation of all materials starts in the shear mode when normal stresses are applied. The diagrams on the right illustrate the geometry of deformation in solids.



Original image from Dieter, 1961.

In researching the processes that form geologic impact structures, it became apparent that there is considerable misunderstanding in the literature and across the scientific and engineering communities regarding the mechanics of deformation and fracture of materials impacted on the surfaces of terrestrial objects. Consequently, this chapter is devoted to a description of the observed flow and fracture behavior of solids, but as we shall see, the basic principles apply equally to liquids. The principles described in this chapter are fundamental to understanding the origin of many of the substructures observed in and around geologic impact structures...e.g. dikes, pseudotachylite and shatter cones.

Deformation and fracture of solids, granular materials, and viscous liquids have been studied extensively, but contrary to many of the popular material models, inelastic deformation and fracture in real solids, semi-solids and liquids starts in the shear mode and continues as a heterogeneous process at all scales. This fundamental mechanical behavior derives from the simple fact that all materials start to permanently deform in a shear mode because shear deformation requires the least stress. In crystalline solids, this initial shear deformation occurs along one or more unique planes. Periodic shear localization in a stressed body is a common behavior. We will examine the basis for this reality mostly for the case of triaxial compressive loading because this stress state dominates in the material surrounding a forming impact structure at all scales...laboratory to full size geologic structures.

As discussed in the previous chapters, the majority of the final structural features of a geologic impact structure are formed during the latter stages of the cratering process, and the structural details of these features are controlled mostly by the mechanical behavior of the target materials...water, rocks, soils, etc. We will start by examining shear deformation in liquids. The resultant stress states that evolve in the materials surrounding an evolving impact crater will be examined...the stress history is generalized in [Figure 2.18](#), and **Equation 2.2** expresses the resolved shear stress. In addition, we will develop an understanding of the effects of temperature on the mechanical behavior of geologic materials because deformation and fracture of materials is associated with the release of significant amounts of heat regardless of the strain rate.

Shear Localization

SECTION TOPICS

4.1.1 Shear localization in Liquids

4.1.2 Shear localization in Metals

4.1.3 Localized Shear Branching

4.1.4 Localized Shear Band Thickening

4.1.5 Shear Localization in Granular Materials

4.1.6 Computer Simulation of Localized Shear Deformation

Shear localization is characterized by shear deformation on singular or periodic, planar structures in solids, semisolids and liquids as a result of the applied stresses (see especially Walley, 2012). The observed deformation and fracture behavior of solid rock under quasi-static, triaxial (confined) compression graphically illustrates the surface manifestations of localized shear flow and fracture inside solids. In [Figure 4.1](#) we see demonstrated the shear deformation and fracture pattern produced on the surface of a marble sample that is caused by an asymmetric, quasi-statically applied, compressive load. This observed deformation and fracture behavior of solid rock under quasi-static, triaxial (confined) compression graphically illustrates the surface manifestations of localized shear flow and fracture inside solids. Localized, $\sim 90^\circ$ complementary, periodic shear planes are clearly indicated on the surface of this triaxially loaded specimen. Two very important characteristics of localized shear in the deformed specimen demonstrated in [Figure 4.1](#) are: 1) the periodic repetition of the shear deformation/failure planes that are exposed on its surface and 2) the geometrically related, periodic bifurcation of the shear planes...termed shear branching in the following discussion.

The stress pattern in material surrounding a forming impact crater can be described quite simply as confined, asymmetric compression...especially during its later stages of crater formation. Localized shear deformation in solids, semi-solids, or liquids under triaxial compressive loading is only possible when the stress field in the loaded body becomes asymmetric...recall

the relation between normal and shear stresses, **Equation 2.2**. In order to demonstrate the connection of stress state to the localized shear deformation and fracture process, we will first examine localized shearing observed in liquids followed by a discussion of shear localization in metals and granular materials. Finally, credible computer simulation of localized shear deformation will be discussed.

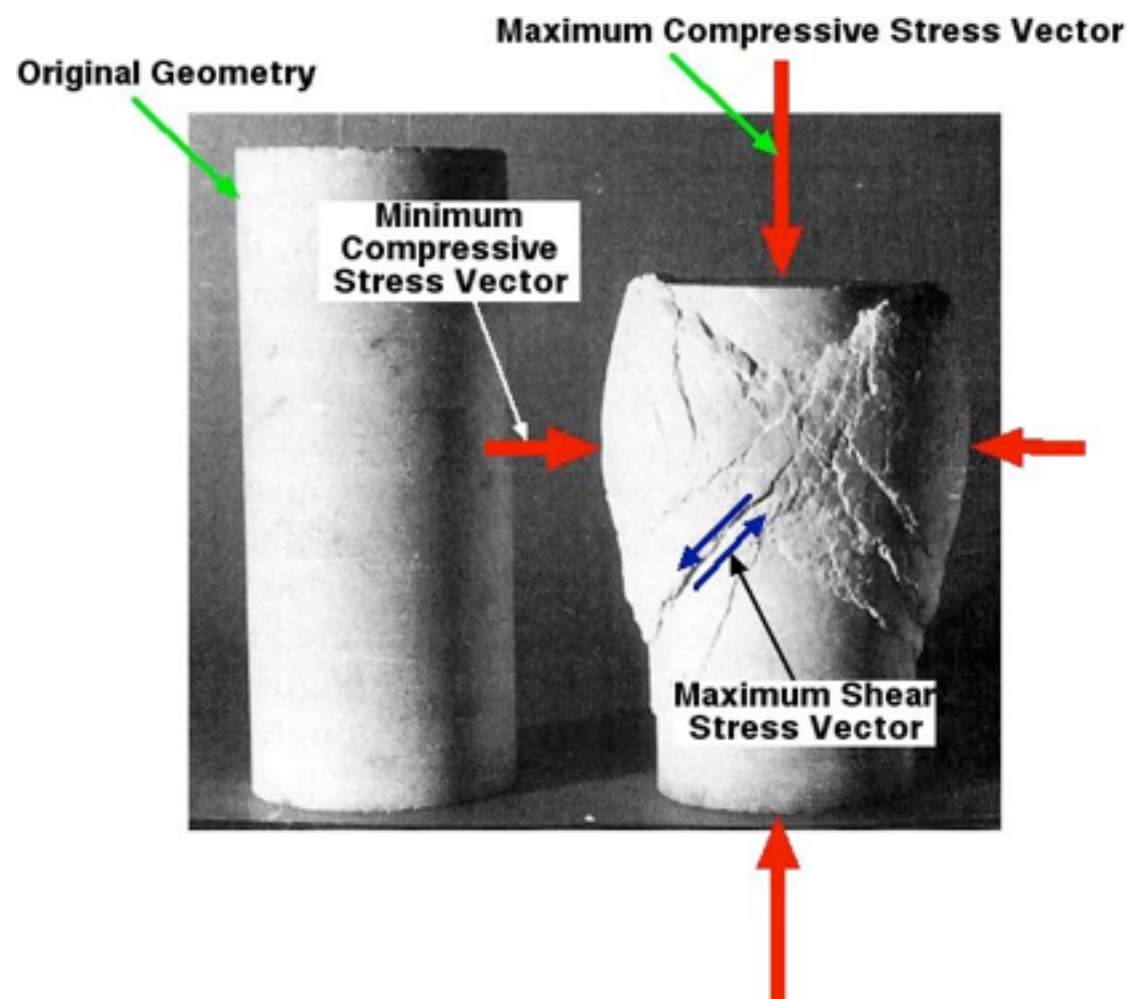


Figure 4.1 Deformation and fracture patterns produced on the surface of a marble cylinder produced by multi-axial, quasi-static compressive stresses. Original photograph from Tarbuck and Lutgens, 2005.

4.1.1 SHEAR LOCALIZATION IN LIQUIDS

Direct observations of shear localization in liquids are highly instructive for developing an understanding of the basic phenomenology that is directly applicable to flow behavior in solids. Shear localization phenomenology in a liquid has recently been graphically demonstrated in the laboratory at moderate strain rates by observing the flow dynamics inside liquid drops that impact the surface of relatively viscous liquids, Zhang, et al., 2011. These researchers used high-speed x-radiography to elucidate the response to the stresses induced inside drops of silicone oils during impact onto surfaces of identical liquids at velocities of 1 to 4 m/s under 0.17 and 1 atmosphere of air. Early stage phenomenologies are revealed in the high speed x-radiograph in [Figure 4.2](#) for an impact at ~ 1.6 m/s under 1 atmosphere of air. Two liquid sheets are seen being extruded radially and parallel to the original surface from inside the drop along periodic localized shear planes that have developed parallel to the target surface.

The two localized shear planes marked in [Figure 4.2](#) have formed inside the impacting drop shortly after contact with the target surface, and liquid has been extruded outward radially along both shear planes. The sharp images of these shear planes should not be confused with the diffuse bands which represent shadowgraphs of liquid that has already exited the impactor drop. The lower shear plane is thicker than the upper because it formed first: shear plane thickening progresses with time due to radial confinement of the material inside the shear plane. These shear planes that form in a viscous liquid

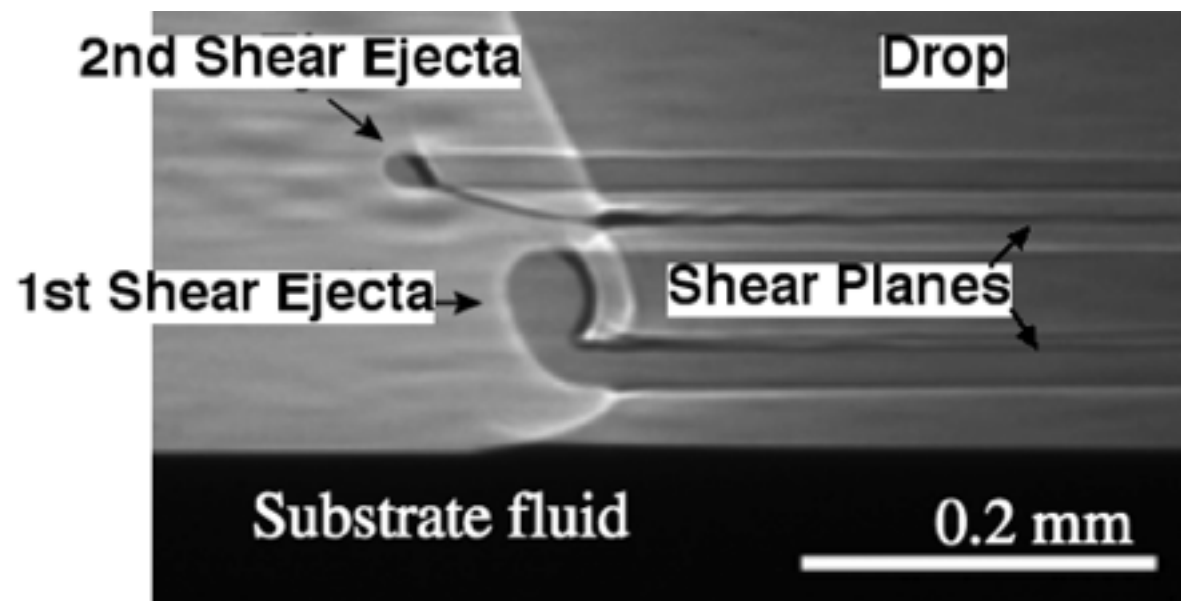


Figure 4.2 High speed x-radiograph of a silicone oil drop that has impacted the surface of the same fluid in 1 atm of air at ~ 1.6 m/s. The drop is moving downward in this radiograph. The original data were published in Zhang, et al., 2011.

at moderate strain rates are direct analogs to the those seen on the surface of the solid marble sample in [Figure 4.1](#) that was loaded asymmetrical at quasi-static strain rates...the loading inside the impacting liquid drop is also asymmetric. However if melting occurs inside these shear planes in a solid due to the heat generated by the deformation and fracture process, molten material can be extruded toward the free surfaces down the pressure gradients.

Surface tension and internal strength (atom-to-atom cohesion) in the shear ejecta curtain seen in [Figure 4.2](#) has caused the extruded ejecta to maintain an annular sheet of liquid that is exited the impactor drop. These circular sheets are terminated with a connected teardrop shaped structure. The downward progression of the impactor drop causes the surface of

the annuli to appear to turn upstream relative to the motion of the drop because outside of the impactor drop the shear ejecta sheet has lost forward momentum relative to that of the drop and is also drug up-range by the ambient atmosphere.

Eventually, circumferential stresses cause the annular ejecta ring to separate into periodically spaced droplets at the outer perimeter of the annular ejecta sheet. The droplets that form at the perimeter of shear ejecta sheets, a contact ejecta jet, and a primary crater ejecta curtain were recorded during impact of a silicone oil drop onto a flat surface of the same material under a reduced atmospheric pressure, Zhang, et al., 2011. High speed, sequential images that reveal the details of the phenomenology produced by the impact event are seen in [Figure 4.3](#). The “Jet Ejecta”, which are the dark zones below the ejecta from the “1st Shear” ejecta in [Figures 4.3\(a\)](#) and (b), represents the ejecta that is launched laterally when the impactor and the target surface make first contact...previously discussed in **Section 2.1.1**.

4.1.2 ADIABATIC SHEAR LOCALIZATION IN METALS

Adiabatic localized shear banding was first described in detail by Tresca, 1878. The essence of the results of his research is summarized in the Wikipedia entry on “adiabatic shear band:” “Tresca forged a bar of platinum (as well as many other metals); at the moment of forging the metal had just cooled down below red heat. The subsequent blow of the steam hammer, which left a depression in the bar and lengthened it, also reheated it in the direction of two lines in the form of a letter X.

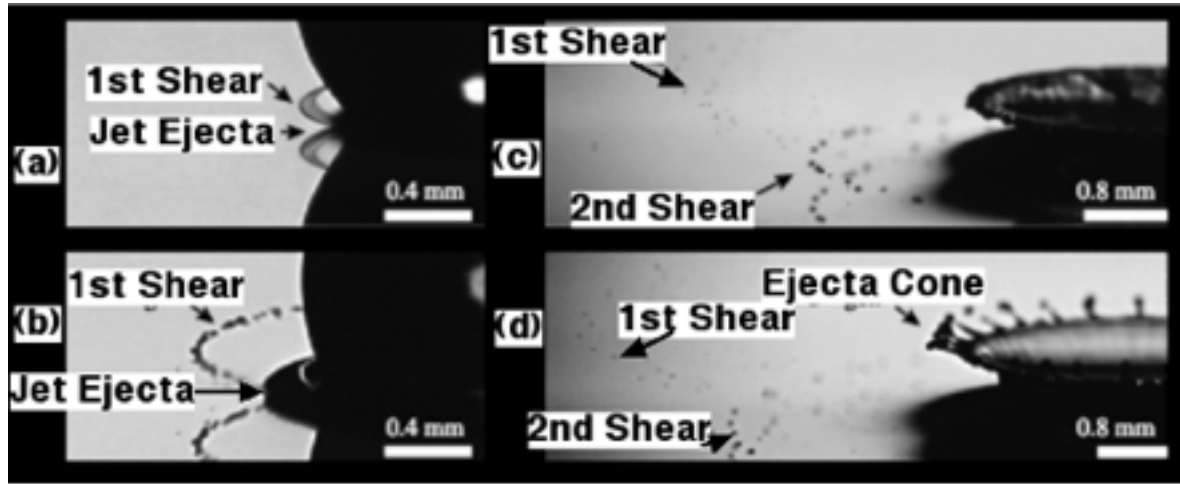


Figure 4.3 Impact of a silicone oil drop onto an identical silicone surface at ~ 5 m/s in 0.17 atm air. (a) 60 μ s, (b) 100 μ s, (c) 500 μ s, and (d) 700 μ s after impact. Original photo data from Zhang, et al., 2011.

So great was this reheating, the metal along these lines was fully restored for some seconds to red heat. Tresca carried out many forging experiments on different metals. Tresca estimated the amount of plastic work converted into heat from a large number of experiments, and it was always above 70%.” Evidence of this phenomenology is commonly observed in geologic materials though seldom if ever recognized.

Shear localization is observed during the deformation of metals over a wide range of strain rates displaying most of the resultant, characteristic structural details produced in solids. A graphic demonstration of high strain rate localized shear flow and fracture in ductile, polycrystalline metals is seen in [Figure 4.4](#). This polycrystalline titanium alloy, Ti-6Al-4V, sample was loaded under uniaxial compression at a high strain rate (4500/s) in a split Hopkinson bar apparatus, Lesuer, 2000. In this experimental setup, the orthogonal applied stresses, σ_1

and σ_3 relative to [Equation 2.2](#), are highly asymmetric with σ_3 being near zero during the deformation process. This is an illustration of the fact that failure has occurred at a shear stress of $\sim \sigma_1/2$. Also as observed in [Figure 4.4](#), the dominant shear fracture plane lies at 45° to the maximum normal stress vector, σ_1 . It should also be noted however that two small branches of the dominant fracture plane have developed along the major fracture plane...one on the left side of the top surface and the other near the center of the cylinder. Similar 45° local shear failure was also observed under high strain rate (5200/s) uniaxial tensile loading, Lesuer, 2000, illustrating the fact that localized shearing is independent of the sign of the normal stresses.

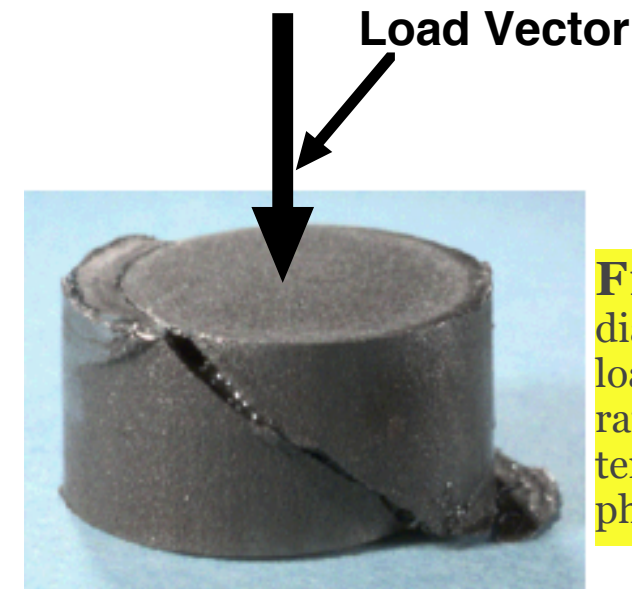


Figure 4.4 A 5-mm-diameter Ti-6Al-4V cylinder loaded uniaxially (σ_1) at a strain rate of 4500/s at room temperature. Original photograph from Lesuer, 2000.

In polycrystalline solids, significant shear localization is manifested at the grain (single crystal) level. For example, Lins, et al, 2007 have studied localized shearing in interstitial free steel, having an average starting grain diameter of 55 μ m, deformed in shear at strain rates up to 3200/s. As illustrated in

[Figure 4.5](#), large numbers of localized, periodic shear bands have been generated within individual grains. These grains were located adjacent to a large displacement shear band produced in a hat-shaped specimen during loading in a split Hopkinson bar apparatus. The Maximum Normal Stress Vector indicated in [Figure 4.5](#) is parallel to this large shear band whose track is slightly rotated from the sample loading vector (SD) due to the sample's geometry.

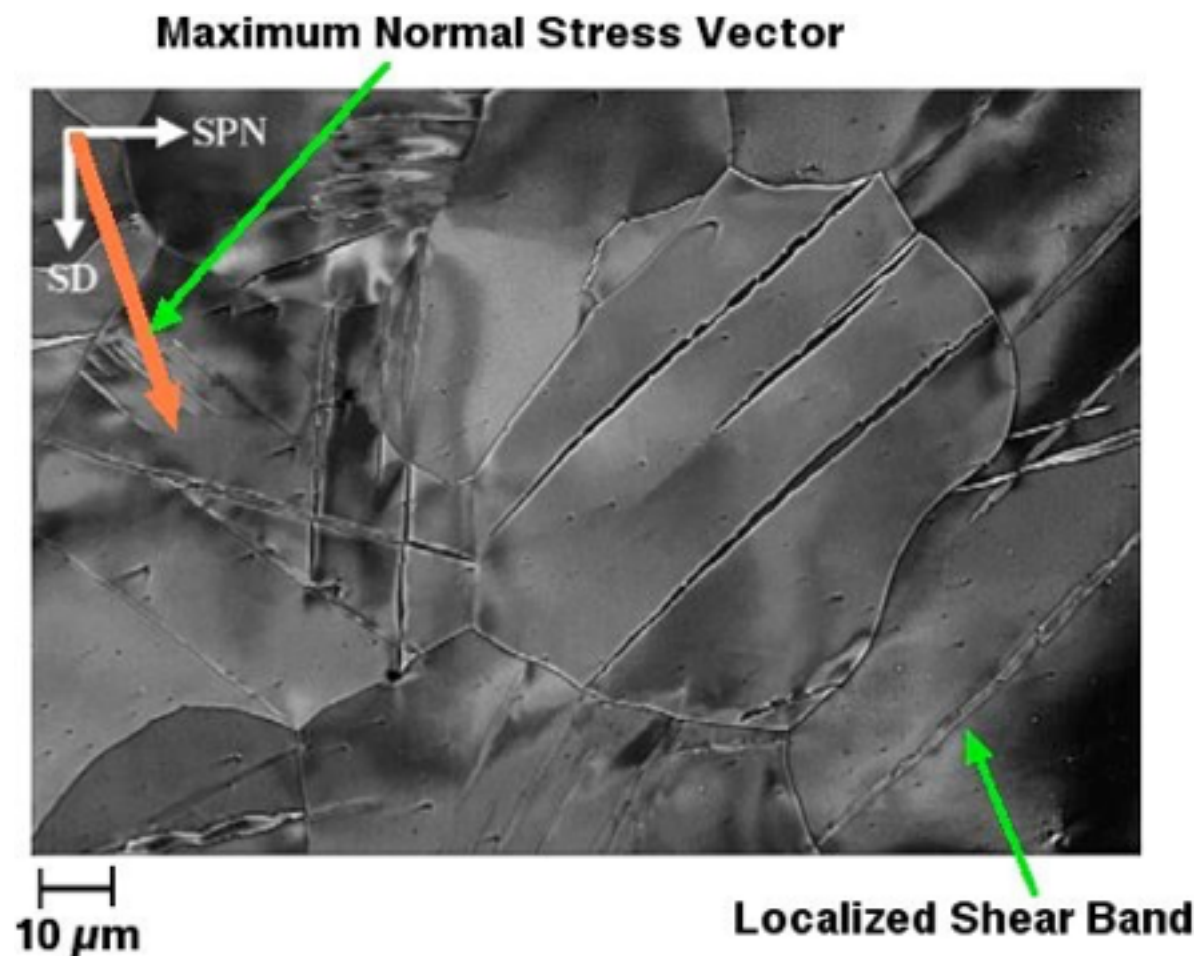


Figure 4.5 Scanning electron micrograph of grains in interstitial free steel located adjacent to a localized shear band that was formed at room temperature at a sample displacement rate of $\sim 3000/s$. Original image from Lins, et al, 2007.

A typical localized shear band that has developed across a grain is indicated in [Figure 4.5](#). It should be noted that this and other shear bands seen in the grains are oriented as expected relative to the Maximum Normal Stress Vector... $\sim 45^\circ$.

Small but measurable shear displacement is seen at the ends of several of the shear bands seen in the center of the frame in [Figure 4.5](#). The shear bands tend to not cross grain boundaries except where complimentary shear bands have developed in crystallographically favorably oriented adjacent grains.

The set of shear bands in the large grain in the center of the micrograph appear to have opened to form cracks. The cracks are expected to have formed by rebound during stress unloading at the end of the test; the residual stresses produced by slight grain rotation probably contributed to the opening of these cracks.

An extension of the fundamentals of shear band formation to structural features seen around hypervelocity impact craters is illustrated in [Figure 4.6](#) where typical morphological features of hypervelocity impact craters in low-ductility, high-strength-low-alloy (HSLA) steel (α -Fe) produced by a low density impactor are observed. As seen previously in [Figure 2.10](#), the 'plastic deformation zone boundary' indicated in [Figure 4.6](#) marks the surface at which the stresses in and around the peak of the shock front have dropped below the yield stress in this alloy...deformed grains were not observed beyond this boundary. The shape of this boundary also reflects that of the

shock front as its peak pressure falls below the quasi-static yield strength of HSLA steel.

Terraced walls generated by localized shear found inside of the crater cross-section in [Figure 4.6](#) are analogs to those observed in the full scale Earth Moon geologic crater Aristar-

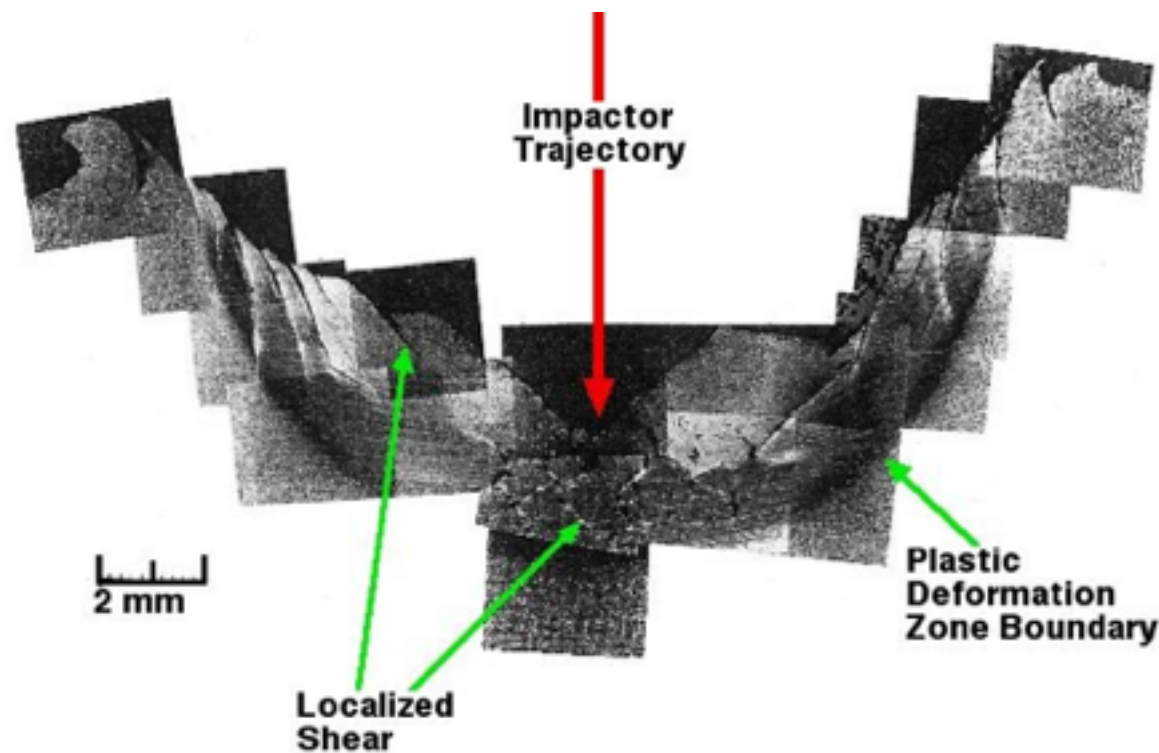


Figure 4.6 Crater cross-section in a high strength, low alloy steel plate produced by normal impact of a water-filled polycarbonate sphere traveling at 6.03 km/s. Original image from Shockey, et al., 1975.

chus...recall [Figure 1.3](#). The terraces seen in cross-section in [Figure 4.6](#) are separated by localized, periodic shear cracks along the crater walls. The localized shear band pattern observed below the bottom of the crater illustrates the formation of complimentary shear planes under asymmetric, confined compressive loading.

In crystalline solids, localized shear is initiated on the closest packed crystallographic planes in directions where the lowest shear strength in the crystal is found. For example, experimental data from high rate (4000/s) compression tests on single crystal copper samples that had been previously subjected to cyclic stresses clearly indicate the correlation between crystallographic planes and localized shear deformation, Li, et al, 2006. Their data show, that when localized shear bands form, the loaded axis of the single crystals rotate toward the [011] pole which is associated with the easiest shear direction in face-centered cubic (FCC) crystals...on the {111} planes.

Localized shearing occurs when the maximum stress is either tensile or compressive. Preferential shearing of favorably oriented grains under tension has also been graphically demonstrated during the early stages of slow bending of a polycrystalline continuous-cast aluminum-magnesium alloy sheet, Davidkov, et al., 2012. Localized, periodic shear banding is seen inside the favorably oriented grains in [Figure 4.7](#) that are under tension, and the vast majority of the shear bands lie close to 45° to the maximum (tensile) stress vector, σ_1 , as expected. Complimentary, 90° shear bands are also seen in this micrograph demonstrating that high plastic strain rates are not a necessary condition for shear localization in metals.

As the plastic strain increases on the outer circumference of the bend, gross shear banding develops and progresses at 45° to the maximum stress vector which is applied normal to the inner radius of the bend. This phenomenon is further illustrated in [Figure 4.8](#). Displacement along the resultant shear

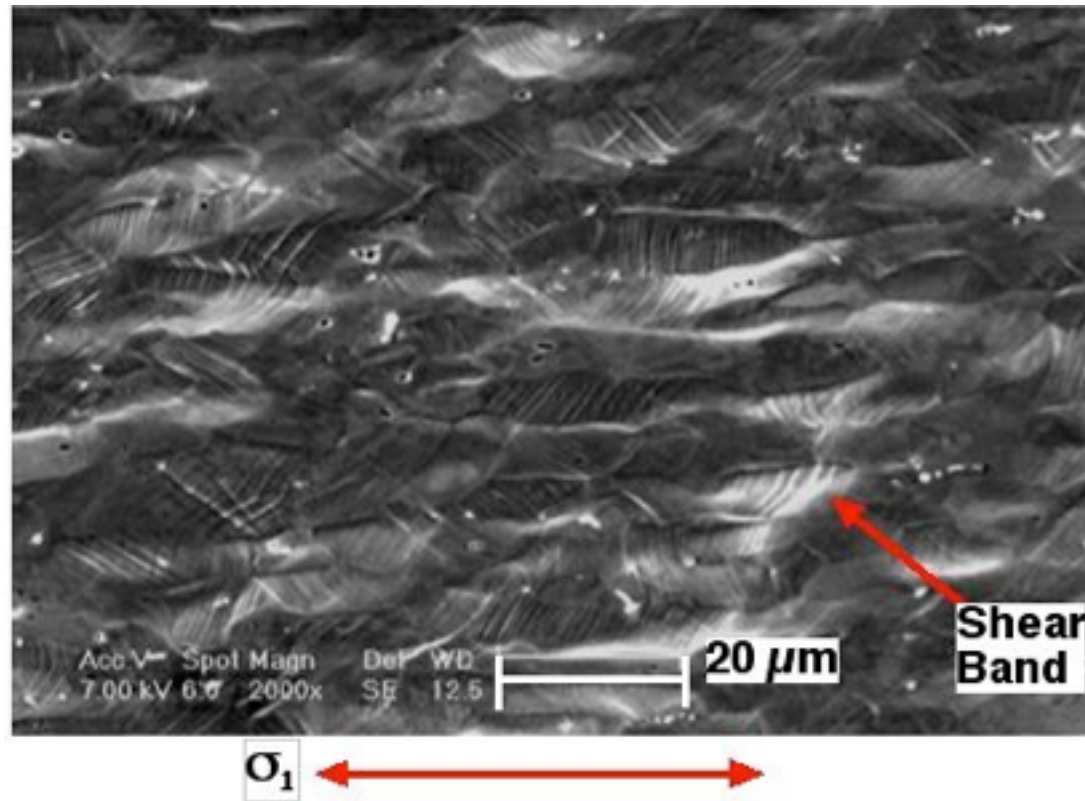


Figure 4.7 Scanning electron micrograph of a surface area that lies near the outer radius of a bent sheet of continuous-cast Al-Mg sheet. A typical localized shear band is indicated. Original image from Davidkov, et al., 2012.

planes produces a series of complimentary parallel cracks that have traveled approximately 45° to tangents to the outer circumference of the bend which are parallel to the maximum tensile stress vector. These cracks ultimately open because the maximum stress vector is tensile. The shear-produced triangles seen in [Figure 4.8](#) along the outer circumference of the bend protrude from the surface toward the viewer due to the Poisson effect acting on the rest of the bending sheet. This triangular pattern is analogous to that previously noted on the perimeters of the secondary craters of both the Upheaval Dome and Vredefort Dome.

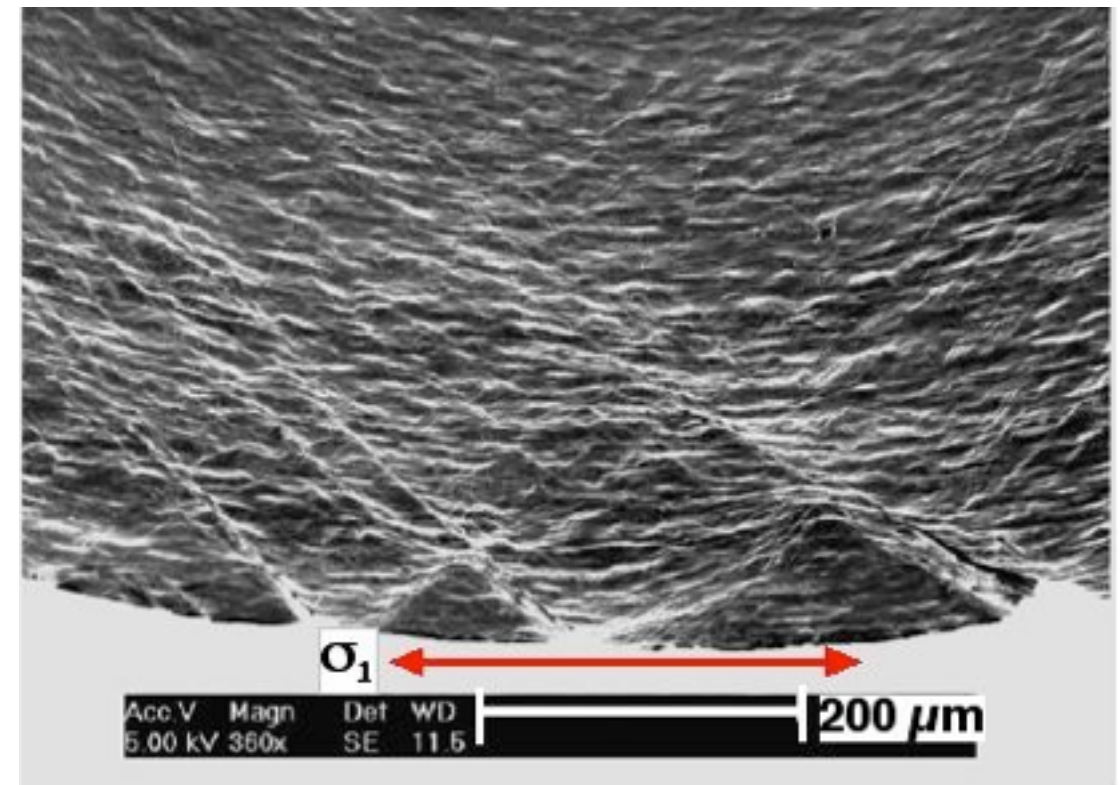


Figure 4.8 SEM image of the surface that lies normal to the outer radius of a bent sheet of continuous-cast Al-Mg sheet. Original image from Davidkov, et al., 2012.

4.1.3 LOCALIZED SHEAR BRANCHING

As we have seen in the previous examples, ordered branching of shear planes is a deformation feature generally associated with localized shear in solids...especially under the asymmetric compressive loading generated around a hypervelocity impact crater. Major and minor branching on the complementary shear planes is illustrated in [Figure 4.9\(a\)](#), especially inside the circle. As is seen in [Figure 4.9\(a\)](#), typical heterogeneous deformation is prominently exhibited in the microstructure below a hypervelocity impact crater in a high strength titanium alloy, Ti-5Al-2.5Sn, Lundberg, et al, 1982. Asymmetric

compressive loading was produced in a zone surrounding the impact crater during the later stages of crater formation. The cross-hatch patterns seen in the microstructure represent surface manifestations of intersecting (branching) shear planes... analogous to the cross-hatch pattern on the surface of the marble sample in [Figure 4.1](#). A similar cross-hatch pattern is also prominently displayed on the bottom surface of this particular impact crater... [Figure 4.9\(b\)](#). Similar cross-hatch patterns

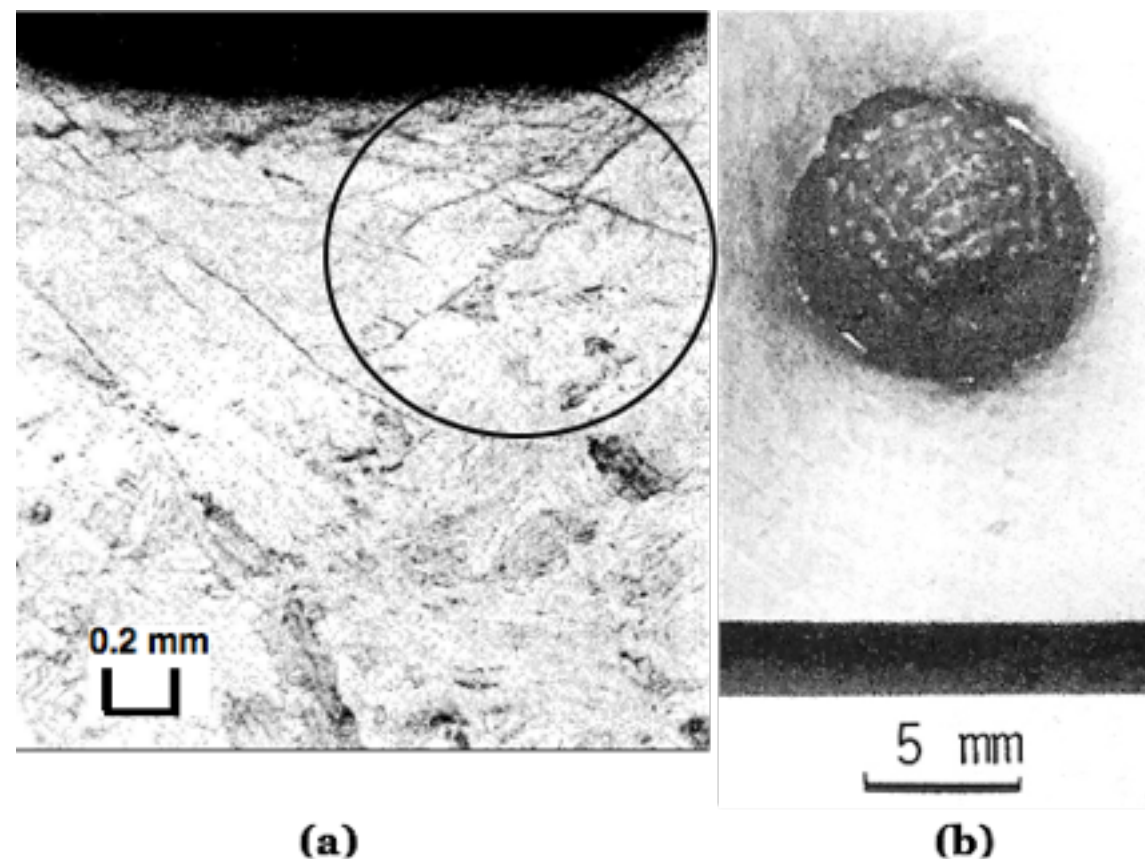


Figure 4.9 Microstructure (a) of Ti-5Al-2.5Sn on a polished and etched centerline cross-section located below the impact crater bottom formed by a 1.56-mm-diameter copper sphere traveling normal to the target surface at 6.96 km/s; (b) overhead view of the crater bottom. The target was heated to 775 K prior to impact. Original photographs from Lundberg, et al, 1982.

have been observed on the floor of a 75-km-diameter impact crater on Mars, Head and Mustard, 2006.

4.1.4 LOCALIZED SHEAR BAND THICKENING

This broadening of shear bands is a basic localized shear process that can develop when stress states are near hydrostatic... $\sigma_1 \approx \sigma_2 \approx \sigma_3$. Because both the peak radial compressive, σ_1 , and confinement stresses, σ_2 and σ_3 , are very high in the material around the inside surface of a forming impact structure during the early stage of the cratering process, the deformed and fractured materials that have not been ejected from the crater remain strongly confined within their original formations, but σ_1 is still greater than either σ_2 or σ_3 . Due to the strong confinement of the stresses around an impact crater, shear displacement is strongly inhibited along all possible resolved shear planes. Consequently rather than produce significant shear displacement along the resolved shear planes or develop branches, the thickness of the shear planes expand normal to the maximum shear stress vector, τ_{\max} .

4.1.5 LOCALIZED SHEARING IN GRANULAR MATERIALS

Understanding the mechanical behavior of granular materials is fundamental to understanding the mechanical behavior of those geologic materials that are made of poorly bonded particles or contain significant porosity, such as sedimentary rocks and soils. As noted by Walley, 2012, localized shear bands are commonly observed in a wide variety of granular materials that are exposed to confined compressive stresses when τ_{\max}

(recall **Equation 2.2**) exceeds the shear strength of the component grains or the intergranular bonding between them.

When shear localization starts at room temperature at quasi-static strain rates, a material made up of moderately bonded brittle grains such as sandstone, grains within the shear line fracture and become highly comminuted. This phenomenology is graphically illustrated in [Figure 4.10](#) for quasi-static compressive loaded sandstone. A damage zone (i.e. fluidized zone) extends beyond and parallel to the comminuted zone inside of the shear band. Comminution of the grains within the shear band also leads to a local, physical densification of the sandstone. A close examination of the *Comminuted Zone* reveals a distinct zigzag pattern which indicates shear branching within the main shear band as deformation and fracture progresses.

Individual grains and grain fragments seen in [Figure 4.10](#) inside the *Damage Zone* display periodic, localized shear deformation. Shear bands are also visible in several grains outside of the *Damage Zone*. The damage zone indicated in [Figure 4.10](#) infers the microstructure inside the localized shear bands seen in marble in [Figure 4.1](#). Actually, the overall structure of the damage zone seen in [Figure 4.10](#) is very similar to that seen in and around a typical earthquake fault...e.g. the San Andreas Fault, Wenk, et al., 2011. This strongly suggests that earthquakes can be initiated by the development of localized shear.

Data on localized shearing over a wide range of strain rates in reactive and granular materials has been recently reviewed by Walley, 2012 where it is mentioned that Lade and Wang, 2001 concluded that shear banding is observed in sand for the normal (orthogonal), multiaxial stress conditions:

$$0.18 \leq (\sigma_2 - \sigma_3)/(\sigma_1 - \sigma_3) \leq 0.85 \quad 4.1$$

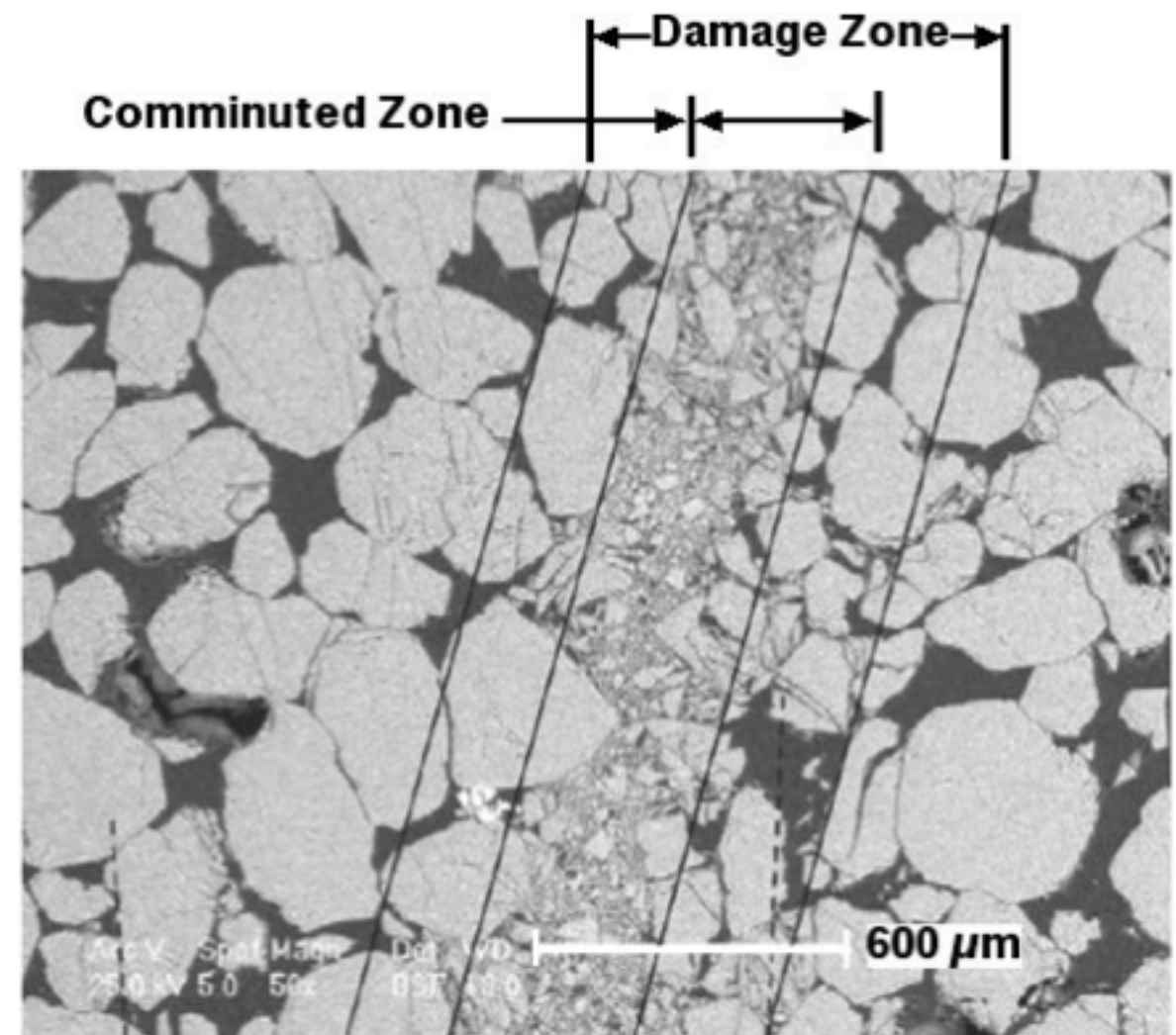


Figure 4.10 Microstructure of a shear band in sandstone that was compressed quasi-statically with a constant confining pressure...monotonically increasing σ_1/σ_3 . Original photomicrograph from El Bied, et al, 2002.

This inequality defines limits to the parameters in **Equation 2.2** relative to the mechanical behavior of sand under triaxial compression. The only other reference to stress state presented in Walley, 2012 indicates that shear localization in sand can occur over a wide range of confined compressive stresses.

The data indicate that inert granular materials generally start to deform by localized shearing within the grains rather than inter-particle shearing or sliding. Frictional heating between the newly formed surfaces of comminuted fragments in shear zones in brittle materials can contribute to the overall heating, but generally the amount of heating due to deformation and fracture in individual grains far exceeds that caused by interfacial friction...largely due to the fact that global shear displacement under confined compression is quite limited which will generate minimal friction heat compared to the large amount of energy released by local deformation and fracture of the individual grains.

4.1.6 COMPUTER SIMULATION OF LOCALIZED SHEAR DEFORMATION

Numerical simulation of shear branching has been achieved with a reasonable degree of agreement with observed behavior using a variety of computer models. For example, Dolinski, et al, 2010 used energy related failure criteria that was added to a version of a commercial, finite element stress analysis code,

“Abaqus/Explicit.” Their computations produced the shear branching seen in [Figure 4.11](#). This computational model replicated a specimen with a fixed base loaded in uniaxial compression at a velocity of only 25 m/s. The localized shear seen at the 45 μ s interval results from the resolved shear stress produced by the compressive loading...recall **Equation 2.2**. The sequential results presented in [Figure 4.11](#) are separated in time by only 2 μ s, and complete fracture was indicated along the shear planes in the following time step producing a kinked

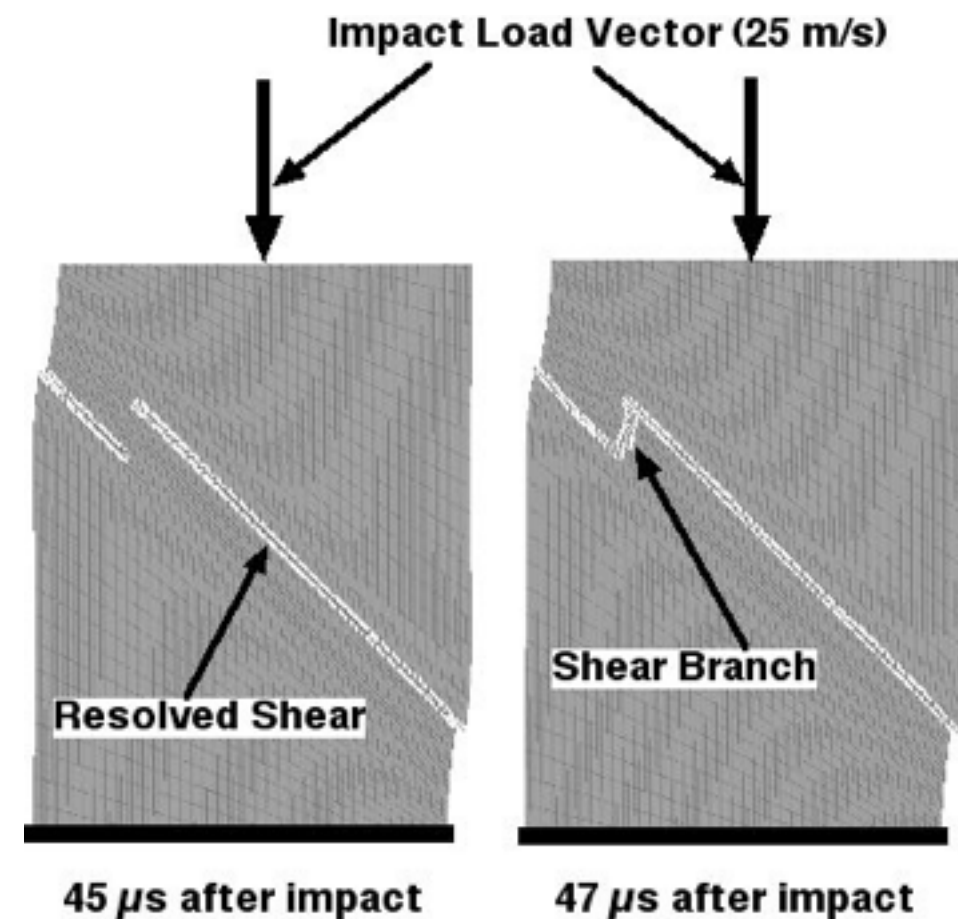


Figure 4.11 Computer simulated shear branching due to compressive impact in a solid with mechanical properties similar to an aluminum-magnesium alloy, AM50. Original image from Dolinski, et al, 2010.

fracture line much like that previously discussed for resolved high strain rate shearing in Ti-6Al-4V...[Figure 4.4](#).

Periodic, localized shear banding has been simulated at slow shear strain rates in Cu₅₇Zr₄₃ bulk metallic glass (BMG), Ogata, et al., 2006, a material that exhibits modest ductility. The results of numerical molecular dynamics simulations of quasi-static, pure shear deformation at 0 K inside this BMG are presented graphically [Figure 4.12](#). The periodicity of the localized shear starts appearing in the image of the smallest shear deformation strain presented...see [Figure 4.12](#), $\gamma=0.12$. All of the shear bands that are periodic in the z-direction appeared simultaneously during the computation, Ogata, et al., 2006. The period of the shear bands does not change with increasing total shear strain, but the thickness of the individual shear bands increases with total strain similar to that observed for liquids...recall **Section 4.1.1**.

The results of the simulations of shear localization in Cu-Zr BMG also indicated that shear deformation induces stresses normal to the shear plane as well as transverse normal stresses in the shear plane, Ogata, et al., 2006. This computational phenomenon is consistent with the observed Poisson Effect seen on the surface of the bent aluminum alloy specimen in [Figure 4.8](#).

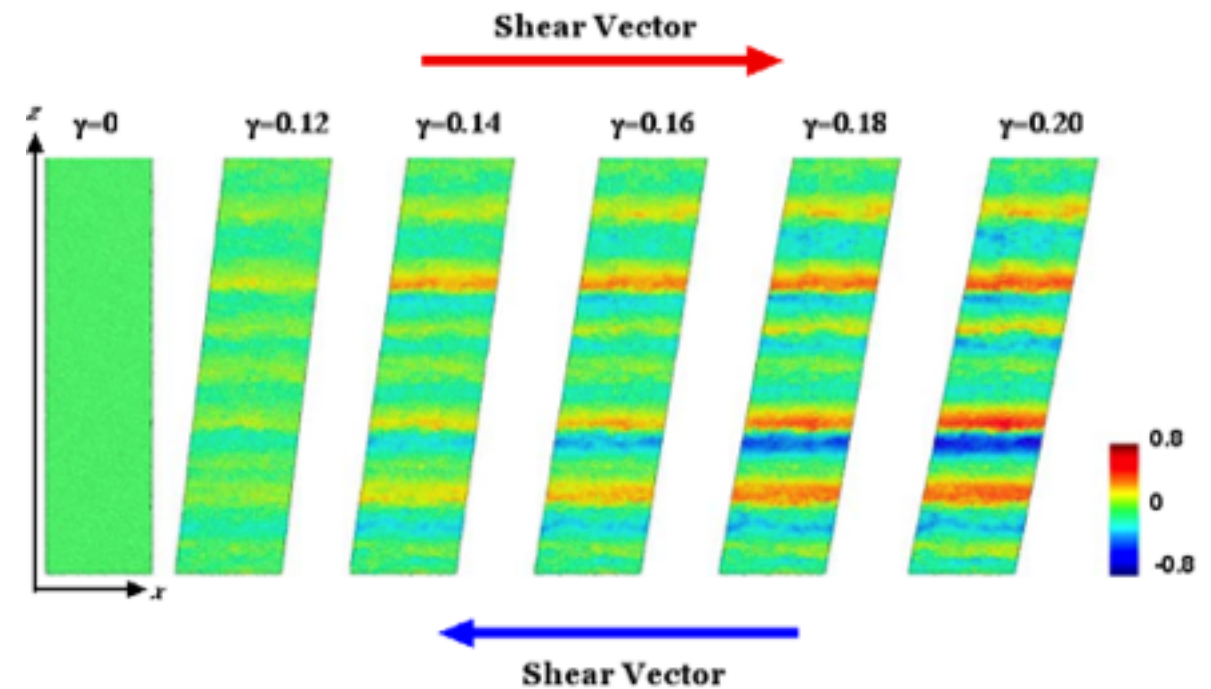


Figure 4.12 Two-dimensional (x-z) view of the results of computer simulation of pure shear strain, γ , in a rectangular Cu-Zr bulk metallic glass specimen with x, y, z dimensions 26.36 x 3.24 x 104.38 nm that contained 524,288 atoms. Colors indicate relative inelastic shear displacement in nanometers along the x-direction. Original image from Ogata, et al., 2006.

Adiabatic Localized Shear

SECTION TOPICS

4.2.1 Adiabatic Shear Deformation in Metals

4.2.2 Rock Deformation at High Temperatures

4.2.3 Localized Shear and Chemical Redistribution

4.2.4 Localized Shearing in Silicate Crystals

As previously discussed in **Section 4.1.2**, it has long been known that significant heating occurs during the deformation and fracture processes in solids due to energy released from atomic bond stretching or breakage...even at quasi-static strain rates. The dispersion of the heat generated by local deformation and fracture is controlled by the material's thermal diffusivity and heat capacity. (Thermal conductivity equals the product of thermal diffusivity and heat capacity.) Because geologic materials tend to be poor heat conductors, the heat generated by deformation and fracture along localized shear planes in these materials is effectively retained (adiabatic heating conditions) within the developing narrow, periodic and branched shear zones inside a stressed body over a wide range of strain rates. Temperatures within the shear zone during deformation can far exceed the softening or melting temperatures of the host solid...see for example Chen, et al., 1997. The resultant localized shear planes seen intersecting on sectioned or naturally exposed surfaces are frequently referred to as *adiabatic shear bands* (ASB's).

4.2.1 ADIABATIC SHEAR DEFORMATION IN METALS

Partly because of the metal's relative low thermal conductivity, melting was commonly observed in titanium (melting point=1941 K) on shear planes exposed around the inside of hypervelocity impact craters, Lundberg, et al, 1982. Beads and smooth, irregular shapes structures formed from melted target material are indicated in [Figure 4.13](#) on the inside surface of a hypervelocity impact crater generated in a titanium alloy, Ti-6242-Si. These features lie on the surfaces of facets

that were formed by shear fracture during impact crater excavation.

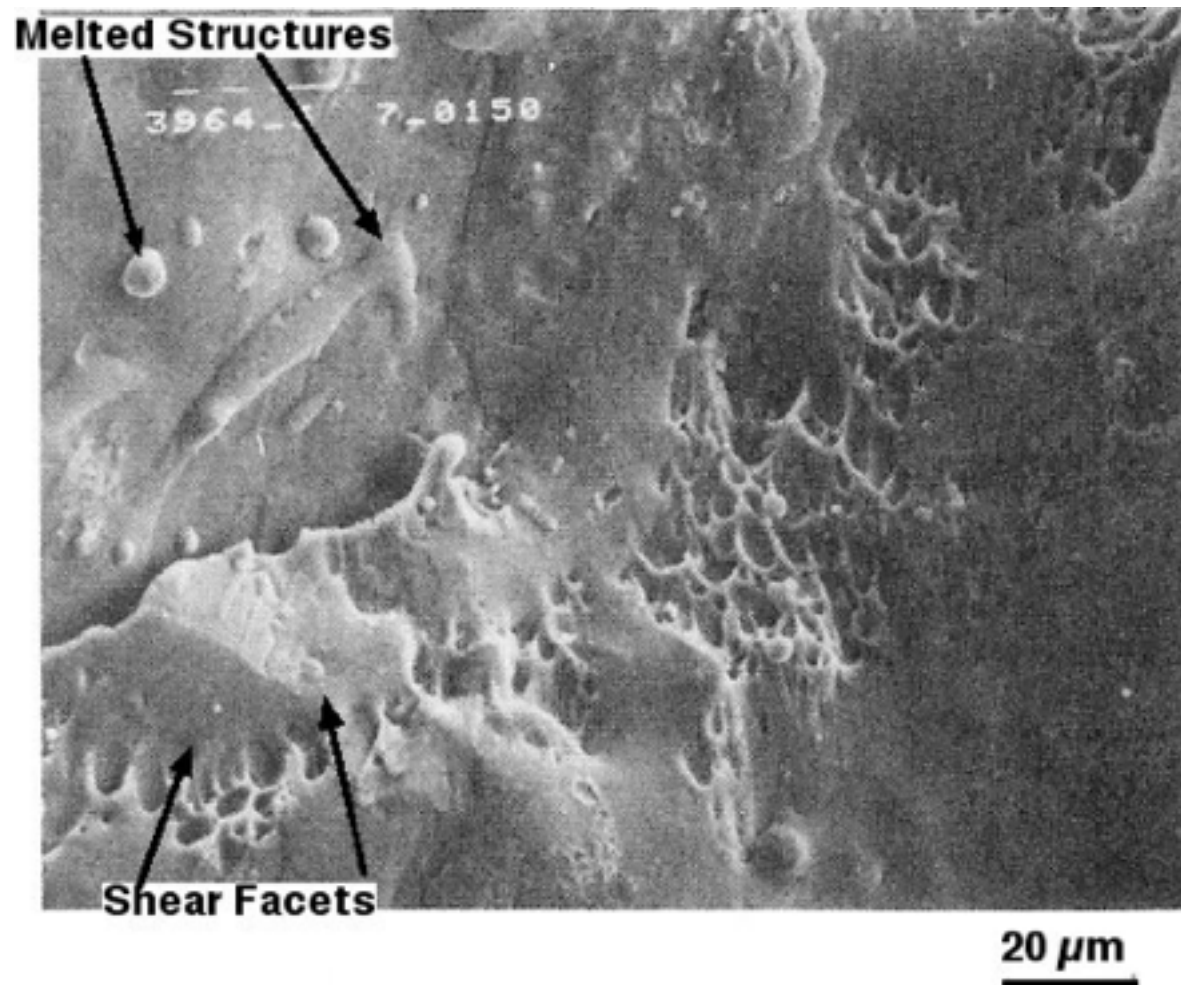


Figure 4.13 Bottom surface of a crater formed by a 1.5-mm-diameter copper sphere traveling at 6.96 km/s in Ti-6242-Si maintained at 775 K. Original photomicrograph from Lundberg, et al, 1982.

The band of dimple structures seen below the shear facets are formed by void development and coalescence that is commonly observed on fracture surfaces of metals. Shear deformation studies on carbon steels clearly indicate that voids formed during plastic deformation grow and produce the dimples at failure like those seen in [Figure 4.13](#), Lee, et al., 2008.

Their data also clearly show that voids coalesce on shear planes to form cracks.

Incidentally, it has been shown that solid explosives are detonated via the local heating produced on local shear planes, and a wide variety of chemical reactions are initiated or enhanced along shear bands due to the heating associated with localized shear deformation, Walley, 2012.

4.2.2 ROCK DEFORMATION AT HIGH TEMPERATURES

In general rocks are brittle at room temperature, but at high temperatures, the melting behavior of rocks is strongly dependent upon their chemical composition. For example, carbonate rocks generally melt at a unique temperature, while silicate rocks transition to a liquid state over a wide temperature range. Silicate igneous rocks, such as granite, melt quite heterogeneously partly due to the fact that they generally contain many different, discrete mineral crystals that melt at a variety of temperatures.

Silicate rocks generally form glasses when completely melted, and these glasses exhibit progressive softening and reduced viscosity with increasing temperature. The homogeneous viscous flow rate (shear strain rate), dy/dt , of glasses formed from silicate rocks due to an imposed shear stress, τ , is described simply below:

$$dy/dt = \tau/\eta \quad 4.2$$

As illustrated in [Figure 4.14](#), the coefficient of viscosity, η , depends strongly on both the silica content of the rock glass and temperature...basalt has lower silica content than sandstone.

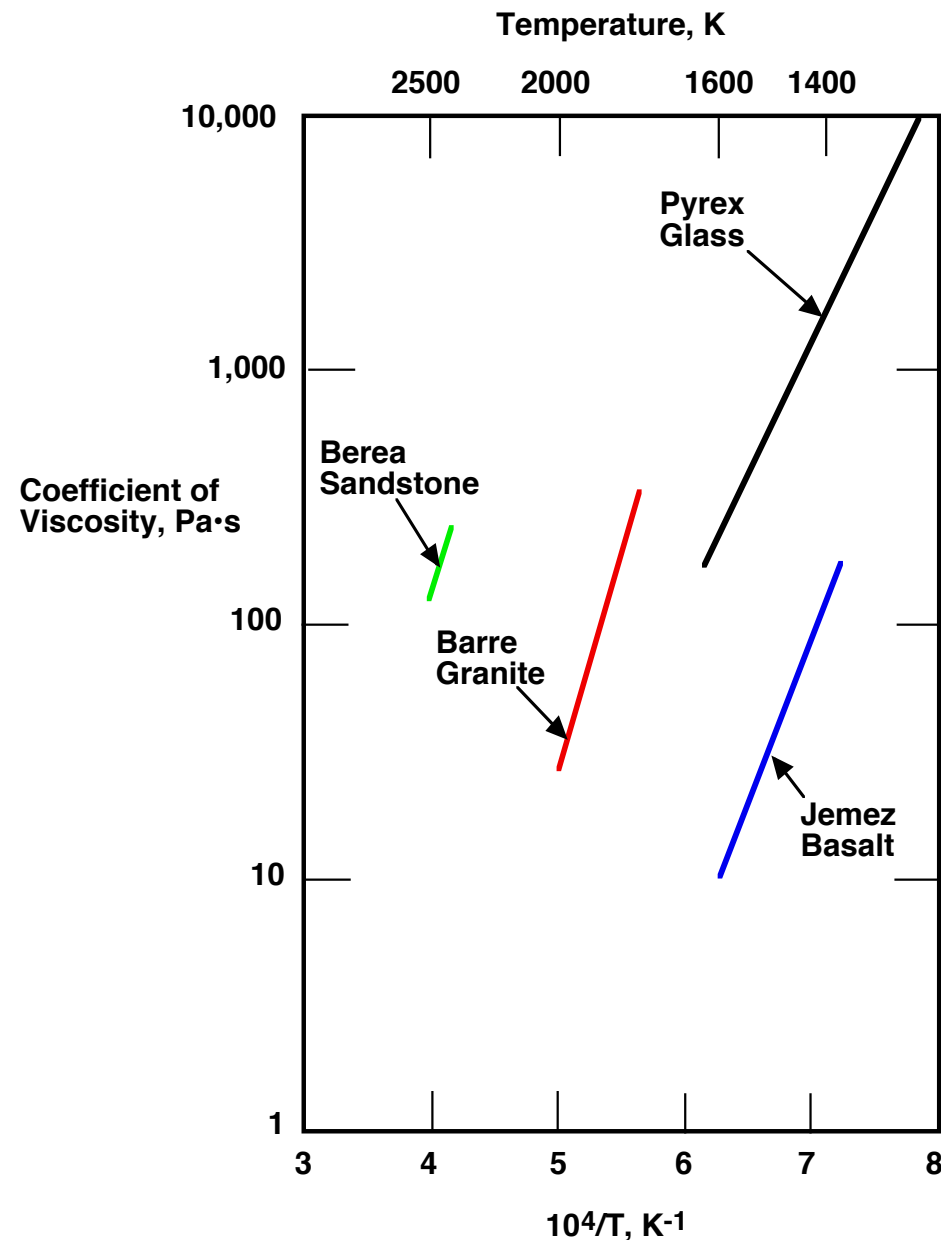


Figure 4.14 Data on the effects of temperature and silica content on coefficient of viscosity of silicate rock glasses, Lundberg, 1975.

According to the data presented in [Figure 4.14](#), a typical basalt at 1 atmosphere pressure does not achieve a viscosity comparable to that of water at room temperature until the lava has been heated to to the neighborhood of 2500 K...the viscosity of water at room temperature and 1 atmosphere is 1 mPa·s.

It is estimated that temperatures in this range are not general found in the Earth's crust until depths greater than about 200 km are reached, Tarbuck and Lutgens, 2005. It is also important to note that bulk rock viscosities will be much higher at depth due to the fact that viscosity generally increases with pressure.

Localized heating associated with localized shear will cause considerable bulk structural weakening in rock structures. Generation of ASB's in solid rock can result in an apparent local 'fluidization' that can produce bulk 'plastic' deformation in large geologic structures. Some of the results of this fluidization in full-scale geologic substructures will be discussed in the next chapter.

4.2.3 LOCALIZED SHEAR AND CHEMICAL REDISTRIBUTION

Heat sufficient to 'melt' silicate rocks can be produced in the localized shear bands during high rate deformation, and high-temperature chemical redistribution inside and around shear bands can result. For example, Langenhorst, et al, 2002 loaded an olivine single crystal using an explosively driven apparatus that promoted shear deformation. Thin sections of localized shear bands produced in the sample were examined using scanning transmission electron microscopic (STEM) tech-

niques. Data derived from these examinations demonstrate that localized shearing causes localized heating leading to melting, glass formation, chemical redistribution, and recrystallization in single crystal olivine.

A typical microstructure of a cross-sectional view of the inside of a shear band is seen in the micrograph presented in [Figure 4.15](#). A glassy phase seen in the center of the shear band is rimmed by very fine, rounded grains which appear to be partly or completely surrounded by the glassy phase. The glassy phase was also seen at triple points of larger grains found inside shear bands. Holes seen in the glassy phase could represent shrinkage voids created during the subsequent cooling and solidification in the shear band, or they could represent micro-voids that are well known to form in solids or semi-solids during plastic deformation. The rounded shape of these rim 'nano-grains' suggests that these grains are in the process of being incorporated into the glass melt rather than crystallizing from the melt as proposed by Langenhorst, et al, 2002.

The chemical compositions of the cores and rims of grains and the glassy phase inside these shear band microstructures are listed in **Table 4.1**. These data indicate that there has been considerable elemental micro-redistribution resulting from the extreme local heating during the formation of the localized shear bands. The data also indicate that iron, calcium, manganese, and nickel are migrating from the host olivine to the glassy phase much more than magnesium. Migration of these

particular elements into the glassy phase will tend to lower its viscosity at high temperatures...recall [Figure 4.14](#).

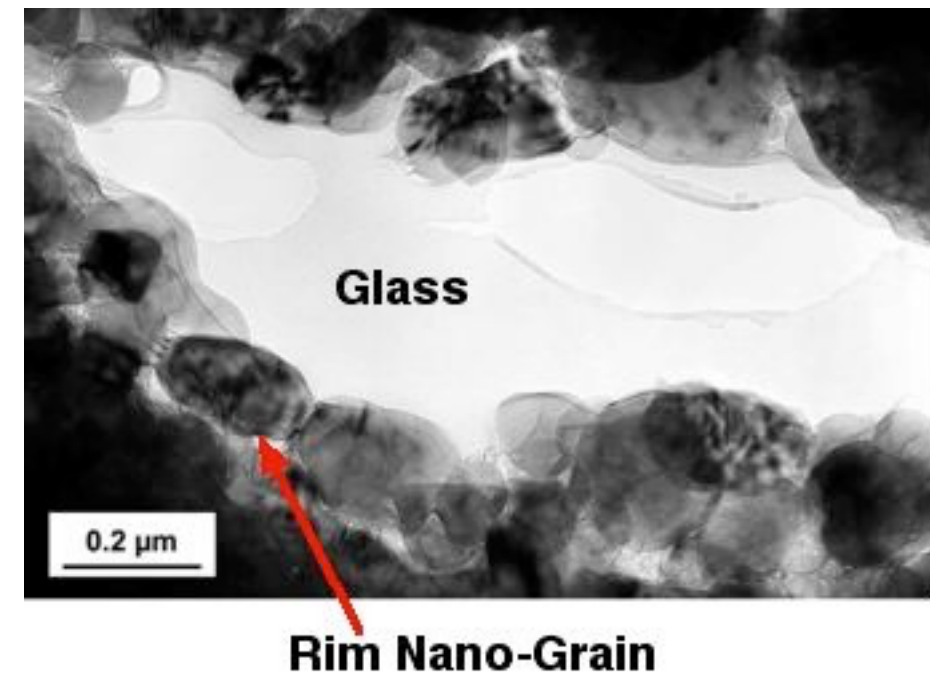


Figure 4.15 Transmission electron micrograph of the cross-section of a shear band in shocked olivine. Original micrograph from Langenhorst, et al, 2002.

The macro-scale chemical data published by Lieger, et al, 2011 for the similar structural features found in pseudotachylites, impact breccia, and dikes found in the Vredefort Dome impact structure are wholly consistent with the micro-scale chemical data found in Langenhorst, et al, 2002. For example, comparing the relative heights of the atomic spectral peaks in the left side of [Figure 4.16](#) with those in the graph on the right side shows that experimental data from Lieger, et al, 2011 indicates iron enrichment and magnesium depletion in a shear branch in a granitoid collar-wall-rock from the Vredefort Dome impact structure. This is consistent with the comparison of the chemical compositions listed in **Table 4.1** for the host olivine and the glassy phase produced by impact shear loading. (The *data* contradict the *statement* in Lieger, et al., 2011

Table 4.1 Chemical composition of shocked olivine.
Original data from Langenhorst, et al, 2002.

Element	Host Olivine Atom Fraction	Grain Core Atom Fraction	Grain Rim Atom Fraction	Glass Atom Fraction
Si	0.1420	0.144	0.1428	0.1461
Fe	0.0306	0.0166	0.0631	0.1922
Mg	0.2544	0.2667	0.2197	0.0801
Ca	0.0005	0	0.0022	0.0059
Mn	0.0004	0.0004	0.0008	0.0019
Ni	0.0007	0.0007	0.0008	0.0018
O	0.5713	0.5716	0.5706	0.5721

that the chemical composition of these two phases are “identical.”) Chemical redistribution in these geologic materials resulting from localized shearing due to confined compressive loading is a real, significant and scalable phenomenon. Differential melting in igneous rocks derived from the presence of phases with widely differing melting temperatures also contributes to the chemical redistribution process.

The chemical migration is controlled by both high temperature thermochemical and thermophysical behavior of these chemical systems and the local stress state. However, Lieger, et al, 2011 did not recognize these fundamental aspects to the formation process for pseudotachylite, impact breccia, and dikes, so they concluded that the difference in chemical composition was attributed to intrusion of matrix materials, found in these impact substructures, which was derived from ‘impact melt’ that is commonly observed on the inside surface of an impact crater.

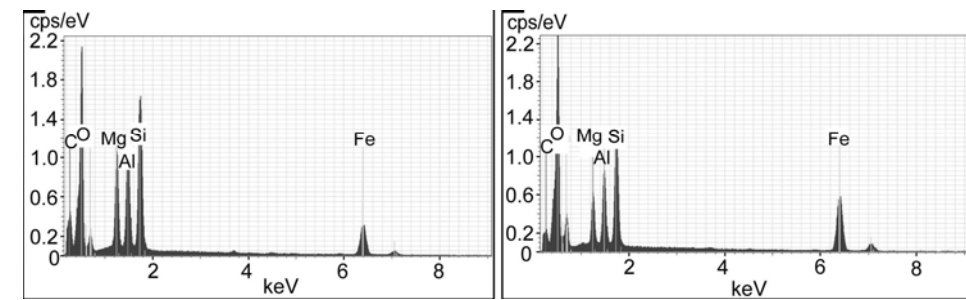


Figure 4.16 Elemental spectral intensity data from a pseudotachylite vein (left) matrix and (right) a shear branch in a granitoid collar-wall-rock from the Vredefort Dome impact structure. Data produced with a scanning electron microprobe (SEM) analysis of the phases found in and around an ‘apophysis’ in a petrographic thin section taken from a wall rock and reported in Lieger, et al, 2011.

4.2.4 LOCALIZED SHEARING IN SILICATE CRYSTALS

Localized, periodic shearing in quartz crystals during crater formation produces features commonly referred to as planar deformation features, PDF’s. The observation of PDF’s in silicate rocks has been used to verify geologic impact structures on Earth. An extended discussion of PDF’s in quartz can be found in French, 1998, but due to his assumption of an incorrect cratering model and a lack of understanding of the effects of localized shearing in silicate rocks, the obvious connection of the formation of PDF’s to the physical and mechanical behavior of real geologic materials is missing from his discussion.

Localized melting in single crystal quartz has been observed as a result of shock loading in a confined compression environment, Fiske, et al., 1995. Their data indicate that shock compression induced local temperatures in quartz can exceed 2000 K.

Considerable data on the details of localized shearing in zircons from the Vredefort Dome crater complex can be found in

Erickson, et al., 2013. In order to further illustrate the response of crystalline solids to mechanical stresses produced around geologic impact structures, a sample of their data presented in [Figure 4.17](#) is analyzed relative to the fundamentals of mechanical behavior of real materials that have been discussed in this chapter.

4.2.4.1 LOCALIZED SHEARING IN ZIRCON CRYSTALS

Zircon (ZrSiO_4) crystals crystallized in igneous rock are commonly utilized for radioisotopic-dating of the host material. However, the derived formation dates of the bodies in which they are found are based on the assumption that the zircons used for dating were crystallized at the time of the impact event. When localized shearing is observed in zircon crystals removed from dikes or similar impact related substructures, the dates determined from isotopic decay analysis may indicate that crystallization occurred as a result of a prior impact event. On the other hand, the data published by Erickson, et al., 2013 reveal the shear patterns that are typical of crystalline solids deformed at high rates under asymmetric compression regardless of their formation date.

High magnification images of an oriented zircon crystal removed from colluvium found in the center of the Vredefort Dome impact structure are seen in [Figure 4.17](#). These images were produced by a variety of analysis techniques and irradiations in order to reveal the internal structural details using visible light, cathodoluminescent emission (CL), electron backscattering (EB), and electron backscattering diffraction (EBSD). The (100) plane of each of these tetragonal crystals lies in the plane of each 2-dimensional image in the figure; the crystallographic orientations of the shear planes visible in these images were determined using EBSD. In spite of the fact that this crystal was found intact,

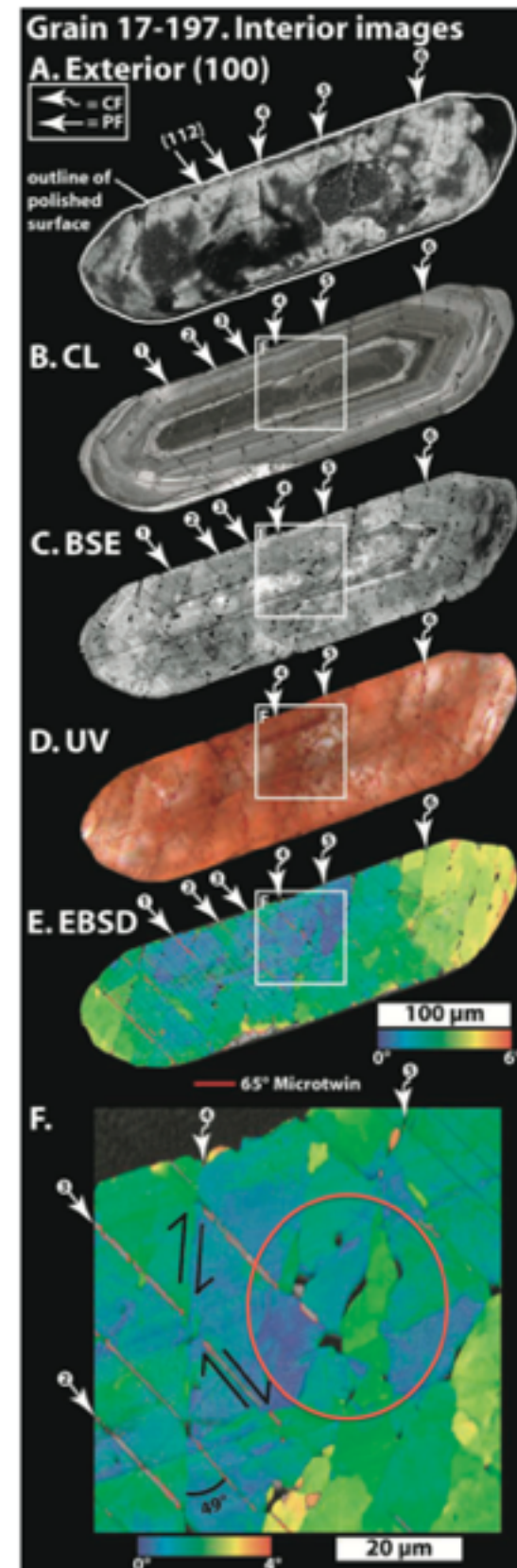


Figure 4.17 Zircon crystal from the colluvium located in the center of the Vredefort Dome impact structure: A. Exterior (100), optical view of (100) face of zircon crystal prior to sectioning and polishing; B.CL, cathodoluminescent image of the polished zircon crystal; C.BSE, backscattered electron image of the polished crystal; D.UV, ultraviolet light image of the polished crystal; E.EBSD, electron backscatter diffraction map of the polished crystal; F. high magnification view of the center of the polished crystal. Original image from Erickson, et al., 2013, Fig. 7.

Erickson, et al., 2013 referred to the visible shear planes as “planar fractures (PF).” These PF’s are actually geometrically related shear lines...not fractures.

Surface exposure of the edges of shear planes is visible in all of the images, and the shear planes inside the crystal were indexed mostly as $\{112\}$. Lesser numbers of shear planes indexed as (100), (010), and (011) were also observed both inside and on the

surface of the crystal. Shear displacement is clearly visible, especially in [Figure 4.17](#) B.CL inside the white box, but local shear displacement is quite small in the crystal. The scale of the shear displacement can be seen along the marked vectors in [Figure 4.17](#) F. For the most part, the stresses have been relieved by the development of complimentary shear planes...a clear example of shear branching along the complimentary planes.

The term “CF” used in [Figure 4.17](#) refers to the term ‘curvilinear fractures’ that was used by Erickson, et al., 2013 to indicate curved ‘fracture’ lines. CF’s are actually indications of rotation of one shear plane toward a crystallographically complimentary shear orientation. Individual grains inside the red oval in [Figure 4.17](#) F. are bent, and correlated cavities have developed at triple points and along grain boundaries. A slight lefthand rotation is also observed across the image around the red oval creating a misalignment of the shear planes across the region. This rotation appears to have contributed to the formation of shear steps along complimentary shear planes seen inside the upper right corner of the image. In addition, the slight curvature exhibited on the upper edge of the images inside the white box in [Figure 4.17](#) appears associated with this rotation...a slight bending of the entire crystal is observed especially in [Figure 4.17](#) D, E and F.

The thicker, orange colored shear line segments in [Figure 4.17](#) F indicate melting due to deformation and fracture heating generated by adiabatic localized shearing. ASB’s in other samples studied by Erickson, et al., 2013 show clear signs of recrystallization inside the shear band inferring that very high temperatures existed during their formation. Incidentally, Erickson, et al., 2013 interpreted the ASB’s (orange bands) as micro-twins. It is possible that high temperature decomposition

of zircon to zirconia and silica was produced during the formation of these ASB’s.

The microstructures seen in [Figure 4.17](#) illustrate the fracture behavior of brittle crystalline solids. Comminution begins with shearing along the planes of least resistance to deformation...{112} in zircon crystals. As illustrated in [Figure 4.17](#) F, shear branching will lead to the production of extremely fine, angular fragments. Melting on the shear planes caused by permanent deformation will lead to overall structural weakening throughout the crystal.

4.2.4.2 LOCALIZED SHEARING IN QUARTZ CRYSTALS

It is commonly agreed that planar deformation features (PDF’s) are produced in quartz crystals found in rocks by the high pressures (*actually high asymmetric stresses*) and high strain rates produced inside and close around a forming impact crater. PDF’s in quartz are usually observed in thin section samples under a microscope, and as seen in [Figure 4.18](#), PDF’s are observed as sets of parallel lines that include crystallographic complimentary planes.

It should be noted in [Figure 4.18](#) that there are many complimentary sets of PDF’s which represent shear deformation on alternate preferred shear planes in this quartz crystal much like that previously observed in [Figure 4.5](#). Material inside the ASB marked in the photomicrograph in [Figure 4.18](#) appears amorphous...a glass. Actually this quartz crystal has been subdivided by the formation of several parallel ASB’s. A large cavity is visible near the center of the marked ASB that appears to be associated with a small change in direction of the shear plane... recall similar features inside the red oval in [Figure 4.17](#).

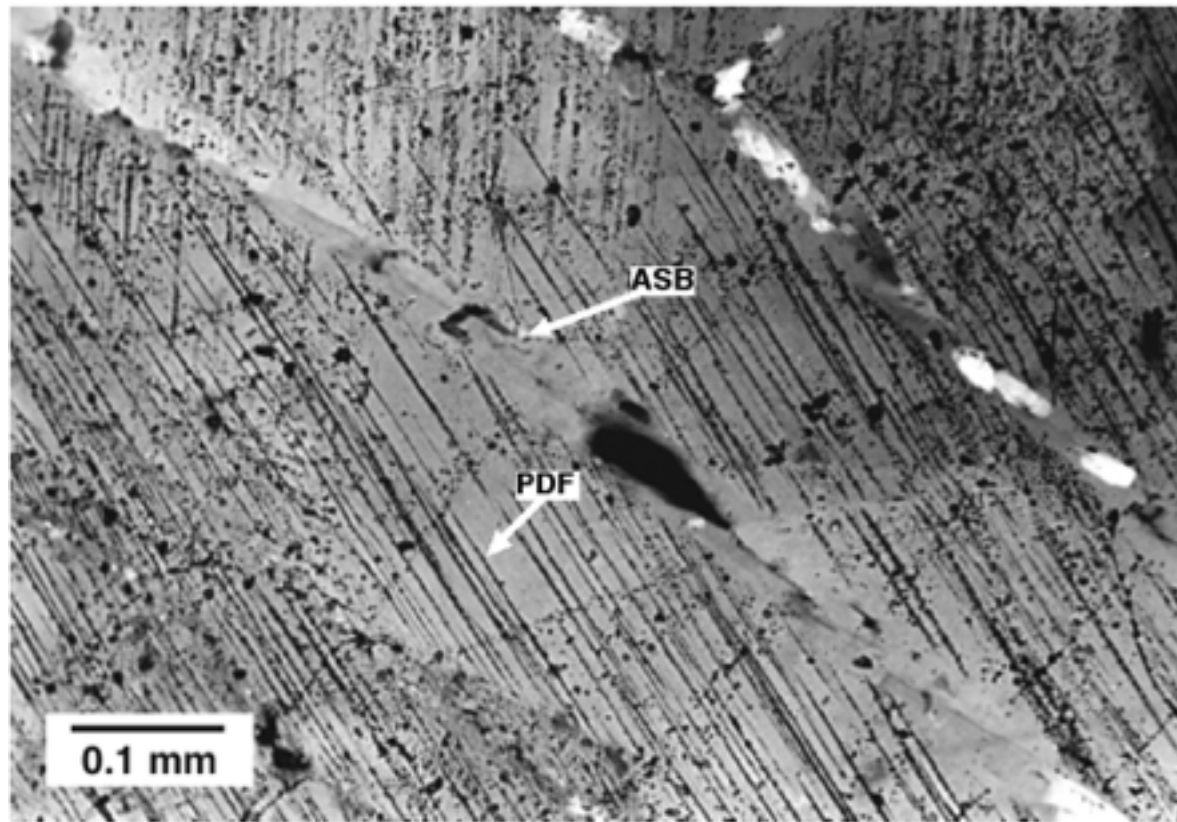


Figure 4.18 Thin-section from a quartz crystal found in Precambrian basement gneiss collected from the central uplift of the Carswell Lake impact structure (Canada) viewed under polarized light. Original image from French, 1998, Fig. 4.22.

Dauphiné twinning in quartz crystals represents a precursor to the formation of PDF's. Dauphiné twinning is a stress induced deformation process that results from loading along the c-axis of the trigonal quartz crystal, and Si-O bonds are not broken during this deformation process, e.g. Bertagnolli, et al, 1978 and Wenk, et al., 2011. In polycrystalline quartz-bearing solids, Dauphiné twinning is observed in grains whose c-axis is oriented parallel to the maximum stress vector, and it is observed to be produced over a wide range of strain rates. Dauphiné twins have been found associated with seismic events as well as impacts, e.g. Wenk, et al., 2011. Also, "In situ neutron diffraction experiments indicate that

twinning initiates at 50–100 MPa and that activation of twinning is temperature dependent," Wenk, et al., 2011.

Black spots decorate many of the PDF's in [Figure 4.18](#). These features represent deformation cavities on shear planes that are approaching complete fracture...recall deformation cavities on the fracture surface caused by hypervelocity impact in Ti-6242-Si in [Figure 4.11](#). (Researchers have generally interpreted these black spots as fluid inclusions, e.g. French, 1998 and Carr and Link, 1999.) These cavities develop as shear deformation progresses, and when sufficient numbers form on the shear planes, fracture can develop on one or more of these deforming shear planes. However at high strain rates, fracture heating can cause local melting producing ASB's along these same shear planes significantly weakening the entire structure.

Chapter 4 References

Bertagnolli, E., Kittinger, E., and Tichy, J., 1978, The observation of reversible elastic Dauphiné twinning in α -quartz, *Le Journal Physique-Letters*, 39, Sept. 1978, p. L-295, <http://dx.doi.org/10.1051/jphyslet:019780039017029500>.

Carr, J., and Link, P. K., 1999, Neoproterozoic Conglomerate and Breccia in the Formation of Leaton Gulch, Grouse Peak, northern Lost River Range, Idaho: Relation to Beaverhead Impact Structure, in Hughes, S.S., and Thackray, G.D., eds., *Guidebook to the Geology of Eastern Idaho: Pocatello*, Idaho Museum of Natural History, p. 21-29.

Davidkov, A., Jain, M. K., Petrov, R. H., Wilkinson, D.S., and Mishra, R. K., 2012, Strain localization and damage development during bending of Al–Mg alloy sheets, *Materials Science and Engineering A* 550, pp. 395–407.

Dieter, G. E., Jr., 1961, *Mechanical Metallurgy*, McGraw-Hill Book Company, Inc., NY.

Erickson, T. M., Cavosie, A. J., Moser, D. E., Barker, I. R., and Radovan, H. A., 2013, Correlating planar microstructures in shocked zircon from the Vredefort Dome at multiple scales: Crystallographic modeling, external and internal imaging, and EBSD structural analysis, *American Mineralogist*, 98, pp. 53-65.

El Bied, A., Sulem, J., and Martineau, F., 2002, Microstructure of shear zones in Fontainebleau sandstone, *International Journal of Rock Mechanics and Mining Science*, 39, pp. 917-932.

Fiske, P. S., Nellis, W. J., Lorenzana, H., Lipp, M., Kikuchi, M. and Syono, Y., 1995, Generation of Pseudotachylites in Shock Experiments: Implications for Impact Cratering Products and Processes, presented at the 1995 APS Conference “Shock Compression of Condensed Matter,” August 13-18, 1995, Seattle, WA; UCRL-JC-121878.

French, B. M., 1998, *Traces of Catastrophe: A Handbook of Shock-Metamorphic Effects in Terrestrial Meteorite Impact Structures*, LPI Contribution No. 954, Lunar and Planetary Institute, Houston, 120 pp.

Head, J. W. and Mustard, J. F., 2006, Breccia dikes and crater-related faults in impact craters on Mars: Erosion and exposure on the floor of a crater 75 km in diameter at the dichotomy boundary, *Meteoritics & Planetary Science* 41, Nr 10, p. 1675–1690.

Kamo, S.L., Reimold, W.U., Krogh, T.E., and Colliston, W.P., 1996, A 2.023 Ga age for the Vredefort impact event and a first report of shock metamorphosed zircons in pseudotachylitic breccias and granophyre. *Earth and Planetary Science Letters*, 144, pp. 369–388.

Lade, P.V. and Wang, Q., 2001, Analysis of shear banding in true triaxial tests on sand, *ASCE Journal of Engineering Mechanics*, 127, pp. 762-768.

Langenhorst, F., Poirier, J-P., Deutsch, A. and Hornemann, 2002, Experimental approach to generate shock veins in single crystal olivine by shear melting, *Meteoritics & Planetary Science*, 37, pp. 1541-1553.

Lesuer, D. R., 2000, *Experimental Investigations of Material Models for Ti-6Al-4V Titanium and 2024-T3 Aluminum,*” FAA Office of Aviation Research Report DOT/FAA/AR-00/25, September 2000. (Available online)

Li, S.X., Yang, R.Q., Li, J.W., and Zhang, Z.F., 2006, Shear localization in dynamic deformation of copper single crystals, *Philosophical Magazine*, Vol. 86, No. 36, 21 December 2006, pp. 5769–5786.

Lieger, D., Riller, U. and Gibson, R. L., 2011, Petrographic and geochemical evidence for an allochthonous origin for pseudotachylite melts with a possible influence of the impact melt sheet in the Vredefort Dome, South Africa, Chapter 4 in *Structural and Geochemical Analyses of fragment-rich pseudotachylite bodies and the Vredefort Granophyre of the Vredefort Impact Structure, South Africa*, Leiger, D., Thesis submitted to the Department of Earth Sciences, Free University of Berlin, Germany, in partial fulfillment of the requirements for the degree of Doctor rerum Naturum.

Lins, J.F.C., Sandim, H.R.Z., Kestenbach, H.-J., Raabe, D., and Vecchio, K.S., 2007, A microstructural investigation of adiabatic shear bands in an interstitial free steel, *Materials Science and Engineering A*, 457, pp. 205–218.

Ogata, S., Shimizu, F., Li, J., Wakeda, M. and Shibutani, Y., 2006, Atomistic simulation of shear localization in Cu–Zr bulk metallic glass, *Intermetallics* 14, p. 1033-1037.

Shockey, D. A., Curran, D. R. and DeCarli, P. S., 1975, Damage in Steel Plates from Hypervelocity Impact. I. Physical Changes and Effects of Projectile Material: *Journal of Applied Physics*, Vol. 46, No. 9, p. 3766-3775.

Tarbutck, E. J. and Lutgens, F. K., 2005, *Earth: An Introduction to Physical Geology*, 8th Ed., Pearson Prentice Hall, Upper Saddle River, NJ.

Tresca, H., 1878, On further applications of the flows of solids, Proceedings of the Institution of Mechanical Engineers, 30, p. 301.

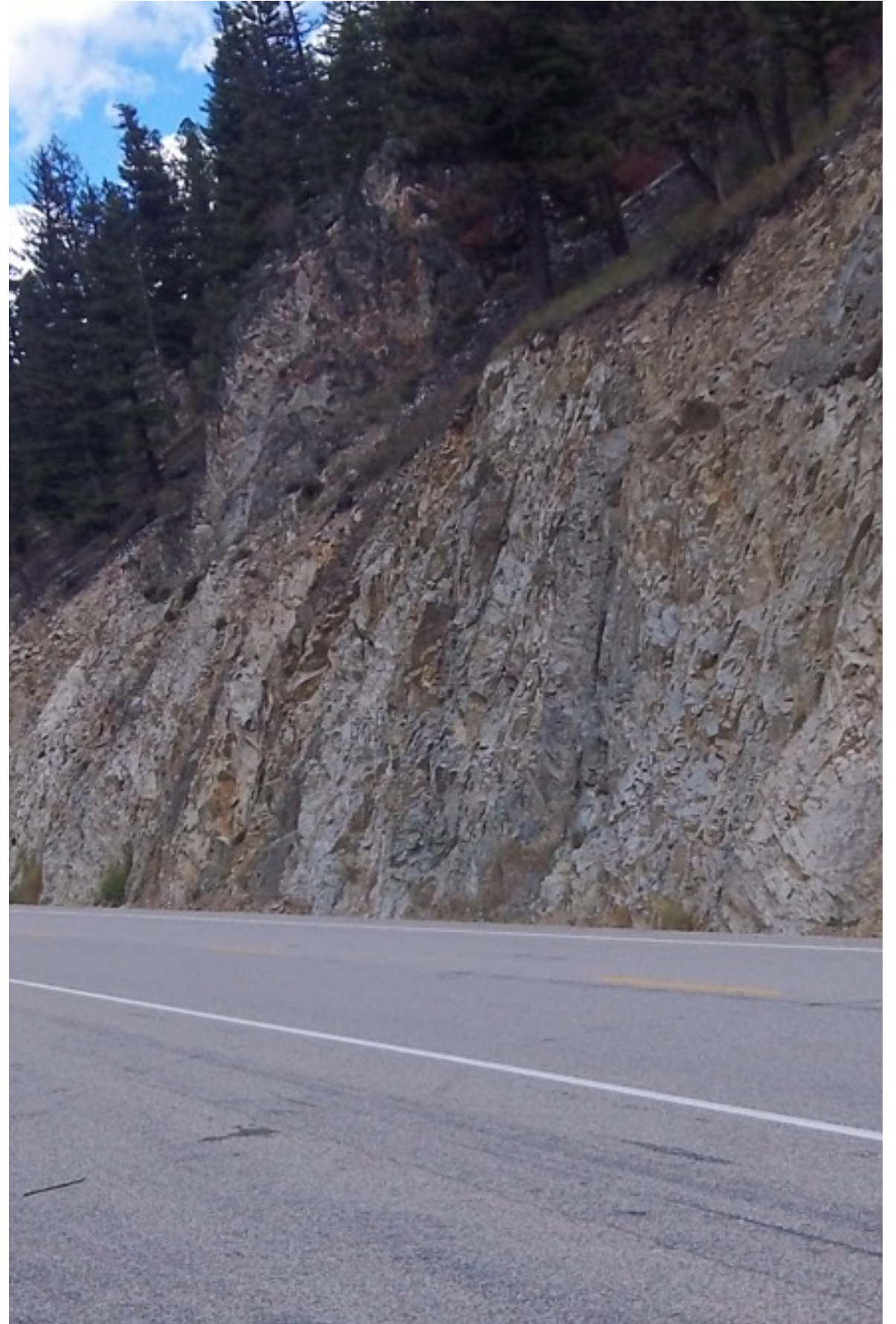
Walley, S. M., 2012, Strain Localization in Energetic and Inert Granular Materials, Chapter 7 in Adiabatic Shear Localization: Frontiers and Advances, Eds. Dodd, B. and Bai, Y., 2nd Edition, Elsevier:, 32 Jamestown Road, London NW1 7BY, pp. 267-310.

Wenk, H-R., Janssen, C., Kenkmann, T. and Dresen, G., 2011, Mechanical twinning in quartz: Shock experiments, impact, pseudotachylites and fault breccias, Tectonophysics, 510, pp. 69-79.

Zhang, L. V., Toole, J., Fezzaa, K. and Deegan, R. D., 2011, Evolution of the ejecta sheet from the impact of a drop with a deep pool, Journal of Fluid Mechanics, 396, doi:10.1017/jfm.2011.396.

Localized Shear in Geologic Structures

This dike littered roadcut lies on the east side of US route 93 north of Lost Trail Pass in southwest Montana.



Examples of localized shear are found everywhere in geologic structures on Earth at all scales and regardless of the rate of formation...impact or tectonic. As emphasized by Walley, 2012 and discussed in previous chapters, localized shear is a fundamental deformation process in dense materials. In a macro geologic context, dikes and faults represent two of the most conspicuous examples of structures formed by localized shear especially in and around impact structures. As will be discussed below, pseudotachylite and shatter cones, which are commonly found in impact structures, are also both formed by localized shear during the late stages of the cratering process. In fact, the presence of structural features formed by localized shear can be used as confirming evidence for many proposed geologic impact structures. Incidentally in the geologic community, the presence of shatter cones has been given the highest priority for crater verification, <http://www.unb.ca/passc/ImpactDatabase/>.

In the latter part of this chapter, we will examine data associated with two widely geographically separated geological structures in the Rocky Mountain chain in the United States that contain large dikes that could be considered as indicators of their impact formation. This discussion is intended to provide background for the following chapter where an exercise in identification of geologic impact structures on the dry surface of Earth will be presented.

Dikes, Faults, Pseudotachylites and Shatter Cones

SECTION TOPICS

5.1.1 Popular Dike Formation Model

5.1.2 Observational Based Dike and Pseudotachylite Formation Model

5.1.3 Dikes/Faults formed at Low Strain Rates

As noted in Chapter 3, uniquely structured dikes, faults and pseudotachylites are commonly found in geologic impact structures. A dike is defined in standard geology textbooks such as Tarbuck and Lutgens, 2005 as: “A tabular-shaped intrusive igneous feature that cuts through the surrounding rock.”, and they define a fault as: “A break in a rock mass along which movement has occurred.” Pseudotachylites were illustrated and briefly discussed in Chapter 3. Shatter cones are generally characterized by a conical structure whose surface appearance resembles a horse’s tail, and it is commonly found inside the primary crater of impact structures in brittle geologic materials.

By applying the concepts of the mechanical behavior of real materials discussed in Chapter 4, we will examine the close relationship of these four geologic substructures based on the the fact that they were all formed by localized shear. However, in order to gain some perspective on the formation of dikes, we first need to examine the currently proposed models for the dike formation process.

5.1.1 POPULAR DIKE FORMATION MODEL

Within the geologic community, it is almost universally believed that dikes and pseudotachylites are formed by either 1) some molten, low viscosity material intrusively flowing inside pre-existing cracks or fissures in surrounding rock down a pressure gradient from a nearby, accessible source (e.g. Wieland, 2006 or Lieger, 2011) or by 2) flow of water soluble components from nearby sources migrating into and precipitating

inside the pre-existing cracks or fissures. Both of these concepts are inconsistent with a variety of basic physical principles, and in actuality there is little or no observational data to support either of these dike formation hypotheses.

As discussed in **Section 4.2.2**, molten silicate rock is quite viscous except at very high temperatures; also its viscosity is extremely temperature sensitive...recall [Figure 4.13](#). Consequently if model 1) described above was valid, evidence of stalled flow in preexisting cracks in silicate rocks due to heat losses that cause a major increase in viscosity along the flow path should be commonly observed. Along with increased viscosity effects, if molten rock is flowing from an external source and melting crack-wall-material as it progresses into the crack, the flow path should steadily narrow away from the source due to diminishing wall melting resulting from progressive heat loss to the crack wall...dike walls are generally parallel for long distances and many can be traced for several kilometers.

Finally in most cases, a reservoir of molten rock that is fluid enough to intrude into preexisting cracks is very rarely accessible...it is estimated that temperatures inside the Earth needed to cause the viscosity of silicate rock to be reduced to that of water at room temperature are not available above depths of ~100 km, Tarbuck and Lutgens, 2005. Except for very large craters, molten material found on the inside surfaces of primary impact craters should not be expected to be accessible to fill pre-existing cracks around an impact structure. Also as illustrated by the examination of the inside surfaces of hyperv-

elocity impact craters in metals, the amount of molten material retained in the shock front around the inside surface of a primary crater after excavation is complete is minimal...recall **Section 2.1.3.2** and [Figure 2.17](#).

With regard to model 2), the presence of an adequate hot water source for aqueous mineral transport is also rare, and a crack would be expected to be quickly filled with impermeable foreign material close to its entrance and become plugged due to precipitation along temperature gradients from the hot water source.

Also as commonly observed, the overall chemical compositions of material inside and nearby to a dike are nearly identical, further indicating that the material found inside the dike was melted or formed in situ rather than introduced from an outside source by an intrusive process...including hydrothermal processes. However as was discussed in **Section 4.2.3**, the more mobile chemical elements can be rapidly redistributed over short distances in the high temperature environment from the surrounding material into and across an ASB during its formation creating some apparent inconsistencies between the chemical composition of the wall-rock and material inside the dike.

5.1.2 OBSERVATIONAL BASED DIKE AND PSEUDOTACHYLITE FORMATION MODEL

After primary crater excavation nears completion and during the late stages of impact cratering, heat generated by target

material deformation and fracture will be deposited primarily within localized shear zones that develop within the central uplift and around the perimeter of the primary crater, and due to the low thermal conductivity of geologic materials, adiabatic conditions exist and melt temperatures can be achieved within the shear planes. As deformation rates increase, the localized heat generation rate in geologic materials increases within localized shear zones. We have previously examined typical dikes formed in *accepted* impact structures...e.g. in the central uplift of the Upheaval Dome, recall [Figure 3.5](#), and the Vredefort Granophyre in the Vredefort Dome, recall [Figure 3.14](#).

Many dikes are formed inside and around an impact structure, and their distinct geometric layouts reflect the stress patterns developed inside and around the crater during the late-stages of its formation. Due to the transient nature of the heating, melting in the shear band is frequently incomplete forming a welded, metastable structure that incorporates both fully melted material surrounding *partially* consumed solid bodies...breccia or conglomerate. As will be discussed, both dikes and pseudotachylites generally contain unmelted bodies of varying sizes. Both breccia dikes and pseudotachylites can be classified as adiabatic shear bands. Fluid flow is possible in these two-phase bodies before solidification occurs, and some molten material that is formed *in situ* can be extruded a short distance along the shear bands toward free surfaces where the confinement stresses approach zero...recall [Figure 4.2](#).

5.1.2.1 IMPACT DIKES AND PSEUDOTACHYLITES IN SILICATE ROCK

The **Breccia Dike** marked in [Figure 5.1](#) might best be termed an impact dike structure because it contains solid pieces of rock welded into a previously melted matrix. This type of geologic substructure is commonly found in and around impact structures. The place-mark (yellow map tack) seen in [Figure 5.2](#) indicates that the location of the breccia dike viewed in [Figure 5.1](#) is near the end of a 1.4-km long ridge that spurs off of Cable Mountain...located in southwestern Montana. The breccia dike location marked in [Figure 5.2](#) is actually just one branch of the **Ridge Dike**. The south end of the ridge dike actually splits into at least two branches oriented about 30° apart near the south end of the ridge.

A closeup view of a fracture surface of one of the many boulders that has broken out of the breccia dike seen in [Figure 5.1](#) can be found in [Figure 5.3](#). Gray rock fragments are contained within the white matrix of the boulder whose overall structure can be classified as a breccia. This boulder is representative of partially melted silicate rock which was generated *in situ* when localized shear formed the dike at high rate as a result of impact. Smaller scale ASB's are displayed inside the contained rock fragments which indicates additional localized shearing produced by high energy, shock compressive loading. As indicated in [Figure 5.3](#), the orientations of the shear bands inside the clasts are angularly related to the maximum compression vector...recall **Equation 2.2**. The primary

(maximum) shear stress vector indicated in [Figure 5.3](#) is defined by the orientation of the exposed shear planes in the clasts.



Figure 5.1 Breccia dike exposed at the nose of a ridge that spurs southeast off of Cable Mountain...located west of Anaconda, MT.

Actually, the fracture surface on the rock displayed in [Figure 5.3](#) is very similar to that of the rock from the Vredefort Granophyre seen in [Figure 3.16](#)...the major difference between the two is the size of the clasts. The smaller clasts in the Vredefort Granophyre rock indicates greater clast dissolution caused by a higher localized shear rate or a slower cooling rate. Also as noted by Weiland, et al., 2005, “narrow veinlets, which typically show a close correspondence between the chemical composition of their matrix and that of their wallrocks, the larger breccias show abundant evidence of mixing of melt from a va-

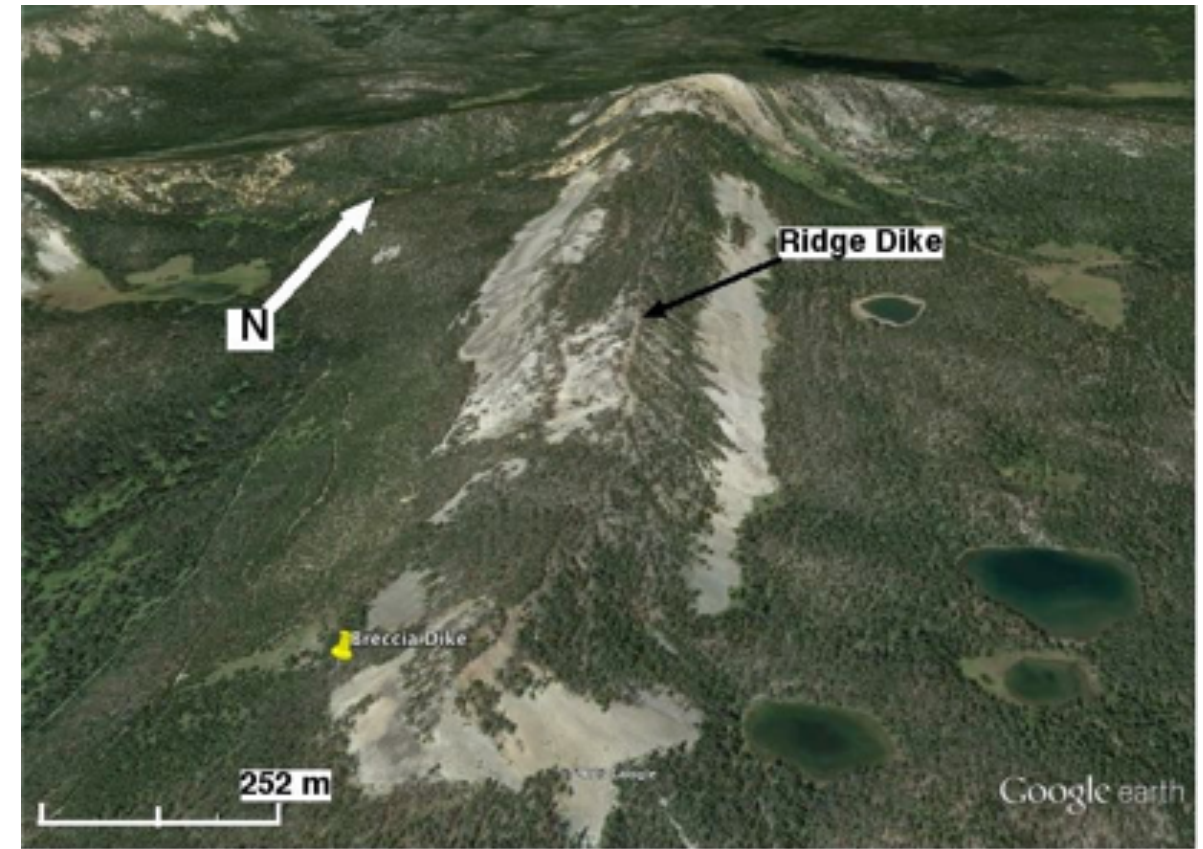


Figure 5.2 Cable Mountain ridge spur from which the breccia dike seen in [Figure 5.1](#) branches. Original image from Google Earth.

riety of sources,” which is consistent with the effects of size upon the cooling rate of the material inside breccia dikes.

Pseudotachylite is general considered to be a separate and distinct substructure associated with impact structures when in fact it represents a variant of a breccia dike. The structure of a typical pseudotachylite can be examined in detail in [Figure 5.4](#). This pseudotachylite is located close to the Parys Quarry inside the Vredefort Dome...recall [Figure 3.19](#), but as opposed to the pseudotachylite seen in [Figure 3.18](#), its cross-section is exposed on the horizontal.

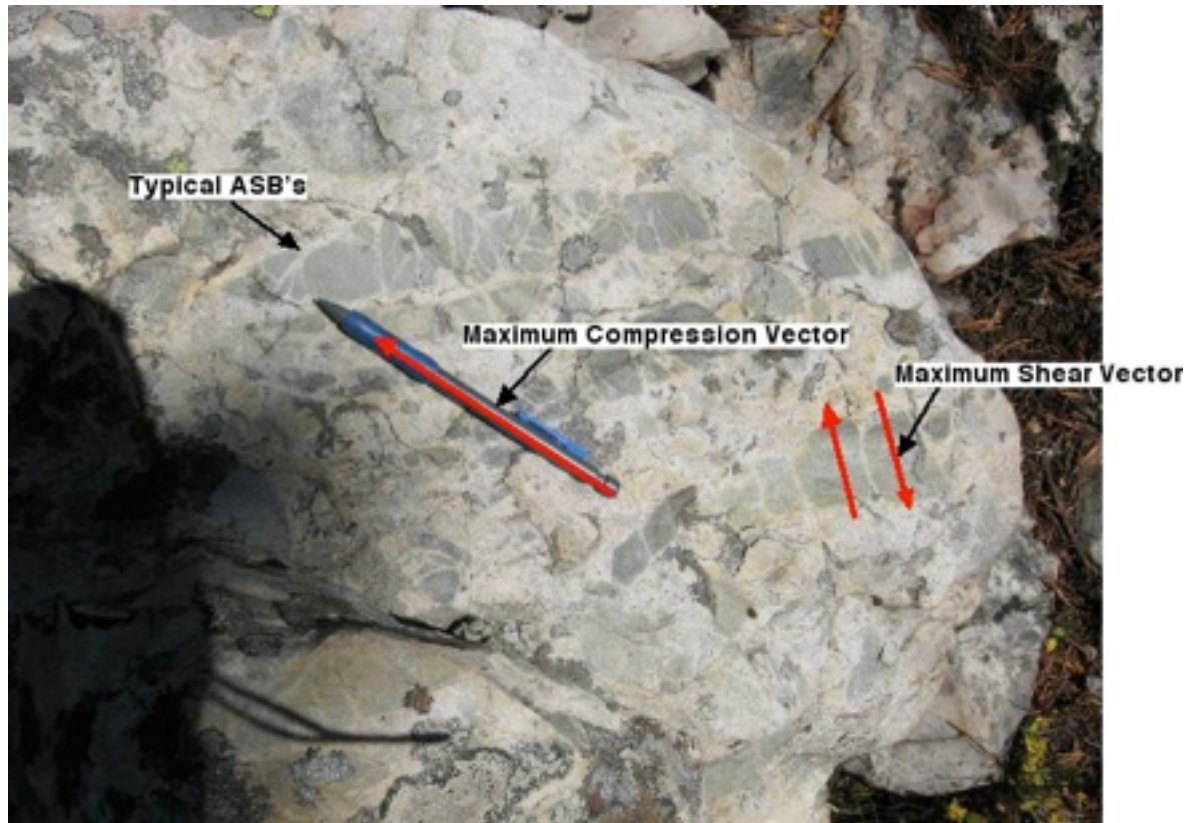


Figure 5.3 Boulder from the exposed breccia dike seen in [Figure 5.1](#). Stress vectors are related to the orientation of adiabatic shear bands. Photo provided by Ted Antonioli and Skip Yates.

Boulder sized clasts are surrounded by a black matrix consisting of solidified wall-rock; the clasts tend to reside in the center of the pseudotachylite shown in [Figure 5.4](#). The general appearance of these clasts is reminiscent of bodies floating in a liquid stream, which accurately reflects its formation process. Although not as well delineated, the cross-sections of these clasts are very similar to that observed in the included rocks seen in [Figure 5.3](#). However, the clasts in the Vredefort Dome pseudotachylite are more rounded...comparable to those typically found in the Sudbury impact structure in southern Ontario, Canada (see photos in French, 1998).



Figure 5.4 Pseudotachylite exposed in a quarry inside the Vredefort Dome primary crater. Original image posted on the internet by Martin Tuchscherer on Panoramio.

The ASB marked in [Figure 5.4](#) indicates the unfinished, metastable boundary of a clast or two. The jagged line of the **ASB**

(vein) is characteristic of localized shear in a near-hydrostatic stress state. Angular incursions into the left wall of this pseudotachylite indicate clast extractions that occurred toward the end of the formation of this pseudotachylite. The black color of matrix of this shear band indicates that it was molten during formation...melted granite is usually black.

The lighter colored band along the right side of the pseudotachylite shown in [Figure 5.4](#) represents a heat affected zone much like that observed around hypervelocity impact craters in metals...recall [Figure 2.17](#). As should be expected, heat affected zones are also observed on the surfaces of clasts found in impact generated breccia dikes/pseudotachylite ...illustrated in [Figure 5.5](#).

5.1.2.2 IMPACT DIKES AND PSEUDOTACHYLITES IN CARBONATE ROCKS

The melting behavior of carbonates is quite different from that of silicates mostly because carbonate rocks generally melt over a narrow temperature range. Under *equilibrium* conditions, carbonates decompose by releasing carbon dioxide. However, high-rate, localized shearing due to impact produces conditions that are far from equilibrium, and melting inside ASB's forming at high rates inside carbonates can be achieved without significant loss of CO₂, at least in part due to the tight solid surroundings that provide effective gas containment.

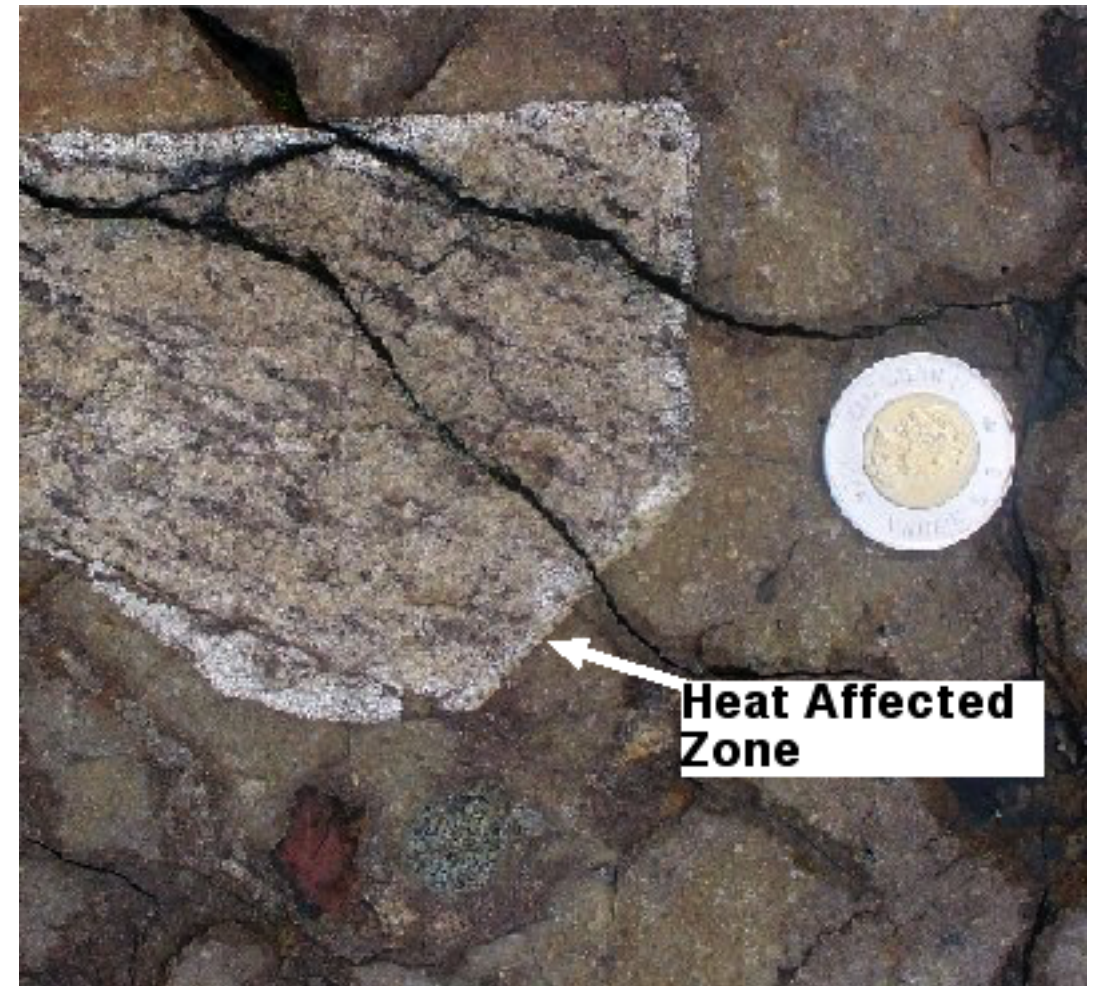


Figure 5.5 Fragment of granite exposed in the matrix of the melt breccia exposed on the surface of the central uplift of the Manicouagan impact structure. Original photo from C. O'Dale website entry on the Manicouagan impact structure.

Carbonate rock melting inside ASB's is illustrated in [Figure 5.6](#) where they have been formed in a dolomite rock that was found near a 3- to 4-cm-wide dike that was exposed across a dolomite stratum that was at least 10 m thick. Columnar crystals are observed to have grown normal to the outer boundaries of the white ASB's during cooling from a molten state. The columnar character of these crystals (grains) is derived

from the heat flow from inside to out inside the ASB as the melt cools and solidifies.

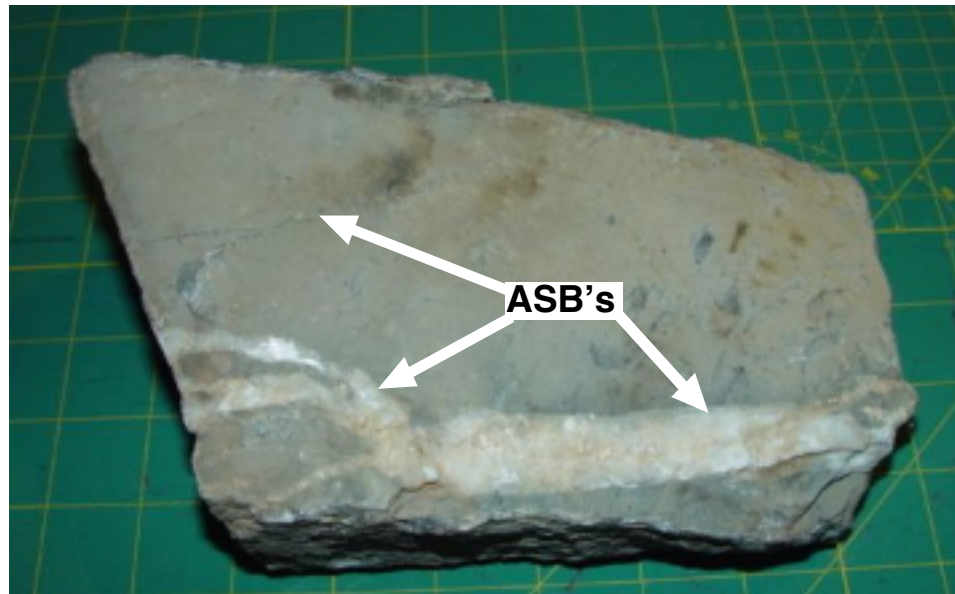


Figure 5.6 Dolomite rock with branched adiabatic shear bands. This rock is representative of talus from a dolomite formation along US 12 east of Garrison, MT that contains many larger shear bands. For scale, the background grid is 1 in. x 1 in.

5.1.2.3 SHATTER CONES

It is generally contended that “Shatter cones are the only diagnostic, macroscopic evidence of shock damage observed as result of the meteorite impact process,” Thompson, 2014. However, shatter cones are also found inside meteorites, McHone, et al., 2012. Also as can be inferred from the previous discussion, it is obvious that shatter cones are not the only diagnostic impact substructure, and as will be demonstrated, shatter cone formation is also produced by localized shear.

Shatter cones are generally found inside the primary crater of impact structures...frequently on the surface of the central uplift, and in brittle geologic materials, they can be characterized as highly branched localized shearing that is produced by high-rate compressive loading in brittle solids. The typical horsetail textured surface structure of a large shatter cone that results from localized shear deformation and fracture is seen in [Figure 5.7](#). Based on the discussion in Chapter 4, we can estimate that the maximum compressive force vector was ap-



Figure 5.7 A silicate rock containing ASB's lying on the surface of a shatter cone exposed on the top of Carpp Ridge located in southwestern Montana. The rock is approximately 25 cm across.

plied from the left parallel to the general orientation of the surface striae.

The rock lying on the surface of this shatter cone displays a network of adiabatic shear bands that were also developed inside the rock by high-rate compressive loading creating conjugate, melted planar structures; this rock was found lying nearby the surface of the shatter cone. Incidentally, the surface appearance of this rock is very similar to the shatter cone on which it lies inferring that it was originally associated with the surface of a shatter cone. The steps observed on the surface of the shatter cone seen in [Figure 5.7](#) normal to the striae are common to many shatter cones produced in geologic materials. These steps are produced by shear branching on a larger scale than for the horsetail surface. The surface of this shatter cone has a slick texture due to the fact that a silicate glass has formed on the exposed shear failure surface of this rock resulting from deformation and fracture heating.

Evidence of melting is commonly observed on the surface of shatter cones in igneous rock...see for example Armstrong, et al, 2003. The 'slick' surfaces commonly seen on shatter cones in igneous, silicate rock indicate that the heating from the localized adiabatic shear has caused a glassy phase to form and cover the surfaces of shatter cones. Incidentally, 'slick rock' is generally not observed on the surfaces of shatter cones in carbonate rocks because it is difficult to form glassy phases in this rock type unless it contains significant amounts of silica or other glass forming compounds.

The fracture surface and a cross-section of a typical small scale shatter cone associated with the accepted Sierra Madera impact structure, located in west Texas, is presented in [Figure 5.8](#). Positive relief imprints of shatter cones, indicated by arrows in [Figure 5.8\(a\)](#), were exposed by cleaving the rock along the dotted line indicated in [Figure 5.8\(b\)](#), while the complementary negative imprints are seen inside the circles in [Figure 5.8\(c\)](#) on the correlated opposing fracture surface. It should be noted that the shatter cones displayed in [Figures 5.8\(a\)](#) and [5.8\(c\)](#) are truncated...a common geometry for shatter cones found in full-scale geologic impact structures. In [Figure 5.8\(d\)](#), the boundaries of a network of incipient shatter cones are seen in cross-section; the boundary of one is indicated with the arrow. These circular structures represent a network of shear bands produced inside the rock as a result of branched, adiabatic localized shearing, and fracture along this array of melt surfaces leads to the horsetail surfaces that are characteristic of shatter cones. The maximum compressive force vector that produced the shear failure surfaces is inferred to be approximately normal to the cut surface in [Figure 5.8\(d\)](#). Besides being found in full scale geologic impact structures, shatter cones have also been produced in rocks in the laboratory by hypervelocity impact...see for example Lundberg, 2009.

The large **Shatter Cone** seen in [Figure 5.9](#) illustrates that the basic structural features are retained when extrapolated upward in scale. This shatter cone was generated in silicate rock and is nominally located on the edge of a central uplift of the

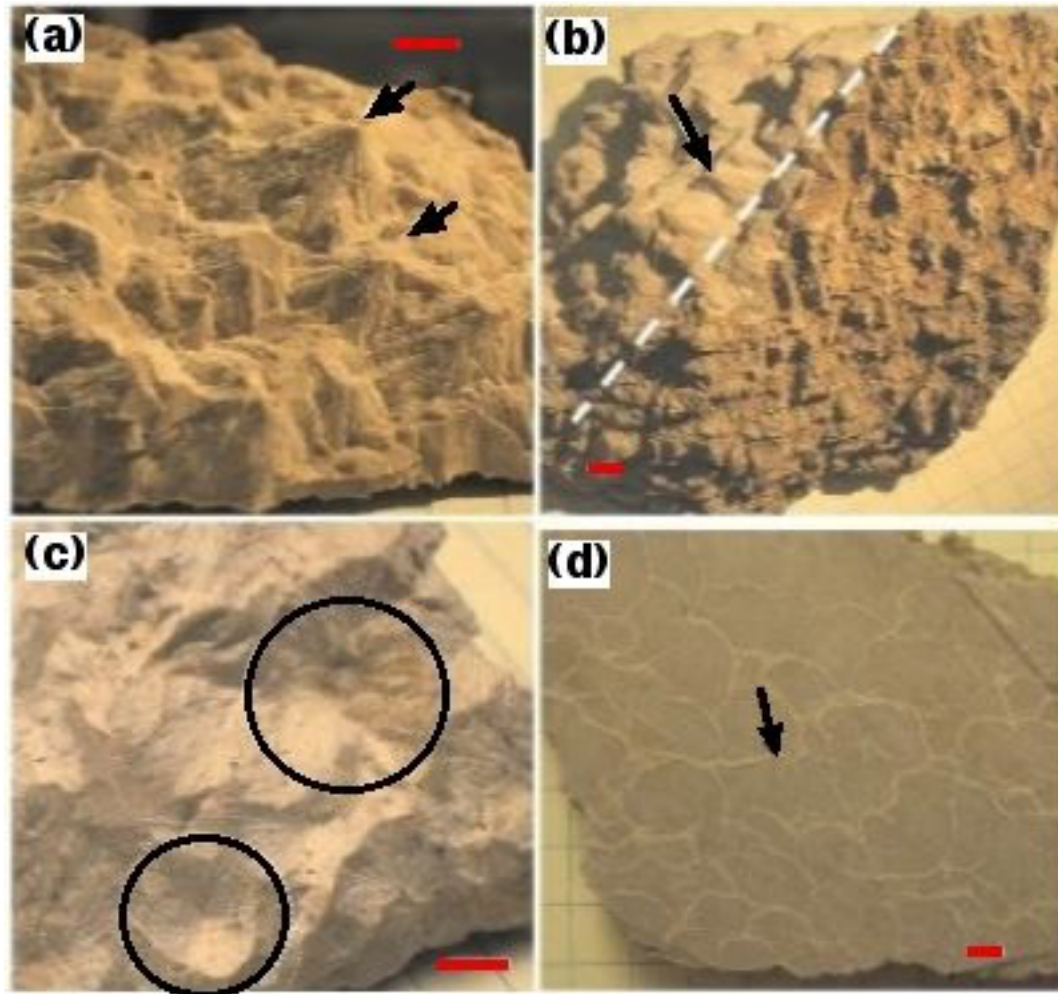


Figure 5.8 Dolomitic limestone rock from inside the Sierra Madera impact crater. Surfaces seen in (a) and (c) were produced by cleaving the rock along the dotted line seen in (b). The surface of a cut face this rock is displayed in (d). Each red scale bar is 5 mm long. Original photos from Adachi and Kletetschka, 2008.

the Slate Islands impact structure located off of the north shore of Lake Superior. The location for these impact sub-structures relative to the impact structure is typical. Additional, smaller, partially exposed shatter cones are visible in the upper left in [Figure 5.9](#).

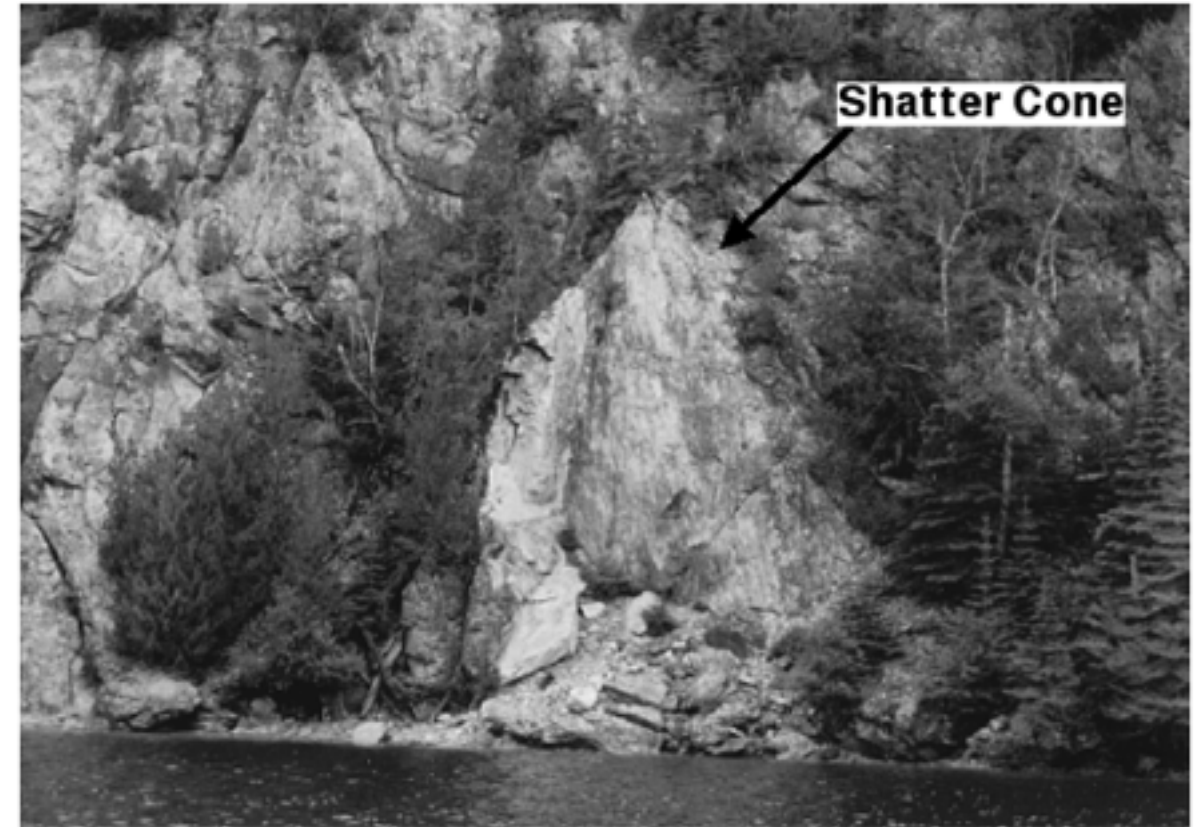


Figure 5.9 Shatter cones on the shoreline of Patterson Island... part of the Slate Islands impact structure located in Lake Superior near Terrace Bay, ON, Canada. The indicated shatter cone is ~10 m high. Original image from French, 1998.

5.1.3 DIKES/FAULTS FORMED AT LOW STRAIN RATES

As the induced shock waves degrade around a forming impact structure, the strain rate imposed on the surrounding intact material by the remnant stresses eventually drops to quasi-static levels. This means that deformation and fracture behavior of materials around an impact structure are governed by their quasi-static mechanical behavior; never-the-less, deformation and fracture are still initiated by localized shear. However as the strain rate slows, the amount and rate of heat gen-

erated by deformation and fracture become insufficient to cause significant melting on the material inside the shear band, and the final structure of brittle materials, e.g. cold rock, inside a localized shear band is characterized as fragmented, crushed or comminuted. The resultant macro behavior of localized shear in brittle materials was previously illustrated in [Figure 4.1](#), and the microstructure of material inside shear bands in silicates was well illustrated in [Figure 4.10](#).

However before we discuss slow strain rate deformation and fracture in rocks, it is instructive to examine the slow strain rate behavior of water-ice because of its modest melting temperature and the effect of pressure on its melting temperature. Water ice is an excellent material for demonstrating most of the basic characteristics of localized shear that are analogous to those observed as a result of deformation of solid rock over the entire range of strain rate...slow to high.

5.1.3.1 DIKES IN ICE

The pressure ice formation seen in [Figure 5.10](#) is commonly created as a result of stresses developed by the collision of large, abutted, snow-covered blocks of ice floating on the surface of large bodies of freshwater...e.g. the North American Great Lakes. Compressive forces at the boundary between the separate ice blocks, frequently driven by surface winds, generate localized, periodic shear bands at the ice block boundary that intersect the surface of the ice. These shear bands thicken and tend to be extruded upward...the arcuate top of the foreground ASB indicates slightly increased upward extru-

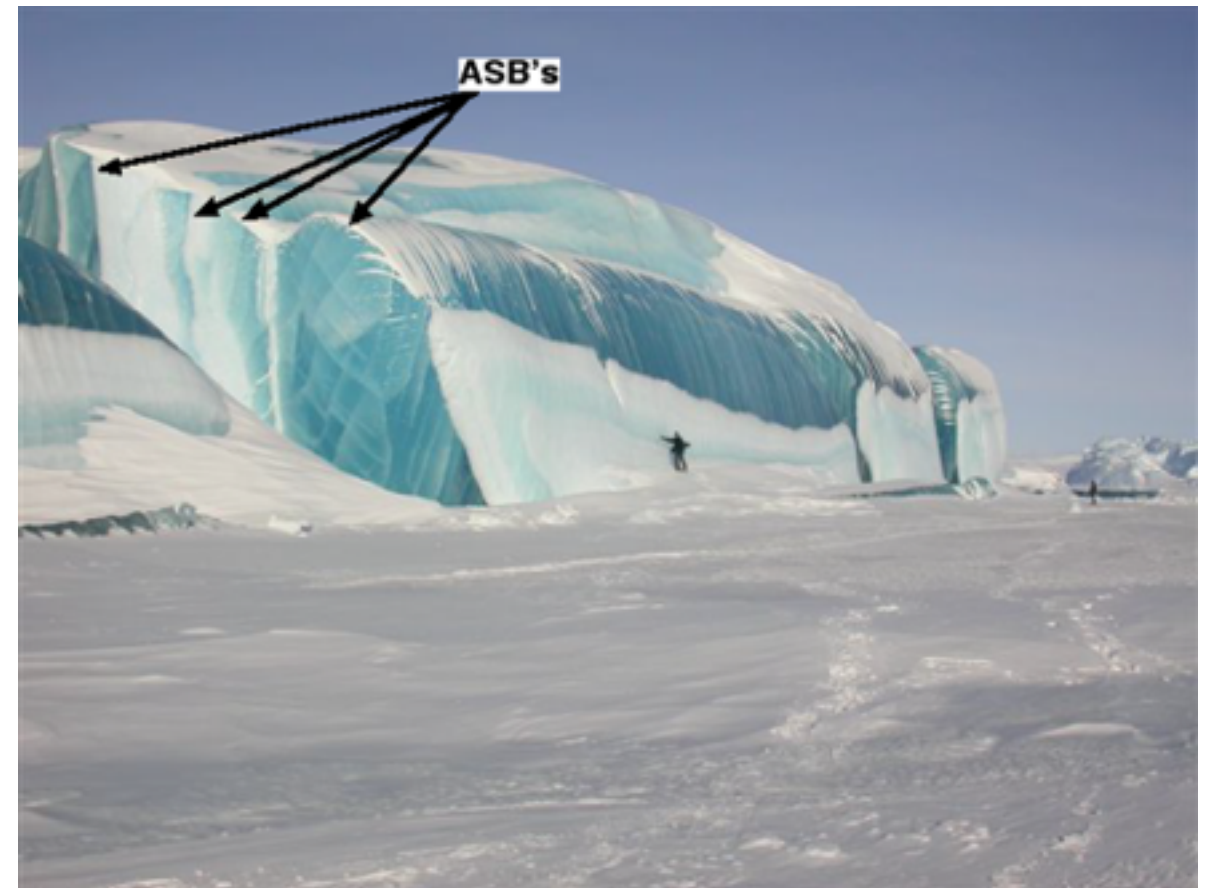


Figure 5.10 Pressure ice formation in Lake Michigan. Original image from the internet, anonymous contribution.

sion of the center of the band. Melting occurs in the shear bands due to the heating caused by local, permanent deformation and failure...the ice melting temperature is reduced by the compressive forces and only a few degrees of heating will produce melting inside and along the edges of the shear band. The temperature at the bottom of the ice sheet will be only a few degrees below the freezing point of water, so only a small amount of deformation and fracture is required to melt the ice inside the band.

There is a large number of small, secondary, crossing, localized shear bands exposed on the upper end of the foreground ASB in [Figure 5.10](#). These shear bands, which are marked by white lines, indicate the gross movement of and within this ASB. The crossing shear bands inside the ASB indicate changing asymmetries of the orthogonal stress vectors within the growing shear band. The curved shear bands at the top of this ASB reflect bending at the top surface that is produced by a higher rate of extrusion at the center of this ASB. Diagonal, crossing, periodic shear bands are also seen in the upper end of the second-back ASB which are comparable to those in the foreground ASB and consistent with the inferred stress pattern.

All of the aspects of the deformation and fracture process in water-ice are especially applicable to rock. For example, there is a one-to-one correlation between the effects of melting on the shear bands...i.e. necessary conditions for melting is dependent mostly on the physical and mechanical behavior of the material in which the shear bands form.

5.1.3.2 SEISMIC DIKES/FAULTS

The internal structure of seismic dikes is representative of the effects of localized shear at a slow strain rate in a strong, brittle material, and when these dikes develop in geologic materials (e.g. rock at room temperature), they contain mostly comminuted material...little or no melting...recall [Figures 4.1](#) and [4.10](#). The structural features of a typical, full scale seismic dike is seen in [Figure 5.11](#). These structures develop as a re-



Figure 5.11 Seismic localized shear dike exposed on a road cut along State Highway 200 in southwest Montana.

sult of localized shear deformation and fracture resulting from stress gradients that have developed over time in a large volume of the surrounding material. The stress release rate caused by the formation of localized shear in a seismic event does not exceed the sonic velocity in the surrounding material. The sudden formation of localized shear bands inside geologic structures caused by asymmetric stress buildup is a primary source of earthquakes.

The internal structure of the dike marked in [Figure 5.11](#) is essentially an extrapolation to a macro-scale of the microstructure of the shear band in sandstone illustrated in [Figure 4.10](#).

In both cases, the total number of broken bonds is relatively small and the strain rate is slow enough to allow the deformation and failure heat to be dissipated fast enough into the adjacent material to prevent significant softening or melting of rock inside or adjacent to the dike. However, generally there is sufficient deformation and fracture heat generated to promote some levels of bonding inside the dike, due in part to sintering of the comminuted debris. These seismic dikes can also be classed as faults because they represent lines of weakness in geologic structures. Seismic dikes can be more easily eroded than the immediately adjacent material which can develop trenches over time like those seen in the rims of both the Upheaval and Vredefort Domes where the strain rate was greatly reduced from early-stage cratering.

Dikes as Indicators of Geologic Impact Structures

SECTION TOPICS

5.2.1 Spanish Peaks Dikes

5.2.2 Black Dikes of the Teton Range

As has been previously noted, dikes and faults are ubiquitous in and around geologic impact structures. Also as discussed previously, especially in Chapter 3, the geometric patterns and the internal structure observed for many dikes and faults can be interpreted as strong indicators of their impact origin. In this section, we will briefly examine examples of dikes and faults found in and around two well known geologic structures...the Spanish Peaks of southern Colorado and the Teton Range of western Wyoming. Neither of these geologic structures have been proposed to have an impact origin, but data will be presented that points to formation of both of these moderately large geologic features by impact rather than tectonic processes.

5.2.1 SPANISH PEAKS DIKES

The prominent, solitary, twin Spanish Peaks of southern Colorado (Las Cumbres Españolas) host a famous dike swarm complex...see for example Johnson, 1968. These two peaks arise on the eastern flank of the nearby northern segment of the Sangre de Cristo Range. There are innumerable large, radial dikes, tens of meters wide that are exposed prominently for tens of kilometers. Many of these radial dikes are focused on the West Spanish Peak, but examples of several very long ridge dikes that form typical cross patterns are seen some distance northeast of the peaks. Many of these dikes are so large that they can be seen from very high altitudes...visible in the in the left side of [Figure 5.12](#). These dikes, which have universally been interpreted to have been formed intrusively, have

been determined to be relatively young...formed 22 to 27 x 10⁶ years ago, Penn and Lindsey, 2009.

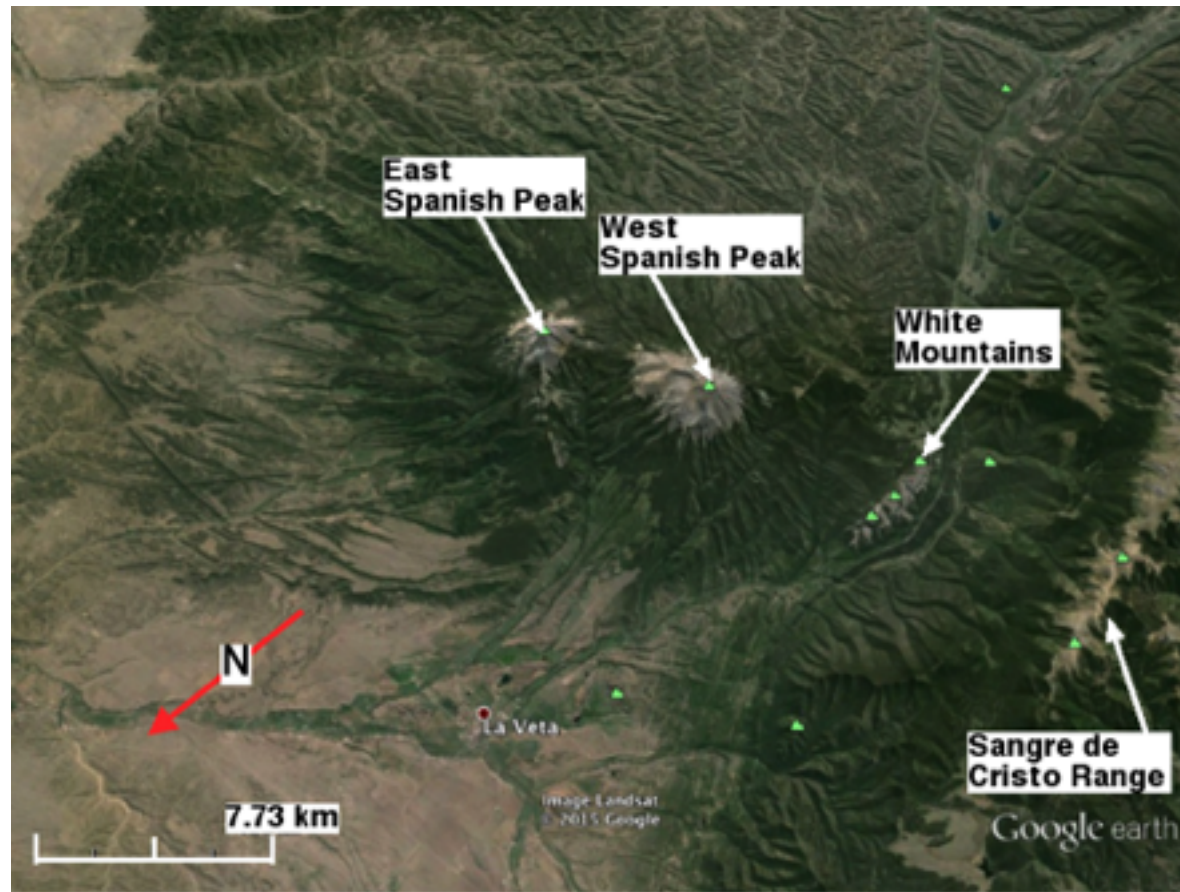


Figure 5.12 Satellite view of the Spanish Peaks of southern Colorado from the northwest. Original image from Google Earth

The overall structural features of one of the long, radial dikes located on the north side of the West Spanish Peak is shown in [Figure 5.13](#). These dikes form the crests of regularly spaced, radiating ridges much like the crest of the ridge previously seen in [Figure 5.2](#), and as can be seen in a closer view of the west side of the peaks in [Figure 5.14](#), many dikes of the Spanish Peaks complex are branched. The internal structure of the Spanish Peaks dikes consists of “granite porphyry,”

Johnson, 1968, but typically, these dikes possess an outer layer that is lighter colored, “bleached sandstone,” Johnson, 1968, indicative of a heat affected zone typical found on the edges of ASB’s, as previously discussed. This layering can be seen in [Figure 5.13](#).



Figure 5.13 Satellite view of a typical dike radiating from the Spanish Peaks of southern Colorado. Original image from Google Earth.

Several arcuate features observed east of the Sangre de Cristo Range can be interpreted as indicators of part of an impact crater rim, and similarly the collection of the Spanish Peaks can be interpreted as the central uplift of this same impact structure. A closer view of a series of periodic arcuate structures



Figure 5.14 Northwest flank of the West Spanish Peak and companion arcuate structures. Original image from Google Earth.

on the west flank of the West Spanish Peak is seen in [Figures 5.14](#) and [5.15](#). It can be noted that the overall periodic structure along the length of the White Peaks range, which is seen to be one of these arcuate structures, closely resembles that observed on the rims of the both the primary and secondary craters of the Vredefort Dome, where periodic segmentation of these rim structures correlates with the production of shear dikes that are derived from circumferential expansion of the crater...recall **Sections 3.2.1.2** and **3.2.1.3**. Another correlated arcuate structure is visible immediately west of the White Peaks in [Figures 5.14](#) and [5.15](#)...the village of Cuchara is

situated in the small valley west of the arcuate White Peaks ridgeline and east of a correlated arcuate ridgeline.

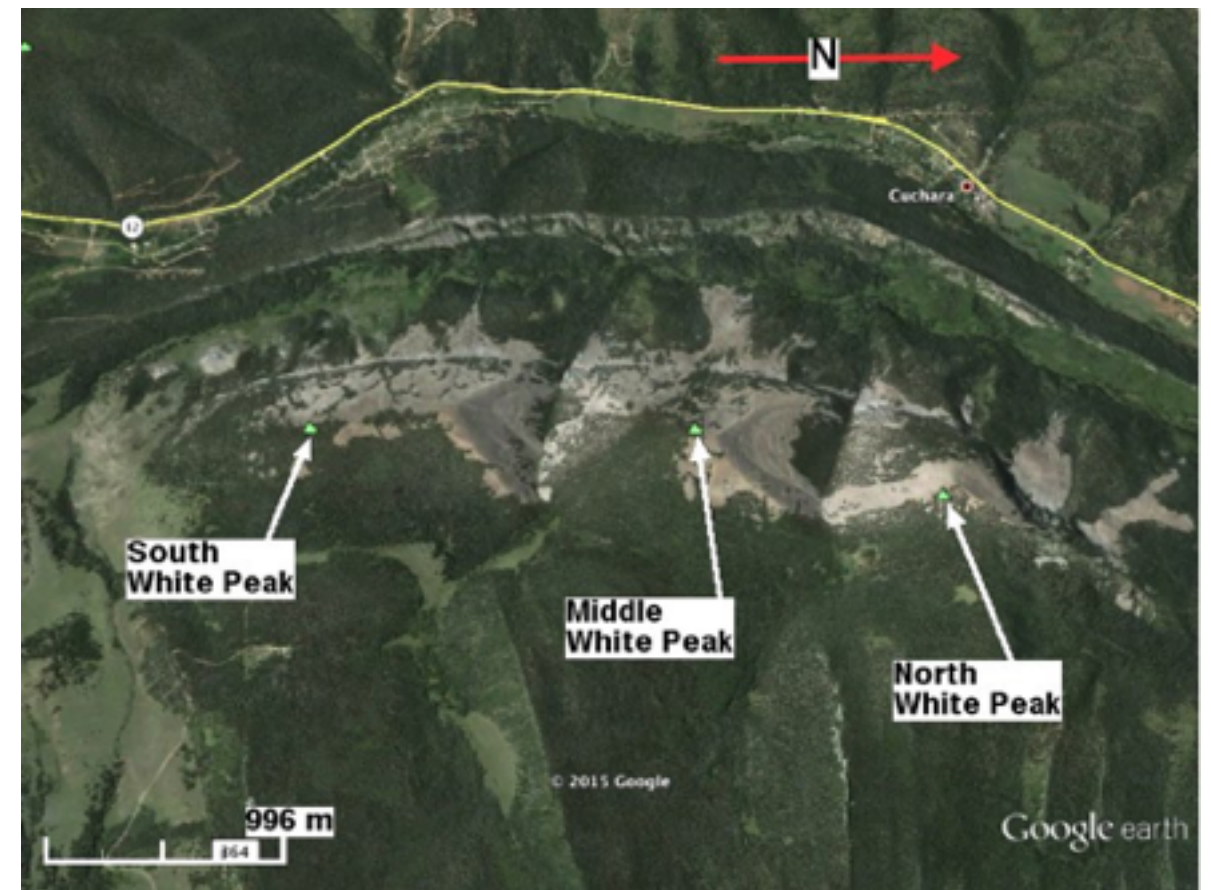


Figure 5.15 Arcuate structures on the west flank of the West Spanish Peak. Original image from Google Earth.

A very prominent pattern of crossed dikes is seen northeast of the East Spanish Peak in [Figure 5.12](#), and a closer view of these dikes along with a set of branched dikes is seen in the lower center of [Figure 5.16](#). All of these dikes appear to be spatially and structurally correlated with the proposed impact structure of the central-uplift Spanish Peaks.

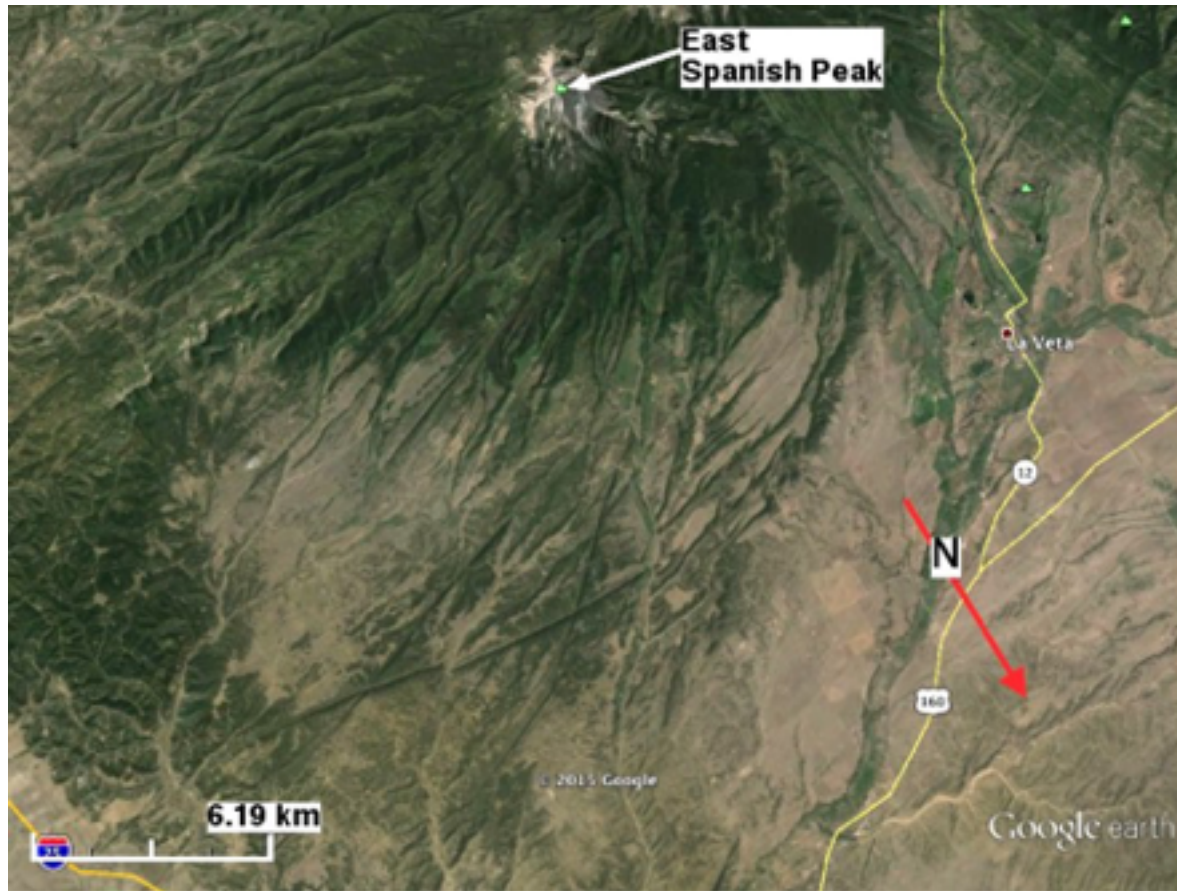


Figure 5.16 Large branched dikes northeast of the East Spanish Peak. Original image from Google Earth

5.2.2 BLACK DIKES OF THE TETON RANGE

The world famous Teton Range that is located in far western Wyoming has been studied by geologists for generations. The arc of the Teton Range is commonly designated as a part of the ‘Yellowstone Country’ which includes and surrounds the Yellowstone National Park located in the center of [Figure 5.17](#). First of all, the west opening arcuate planform of the Teton Range suggests that it might be the remnant of an impact structure. Incidentally, the arcuate character of the other marked mountain ranges in [Figure 5.17](#), Beartooths, Bighorns

and Bitterroots, suggest that these are also candidate impact structures.

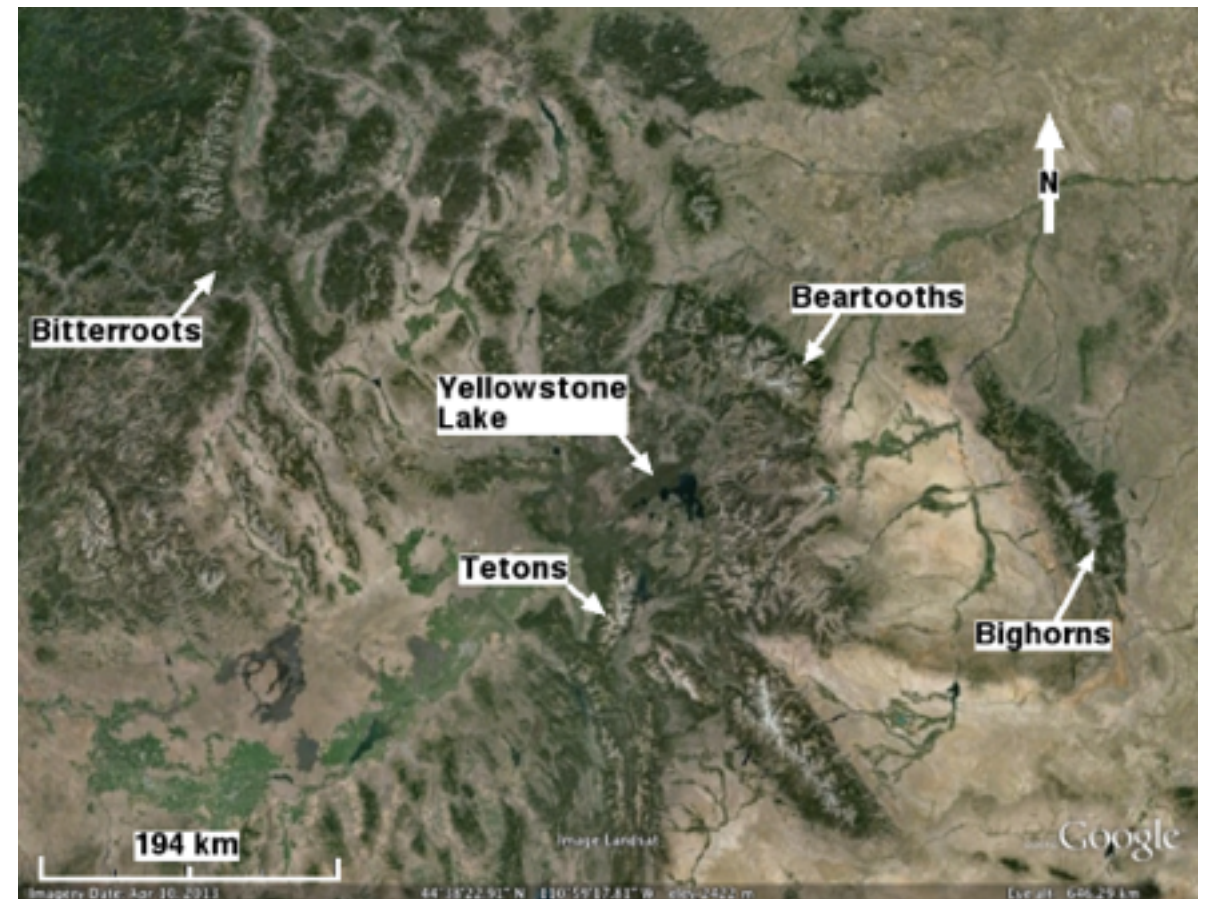


Figure 5.17 Contextual view of the Teton Range. Original image from Google Earth

Structural features that can be readily viewed in great detail, using Google Earth for example, also suggest that the Teton Range has been truncated on the south by a more recent impact structure. Traces of the Teton Range can still be seen in high altitude images all the way to Mount Baird that is located on the east edge of the Palisades Valley, but structural features related to a younger structure (also possibly derived from impact) appear to overlap the Teton Range up to about

Teton Pass. On the north, the Teton Range is truncated by the much younger, chaotic geology within and immediately around the Yellowstone National Park. The core of the Tetons has been determined to be Precambrian, and the origin of the range is popularly *believed* to have been due to tectonic processes, Love, et al., 2003.

An example of a large collection of well researched, branched dikes, that we can conclude was formed at high strain rate localized shear rather than by intrusion, is prominently exposed in solid granite on the east face and over the top of Mount Moran toward the west in the Teton Range. The Mount Moran Black Dike complex, indicated in [Figure 5.18](#), has been tracked west across the Teton Range for as far as 11 km, Love, et al., 2003. The width of the exposure of the main branch of this dike is observed to be as great as ~50 m. The main line of the Black Dike and its tributaries mostly define the crests of ridges. Similar smaller black dikes are also exposed on the east faces of the Middle Teton...[Figure 5.19](#)...and the south face of the Grand Teton.

The presence of these black dikes in the Teton Range strongly suggests that the Teton Range was initially formed by an impact event. If indeed the Teton Range was formed by impact and represents a remnant of a primary crater rim, the original impact structure could have been ~200 km across and was probably formed by an oblique impact from the northwest.

There is clear evidence that melting has occurred inside the Black Dike in Mount Moran, Love, et al, 2003, but an intru-

sive source of the melted material has not been identified...as you might expect. The erosion rate of material inside these black dikes is slightly less than that of the surrounding older granite which causes them to stand above the adjacent material. The orientation of the line of these black dikes relative to the generally north-south trace of the Teton Range is analogous to the radial dikes previously discussed relative to the Upheaval Dome, Vredefort Dome, and the Spanish Peaks.

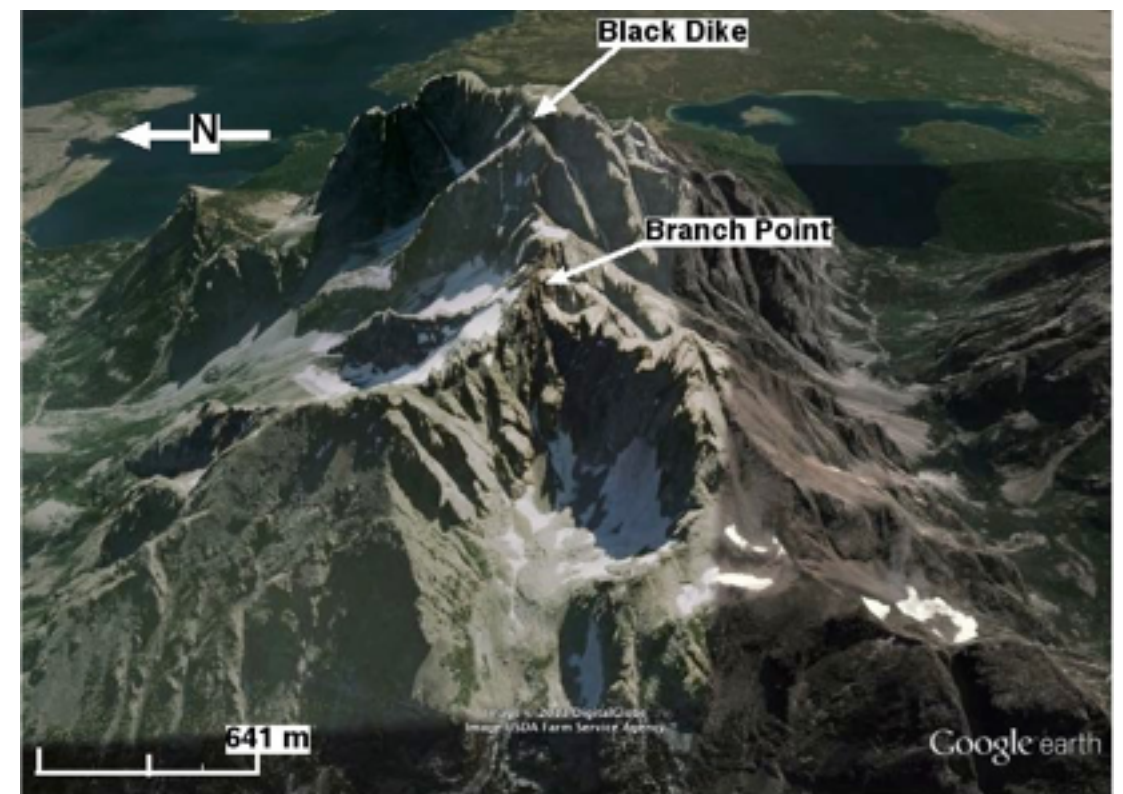


Figure 5.18 Exposure of the Mount Moran Black Dike and its branches...viewed from the west side of Mount Moran. Original image from Google Earth.

The structural features of the interior of the Black Dike are melt derived from the surrounding granite which gave it its black color...rather than basalt from an outside source as generally proposed. From data presented by Love, et al., 2003,

incomplete melting along the boundaries between the dike and the surrounding granite is indicated. Larger crystals were found toward the center of these dikes indicating that high temperatures were maintained toward the centerline of the dikes for substantial periods which allowed significant grain growth after solidification.

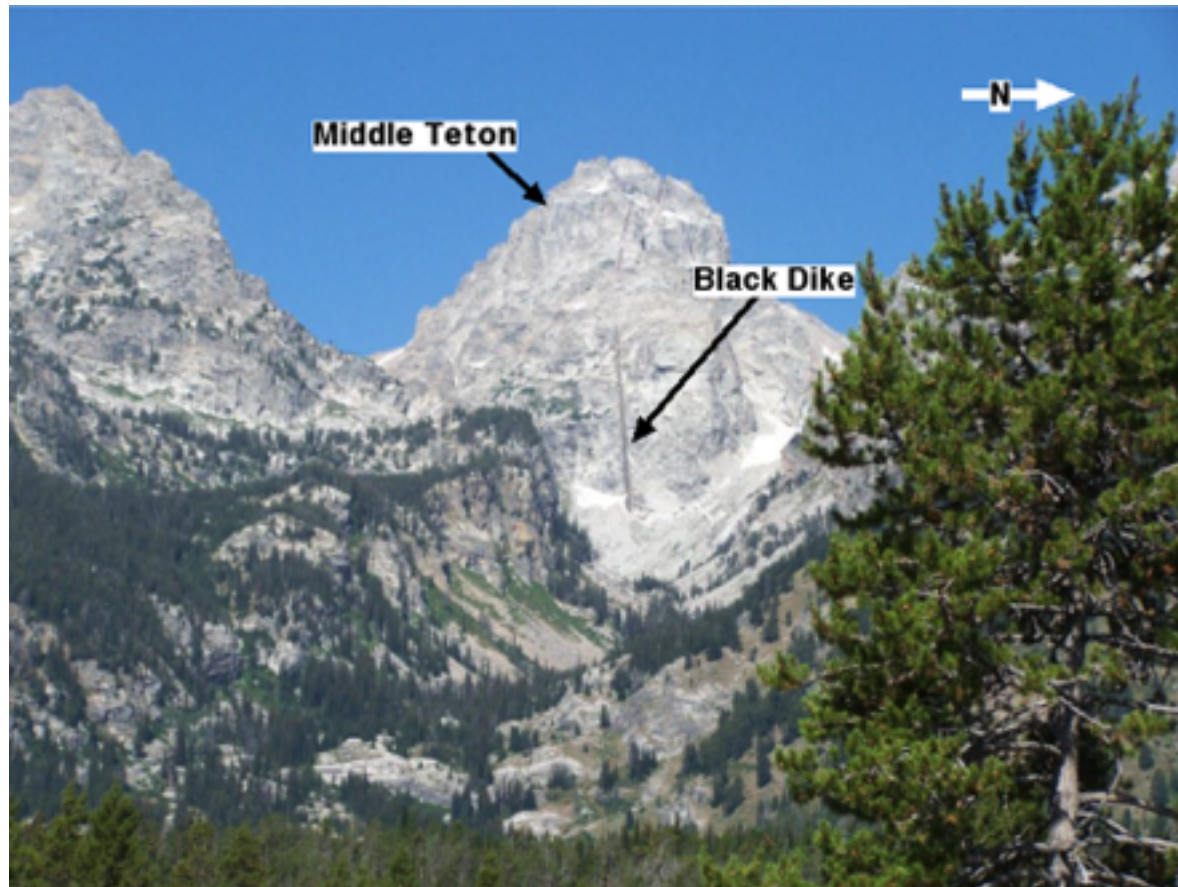


Figure 5.19 A typical black dike exposed in the Teton Range on the east face of the Middle Teton.

Because the black dikes of the Teton Range were formed *in situ* via localized shear rather than by an intrusive process, their age can be used to infer the formation time of the entire mountain range...assuming it was formed via an impact event.

The $^{40}\text{Ar}/^{39}\text{Ar}$ age of plagioclase extracted from the center of the Black Dike has been determined to range from 583 to 396 $\times 10^6$ years, Reed and Zartman, 1973, but these same authors determined the $^{40}\text{Ar}/^{39}\text{Ar}$ age of the chilled edge to be 775 $\times 10^6$ years. Harlan, et al., 1997 determined that the age of hornblende samples from the Black Dike are close to that reported by Reed and Zartman, 1973 for the chilled margin. Because the dike represents a melted body derived from the wall rock during its formation, $^{40}\text{Ar}/^{39}\text{Ar}$ age samples from the central region of the Black Dike should yield the most reliable formation time, i.e. 583 to 396 $\times 10^6$ years. The older of these ages is preferably indicated by the fact that an $\sim 500 \times 10^6$ year old layer of Flathead Sandstone rests on the top of Mount Moran, Love, et al., 2003. Also, it is estimated that dolomite marine deposited formations on the west slope of the Teton Range started developing $\sim 500 \times 10^6$ years ago. Unfortunately as discussed in **Section 4.2.4.1** and demonstrated by Mulch and Cosca, 2004, the results of $^{40}\text{Ar}/^{39}\text{Ar}$ age analysis are very sensitive to sample microstructure and micro-chemical variations. In spite of the large variation in the reported $^{40}\text{Ar}/^{39}\text{Ar}$ ages, these quoted formation age estimates for the Tetons are radically older than the popular, proposed tectonic formation of the Range...67 to 80 $\times 10^6$ years ago, Love, et al., 2003.

Chapter 5 References

Adachi, T. and Kletetschka, G., 2008, Impact-pressure controlled orientation of shatter cone magnetizations in Sierra Madera, Texas, USA, *Studia Geophysica Et Geodaetica*, 52, pp. 237-254.

Armstrong, R., Reimold, W. U., Charlesworth, E. G., and Ortlepp, W. D., 2003, Comparison of the fractography of rockbursts and impacts structures, ISRM 2003–Technology roadmap for rock mechanics, South African Institute of Mining and Metallurgy, pp. 49-55.

French, B. M., 1998, *Traces of Catastrophe: A Handbook of Shock-Metamorphic Effects in Terrestrial Meteorite Impact Structures*, LPI Contribution No. 954, Lunar and Planetary Institute, Houston, 120 pp.

Harlan, S. S., Geissman, J. W., and Snee, L. W., 1997, Paleomagnetic and $^{40}\text{Ar}/^{39}\text{Ar}$ Geochronological Data from Late Proterozoic Mafic Dikes and Sills, Montana and Wyoming,

U.S. Geologic Survey Professional Paper 1580, United States Government Printing Office, Washington: 1997.

Johnson, R. B., 1968, *Geology of the Igneous Rocks of the Spanish Peaks Region Colorado*, Geological Survey Professional Paper 594-G, United States Government Printing Office, Washington, D.C.

Lieger, D., 2011, *Structural and Geochemical Analyses of fragment-rich pseudotachylite bodies and the Vredefort Granophyre of the Vredefort Impact Structure, South Africa*, Thesis submitted to the Department of Earth Sciences, Free University of Berlin, Germany, in partial fulfilment of the requirements for the degree of Doctor rerum Naturum.

Love, J. D., Reed, J. C., Jr. and Pierce, K. L., 2003, *Creation of the Teton Landscape: A Geological Chronicle of Jackson Hole and the Teton Range*, Grand Teton Natural History Association, Moose, WY.

Lundberg, L. B., 2009, *Impact Geology: Fundamentals of Impact Crater Formation*, *Northwest Geology*, 38, pp. 67-88.

McHone, J. F., Shoemaker, C., Kilgore, M., and Kilgore, K., 2012, *Two Shatter-Coned NWA Meteorites*, presented at the 43rd Lunar and Planetary Science Conference (20124), Abstract No. 2359.pdf.

Mulch, A. and Cosca, M. A., 2004, Recrystallization or cooling ages: in situ UV-laser $^{40}\text{Ar}/^{39}\text{Ar}$ geochronology of muscovite in mylonitic rocks, *Journal of the Geological Society, London*, Vol. 161, pp. 573–582.

Penn, B. S. and Lindsey, D. A., 2009, $^{40}\text{Ar}/^{39}\text{Ar}$ dates for the Spanish Peaks intrusions in south-central Colorado, *Rocky Mountain Geology*, Spring, 2009, v. 44, pp. 17-32.

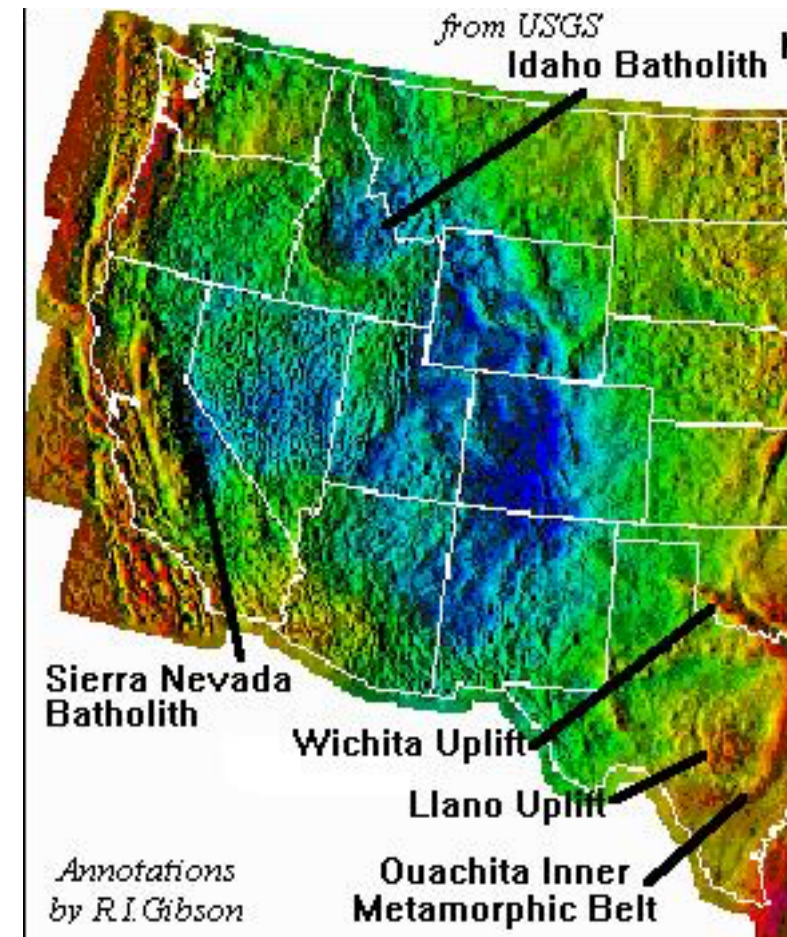
Reed, J.C., Jr. and Zartman, R. E., 1973, Geochronology of Precambrian rocks of the Teton Range, Wyoming, *Geological Society of America Bulletin*, v. 84, p. 561-582.

Tarbuck, Edward J. and Lutgens, Fredrick K., 2005, *Earth: An Introduction to Physical Geology*, 8th Ed., Pearson Prentice Hall, Upper Saddle River, NJ.

Thompson, L. M., 2014, Radial Distribution of Impact Damage at Manicougan: Shock, Comminution and Shatter Cones, presented at the 45th Lunar and Planetary Science Conference (2014), Abstract No. 2017.pdf.

Wieland, F., 2006, Structural analysis of impact-related deformation in the collar rocks of the Vredefort Dome, South Africa, Thesis submitted to the Faculty of Science, University of the Witwatersrand, Johannesburg, South Africa, in fulfillment of the requirements for the degree of Doctor of Philosophy.

Geologic Impact Structure Identification and Verification



The Bouguer gravity anomaly map above is considered an indicator of impact structures. This map of the western United States suggests for example that the Idaho Batholith might in fact represent a part of an impact structure...possibly the central uplift.

Throughout this volume we have been examining the structural features of geologic impact structures found primarily on the dry-land surfaces of Earth...both accepted and proposed. However so far in this volume, crater identification has not been examined explicitly. There have been several published attempts at describing the rules of impact structure recognition...e.g. Therriault, et al., 2002 and Pati and Reimold, 2007, but in general, these authors and most others dealing with this subject have not reflected an accurate understanding of the fundamentals of impact cratering leading to an inability to recognize many of the salient identifying features of geologic impact structures. For the most part, the credibility of their guidance in recognizing terrestrial impact structures is questionable or at least insufficient. For example, Therriault, et al., 2002 contend that ‘crater mechanics cannot be extrapolated;’ whereas, the previous discussion clearly demonstrates that every aspect of hypervelocity impact crater formation can be extrapolated directly from laboratory-scale to full size geologic impact structures.

The identification and verification of geologic impact structures is much like assembling a large jig-saw puzzle that contains thousands of pieces. However, the best way to start to assemble a jigsaw puzzle is to examine a picture of the final assembly, so the first step in the identification of a dry-land impact structure on Earth is a detailed examination of high resolution (down to a few meters) satellite imagery using tools such as Google Earth which have the capability of easily viewing Earth’s surface from a variety of altitudes and view angles.

Consequently, many puzzle pieces that are consistent with expected structural features can be identified remotely. Nevertheless, impact structure verification still requires ground examination and verification of substructural features that are unique to geologic impact structures.

In Chapter 3, we examined structural details of the *accepted* Upheaval Dome and Vredefort Dome impact structures, while in Chapter 5 we expanded the impact structure identification discussion by concentrating on substructural features that are found to be peculiar to geologic impact structures. The Rocky Mountains of the western United States and Canada are littered up and down the mountain chain with easily identifiable candidate impact structures. Based on analysis of areal impact frequency data presented in [Figure 1.6](#), there should be at least 295 impact structures with diameters >1 km in the satellite image presented in [Figure 6.1](#) that have been formed in the last 900×10^6 years.

The following discussion will briefly examine two probable impact structures, among the many, that are located mostly in southwestern Montana where segments of their rims define the Montana-Idaho border. We will first examine a probable impact structure rimmed on the south by the Beaverhead mountain range, and the second will be a probable impact structure whose western rim is partially defined by the Bitterroot range. The context of these proposed impact structures can be seen in the high altitude satellite imagery presented in [Figure 6.1](#), where we can see several large candidate

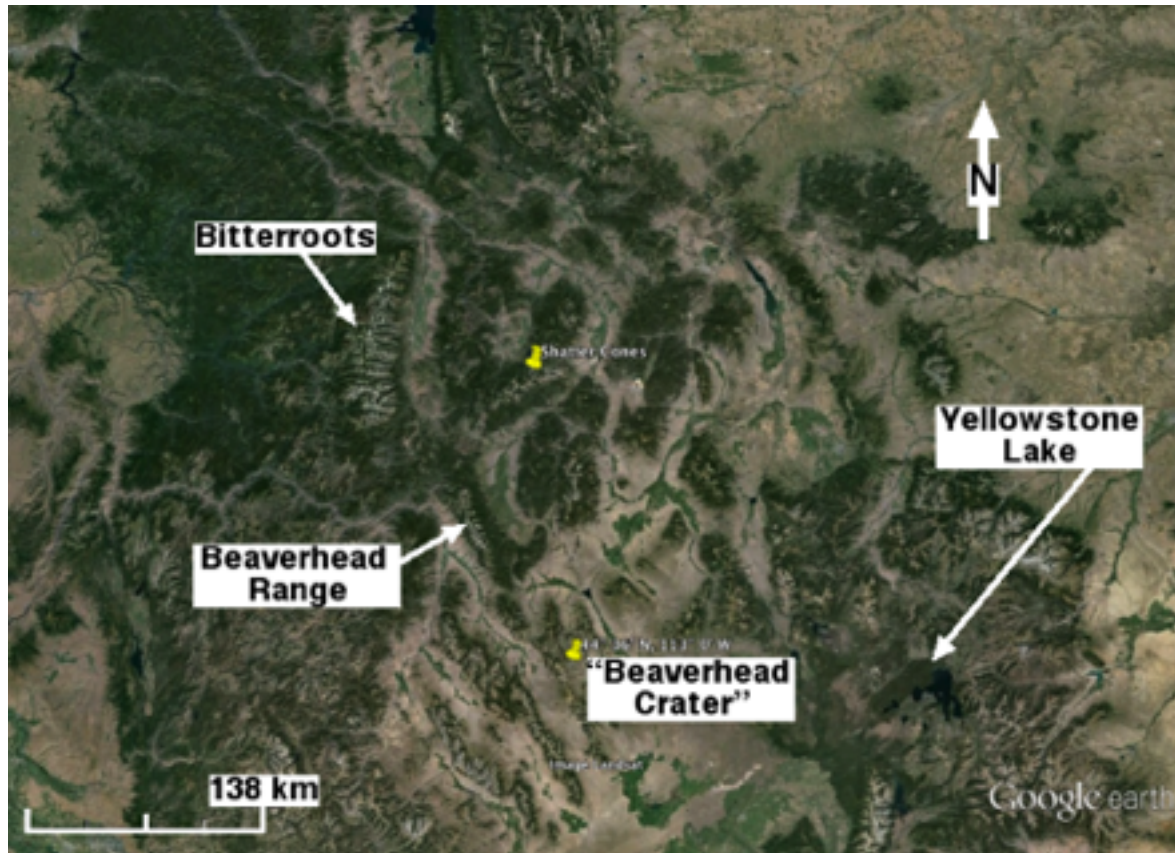


Figure 6.1 High altitude view of southwest Montana along the border with Idaho and northwest Wyoming. Original image from Google Earth.

impact structures...including the circular structure around Yellowstone Lake.

These two proposed impact structures are being examined because they are large, not unique (actually partially overlapping) and both appear to have been created by oblique impacts, the most common type of geologic impact structure, during separate impact events. The impact structure bounded on the west by the Bitterroots appears to be the older of the two, as it appears to have been partially overprinted by another large impact structure whose rim is defined by the

Beaverhead and Anaconda Ranges. It is very likely that both of these two impact structures overprinted older impact structures, and as will be discussed, there is evidence of subsequent impact overprinting of both of these structures.

The goal of the following discussion is to provide, by example, a practical framework for the identification and confirmation of geologic impact structures on the dry surfaces of Earth. However due to a shortage of relevant ground data, the following exercises will only be an introduction to the ground confirmation process. In fact, much of the ground-data presented and discussed will be derived from publications where the interpretation of the data is based on tectonic models for the formation of geologic structures. In every case, the authors did not demonstrate an awareness of the applicability of their data to interpretations based on Impact Geology.

Beaverhead/Anaconda Impact Structure

SECTION TOPICS

6.1.1 B/A-IS Rim Structure

6.1.2 Central Uplift of the B/A-IS

As can be seen in [Figure 6.1](#), the Beaverhead Range has a distinct arcuate planform that extends northward along the Idaho-Montana border and makes a connection with the arc of the Anaconda Range, which continues the arc eastward. The arcuate feature defined by a combination of these two mountain ranges is proposed as the downrange rim of the Beaverhead/Anaconda Impact Structure (B/A-IS). A closer view of the full arc and other features of the B/A-IS can be seen in [Figure 6.2](#). The full arc of the B/A-IS forms a 'collar wall' much like that exhibited along the outer perimeter of the Vredefort Dome...described and discussed in **Section 3.2**. The collar wall of the B/A-IS appears to be a remnant of the rim of a primary crater.

Graphically extending the arc that is defined by the combined Beaverhead and Anaconda Ranges indicates the perimeter of the B/A-IS to be about 120 km across. The fact that only about one quarter of the rim of this impact structure is still exposed along with its general planform indicates that the impactor was traveling along a trajectory $<45^\circ$ above the horizon generally from the east. The center section of the rim of the B/A-IS (west side between the Beaverhead and Anaconda Ranges) consists of a set of less rugged hills/mountains. Examination of the satellite imagery reveals a circular structure in this section of the B/A-IS rim that is ~ 30 km across...suggesting an overprint impact structure that has modified the rim structure of the B/A-IS at this location much like those seen on the rim of the Einstein crater on Earth's Moon...recall [Figure 1.2](#).

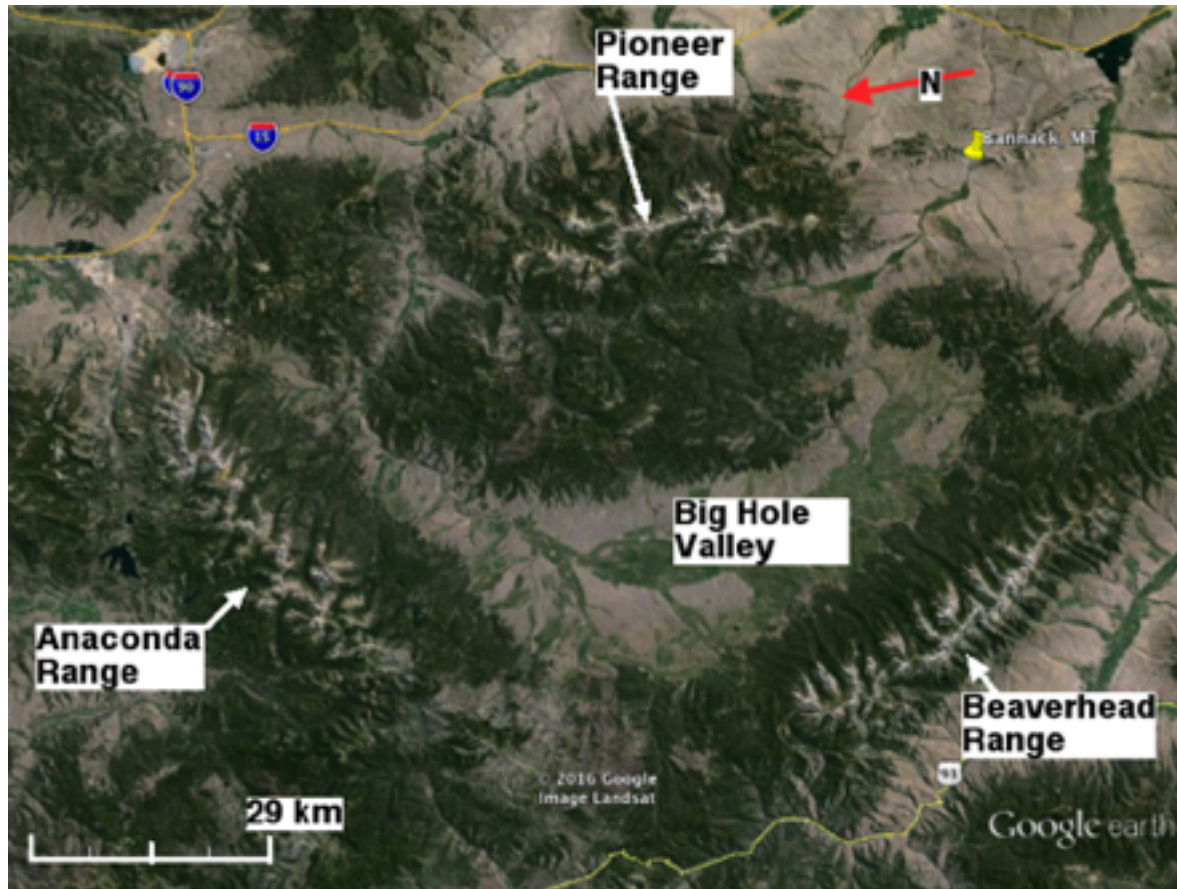


Figure 6.2 View of a proposed large impact structure that is rimmed by the Beaverhead and Anaconda Ranges. Modified Google Earth image.

The hook shaped feature seen in the righthand of the image in [Figure 6.2](#) probably indicates one or more additional overprint impact structures. This region of the B/A-IS, which appears to contain several overprint impact structures, will be identified and examined in some detail later in **Subsection 6.1.1.2.**

From a historical and regional perspective on impact structure identification, the center of an *accepted* ~100-km-diameter impact structure marked as the “Beaverhead Crater” in [Figure 6.1](#). This impact structure was originally proposed

by Fiske and Hargraves, 1994 mostly on the basis of the presence of shatter cones found near the location marked in [Figure 6.1](#). In spite of the fact that shatter cones are found around this location, there is no visible surface indication of an unique impact structure of this size centered around the mark. (Fiske and Hargraves, 1994 attempted to explain this inconsistency by proposing a tectonic shift of surface indicators of the crater center...shatter cones.)

An arcuate feature that is marked B/A-IS in the Bouguer gravity map in [Figure 6.3](#) maps closely with the arc of the combined Beaverhead and Anaconda Ranges. Aeromagnetic surveys are used to identify and define the general shape of impact structures on Earth...see for example Anhaeusser, et al., 2010. The Bouguer gravity map seen in [Figure 6.3](#) shows several additional anomalous areas that are consistent with satellite imagery of other probable impact structures. For example, this map has also been used to indicate the location of the original center of the accepted Beaverhead impact structure before *hypothesized* significant eastern migration of its surface manifestations (shatter cones)...at the location identified in [Figure 6.1](#). However, it is more likely that the blue area inside the square in [Figure 6.3](#) is related to the central uplift of an older, very large (perhaps over 600 km across) impact structure that is heavily overprinted by many subsequent impacts and whose outer rim is partially defined by the trace of the Snake River Plain and its southern boundary...clearly visible in the high altitude view of the western United States in [Figure 1.11](#).

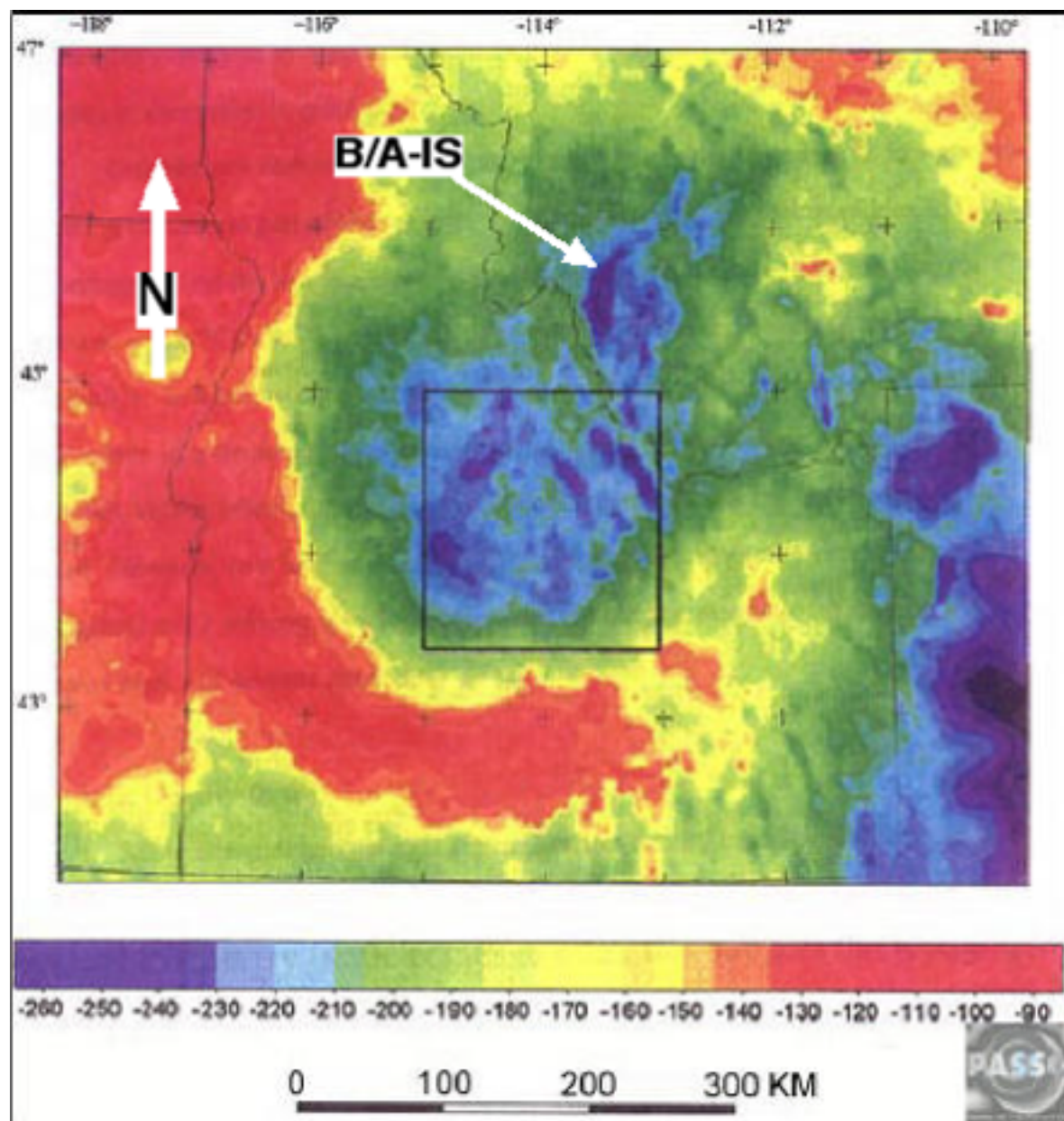


Figure 6.3 Bouguer gravity anomaly map of central Idaho and southwest Montana. Modified from an image found at <http://www.unb.ca/passc/ImpactDatabase/>.

6.1.1 B/A-IS RIM STRUCTURE

The rim of the B/A-IS is structurally similar to that observed for the secondary crater rims of both the Aristarchus crater on Earth's moon ([Figure 1.3](#)) and the Vredefort Dome impact

structure (collar wall) on Earth ([Figure 3.13](#)). Recent structural mapping of the northern segment of the Beaverhead Range, Lonn, et al., 2013, has defined many substructural features that are consistent with an impact origin even though the authors never considered this possibility. In the following sections, these published data plus additional original field-research data will be mentioned and discussed to support the proposition that the combined Beaverhead and Anaconda Ranges define the rim of an impact structure.

6.1.1.1 BEAVERHEAD RANGE AND THE B/A-IS

A satellite image of the northern segment of the Beaverhead Range that was mapped by Lonn, et al., 2013 can be seen in [Figure 6.4](#). The ridgeline of the Beaverhead Range marked with a blue line defines the border between Idaho and Montana. The locations of Freeman Peak and Bloody Dick Peak are indicated to aid in orienting the viewer.

The segment of the Beaverhead Range seen in [Figure 6.4](#) measures only about 14 km across, and the slope of the range is much more extreme on its southwest side. This slope asymmetry is characteristic of the rim of an impact crater. This segment of the Beaverhead Range is made up mostly of basement rock which contains many examples of localized shear that are currently exposed as dikes or faults. The ridgelines that are normal to both sides of the longitudinal ridgeline of the range are strikingly periodic along the length of the range...the ridgeline frequency is notably higher on the southwest side which would be expected for an impact crater rim that is expanding



Figure 6.4 Satellite view of the section of the Beaverhead Range mapped by Lonn, et al., 2013. The light blue line marks the Idaho-Montana border. Modified from a Google Earth image.

radially and circumferentially due to force vectors around a growing impact crater. This pattern of canyon traces compares to the periodicity of the radial canyons through the primary and secondary crater rims of the Vredefort Dome, discussed in Chapter 3, which formed as a result of the late-stage, radial and complementary circumferential expansion of the impact crater...also comparable to the radial canyons in the White Peaks west of the Spanish Peaks, recall [Figure 5.15](#). Incidentally, the canyon pattern is also consistent with an ex-

trapolation of the radial crack pattern illustrated in [Figure 4.19](#) that was produced in the laboratory.

Major faults run parallel along the length of the southwest side of the northern Beaverhead Range...mapped by Lonn, et al., 2013. The pattern of these faults can be compared to the circumferential crack pattern illustrated in [Figure 4.19](#). Welded breccia and sheared mylonite are exposed along these fault traces indicating localized adiabatic shear deformation. Complimentary crossing faults/dikes are also reported along these faults. These features can be interpreted as ‘circumferential’ and radial faults that are commonly formed across the rims of impact craters.

Freeman Peak, marked in [Figures 6.4](#) and [6.5](#), possesses a set of parallel dikes/faults exposed on its northwestern flank that step periodically along the entire length of the peak’s ridgeline and are oriented normal to a branched ridge dike. The periodicity of these dikes/faults is graphically illustrated in the closer view in [Figure 6.5](#). The traces of these dikes/faults appear to be less easily eroded than the material between...this would have caused the periodic vertical ravines between the ridges to deepen relative to the adjacent ridgeline rock over time. A similar ridge face that contains periodic layers of “Thin bedded quartzite, siltite, and argillite” was observed on the north side of the northern Beaverhead Range, Burmester, et al., 2013. The quartzite layers lie parallel to the length of the range, so they can be interpreted as ASB’s resulting from impact cratering.

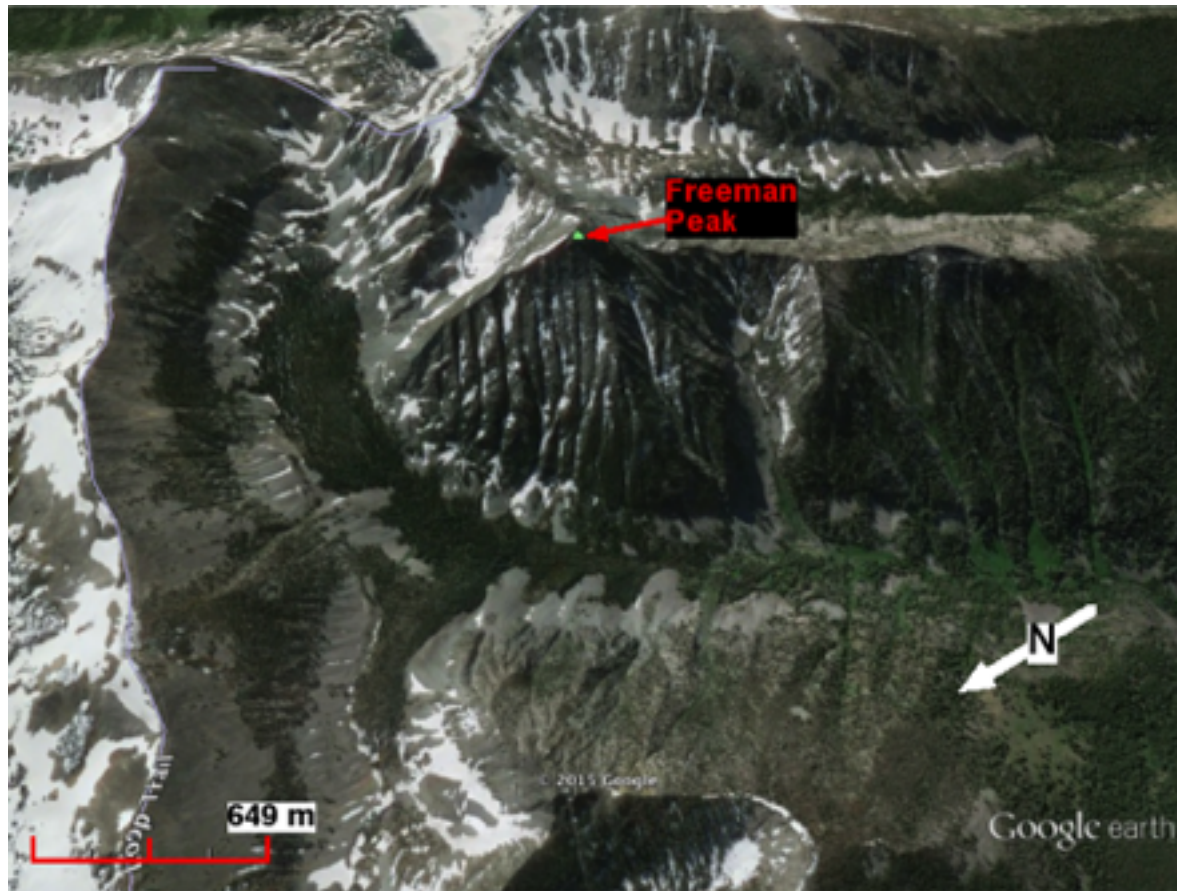


Figure 6.5 Northwest flank of Freeman Peak in the Beaverhead Range. The light blue line marks the Idaho-Montana border and the divide ridge of the Range. Modified Google Earth image.

Many additional substructural features peculiar to impact structures are found throughout the northern Beaverhead Range. For example, a photograph of the surface of a shatter cone found on the north slope of the Beaverhead Range in the Shewag Lake quadrangle is presented as Figure 6 in Steel and Link, 2013...these authors classified the shatter cone as “Trough crossbedding.” Bands of welded breccia are also found in the “Swauger Formation” located west of Homer Youngs Peak (this peak is located about 5 km north of Freeman Peak)...photo presented as Figure 4 in Burmester, et al.,

2013. A photograph of a rock (in Swauger Formation) found in this same publication was interpreted by the authors to contain “Large mud cracks” when in fact these ‘cracks’ are clearly ASB’s that were probably formed by impact...see the photograph reproduced here in [Figure 6.6](#). As we have discussed previously, this shear band pattern is characteristic of ASB’s formed in dense rocks by asymmetric triaxial stresses during the late-stage impact cratering process.



Figure 6.6 Adiabatic localized shear bands in a rock found between Homer Youngs Peak and Miner Creek on the north slope of the Beaverhead Range. Photographic data from Burmester, et al., 2013, Figure 5.

The gentle slopes immediately below the southwest side of the Range seen in [Figure 6.7](#) (below the treeline, the bottom line of which marks the “Salmon Basin Detachment Fault” (defined by Steel and Link, 2013 and others) are covered with sedimentary debris much of which looks very much like regolith found on Earth’s moon...recall [Figure 1.5](#). In fact, many

loose rocks found scattered over the surfaces of these slopes contain adiabatic shear veins similar to those previously seen in the clasts in [Figure 5.3](#) and the rock in [Figure 5.7](#). Furthermore, the shallow sloping approach to the southwest side of the Beaverhead Range is divided periodically along the length of the Range into chevrons whose apices point to the main ridgeline to the Range...recall similar features observed in the laboratory and around the Upheaval Dome, e.g. [Figure 3.6](#), and the Vredefort Dome, e.g. [Figure 3.21](#).

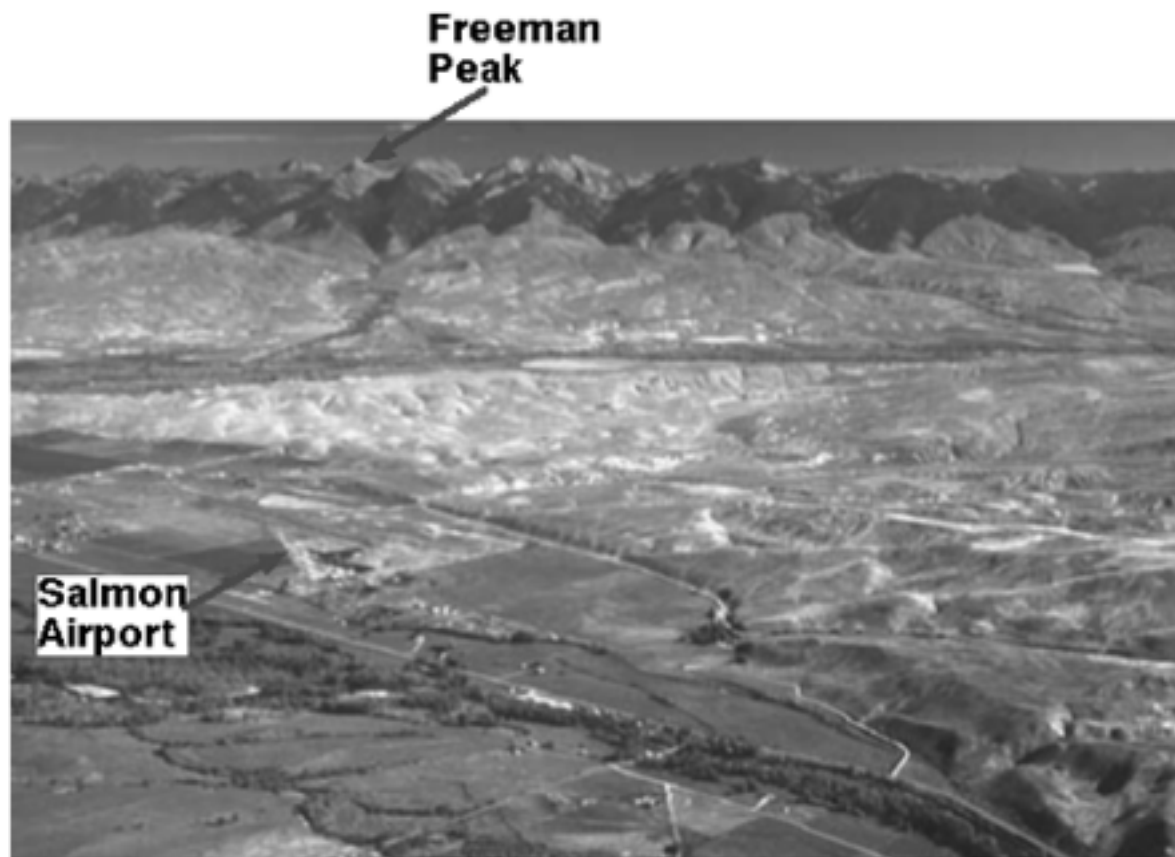


Figure 6.7 View north across the Salmon Basin toward the Beaverhead Range. Original image from Link and Janecke, 1999.

The Lemhi River flows from right to left across the view presented in [Figure 6.7](#), which is a tributary of the Salmon River that flows from the lower righthand corner of the photograph. An alluvial fan is observed above the Lemhi River below Freeman Peak, which suggests that the material below the “Salmon Basin Detachment Fault” is easily eroded as would be expected for impact ejecta (regolith).

6.1.1.2 B/A-IS OVERPRINT IMPACT STRUCTURES AT THE SOUTH END OF THE NORTHERN BEAVERHEAD RANGE

The presence of overprint impact structures complicates the definition of the bounding features of the larger, main B/A-IS impact structure. It has already been pointed out that a relative small impact structure appears to divide the west rim of the B/A-IS.

Extrapolating from data for the crater density measured for the area around the North Ray crater on Earth’s moon, which was determined to have formed about 53×10^6 years ago (see Table 9 in Le Feuvre and Wieczorek, 2011), approximately 1 overprint impact structure with a diameter >1 km should be visible in [Figure 6.2](#). However in fact, at least 7 candidate B/A-IS overprint impact structures that possess diameters >5 km can be found by close examination of the satellite image in [Figure 6.2](#). This is nearly an order-of-magnitude underestimation of the crater surface areal density that resulted from impacts after the B/A-IS was formed.

Fragments of the rims of three candidate overprint impact structures found in the hook structural feature observed in the right side of [Figure 6.2](#) appear to be a collection of several U-shaped features in [Figure 6.8](#). The probable trajectories of the impactors that formed these candidate overprint impact structures are indicated by yellow arrows in [Figure 6.8](#)...derived from the general shape of the crater rim remnants. The nearly parallel impactor trajectories for the structure that track north of Bloody Dick Peak and the structural feature that includes Maiden Peak on the east and tracks around a hyperbolic arc to Lemhi Pass on the west suggests that both might have been formed during the same event by moderately sized, slightly separated impactor fragments. The third inferred impactor trajectory appears to have formed the arcuate structure north of Bloody Dick Peak appears to have overrun the east side of the hook impact structure. At this point, there isn't sufficient data to conclude which event formed Bloody Dick Peak. Verification of these three plus the probable 4+ additional candidate overprint impact structures observed in [Figure 6.2](#) will require the collection and correlation of considerable quantities of ground data. Age dating the matrices of welded breccia or dikes in the overprint impact structures can provide supporting data for the age of the main B/A-IS impact structure.

6.1.1.3 ANACONDA RANGE AND THE B/A-IS

The planform of the Anaconda Range which is seen at high altitude in [Figure 6.9](#) completes the arc of the remnant of the downrange rim of the B/A-IS. The consensus among traditional geologists indicates that the Anaconda Range starts a

few kilometers northeast of Lost Trail Pass and terminates just short to the historic copper smelting town of Anaconda, MT...this definition of the range is ~55 km in length. The Flint Creek Range, which will be discussed in the following sections relative to the central uplift of the Bitterroot Impact Structure, abuts the north end of the Anaconda Range. The breadth of the Anaconda Range measures up to about 18 km.

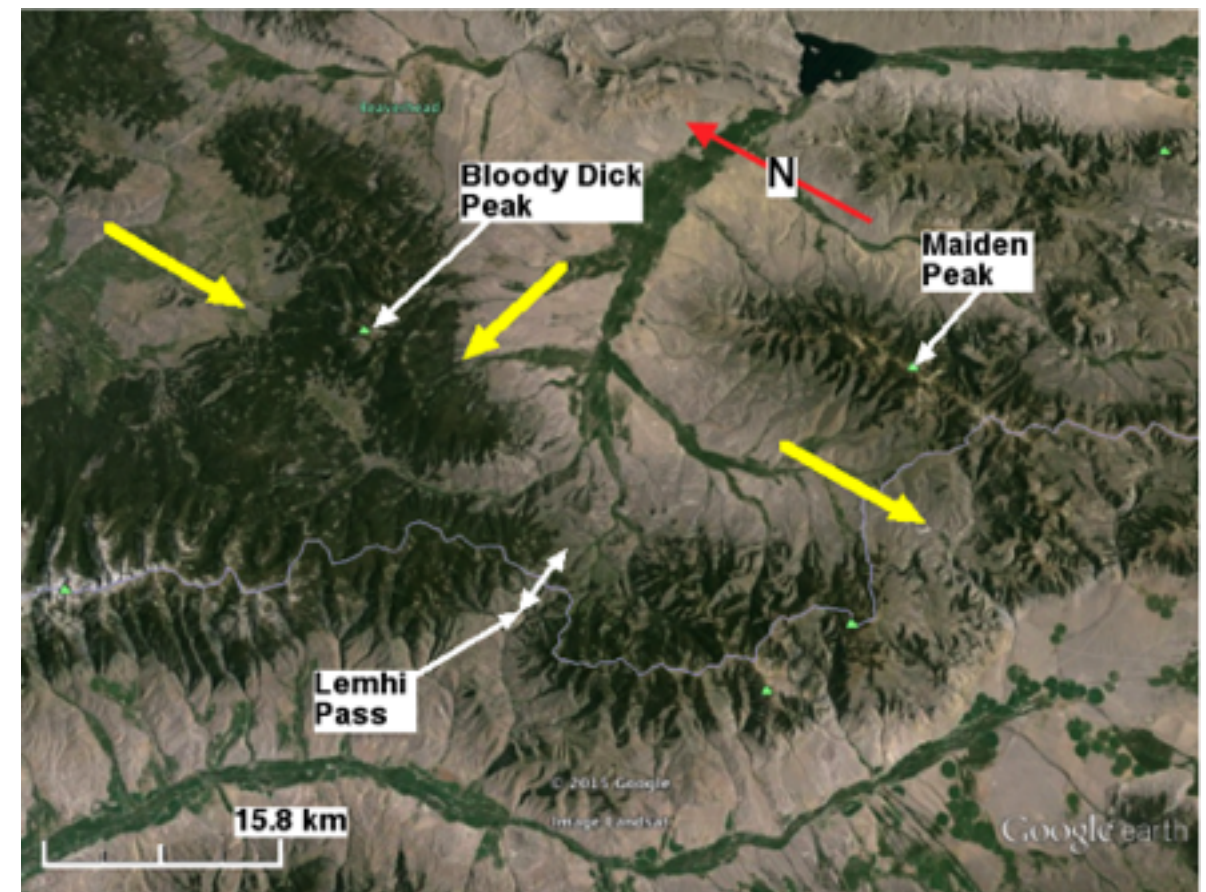


Figure 6.8 View of proposed overprint impact structures along the inside of the southern rim of the Beaverhead/Anaconda Impact Structure. The yellow arrows indicated proposed impactor trajectories. Modified Google Earth image.

A strip of exposed “Eocene Mylonite,” marked in [Figure 6.9](#), is observed all along the east side of the Anaconda Range...see

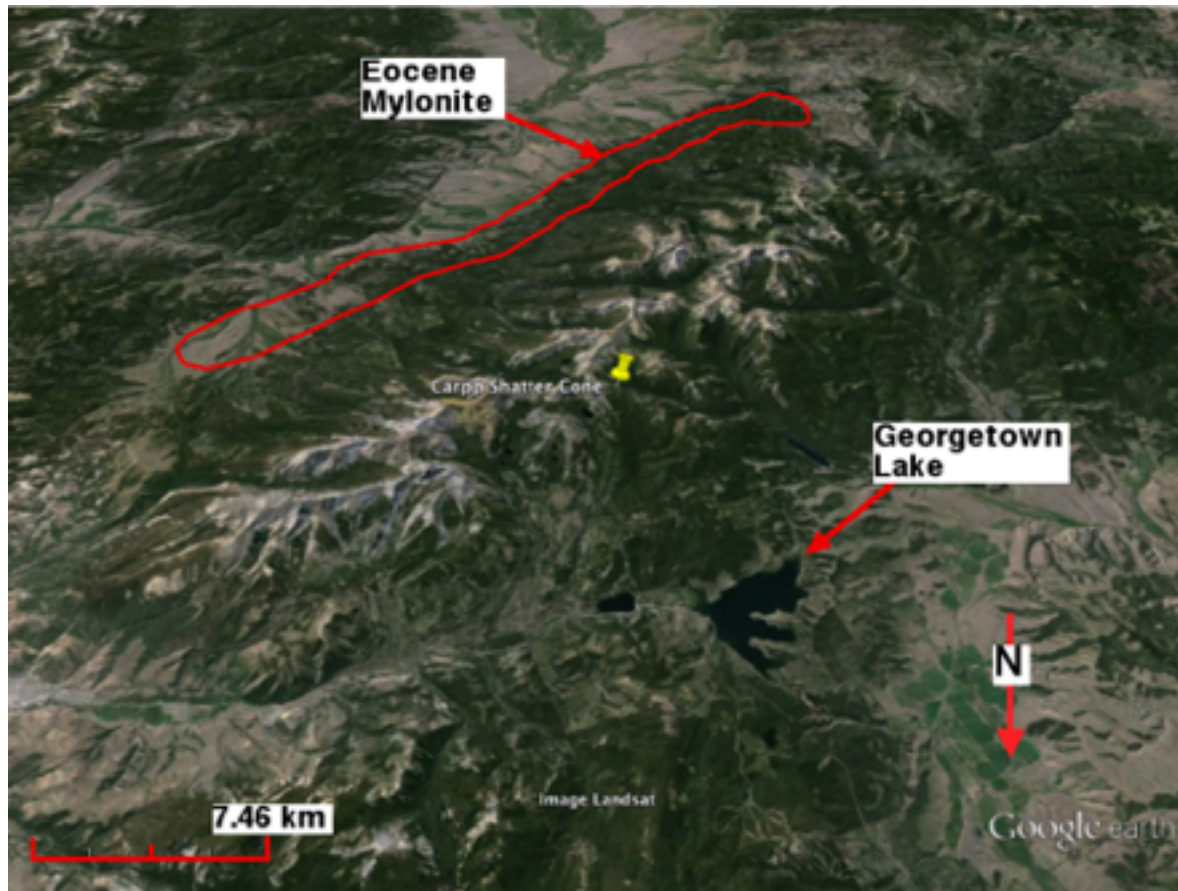


Figure 6.9 High altitude view looking south at the Anaconda Range and environs. Modified Google Earth image.

for example Haney, 2008 or Foster, et al., 2010. Mylonite is defined by geologists as: *a fine-grained metamorphic rock, typically banded, resulting from the grinding or crushing of other rocks*. As previously discussed, the grinding or crushing of rock produces sufficient heat to cause local melting in the localized shear bands. A photograph of the macrostructure of a typical sample of mylonite is presented in [Figure 6.10](#), which displays a melted matrix and partially melted clasts...for comparison recall for example [Figure 5.4](#). As will be discussed in **Section 6.2**, a similar strip of mylonite is exposed along the base of the east side of the Bitterroot Range. It is worth a men-

tion at this point that the structure of this rock is typical of a welded breccia which is a common structure found inside ASB's formed in silicate rock, especially along their margins...recall the discussion in **Section 5.1.1**. The small ASB marked in [Figure 6.10](#) was probably formed by stresses that remained in the mylonite sheet after the clast structure had been established during late-stage cratering.



Figure 6.10 Typical mylonite sample found along the east flank of the Bitterroot Range.

The structure of mylonite typical to the Anaconda Range shown by Foster, et al., 2010 in their Figure 5(A) appears to grade from a sheared laminate structure to one very similar to that seen in [Figure 6.10](#). Foster, et al., 2010 also indicate that a sheet of this mylonite can be extrapolated from the eastern footwall of the Anaconda Range to ~10 km beneath the 'Boulder Batholith,' a.k.a. the central uplift of the B/A-IS, based on

2 cores from ≥ 5 km depth taken from drill holes along the west edge of the Deer Lodge Valley. It is logical to conclude that this mylonite sheet is indicative of a melt sheet that lines the inside of the B/A-IS primary crater.

Because the Anaconda Range partially overlaps the Bitterroot Impact structure (recall [Figure 6.1](#)), the general structure of the Anaconda Range is far more complex than that of the northern Beaverhead Range. Besides the overprint impact structure that appears to be located near the middle of the rim-arc of the B/A-IS, there appears to be several additional overprint impact structures that have caused significant structural modifications to the north end of the Anaconda Range. At least three apparent small overprint impact structures can be seen inside the Anaconda Range in [Figure 6.11](#). These three overprint impact structures are in addition to the 7 that are visible in [Figure 6.2](#).

Mount Tiny sits on the remains of the southwest rim of an apparent oblique impact structure which is over 1 km across. As should be observed in [Figure 6.11](#), the rim of the Mount Tiny impact structure appears to consist of an overlap of two similar sized arcs...the left arc is better defined. The proximity of these two impact structures could be related to the impact points of two fragments from the same impactor whose impact points are separated by the rotation of the Earth. The U-shape of the rim structures produced by these two impacts, seen in [Figure 6.11](#), has a combined width of approximately 3 km. At least one central uplift of this impact structure appears to remain northeast of Mount Tiny; this central uplift in-

cludes a central depression. The suggestion of a second central uplift appears as an extension southeast of the rim of the larger central uplift. Incidentally, Storm Lake lies between the crater rim and the central uplift on the floor of the crater north-northeast of Mount Tiny.

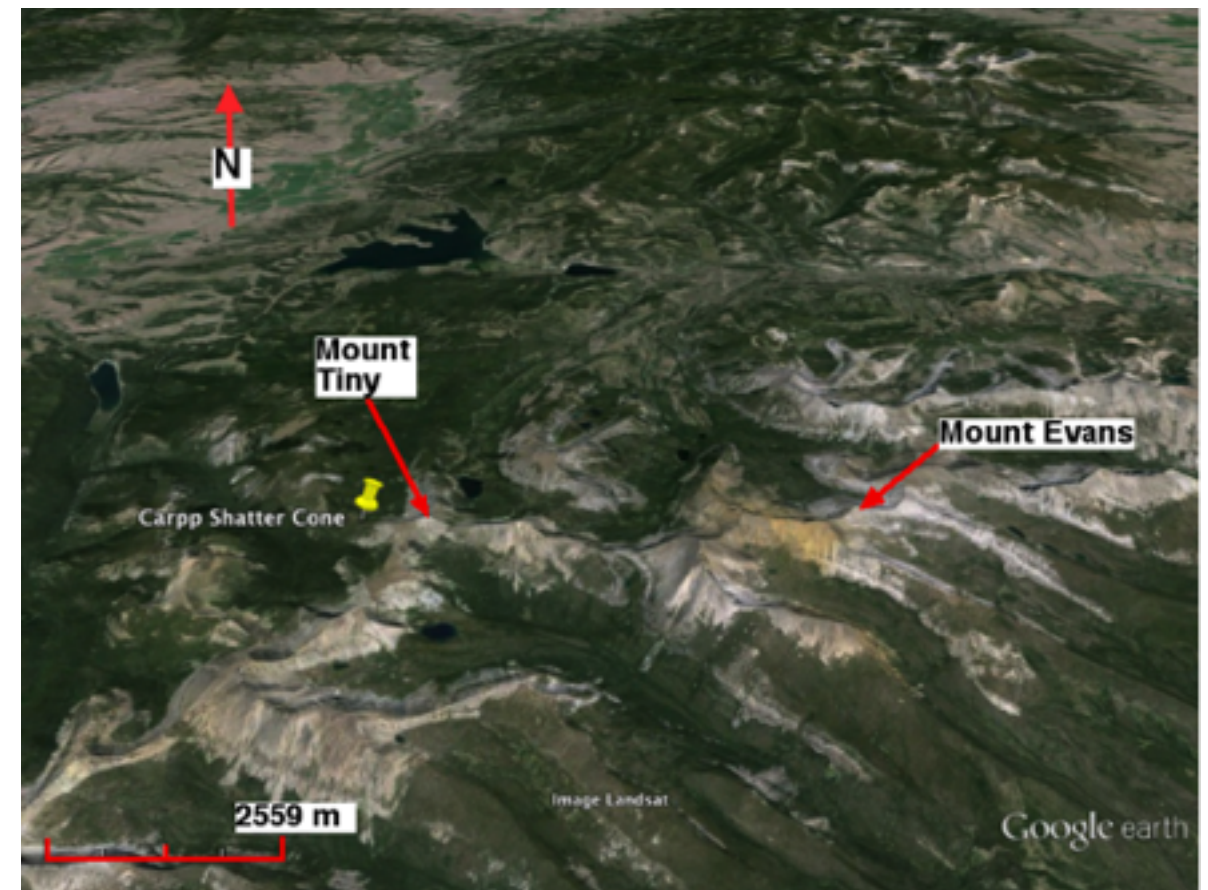


Figure 6.11 View north of the north end of the Anaconda Range. Modified Google Earth image.

The location of the shatter cones (recall [Figure 5.7](#)) found on Carpp Ridge is also indicated in the satellite images in [Figures 6.11](#) and [6.12](#). The geometry of Carpp Ridge and its surroundings suggests another overprint impact structure. The Carpp Ridge overprint impact structure appears to have been itself

partially overprinted by the west side of the Mount Tiny impact structure. Storm Lake, which possesses a typical impact structural feature, is seen east of Mount Tiny in [Figure 6.12](#).

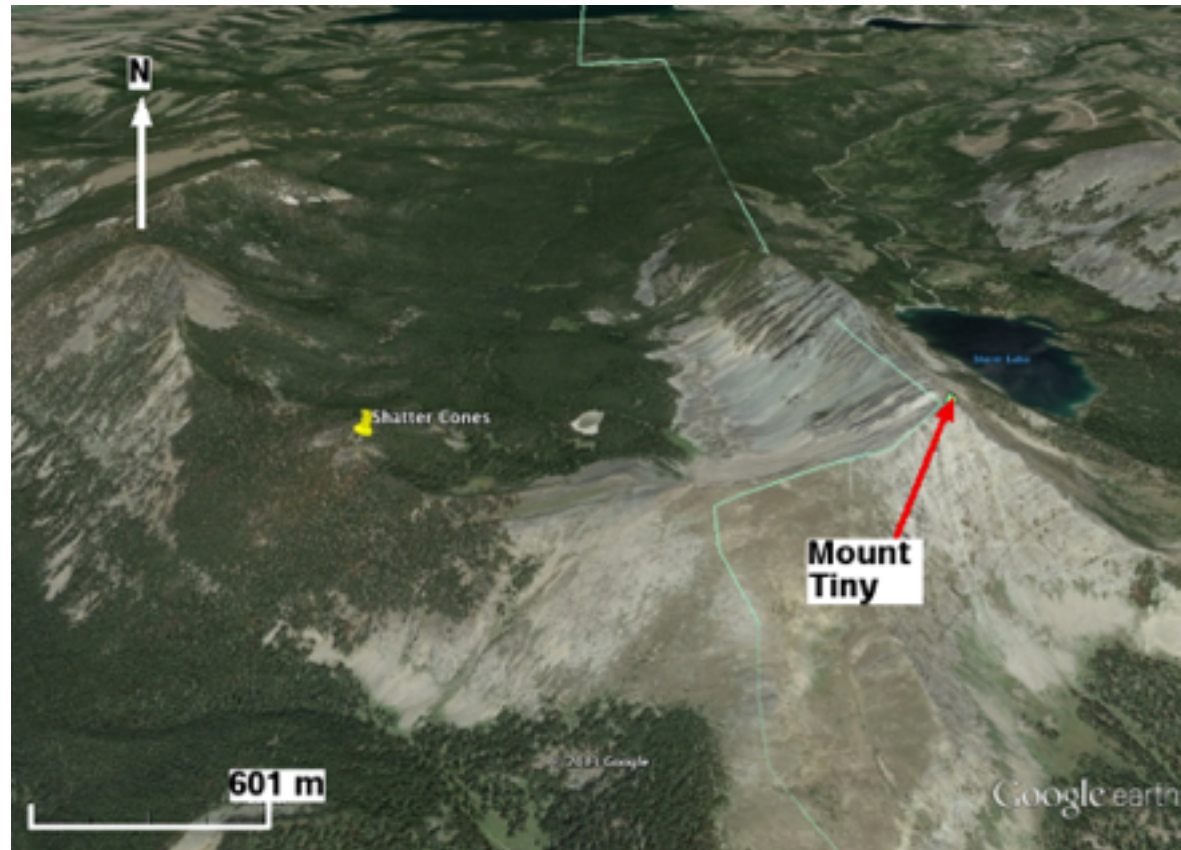


Figure 6.12 View of Carpp Ridge and Mount Tiny from the south...Anaconda Range to the right. Modified Google Earth image.

There are other many structural features, in addition to shatter cones, that support the hypothesis that Carpp Ridge can be interpreted as a remnant of the rim of an impact structure. An easterly view along the top of Carpp Ridge, observed in [Figure 6.13](#), reveals a large collection of localized shear bands whose orientations indicate they were formed by a strong force from the left (north). These shear bands are delineated on the surfaces of several cliffs in the view in [Figure 6.13](#) by

parallel lines that tilt upward to the left and are crossed at an angle of $\sim 45^\circ$ by complimentary parallel shear lines.



Figure 6.13 View along Carpp Ridge to the east toward Mount Tiny, which is hidden behind the highest peak in the distance.

A closer view of examples of these localized shear bands that were formed at high rate is seen in [Figure 6.14](#)...their structure indicates adiabatic localized shear melting, i.e. ASB's. The planar vector of these periodic shear bands lies normal to the rim of Carpp Ridge along with a few complimentary shear bands which lie $\sim 45^\circ$ to the ASB's oriented normal to the maximum compression vector.



Figure 6.14 Examples of localized adiabatic shear bands on the top of Carpp Ridge. The view is east, and the thickness of the marked ASB is approximately 0.5 m.

If we put the Carpp Ridge impact structure in context, it is not unreasonable to conclude that it is contemporaneous with the two impact structures previously discussed east of Mount Tiny. Actually, the overall structure of the ridge that projects north from Mount Tiny suggests that it has seen a slight displacement to the west that could indicate that it was formed by an impactor fragment first in a sequence of impacts that string to the east forming the two Mount Tiny impact structure previously discussed.

The half-rim of a probable related oblique impact crater east of Mount Tiny includes Mount Evans...marked in [Figure 6.11](#). The west rim of this slightly smaller impact appears to have partially overprinted the east side of the Mount Tiny crater, and Mount Evans appears to stand as a prominent feature of the east end of the rim. The orientation of the arc of the Mount Evans impact structure is very similar to that of the Mount Tiny structure, so as previously postulated, both of these craters are likely to have been formed by related impactor fragments during the same impact event.

There is a plethora of large, periodically spaced ASB's that cross the ridgeline on which Mount Evans sits that strongly indicate an impact origin for the entire ridge. A prominent example that is nearly 20 m wide and runs normal to the ridgeline of the crater can be seen in [Figure 6.15](#). The ASB marked in [Figure 6.15](#) is one of several periodically exposed along the Mount Evans ridgeline. Incidentally, the ASB marked in [Figure 6.15](#) displays a rind along its left side that suggests an incomplete melting along the boundary with the surrounding rock, very much like that previously noted lying along the borders of the dikes located around the Spanish Peaks in southern Colorado...recall for example [Figure 5.13](#).

Thermochronologic data derived from samples extracted from the north end of the Anaconda Range and published by Foster, et al., 2010 can be used to approximate the age of the B/A-IS and associated overprint impact structures. For example, the age of a sample from a "dacite dike" whose location is pinpointed in [Figure 6.16](#) has been determined to be 48.5 ± 0.6

$\times 10^6$ years, using $^{40}\text{Ar}/^{39}\text{Ar}$ age dating techniques, Foster, et al., 2010. It is noteworthy that the map coordinate marking the reported location of the “dacite dike” in [Figure 6.16](#), Foster, et al., 2010, lies at the end of the rim of a smaller, oblique impact structure that partially overprints the Mount Evans Impact Structure and is one of three arcuate structures that are aligned in a row.

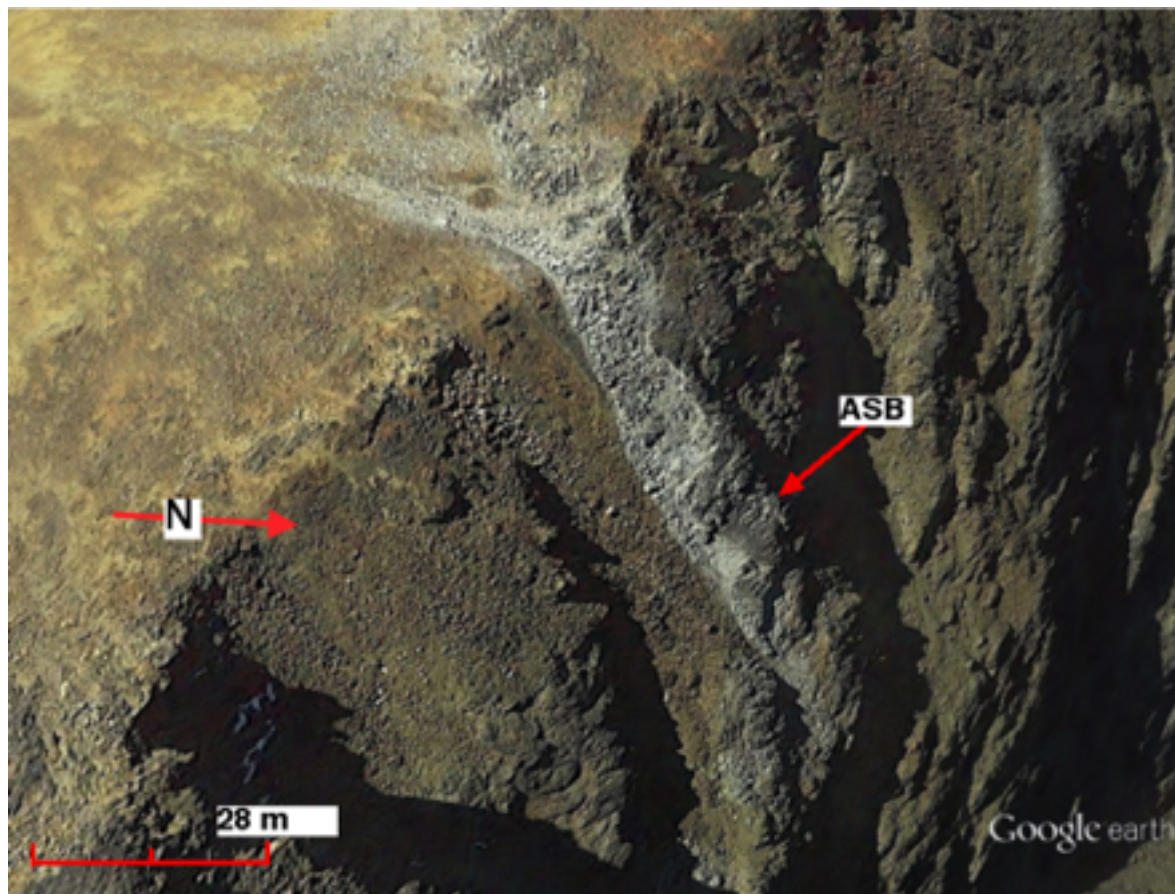


Figure 6.15 Example of a localized adiabatic shear band across the top of the proposed rim of the Mount Evans impact structure in the Anaconda Range. Modified Google Earth image.

Foster, et al., 2010 report thermochronologic ages for the Anaconda Range ranging from 53×10^6 to 39×10^6 years which they interpreted as the time span associated with the tectonic

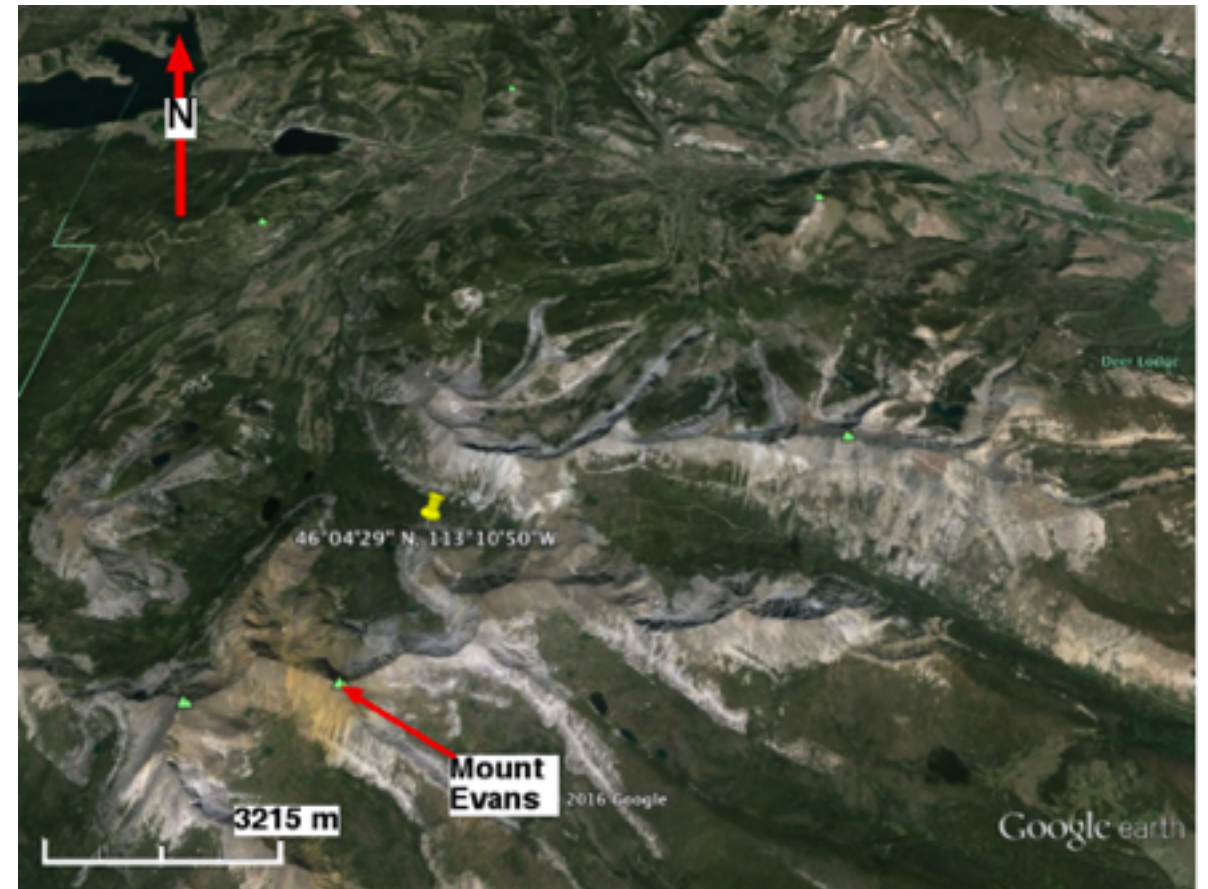


Figure 6.16 View of the Mount Evans impact structure in the Anaconda Range along with additional candidate overprint impact structures. Thermochronologic data for the “dacite dike” located at $46^{\circ}04'29''$ N, $113^{\circ}10'50''$ W is discussed in the text. Modified Google Earth image.

formation of the mountain range...no connection to impact formation was ever mentioned by these authors. From the point of view of Impact Geology, this relatively large time span can be attributed to 1) ages associated with impact overprint structures formed at different times or 2) variability due to the precise field locations of the samples analyzed...recall the huge variability of age measurements for the Black Dikes in the Teton Range due to the sample location within a given dike that

relate to the approach to the final thermal conditions...recall **Section 5.2.2**.

Lonn, et al., 2013 mentioned the formation date of a fault in the Beaverhead Range at 46×10^6 years ago that could also infer the formation date of the B/A-IS. It is readily apparent at this point that the age of the B/A-IS is not precisely defined. However, we can conclude that it is younger than the proposed Bitterroot Impact Structure which is partially overridden by the B/A-IS...to be discussed in **Section 6.2**.

6.1.2 CENTRAL UPLIFT OF THE B/A-IS

A structure that possesses the general features and proximity to the collar wall of the central uplift for the B/A-IS is visible in [Figure 6.2](#). This proposed impact substructure includes the Pioneer Range and two additional mountain complexes located immediately to the west and north of the center of the B/A-IS uplift complex. The separation between these three mountain complexes that appear to define the central uplift is consistent with a wave pattern that can develop in the target material as a result of an oblique impact. The small mountain complex immediately north of the Pioneer Range might be a remnant of the east rim of the Bitterroot Impact Structure which has been modified by the later, overlapping formation of the B/A-IS. An area of gravitational anomaly that maps close to the central uplift can also be seen to the right of the collar wall anomaly in [Figure 6.3](#).

The Big Hole Valley lies between the central uplift complex and the exposed section of the rim of the B/A-IS. The Big

Hole River flows northward along the valley floor eventually coursing eastward around a circular feature to flow into the Beaverhead River, a tributary of the Missouri River...visible inside the B/A-IS impact structure in [Figure 6.2](#). This circular feature has smaller ones lying just to its left and right...all could represent overprint impact structures or rebound substructures. These substructures will require field studies to be properly identified and confirmed.

Bitterroot Impact Structure

SECTION TOPICS

6.2.1 Bitterroot Mylonites

6.2.2 Bitterroot Rim Dikes

6.2.3 Bitterroot Central Uplift

The geologic community has proposed that the Bitterroot Range was formed by an *enigmatic* tectonic unroofing process that has exhumed and exposed the core complex over several million years...see for example Hodges and Applegate, 1993 who proposed a formation interval of 45.5×10^6 to 43.5×10^6 years ago. However, the arcuate Bitterroot Range, marked “Bitterroots” in [Figures 6.1](#) and [6.17](#) can be interpreted as the western rim of a large, oblique impact crater that is older than the B/A-IS.

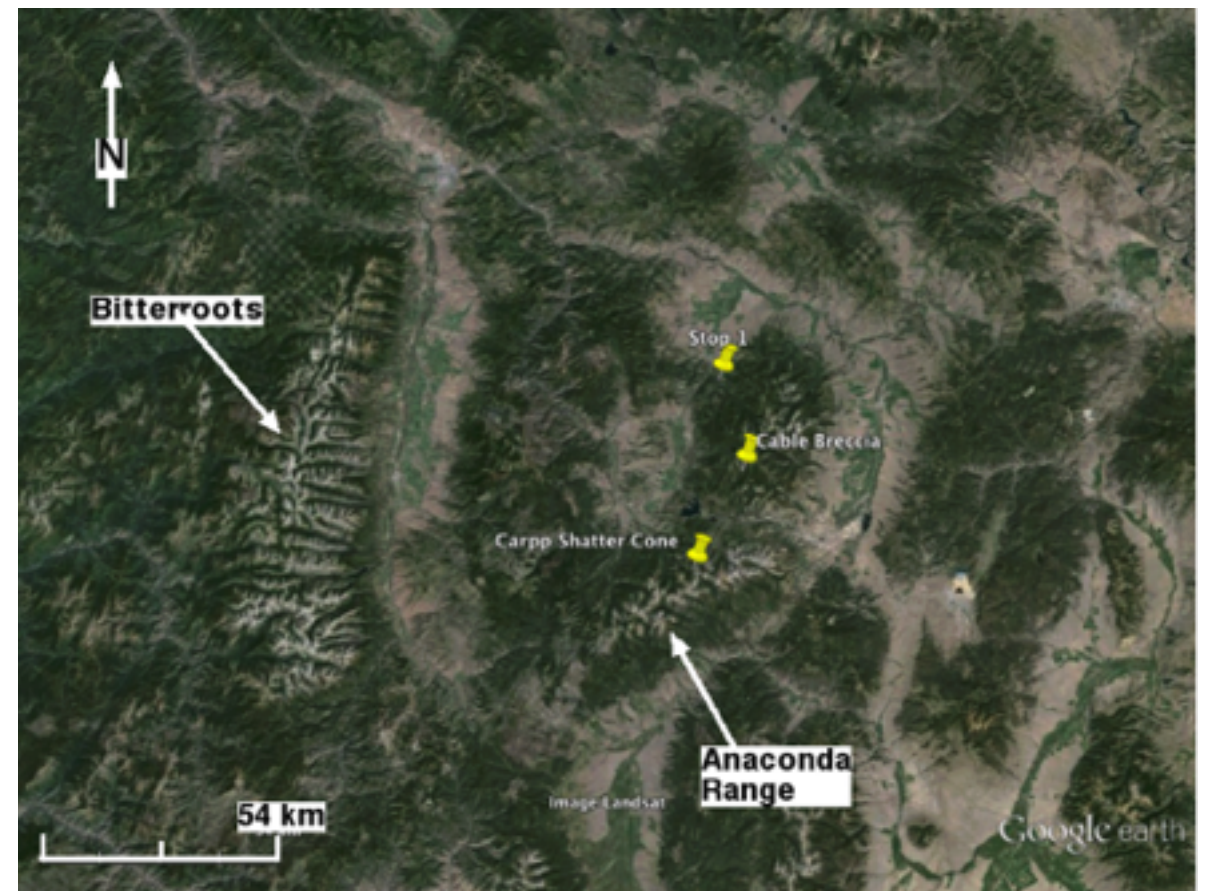


Figure 6.17 High altitude view of the Bitterroot Impact Structure. Original image from Google Earth.

The overall planform of the Bitterroot Impact Structure suggests an oblique impact from the north-northeast that left a hyperbolic shaped impact crater that is ~150 km across at its widest and at least 140 km long. The Bitterroot Valley lies between an elliptical-shaped central uplift and a segment of the western crater rim partially defined by the Bitterroot Range. As can be seen in [Figure 6.17](#), the north end of the Bitterroot Range appears to be terminated by an overprint impact structure that is perhaps as large as 40 km across. Additional impact structures that overprint the Bitterroot Impact Structure will be discussed in the section.

The central uplift of the Bitterroot Impact Structure, which includes both the “Sapphire Batholith” and the Flint Creek Range, is structurally similar to the ring shaped central uplift of the Upheaval Dome (recall [Figure 3.4](#)), and it is similar to the proposed Mount Tiny overprint impact structure previously discussed in **Section 6.1.2.3** relative to the B/A-IS. Also as can be seen in [Figures 6.1](#) and [6.17](#), both the rim and central uplift of the Bitterroot Impact Structure appears to have been partially overlapped on their southeast quadrant by a more recent, comparably-sized impact structure...the previously discussed B/A-IS. The arcuate planform of both of the remnants of these two impact structures suggests impactor trajectories that were approximately 90° apart, clearly indicating two separate impact events.

The syncline outside of the east side of the central uplift of the Bitterroot Impact Structure, through which the Clark Fork River flows out of the Deer Lodge Valley, lies inside of the rem-

nants of the northeast corner its east rim. The northern extreme of the Bitterroot Impact Structure is nominally marked by the mountains north of the course of the Clark Fork River along its westward flow toward Missoula, MT. The southern rim of the impact structure is defined by the arc of the Bitterroots that runs through and across Lost Trail Pass, which is close to the north end of the Beaverhead Range.

6.2.1 BITTERROOT MYLONITES

The Bitterroot Range is well known for its extensive exposure of a mylonite layer that runs for ~100 km along the eastern base of the range. The general location of this mylonite layer is seen in [Figure 6.18](#), and a view of a typical Bitterroot mylonite outcrop is presented in [Figure 6.19](#). Geologists almost universally believe that the mylonite band marks a shear zone that is associated with the ‘tectonic unroofing’ of the Bitterroot Range...see for example Hodges and Applegate, 1993; whereas, the overall structure and location of this mylonite band is totally consistent with formation by impact. In fact, the overall structural features of material in the Bitterroot mylonite band suggest that it represents a partial exposure of a ‘melt sheet’ that commonly lines the bottom of a primary, hypervelocity impact crater...as previously suggested for a similar formation in the B/A-IS. This mylonite layer was probably formed toward the end of early-stage cratering. The columnar structure seen extending through the layer in [Figure 6.19](#) results from cooling and subsequent solidification that progressed normal to the layer after impact deformation ceas-



Figure 6.18 Mylonite distribution (~100 km of gray shading) along the east flank of the Bitterroot Range. North is at the top of the modified Google Earth image.

ed...the heat flow direction governs the orientation of the axis of a column.

A typical macrostructure of the Bitterroot mylonite has been previously shown in [Figure 6.10](#). In reality, this macrostructure is indistinguishable from that of welded breccia that is typically found in and around geologic impact structures...recall for example a pseudotachylite can be generally classed as a welded breccia.



Figure 6.19 Mylonite outcrop exposed on the east flank of the Bitterroot Range west of Florence, MT. The mountain range is to the left in the photo.

If the Bitterroot mylonite layer truly represents an impact melt sheet, the age of the Bitterroot Impact Structure should be inferable from the age of the Bitterroot mylonite. House and Hodges, 1993 measured $^{40}\text{Ar}/^{39}\text{Ar}$ thermochronological ages of $47.9 \pm 0.9 \times 10^6$ and $49 \pm 1 \times 10^6$ years for hornblende samples separated from “deformed amphibolite pods” found in the northeast border of the Bitterroot mylonite zone. These “deformed amphibolite pods” might be classified as pseudotachylites like those commonly found as ‘pods’ inside an *accepted* impact structure such as the Vredefort Dome Impact Structure...recall **Section 5.1.1.1**. Because these authors did not

specify whether the hornblende samples were derived from the clasts or matrix material or indicate the location within the 'pod' (center or edge), the precision of the inferred age of the event that formed the mylonite is uncertain. However, it must be recalled that these ages are older than the age of the B/A-IS reported by Lonn, et al., 2013 and others and because the rim of the B/A-IS overlaps the Bitterroot Impact Structure, the Bitterroot Impact Structure must be considered to be the older of the two.

6.2.2 BITTERROOT RIM DIKES

The Bitterroot Range contains innumerable very large dikes similar to those previously discussed for the B/A-IS. Ridge-line dikes mark the main radial ridge pattern that cuts through the Bitterroot Range east to west. The east side radial ridge dikes terminate at the Bitterroot Divide that runs along the length of the Range...recall [Figure 6.17](#) and marked by the purple line in [Figure 6.20](#). These east-west ridge-lines seen in [Figure 6.20](#) are cut by periodically repeated dikes that lie at right angles to the ridge-lines, but it should be noted that the frequency of the periodicity frequency is higher on the south side of these east-west ridge-lines. This asymmetry in ridge-line frequency is likely a result of the oblique trajectory of the impactor which would have imposed the strong compressive stress vector generally from the north (left to right in the photo) in addition to the maximum compressive stress vector that aimed in a westerly direction derived from the impact induced shock wave.

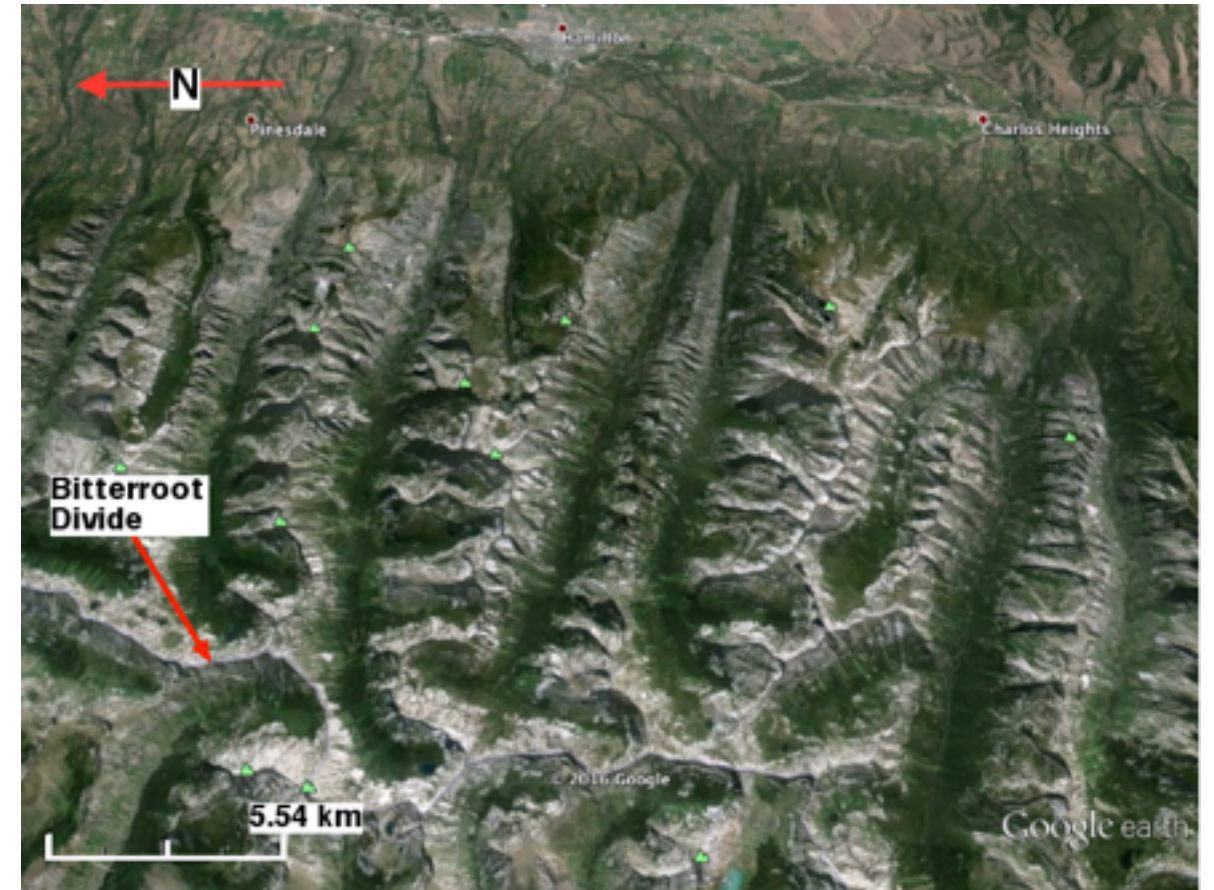


Figure 6.20 Overhead view of the Bitterroot Range west of Hamilton, MT. Original image from Google Earth.

Three or more arcuate structures can be seen strung along a ridge in [Figure 6.21](#)...the rim of one of these structures is marked "3 Craters Dikes" which is located at $45^{\circ}50'52.54''$ N, $114^{\circ}21'24.00''$ W. These arcuate structures could represent a string of overprint impact structures that were formed during a single event by a fragmented impactor that occurred after the Bitterroot Impact Structure formed. A closer view of the dikes located below the mark in [Figure 6.21](#) are presented in [Figure 6.22](#).

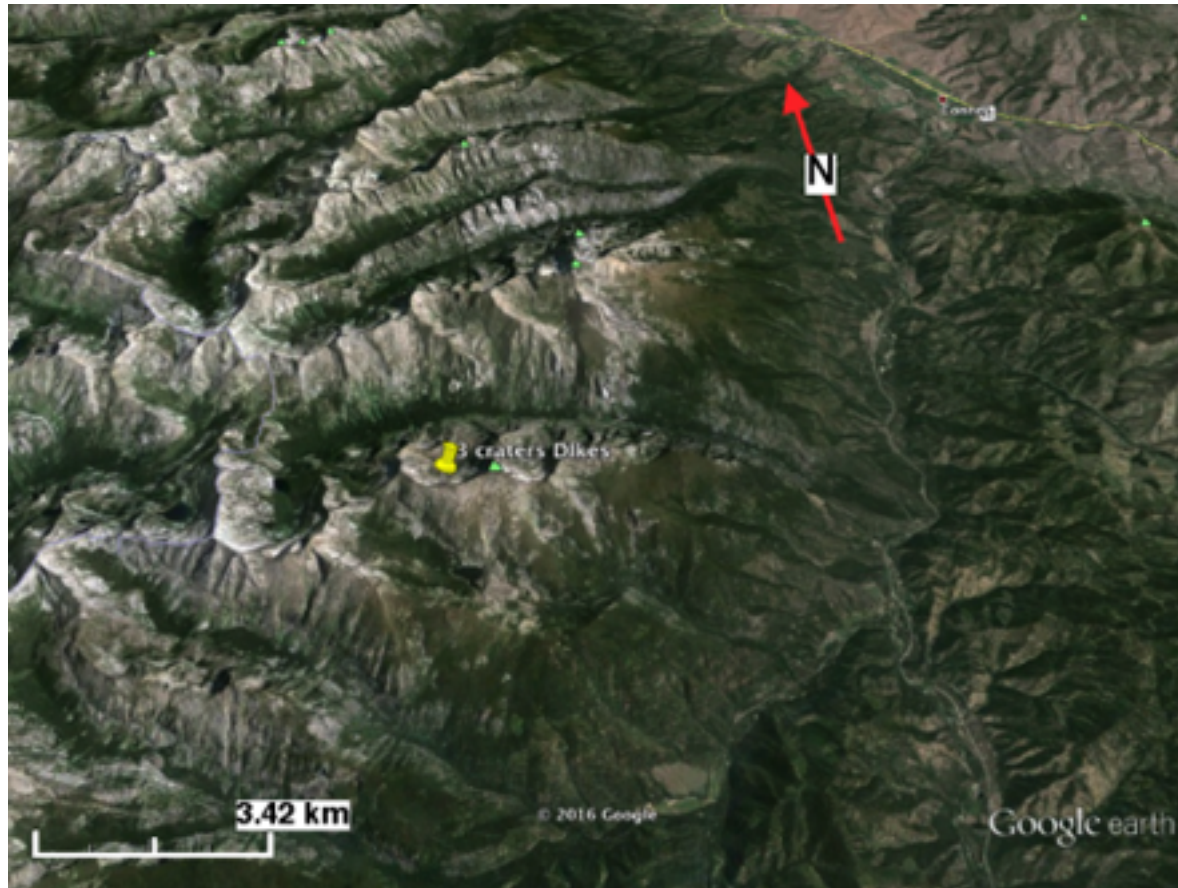


Figure 6.21 View of the southwest end of the Bitterroot Range. Original image from Google Earth.

The chevron pattern anchored on the prototypic Ridge Dike in the vicinity of the 3-craters Dikes mark in [Figure 6.22](#) illustrates branched localized shear deformation. There are even complimentary near vertical shear bands seen within the chevron pattern along the right side of the Ridge Dike. The chevron pattern seen here is analogous to those seen at a much broader scale in [Figures 6.20](#) and [6.21](#). The orientation of the Ridge Dike and other nearby dikes relative to either the stress pattern related to the proposed overprint impact structure or that which produced the Bitterroot Range is ambiguous; this situation illustrates the seminal character of this discussion

and underlines the need for considerable field research to understand and verify the true origin of these structures.

The Bitterroot Impact Structure is further validated by the exposure of a large number of geometrically related dikes on the face of the road-cut for US-93 along the north side of Lost Trail Pass...located on its downrange (south) rim. A sample of these dikes (ASB's) exposed near the bottom of the north side of the Lost Trail Pass is marked in [Figure 6.23](#). There is also a large (perhaps 10 m wide) dike visible in this photo-



Figure 6.22 Dikes below the mark in [Figure 6.21](#) located in the southwest end of the Bitterroot Range. Original image from Google Earth.

graph that runs from the ridge-line above the ASB's nearly to the road surface. This large dike is oriented $\sim 45^\circ$ to the adjacent ASB's and appears to be complimentary to them. These periodic, parallel and complimentary dikes are strikingly similar to localized shear structures previously discussed...recall similar features in the Vredefort Dome ([Figure 3.17](#)) and ice ([Figure 5.10](#)).

A closer view of similar dikes (ASB's), exposed along the eastern side of US-93 on the surface of the roadcut further up the north approach to Lost Trail Pass, [Figure 6.24](#), demonstrates several of the typical characteristics of localized shear deformation that is produced by impact. For example, the four dikes in this collection are clearly distributed periodically right to



Figure 6.23 View north along US-93 near the bottom of Lost Trail Pass in southwest Montana.

left, plus they are occasionally branched. The imbrication of the formation observed in the lower left quarter of the photograph represents deformation that is geometrically complimentary to the dike next to it. Collectively, these dikes are representative of a swarm that is exposed along US-93 heading south to the top of Lost Trail Pass...discussed and age-dated by Bausch, et al., 2013. It is logical to conclude that this dike swarm was formed by late-stage stresses that were generated at the downrange end of an oblique impact structure.

6.2.3 BITTERROOT CENTRAL UPLIFT

The planform of the remnants of the central uplift of the Bitterroot Impact structure can be clearly seen in the satellite



Figure 6.24 Dikes along US-93 viewing east on the north side of Lost Trail Pass. The ASB on the left is ~ 1 m wide at the branch point.

imagine in [Figure 6.17](#), and a closer perspective view of the center of this central uplift is presented in [Figure 6.25](#). The overall structure of the central uplift is represented by an ellipse bound by the Sapphire and Flint Creek Ranges. Both of these ranges have been cut off on the southeast by the Anaconda Range segment of the B/A-IS. The Sapphire and Flint Creek Ranges collectively surround a major depression (basin) that encloses an elliptical uplift near the basin center...see [Figure 6.25](#). This interior of the uplift rises to elevations close to those found in the surrounding rim mountain ranges.

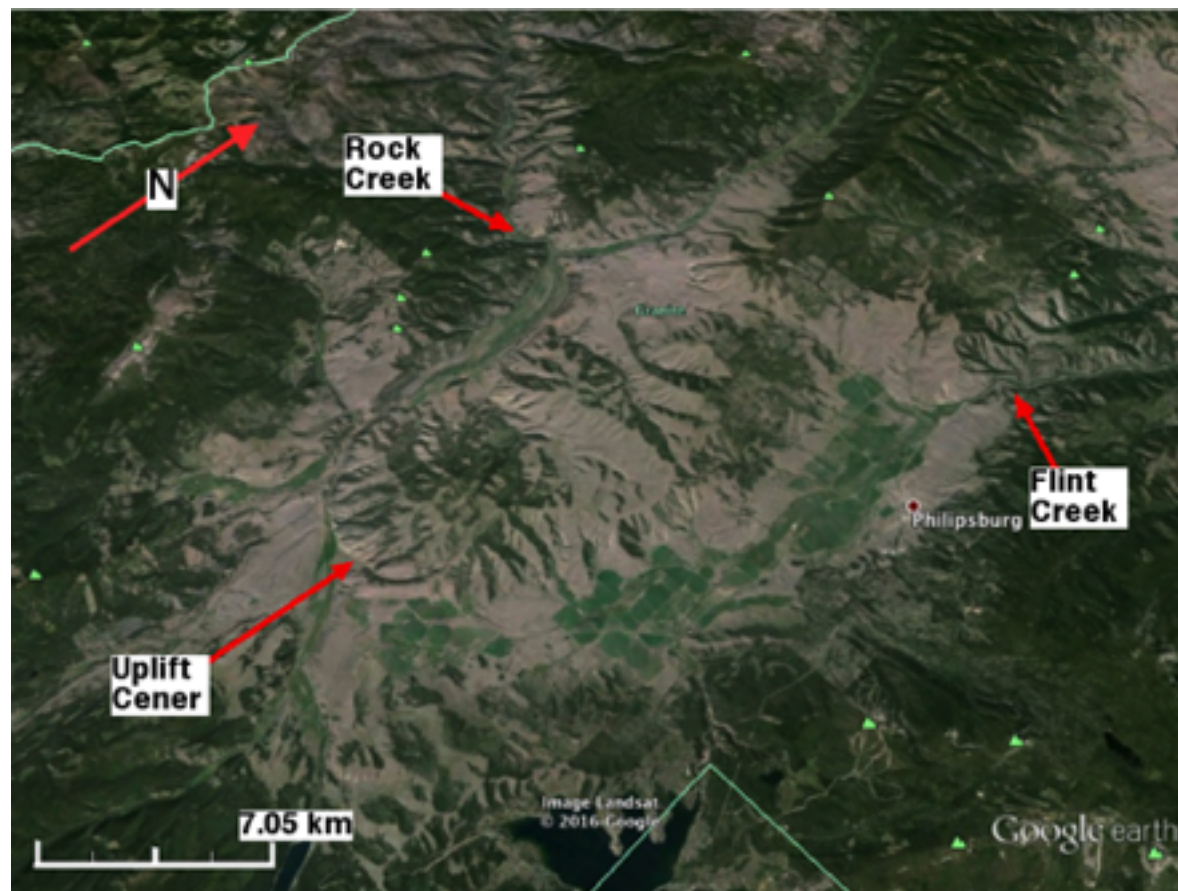


Figure 6.25 Central basin and uplift for the Bitterroot Impact Structure. Original image from Google Earth.

The central basin of this central uplift complex drains out of its lower (northern) end down Flint Creek to the north and Rock Creek to the northwest. This basin drainage pattern is consistent with an oblique impact from the north. Coincidentally, the major axis of the ellipse of the central uplift seen in [Figure 6.25](#) is also aligned with the proposed impactor trajectory.

A pattern of radially oriented valleys or canyons in the outer rim of the central uplift complex (visible especially on the north and west sides) can be seen in [Figure 6.17](#). This radial valley/canyon pattern, which is vividly displayed in both the Bitterroot and Beaverhead Ranges, is an indication of circumferential expansion of the rim of an arcuate structure that formed around the impact point. These valley/canyon patterns are also similar to the canyon pattern formed around the primary crater of the Vredefort Dome by localized shear deformation during late-stage cratering...recall the chevron pattern of the canyons and radial dikes in [Figure 3.21](#).

Localized shear features are also found in the rim of the central uplift. The location of a set of parallel ASB's exposed in the Flint Creek Range east of Maxville, MT is marked in [Figure 6.17](#) as "Stop 1." A large number of these parallel, vertical running ASB's are visible in [Figure 6.26](#) in the 'Silver Hill Formation' along with several geometrically complimentary ASB's...upper right in the photograph. The location and orientation of the trace of this set of ASB's is consistent with the hypothesis that it is associated with the outer rim of the central uplift complex of the Bitterroot Impact Structure. The vertical

orientation of the very old Silver Hill and Flathead Formations seen in [Figure 6.26](#) also suggests they were reoriented by a very large impact force, and the ASB's were formed in the strata by impact long after these formations were deposited.

The "Cable Breccia" whose structure has been previously discussed ([Section 5.1.1.1](#)) appears to be located along the eastern side of the central uplift structure of the Bitterroot Impact



Figure 6.26 Silver Hill Formation adjacent to an example of Flathead Formation (beige band in the background left-center) in the Flint Creek Range at 'Stop 1' in McDonald and Lonn, 2009. The view is approximately north.

Structure, but there is a strong indication that the Cable Breccia is associated with an overprint impact structure that can be seen in [Figure 6.27](#). Cable Mountain can be considered to be defining the west rim of this overprint impact structure which has the planform of a typical oblique impact crater. The downward southwest tilt of both the Cable Breccia dike (see [Figure 5.1](#)) and the related Ridge Dike (see [Figure 5.2](#)) indicates a force vector parallel to the long dimension of the oblique Cable Mountain overprint impact structure seen in

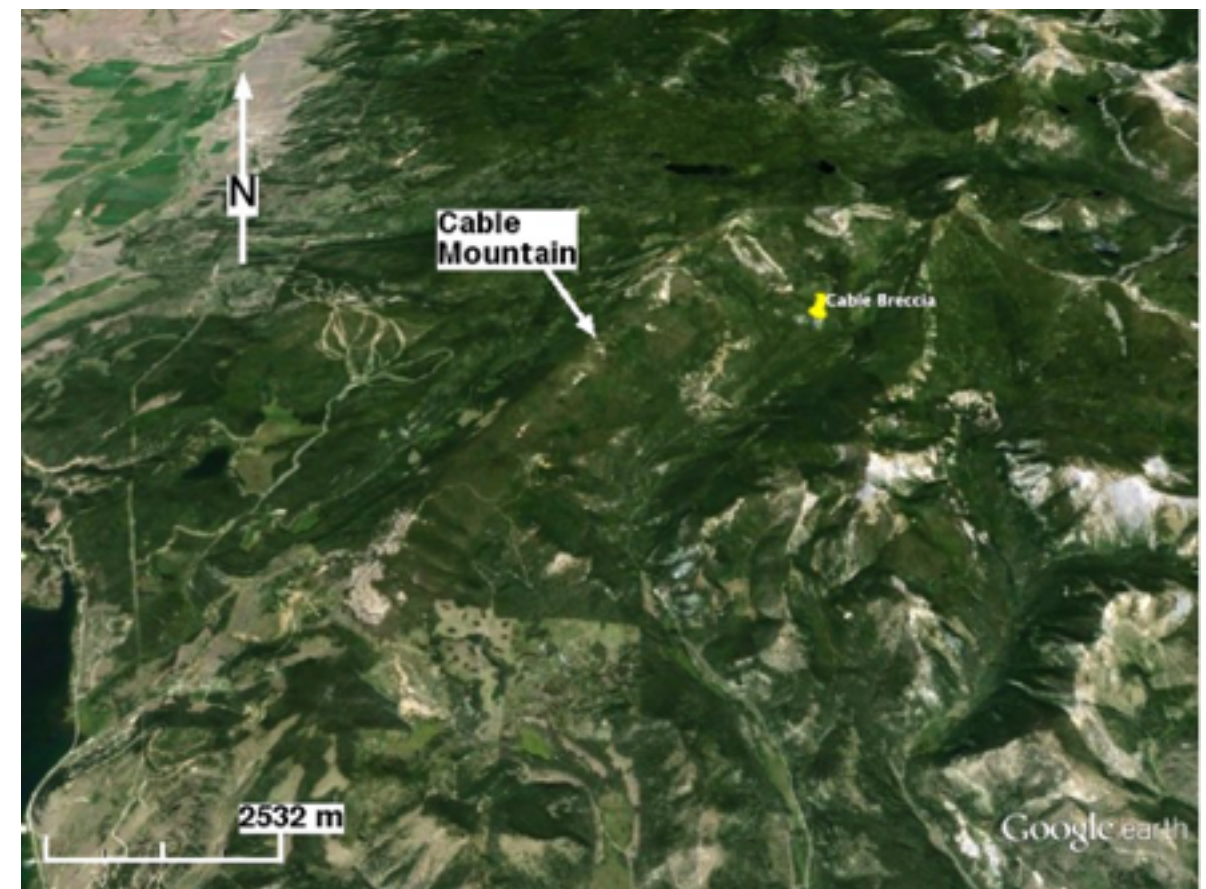


Figure 6.27 Satellite view of Cable Mountain and environs... southeast corner of the Bitterroot central uplift complex. Original image from Google Earth.

[Figure 6.27](#). The shear veins exposed on the fracture surface of a piece of talus found along foot of the southeast face of Cable Mountain, seen in [Figure 6.28](#), along with ASB's exposed on the face of a roadcut at the base of the northeast side of Cable Mountain, represent additional evidence of an overprint impact structure.



Figure 6.28 Talus fragment from the southeast face of Cable Mountain. The vein bearing rock is approximately 0.2 m across.

The discussion in this chapter can serve as guide to future field work aimed at verifying the impact origin of these two geologic structures. Even though the verification of the B/A-IS and the Bitterroot Impact Structure is incomplete, the data presented supporting the proposition that they both are typical large, oblique, impact structures formed during the Eocene epoch is compelling. The definition of both the B/A-IS and Bitterroot Impact Structure illustrates the point that major

mountain ranges can be identified as products of impact cratering on Earth.

Chapter 6 References

- Anhaeusser, C. R., Stettler, E., Gibson, R. L., and Cooper, G. R. J., 2010, A possible mesoarchean impact structure at Setlagole, North West Province, South Africa: Aeromagnetic and field evidence, *South African Journal of Geology*, Volume 113.4, pp. 413-436, doi:10.2113/gssajg.113.4.413.
- Bausch, W. G., Baldwin, J. A., and Foster, D. A., 2013, Synextensional Emplacement and Cooling of the East Fork Dike Swarm at Lost Trail Pass, Southwest, Montana, *Northwest Geology*, v. 42, pp. 299-308.
- Burmester, R. F., Lonn, J. D., Lewis, R. S., and Mcfaddan, M D., 2013, Toward a Grand Unified Theory for Stratigraphy of the Lemhi Subbasin of the Belt Supergroup, *Northwest Geology*, v. 42, pp. 1-20.
- Fiske, P. S. and Hargraves, R. B., 1994, The Beaverhead Impact Structure, SW Montana and Idaho: Implications for the Regional Geology of the Western U.S., Lawrence Livermore National Laboratory report No. UCRL-JC-116524 submitted to Proceedings of the Belt Symposium III, August 14-21, 1993, Whitefish, MT, R. Berg, Editor.
- Foster, D. A. and Fanning, M., 1997, Geochronology of the northern Idaho batholith and the Bitterroot metamorphic core complex: Magmatism preceding and contemporaneous with extension, *GSA Bulletin*, April 1997, v. 109 no. 4 p. 379-394, doi: 10.1130/0016-7606(1997)109<0379:GOTNIB>2.3.CO;2.
- Foster, D. A., Grice, W. A., Jr., and Kalakay, T. J., 2010, Extension of the Anaconda metamorphic core complex: $^{40}\text{Ar}/^{39}\text{Ar}$ thermochronology and implications for Eocene tectonics of the northern Rocky Mountains and the Boulder batholith, *Lithosphere*, August 2010, v. 2, p. 232-246, doi:10.1130/L94.1
- Haney, E., 2008, Pressure-temperature evolution of metapelites within the Anaconda metamorphic core complex, southwestern Montana, in *Theses, Dissertations, Professional Papers*, Paper 1262.
- Hodges, K. V. and Applegate, J. D., 1993, Age of Tertiary extension in the Bitterroot metamorphic core complex, Montana and Idaho, *Geology*, v. 21, pp. 161-164.

House, M. A. and Hodges, K. V., 1993, $^{40}\text{Ar}/^{39}\text{Ar}$ thermochronology in the northern Bitterroot mylonite zone, MT, Geological Society of America, Abstracts with Programs; Journal Volume: 25:5; Conference: 89. Annual meeting of the Cordilleran Section and the 46th annual meeting of the Rocky Mountain Section of the Geological Society of America, Reno, NV, 19-21 May 1993.

Le Feuvre, M. and Wieczorek, M. A., 2011, Nonuniform cratering of the Moon and a revised crater chronology of the inner Solar System, *Icarus*, 214, pp. 1-20.

Link, P. K. and Janecke, S. U., 1999, Geology of East-Central Idaho: Geologic Roadlogs for the Big and Little Lost River, Lemhi, and Salmon River Valleys, in Hughes, S.S., and Thackray, G.D., eds., *Guidebook to the Geology of Eastern Idaho: Pocatello*, Idaho Museum of Natural History, p. 321.

Lonn, J. D., Lewis, R. S., Burmester, R. F., and McFadden, M. D., 2013, The Complex Geology of the Northern Beaverhead Mountains, Montana and Idaho, *Northwest Geology*, v. 42, pp. 111-130.

McDonald, C. and Lonn, J., 2009, The Cambrian Flathead and Silver Hill Formations in the Northern Flint Creek Range near Maxville, Montana, *Northwest Geology*, v. 38, pp. 112-120.

Pati, J. K. and Reimold, W. U., 2007, Impact cratering - fundamental process in geoscience and planetary science, *Journal of Earth Systems Science*, 116, No. 2, April 2007, pp. 81-98.

Steel, T. D. and Link, P. K., Mesoproterozoic Strata in the Shewag Lake Quadrangle, Idaho and Montana, 2013, *Northwest Geology*, v. 42, pp. 57-70.

Therriault, A. M., Grieve, R. A and Pilkington, M., 2002, *Bulletin of the Czech Geological Survey*, Vol. 77, No. 4, pp. 253-263.

Epilogue

This boulder with crossed adiabatic shear bands is lying on the surface of a pseudotachylite located near Musigbrod Lake in southwest Montana. These impact substructures are associated with the proposed Beaverhead/Anaconda Impact structure.



As has been discussed in these chapters, many candidate large impact structures and smaller overprint impact structures are observed on the dry surface areas of Earth and most of the solid terrestrial objects in our solar system. The areal density of impact structures in the surface area examined in the previous chapter suggest a higher value than predicted based on impact crater density on Earth's moon. It is hoped that the reader has concluded that impact structures on Earth are so numerous that at least one example could be found on a casual drive through almost any nearby countryside. It can be stated with great confidence that many of us unknowingly reside inside or close to a large impact structure. It has been demonstrated in this volume that the list of accepted impact structures needs to be reevaluated and vastly expanded on the basis of the principles discussed herein.

The importance of the discussion of the real mechanical behavior of materials found in this volume cannot be overemphasized because it represents an accurate description of the mechanical behavior of geologic materials. For example, the assumption of the formation of dikes via intrusion has been effectively challenged based on analysis of data on the observed mechanical behavior of solids and liquids. Dikes are formed by adiabatic shear induced from the compressive stresses produced during an impact cratering event. In addition, an accurate understanding of the deformation and fracture of materials is essential to the development of true models for the formation of most geologic structures and geologic processes such as earthquakes.

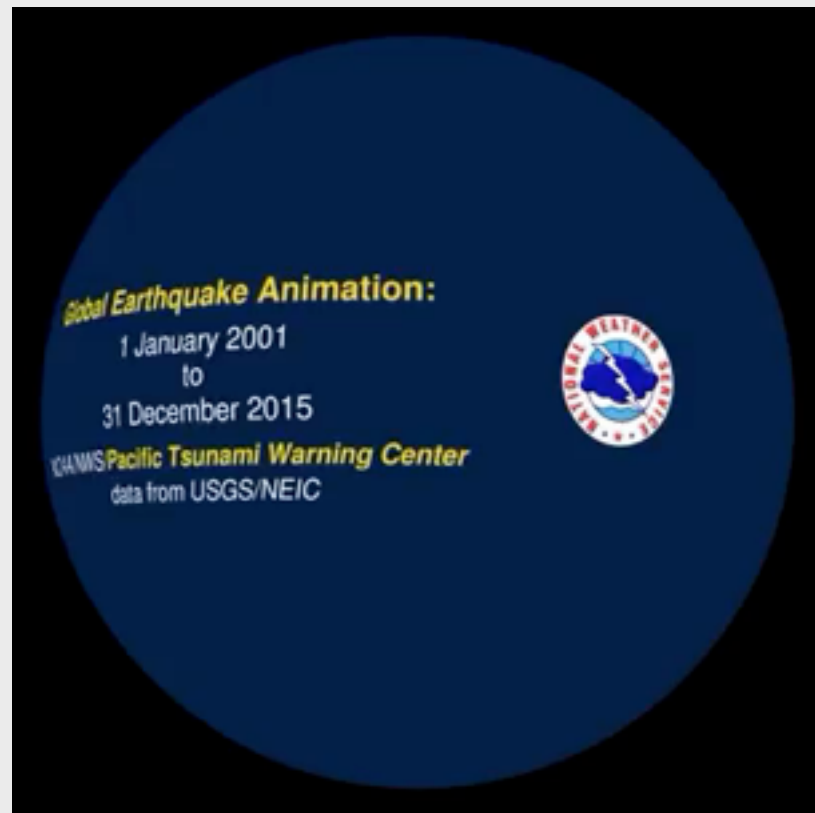
In spite of the fact that in this volume an equation for relating **both** the energy and momentum of an impactor with the amount of ejecta from an impact has been established based on laboratory-scale data, at this writing it is clear that the full set of scientific principles that govern impact behavior of geologic materials have not been incorporated into a comprehensive computational model for the impact cratering process. At this stage, the high pressure physics aspects that govern the early-stage cratering have not been coupled appropriately into any currently known computer model that accurately incorporates the processes in play during late-stage cratering. Hopefully, the discussion in this volume will guide and encourage the development of an accurate computer model.

This book should be considered only as a starting point for the study of Impact Geology. Hopefully the preceding pages have provided many of the pieces and assembled enough of the jigsaw puzzle that represents the field of Impact Geology to cause major progress in the development of this science. Significant progress in any branch of science is only achieved when the fundamentals are elucidated and widely recognized. With the basic ideas presented in this volume, one can progress to the development of an accurate geologic history of the Earth.

As a final footnote, the following video, assembled by the USGS and recently posted on the internet, should provide considerable food for thought regarding the relationship between bands of earthquakes and the rims of very large impact structures on Earth. It is obvious that the patterns of most of these

earthquake bands display an arcuate geometry...a strong indication of rims of impact structures. As can be seen in the video, there are many arcuate earthquake patterns around our globe that are coincidental with prominent geologic features... e.g. the Aleutian Island chain, the Greater Sunda Islands, and the Himalayas along with the Tibetan Plateau.

MOVIE 7.1 Global earthquake record from 1/1/2001 to 12/31/2015. Animation of data from USGS/NEIC.



Circle diameters indicate earthquake magnitude, and the color indicates depth of the quake.